

# **Twisted, localized, and modulated states described in the phenomenological theory of chiral and nanoscale ferromagnets**

**D I S S E R T A T I O N**

**zur Erlangung des akademischen Grades**

**Doctor rerum naturalium  
(Dr. rer. nat.)**

**Vorgelegt**

**der Fakultät Mathematik und Naturwissenschaften  
der Technischen Universität Dresden**

**von**

**DIPL. PHYS. ANDRIY LEONOV**

**geboren am 13.04.1980 in Kramatorsk, Ukraine**

**Eingereicht am**

Die Dissertation wurde in der Zeit von 08/2008 bis  
08/2011 im Institut für Theoretische Festkörperphysik angefertigt.

1. Reviewer:
2. Reviewer:

Day of the defense:

Signature from head of PhD committee

# Abstract

The goal of the present thesis is to treat a wide diversity of problems in magnets by the tools of the modern computational micromagnetism. As an application of the self-elaborated numerical techniques this thesis includes a phenomenological description of magnetic phenomena in magnets with different geometry on nanoscale (**part I**) and in non-centrosymmetric magnets with chiral Dzyaloshinskii-Moriya interactions (**part II**).

**Part I.** *Nanomagnetic systems* are well-prepared and controlled objects which induce growing interest for the understanding of magnetic behavior down to nanoscale. From one side, experiments on these carefully prepared and defect-free nanoobjects can serve as tests on classical results from micromagnetism. From the other side, nanosystems with multiformity of structural design provide an arena for the research of different aspects of surface-induced interactions. Surface-induced interactions in nanomagnets appear due to complex changes of the electrical and magnetic properties of surface layers and essentially modify their properties. The role of surface-induced contributions substantially increases with a perpetual miniaturization of magnetic nanostructures. Theoretical studies of the present thesis focus mainly on the effect of surface-induced uniaxial anisotropy in the stability and phase transitions of different homogeneous and inhomogeneous magnetization distributions in nanomagnets. Surface anisotropy competing with the intrinsic magnetocrystalline cubic anisotropy is found to influence the magnetization processes in various geometries of nanosystems, such as extended magnetic nanolayers, nanowires/nanotubes, and very small single-domain nanoparticles. In the present thesis, a micromagnetic model to describe magnetization processes in systems with competing magnetic anisotropies has been extended, generalized, and adapted to investigate nanomagnetic systems. Micromagnetic calculations have been implemented for detailed analysis of recent experimental results:

(i) In layered magnetic nanostructures, e. g., in diluted magnetic semiconductors as (Ga,Mn)As and (In,Mn)As, competing anisotropies are known to result in the formation of specific multidomain states. A comprehensive analysis of the spin configurations in coexisting phases and parameters of domain structures versus the applied field is given for different values of the magnetic anisotropies and relative orientations of the anisotropy axes. Phase diagrams in components of applied and internal magnetic fields have been presented for such systems. These phase diagrams display regions of multi-phase domain structures. Lability lines of the phase diagrams span the regions with a remarkable transformation of the internal do-

---

main walls. Transformations for a single domain wall pinned in a constriction of a (Ga,Mn)As microdevice have been analysed theoretically. As a result, the strongly changing width and profile of the domain wall may have measurable consequences in these materials. Finally, for epilayers with perpendicular anisotropy, a theory of the depolarization effects has been presented and the geometrical parameters of stripe and bubble domains as functions of a bias field have been calculated.

(ii) In magnetic nanoparticles according to numerous experiments, the magnetic states are also strongly affected by the competition of surface induced and intrinsic magnetic anisotropies. Micromagnetic calculations done in the present thesis show that a proper choice of nanoparticle shape and surface preparation can be used to adjust their magnetic properties, in particular to stabilize the magnetization along one direction and to suppress superparamagnetism. It has been found out that the competition of various contributions to the effective anisotropy entails multiple magnetization states and the possibility to switch magnetization from one stable homogeneous state to another that are not necessarily equilibrium states. It has been demonstrated how to take into account the demagnetizing effect of the nanoparticle surface, which cannot be included in an effective uniaxial anisotropy. The analysis of the topologically different phase diagrams gives full information on stable states and the magnetic switching fields. The calculated magnetic phase diagrams include different magnetization processes alternative to the classical Stoner-Wohlfarth scenario.

(iii) In ferromagnetic nanowires and nanotubes magnetic couplings induced by lateral surfaces can overcome the stray-field forces and stabilize inhomogeneous states where the magnetization vector rotates along or perpendicular to radial directions as Néel or Bloch vortex, respectively. Depending on the surface anisotropy constants vortices are formed by a continuous rotation of the magnetization vector away from the homogeneous state with collinear longitudinal magnetization. Depending on the material and geometrical parameters different types of Néel and Bloch vortices can exist in nanowires and nanotubes. The phase diagram of the solutions includes stability regions of different vortex states and homogeneous phases with longitudinal or transverse magnetization separated by first- or second-order transition lines. Signatures of vortex states are discussed in relation to experimental observations on magnetization processes in magnetic nanowires. In particular, vortex states may be responsible for certain anomalies of the magnetoresistance in nanowires. For nanotubes solutions for twisted states exist similar to the inhomogeneous phases in ferromagnetic nanolayers.

**Part II.** In *non-centrosymmetric magnets* with the chiral Dzyaloshinskii-Moriya exchange, micromagnetic calculations are done as applied to modulated states unconventional in magnetism — one-dimensional spiral states and two-dimensional chiral skyrmions. All the calculations have been implemented within the phenomenological Dzyaloshinskii theory for chiral magnets. But due to the deep connection of phenomenological models for different condensed-matter systems, the results of numerical simulations may also address solitonic textures in chiral liquid crystals, ferroelectrics, multiferroics, or metallic glasses. The thesis mainly focuses on the uncom-



---

mon properties of chiral skyrmions — isolated or composed into extensive skyrmion lattices. It is shown that isolated skyrmions are smooth, topological, and static spin textures embedded into homogeneously magnetized 'parental' state. The relevant length scale of magnetic inhomogeneity squeezed into skyrmionic knot is tuned by the competition between direct and chiral exchange. Such localized skyrmionic excitations may be controlled and manipulated, and therefore, may find application in spintronic devices. Skyrmionic "particles" may be also driven together to form complex non-collinear magnetic textures – skyrmion lattices. The formation of the lattice is determined by the stability of the localized solitonic cores and their geometrical incompatibility that frustrates homogeneous space-filling. During the last years an intensive search for such skyrmions has been undertaken in chiral helimagnets with the cubic chiral B20-structure like MnSi and FeGe. Recent experimental results clearly indicate a complex multidimensional character of chiral modulated magnetic states in small regions of the phase diagrams of chiral magnets near the ordering temperatures. Two years ago, chiral skyrmions (isolated and bound into hexagonal lattices) have been microscopically observed in thin layers of cubic helimagnets (Fe,Co)Si and FeGe in a broad range of temperatures and magnetic fields far below the precursor regions. Such an intensive quest for skyrmions has been inspired, from one side, by earlier experimental observations of unconventional magnetic properties in precursor regions and, from the other side, by theoretical predictions on skyrmion matter made by A. N. Bogdanov et al. starting in 1989 and subsequent works. The numerical calculations carried out in the present thesis extend the previous theoretical results and provide a theoretical basis for the description of experimental results.

(i) Skyrmion and helical states with constant length of the magnetization  $M = \text{const}$  are considered to be a good approximation for the structure of modulated states far from the ordering temperature. Distribution of the magnetization in these textures is characterized only by the angular order parameter, and the magnetization processes are accompanied by the change of characteristic sizes — the skyrmion lattice periods or circular skyrmionic cores. Because of a fixed sense of rotation, the soliton-soliton interaction bears repulsive character. The equilibrium parameters of skyrmion lattices so far have been calculated within the circular-cell approximation: the actual hexagonal cell of the skyrmion lattice in micromagnetic calculations had been substituted by the circle. Numerical methods of the present thesis eliminate this deficiency and treat the skyrmion solutions on two-dimensional numerical grids. As the energy difference between various modulated phases is very small, rigorous solutions for skyrmions allow to address the problem of skyrmion thermodynamical stability more precisely. The influence of small anisotropic energy terms (uniaxial, cubic, and exchange anisotropies) on the skyrmion structures and the related question of skyrmion stability are comprehensively answered in the present thesis. It is shown that, due to the combined effect of magnetic field and small anisotropic contributions, skyrmion lattices can be formed as thermodynamically stable states in large intervals of magnetic field and temperatures in cubic helimagnets. It is argued that this mechanism is responsible for the formation of skyrmion states observed in

---

thin layers of (Fe,Co)Si and FeGe.

(ii) Close to the Curie temperature  $T_c$ , it was found that the interaction between separate localized skyrmions, being repulsive in a broad temperature range, becomes attractive. A fundamental parameter, the confinement temperature  $T_L$ , separates the temperature interval into the part with regular helical and skyrmion textures ( $0 < T < T_L$ ) and a narrow region with attractive (confined) modulations ( $T_L < T < T_c$ ). The structure of skyrmion solutions in the region of confinement is characterized by the longitudinal and angular order parameters. Different skyrmion lattices may be "designed" with soft modulus. Skyrmion textures respond to the applied magnetic field and changes of temperature by simply adjusting the length of the magnetization and can be even continuously transformed into each other. Detailed numerical analysis on two dimensional models shows that bound skyrmion states arise as hexagonal lattices of  $\pm\pi$ -skyrmions and square staggered lattices of  $\pi/2$ -skyrmions. Skyrmionic states can be rendered into thermodynamically stable phases by including into isotropic phenomenological model (which consists of exchange, DMI, and Zeeman energy terms) additional small magnetic couplings. It has been shown that the confinement of skyrmions provides the physical mechanism underlying unconventional effects observed near the ordering temperature of chiral magnets. The formation of skyrmionic matter by thermally driven transitions provides an example where mesoscale solitonic units are simultaneously nucleated and bound into extended modulated phases. These peculiarities of the skyrmionic matter near the ordering temperature may be responsible for experimentally observed precursor effects.

(iii) Micromagnetic simulations on skyrmion states in confined nanosystems allow to investigate systematically the influence of surface-induced interactions (in particular, surface-induced anisotropy) on skyrmion stability and structure. It has been shown that the interplay between intrinsic chiral interactions and surface/interface induced anchoring effects gives birth to a new class of multidimensional chiral modulations, convex-shaped "spherulitic" skyrmions. The shape of spherulites reflects the modifying effect of the layer surfaces, and their stability limits depend strongly on values of the material and geometrical parameters of the system. The equilibrium parameters of spherulitic modulations in layered nanosystems have been calculated as functions of applied fields, layer thicknesses, and values of surface and volume uniaxial anisotropies. Magnetic phase diagrams plotted in the space of control parameters, the values of the field and anisotropic constants, allow to find optimal parameters for stable spherulitic states in magnetic nanolayers. It is also argued that the solutions for spherulites may represent a defect-free alternative to the textures realized in liquid crystals and based on the different types of defects.

# Contents

<b>Introduction</b>	<b>1</b>
0.0.1. Thesis outline . . . . .	8
<b>1. The main principles of micromagnetism</b>	<b>13</b>
1.1. The purpose of micromagnetism . . . . .	13
1.2. Key Energy Terms of a Ferromagnet . . . . .	15
1.2.1. Exchange interaction . . . . .	15
1.2.2. Anisotropy energy . . . . .	19
1.2.3. Zeeman energy . . . . .	25
1.2.4. Stray field energy . . . . .	25
1.2.5. Energy contributions imposed by the variation of the magnetization modulus . . . . .	26
1.3. One-dimensional distributions of the magnetic vectors: domain walls and spirals . . . . .	26
1.3.1. Domain walls in uniaxial magnets: Bloch and Néel walls . . .	27
1.3.2. One-dimensional spiral modulations . . . . .	29
1.4. Two-dimensional distributions of the magnetic vectors - skyrmions .	31
1.4.1. Chiral flux-lines as the building blocks of skyrmionic matter .	31
1.4.2. Skyrmion lattices . . . . .	34
<b>I. Phenomenological theory of magnetization reversal in nanosystems with competing anisotropies</b>	<b>37</b>
<b>2. Reorientation transitions, multidomain states and domain walls in magnetic nanolayers with competing anisotropies</b>	<b>39</b>
2.1. Introduction . . . . .	39
2.2. Phenomenological model . . . . .	40
2.3. Phase diagrams in internal field components . . . . .	41
2.4. Magnetic phase diagrams in external field components . . . . .	50
2.5. Comparison with experiment . . . . .	54
2.6. Multidomain patterns . . . . .	58
2.6.1. The structure of domain walls . . . . .	58
2.6.2. Parameters of stripe domains . . . . .	61

2.7. Surface-induced anisotropy and multiple states in elongated magnetic nanoparticles . . . . .	65
2.7.1. "Shape factors" of surface-induced anisotropy . . . . .	66
2.7.2. Magnetization processes and multiple states in magnetic nanoparticles . . . . .	68
2.8. Summary and Conclusions . . . . .	70
<b>3. Surface-induced anisotropy and vortex states in ferromagnetic nanowires and nanotubes</b>	<b>73</b>
3.1. Introduction . . . . .	73
3.2. Micromagnetic equations . . . . .	75
3.3. Solutions for vortex profiles . . . . .	80
3.4. Conclusions . . . . .	82
 <b>II. Phenomenological theory of skyrmion and helical states in magnets with intrinsic and induced chirality</b>	 <b>87</b>
<b>4. Chiral skyrmion states in non-centrosymmetric magnets</b>	<b>89</b>
4.1. Introduction . . . . .	89
4.2. Phenomenological theory of modulated states in chiral helimagnets . . . . .	90
4.2.1. The general micromagnetic energy functional . . . . .	90
4.2.2. Reduced variables and characteristic lengths . . . . .	91
4.3. One-dimensional chiral modulations . . . . .	92
4.3.1. Helicoids . . . . .	93
4.3.2. Cone . . . . .	94
4.4. Chiral localized skyrmions: the building blocks for skyrmionic textures . . . . .	95
4.4.1. Equations . . . . .	95
4.4.2. Methods . . . . .	96
4.4.3. Analytical results for the linear ansatz . . . . .	98
4.4.4. Inter-skyrmion interaction and condensation of isolated skyrmions into the lattice . . . . .	99
4.4.5. Distinction of solutions for localized skyrmions from Belavin-Polyakov solitons . . . . .	99
4.5. Properties of ideal skyrmion lattices: double twist versus compatibility . . . . .	100
4.5.1. Methods: numerical recipes . . . . .	101
4.5.2. Features of ideal skyrmion lattices . . . . .	102
4.6. Competition of skyrmions with helicoids within the isotropic phenomenological model . . . . .	106
4.7. Stabilization of skyrmion textures by uniaxial distortions in non-centrosymmetric cubic helimagnets. . . . .	111
4.7.1. Isolated skyrmions in chiral helimagnets with uniaxial anisotropy	111

4.7.2.	Localized skyrmions and the manifold of solutions of micro-magnetic equations: the question of radial stability . . . . .	114
4.7.3.	Transformation of hexagonal skyrmion lattice under influence of uniaxial anisotropy . . . . .	118
4.7.4.	Stabilization effect of uniaxial anisotropy on skyrmion states .	118
4.7.5.	Magnetization curves . . . . .	119
4.8.	Stabilization effect of exchange anisotropy on skyrmion states. Phase diagram of states . . . . .	119
4.9.	Stabilization of skyrmion textures by cubic anisotropy . . . . .	122
4.9.1.	Distorted conical phase in the presence of cubic anisotropy . .	125
4.9.2.	Distorted helicoid in the presence of cubic anisotropy . . . . .	131
4.9.3.	Transformation of the hexagonal skyrmion lattice in the presence of cubic anisotropy . . . . .	134
4.9.4.	The phase diagrams of states in the presence of magnetocrystalline cubic anisotropy . . . . .	137
4.10.	Candidate materials for experimental observation of skyrmion textures	139
4.11.	Conclusions . . . . .	142
<b>5.</b>	<b>Skyrmion and helical states in thin layers of magnets and liquid crystals</b>	<b>145</b>
5.1.	Introduction . . . . .	145
5.2.	Phenomenological model of modulated states in thin magnetic films .	146
5.3.	Isolated skyrmionic states . . . . .	147
5.4.	Condensation of repulsive skyrmions into a lattice . . . . .	150
5.5.	Skyrmion lattices versus helicoids. Phase diagram of solutions . . . .	152
5.6.	Magnetostatic problem for isolated skyrmions . . . . .	153
5.7.	Observations of skyrmionic and helical textures in $\text{Fe}_{0.5}\text{Co}_{0.5}\text{Si}$ nanolayers: theoretical analysis . . . . .	156
5.8.	Observation of skyrmion states in chiral liquid crystals . . . . .	159
5.9.	Conclusions . . . . .	160
<b>6.</b>	<b>Confinement of skyrmion states in non-centrosymmetric magnets near ordering temperatures</b>	<b>163</b>
6.1.	Introduction . . . . .	163
6.2.	Phenomenological theory and equations . . . . .	166
6.3.	Solutions for high-temperature isolated skyrmions . . . . .	166
6.3.1.	Crossover of skyrmion-skyrmion interactions . . . . .	167
6.3.2.	Collapse of skyrmions at high fields . . . . .	168
6.3.3.	Phenomenon of confinement . . . . .	168
6.4.	The structure and properties of confined skyrmions . . . . .	170
6.4.1.	Condensation of isolated skyrmions into the lattice . . . . .	172
6.4.2.	Peculiar properties of bound skyrmions in the region of confinement . . . . .	175
6.4.3.	The structure of staggered half-skyrmion lattices . . . . .	176
6.5.	The field-driven transformation of skyrmion lattices near the ordering temperature . . . . .	179

6.5.1. Transformation of $-\pi$ -skyrmion lattice . . . . .	179
6.5.2. Field- and temperature-driven transformation of the staggered half-skyrmion lattice . . . . .	185
6.5.3. Field-driven transformation of $+\pi$ -skyrmion lattice . . . . .	185
6.6. Phase diagram of solutions for cubic helimagnets . . . . .	186
6.7. Chiral modulations in non-Heisenberg models . . . . .	189
6.7.1. Field- and temperature-driven transformation of modulated states for $\eta = 0.8$ . . . . .	190
6.7.2. Phase diagram of solutions for $\eta = 0.8$ . . . . .	193
6.8. Conclusions . . . . .	196
<b>7. Supercooled and glass-forming liquids as skyrmionic textures</b>	<b>199</b>
7.1. Introduction . . . . .	199
7.2. The frustration models for glasses . . . . .	200
7.3. SU(2) model of metallic supercooled liquids and glasses and the rela- tion to the Skyrme model . . . . .	201
7.4. Soft skyrmions in the SU(2) model . . . . .	203
7.5. Discussion . . . . .	206
7.6. Conclusions . . . . .	207
<b>Conclusions</b>	<b>209</b>
<b>List of original papers</b>	<b>213</b>
<b>Conferences</b>	<b>215</b>
<b>List of abbreviations</b>	<b>219</b>
<b>Bibliography</b>	<b>221</b>
<b>Acknowledgments</b>	<b>237</b>

# Introduction

Continuing miniaturization of artificial magnetic materials (ultrathin films, various multilayered systems, nanowires, assemblies of magnetic nanoparticles, and nanoclusters) leads to the appearance of a broad spectrum of extraordinary physical properties unknown in bulk materials and characterized as specific "nanomagnetic" phenomena [1–4]. Among them are exchange bias, strongly enhanced magnetoresistance, uniaxial anisotropy, magnetic modulations and others. Due to the complex physical and chemical processes on surfaces and interfaces, the surface-induced interactions in nanoscale magnets extend to the entire volume of a sample and modify substantially its electronic and magnetic properties [5–7]. The unique features of nanomagnets have already found their application in modern magnetoelectronic devices such as spin-valves and/or magnetoresistive heads. Besides, magnetic nanostructures provide a physical basis for ultradense data storage [8–10]. However to understand the magnetic properties in general and to use the whole potential provided by reduced dimensions, the comprehensive and systematic study of surface-induced effects is indispensable.

Magnetic thin films may be considered as excellent model systems for the investigation of magnetism in reduced dimensions. One of the key properties of magnetic layered systems is a *surface-induced magnetic anisotropy* [5, 11]. Numerous experiments on a wide variety of thin films demonstrate that this anisotropy is thickness-dependent and, moreover, may exceed the value of the intrinsic magnetic anisotropy by order of magnitude [5, 12]. The induced anisotropy stabilizes different inhomogeneous phases and as a consequence leads to the thickness-driven phase transitions between them [11, 13]. In a number of nanolayered systems, the intrinsic magnetocrystalline and induced anisotropies are comparable in the magnitude and compete with each other [VII]. This competition results in complex magnetization processes, especially in an applied magnetic field oblique to the easy anisotropy directions [12, 14]. The hysteresis magnetization curves in this case consist of two or even three subloops and are characterized by the formation of multidomain states [I-IV],[V-VII]. Such phenomena are also observed in ferromagnet- antiferromagnet bilayers, where the induced unidirectional anisotropy results in exchange-biased hysteresis curves [15, 16].

The first-principle numerical calculations offer considerable insight into the phenomena of surface-induced magnetic anisotropy [17, 18]. However, these *ab initio* calculations still cannot give a comprehensive manual of the magnetic structures and magnetization processes in real thin-layered objects. Traditional micromagnetic simulations, on the contrary, represent a consistent method successfully adapted to

---

nanosystems (chapter 1). In the **first part** of the present thesis, the micromagnetic framework based on the phenomenological theory of surface-induced interactions is applied to magnetic nanolayers (chapter 2), nanoparticles (chapter 2), and nanowires (chapter 3). The problem of competition between surface-induced and intrinsic interactions in the stabilization of multiple homogeneous states and inhomogeneous magnetic distributions is addressed. The evolution of magnetic states is studied under a variation of the applied magnetic field and different material constants. The peculiarities of magnetization processes, effects of hysteresis, wide diversity of magnetic field-driven phase transitions, and corresponding multidomain states are within the scope.

Magnetic surfaces and interfaces are also the prominent arena for the chiral magnetism. In magnetic nanostructures reduced dimensionality and complex interactions on surfaces and interfaces break inversion symmetry and induce *asymmetric (Dzyaloshinskii-Moriya) exchange coupling* [5,19,20]. As a result, the inhomogeneous magnetic textures acquire a definite chirality, i.e. the preferable (and only one) sense of the magnetization twisting. The decisive importance of the chiral energy contributions becomes apparent in the stabilization of multidimensional localized structures - chiral skyrmions [21–23] [IX-XI]. These magnetic inhomogeneities squeezed into the spots of nanometer scale have perspectives to be used in a completely new generation of spintronic and data storage devices where the skyrmionic units may be created, manipulated, and eventually driven together to form versatile magnetic patterns [IX-XI]. The chiral skyrmions are static topological solitons. Therefore, they may have advantages for applications [23] over other axisymmetric two-dimensional magnetization distributions like magnetic bubble domains [24] or vortices appearing in the magnetic nanodots [VIII]. The discovery of chiral magnetic skyrmions can be hardly overestimated and marks the inception of a new era in magnetism on nanoscale. Recently chiral skyrmion lattices stabilized by the induced DMI have been observed in monolayers of Fe on Ir(111) substrate [25]. Intensive attempts have been also made to observe skyrmionic states in other magnetic nanolayers and nanowires [26, 27]. The realm of chiral magnetism in thin-layered systems gained an increasing interest with the visual observation of chiral skyrmions in nanolayers of (Fe,Co)Si and FeGe [28, 29]. These compounds are cubic helimagnets itself and feature the chiral interactions due to asymmetry of the underlying crystallographic structure. Prepared as thin layers these compounds may introduce the controlled impact on the chiral modulations, for instance, by surface-induced anisotropy. It is expected that magnetic nanostructures as systems with induced chirality should display similar properties as magnetically ordered non-centrosymmetric crystals with intrinsic magnetic chirality. The **second (main) part** of the present thesis focuses on the systematic study of chiral one- and two-dimensional modulations in bulk non-centrosymmetric helimagnets (chapter 4) and investigation of their modification in confined systems under influence of surface uniaxial anisotropy (chapter 5). Additional effects related to the change of magnitude of the magnetization modulus near the ordering temperature (here called precursor effect) are considered in chapter 6.



---

Multidimensional localized structures (topological defects or localized states) are the focus of research in many fields of modern physics [30, 31]. Since the late 1960s, the problem of soliton-like solutions of non-linear field equations has been addressed in condensed matter physics, biophysics, in particle and nuclear physics, in astrophysics, and cosmology [32]. From fundamental point of view, the interest in such solutions is related to the explanation of countable particles in continuous fields. Within the structural theory the particle-like properties are ascribed to localized solutions of nonlinear field equations and the physical fields are described by the asymptotic behavior of corresponding solutions. Hobart and Derrick [33, 34], however, found with general arguments that multidimensional localized states are unstable in many physical field models: inhomogeneous states may appear only as dynamic excitations, but static configurations collapse spontaneously into topological singularities [34]. As a consequence, the solutions of corresponding non-linear field equations are restricted to one-dimensional solitons.

The instabilities of localized field configurations can be overcome, if the energy functionals contain, for example, contributions with higher-order spatial derivatives. This original idea of Tony Skyrme in 1960s succeeded in describing the nuclear particles as localized states [35]. And the name "skyrmion" after Skyrme implies these localized solutions. From the other side as it was mentioned earlier, the instability of multidimensional localized states may be avoided in condensed matter systems with broken inversion symmetry, where chiral interactions (energy terms linear with respect to spatial derivatives of order parameters) play the crucial role in their stability. In condensed matter physics chiral interactions arise due to structural handedness. Particularly, in magnetic non-centrosymmetric crystals chiral asymmetry of exchange interactions originates from quantum-mechanical Dzyaloshinskii-Moriya (DM) coupling [36, 37]. In chiral liquid crystals (LC), the acentric shape of underlying molecules is at the heart of chiral effects. Chiral interactions may appear also in many other systems: in ferroelectrics with a non-centrosymmetric parent paraelectric phase, non-centrosymmetric superconductors, multiferroics [20, 27, 38], or even in metallic supercooled liquids and glasses [39, 40]. Localized states in these systems are also named skyrmions by analogy with the Skyrme model for mesons and baryons [35].

In a large class of ordered condensed media, chiral couplings present the only mechanism to stabilize skyrmionic textures, as there exist no physical interactions providing the energy contributions with higher-order derivatives considered by Skyrme [35]. This fact singles out chiral condensed-matter systems into a particular class of materials with unique skyrmionic states. In the present thesis I consider a special type of localized configurations in a classical three-dimensional vector field  $\mathbf{m}$ , which has three components  $(m_x, m_y, m_z)$ . Multiple modulations occur as textures with localized twists in two spatial directions, which can be homogeneously extended into the third direction  $z$  as skyrmionic filaments or string. The vector  $\mathbf{m}$  is parallel to  $z$ -axis at the center and antiparallel at the boundary (Fig. 0.1 (a)). Skyrmionic matter is created by the condensation of these solitonic units (Fig. 0.1 (b), (c)). Such two-dimensional localized states may be also called "baby-skyrmions" to distinguish them from three-dimensional solutions of the Skyrme model [35].

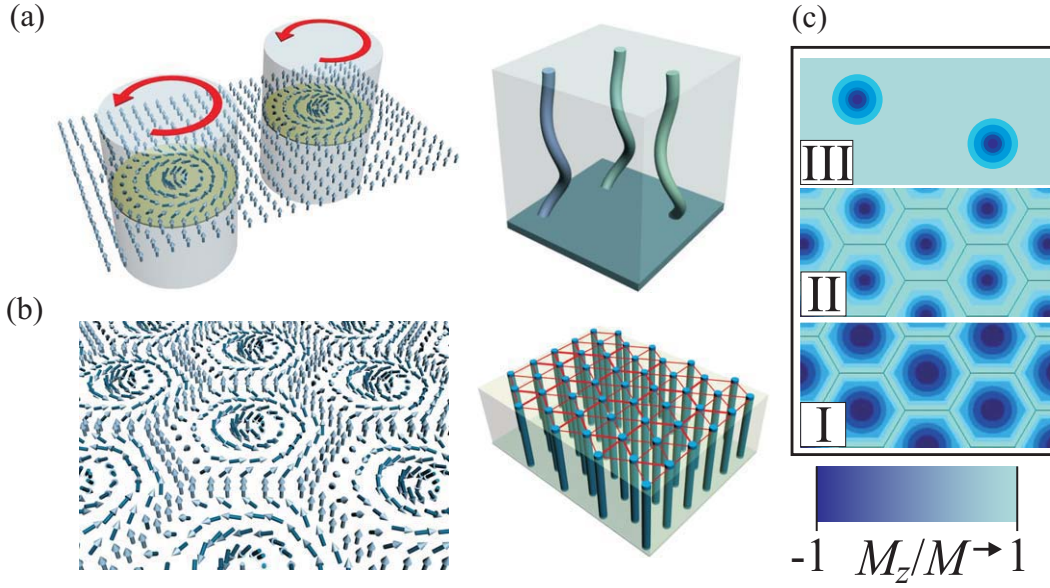


Figure 0.1.: Sketch of the axisymmetric distribution of the magnetization in isolated skyrmions (a) and hexagonal skyrmion lattice (b). (c) the evolution of skyrmion states with increasing magnetic field shown as snapshots of the  $m_z$ -component of the magnetization: hexagonal lattice (I) by expanding its period (II) transforms into the system of isolated repulsive skyrmions (III).

The investigations of chiral modulation in magnetism have been started by Dzyaloshinskii in 1964 [41] which can be considered as the birth year of chiral magnetism. Dzyaloshinskii demonstrated that chiral interactions can stabilize spatially modulated structures with a fixed rotation sense of the magnetization [41–43]. Within a phenomenological theory he derived solutions for the magnetization distribution in one-dimensional modulated states (spirals or helices) (see Fig. 4.1 (a)) [43]. Following the pioneering works of Dzyaloshinskii [41–43] chiral one-dimensional modulations have been investigated theoretically in different classes of non-centrosymmetric magnetic crystals (see bibliography in Refs. [44, 45]). Phenomenological functionals introduced by Dzyaloshinskii (see Eq. (4.1)) and their variations have been used as basic models for interpretation of experimental results in non-centrosymmetric magnetic materials, and beyond as a general foundation for the study of modulated phases [46, 47]. The phenomenological model of Dzyaloshinskii plays a similar role in chiral magnetism as the Frank energy in liquid crystals [48] and the Landau-Ginzburg functional in superconductivity [49, 50]. In non-centrosymmetric magnetic and liquid crystal systems chiral states are stabilized by the energy contributions, which have the same phenomenological form. Deep physical relations and common physical features of inhomogeneous textures in magnetic and liquid crystal materials are reflected in mathematical similarity of phenomenological equations for both systems. Important common physical aspects and mathematical relations also exist between chiral skyrmions in non-centrosymmetric magnets and Abrikosov vortices

---

and skyrmions in type II superconductors.

During last decades the spatially inhomogeneous spiral states have been experimentally discovered in several classes of magnetic bulk crystals. Most prominently, chiral modulations have been observed in a group of cubic non-centrosymmetric magnets (MnSi, FeGe and (Mn,Co)Si, (Fe,Co)Si, (Cr,Mn)Ge alloys) [28, 29, 44, 51, 52], in easy-plane hexagonal magnets as CsCuCl<sub>3</sub> and RuCuCl<sub>3</sub> [53–55], in a group of tetragonal antiferromagnets [56–58], and some other magnetically ordered crystals [44, 45]. It was also found that chiral interactions play an important role in multiferroic systems [59]. Helical magnetic order was identified as a mechanism for the magneto-electric (ME) effect in several materials like, e.g., RMnO<sub>3</sub> (with R=Tb, Gd) [61] and RMn<sub>2</sub>O<sub>5</sub> (R=Tb, Dy, Ho) [59, 60]. Strong influence of chiral interactions on the magnetic properties of non-centrosymmetric magnetic metals was considered in Refs. [31, 62] and recently discovered non-centrosymmetric superconductors [63]. It should be mentioned, however, that the spiral structures in such non-centrosymmetric helimagnets are essentially different from numerous other spatially modulated states in systems with competing exchange interactions [44]. The latter are characterized by rather short periods, usually including only few unit cells, and an arbitrary rotation sense. Quite to the contrary, chiral modulations usually have long period and a fixed sense of rotation. For example, in cubic helimagnet FeGe the periodicity length of the helix in zero field was found to be 70 nm (or 149 unit cells), and cubic B20 alloys Fe<sub>x</sub>Co<sub>1-x</sub>Si have even larger period (with maximal value of 230 nm for  $x = 0.3$ ) [51, 64].

The assumption of an important role of Dzyalshinskii-Moriya interactions in magnetic nanostructures is supported by recent spin-sensitive scanning tunnelling microscopy (STM) of chiral helical structures in ultrathin magnetic films of Mn atoms grown on a tungsten (110) substrate by Bode et al. [27]. The unique chirality of the spiral state was identified by the shift of the pattern in an applied magnetic field. The experimental results were combined with sophisticated first-principle calculations of the electronic structure of the manganese surface. Such a system used by Bode et al. [27] is an outstanding example of the phenomena that the crystalline materials with full inversion symmetry lose it when prepared as thin layers. Observations and investigations of physical effects imposed by the induced Dzyaloshinskii-Moriya interactions have been started only during the last years [27, 65, 66]. The effects of induced chiral interactions have been experimentally observed in Dy/Y multilayer films [65], in magnetic nanodisks [67] [VIII], and FePt films [68].

Investigations of chiral skyrmions in condensed-matter systems for a long time have been restricted to theoretical studies. In magnetism, existence of such particle-like states was predicted by A. N. Bogdanov in 1989 [69] and investigated theoretically in a series of papers [21, 22, 31, 45, 70]. The main achievement of Ref. [69] is the recognition of skyrmion states - an alternative to one-dimensional (helical) modulations - being the solutions of the field equations of Dzyaloshinskii's theory. A comprehensive analysis of possible skyrmion states with constant value of the magnetization in non-centrosymmetric magnets with different crystallographic symmetry and their radial stabilities have been carried out in Refs. [21, 70, 71]. The theoretical

---

results revealed a complex evolution of these particle-like patterns under the influence of the applied magnetic field and the values of magnetic uniaxial anisotropy. The total energy of the skyrmion textures is determined by a balance of two competing energy contributions, namely, a low-energy core and a high-energy edge area [31]. In the applied magnetic field, the extended magnetic states (skyrmion lattices) can be decomposed into an assembly of molecular units (isolated skyrmions). The existence of mesophases, composed of skyrmions as "molecular units", similar to vortex matter in type-II superconductors [72], was considered first in Ref. [31]. Helices as one-dimensional modulations are also only successions of localized domain walls, i. e. helical kinks. Existence of such localized states and the mechanism of their condensation into modulated states are the ruling principles of condensed matter systems described by Dzyaloshinskii's theory. In Ref. [21, 70, 73] it was proved that in uniaxial non-centrosymmetric ferromagnets skyrmion lattices are thermodynamically stable in a broad range of the applied magnetic fields. In the following papers the isolated and interacting skyrmions have been investigated theoretically in bulk non-centrosymmetric uniaxial ferromagnets [21, 69, 74, 75], antiferromagnets [45, 76, 77], and isotropic helimagnets [31, 77] as well as in confined centrosymmetric magnetic systems with surface/interface-induced chiral interactions (e. g. nanolayers of magnetic metals) [20]. In Ref. [31], the idea of skyrmionic matter at the boundary between the isotropic paramagnetic phase and the helical ground state was formulated for non-centrosymmetric magnetic metals. These textures can arise spontaneously during the formation of the ordered state at the Curie temperature and create thermodynamically stable states of a chiral magnet in a certain temperature range. The localization of the skyrmion core by the antiparallel magnetic field and spatial modulation of the magnetization length represent two different mechanisms providing the thermodynamical stability of these skyrmion states near the ordering temperature [45, 69].

The theoretical ideas of skyrmions in chiral magnets have triggered various experimental efforts to find evidence for these twisted textures [78, 79]. These experiments collected an impressive range of data that suggest complex magnetic order phenomena. A periodic skyrmion lattice has recently been proposed to form in the A-phase of MnSi under a magnetic field [79] or directly seen in FeGe [29] and (Fe,Co)Si [28] layers by Lorentz transmission electron microscopy.

MnSi is considered to be the most investigated chiral helimagnet - the "toy-tool" of the chiral magnetism, at least in theory - which keeps attracting a great deal of scientific interest [78–81]. Various effects observed in MnSi and other cubic helimagnets with B20 structure [51, 83] indicate multidimensionally modulated magnetic states conforming with the theoretical predictions of skyrmions and their properties [21, 31]. MnSi is an itinerant helimagnet with the ordering temperature  $T_c$  of about 29 K. Below  $T_c$  MnSi orders into the helical state with a period of about 18 nm and propagation vector along  $\langle 111 \rangle$  crystallographic directions. An experimental technique that is highly powerful for the investigation of bulk chiral helimagnets like MnSi is neutron scattering [84]. Neutrons carry magnetic moments and are proved to be a suitable tool to probe the underlying magnetic structures in condensed matter

---

systems. In the helical order for  $T < T_c$  small angle neutron scattering shows well defined Bragg peaks of the same intensity for equivalent  $\langle 111 \rangle$  directions. For  $T > T_c$ , however, a ring appears in the neutron scattering spectra [81, 82], which transforms into a half-moon for polarized neutrons. Such an unconventional diffuse scattering above  $T_c$  may be attributed to the existence of skyrmion-like textures. This is also accompanied by the strong anomalies of the heat capacity, thermal expansion, resistivity, and elastic properties of a high quality single crystal of MnSi [85, 86].

In the applied magnetic field the spiral state in MnSi transforms into a conical phase with the propagation direction along the field as shown by Ishikawa et al. [87]. Under increasing field the cone angle decreases and becomes zero at the critical field 600 mT. For higher fields only the homogeneously magnetized state can exist. Just below  $T_c$  an additional magnetic phase develops as a pocket inside the region of the conical phase. This magnetic phase is called A-phase, and the attempts to explain its structure are directly related to the search for skyrmion states. The small angle neutron pattern has a sixfold intensity for a random orientation of a sample in the A-pocket [79].

Recently, the existence of skyrmions was clearly revealed by microscopic observation in experiments on thin layers of cubic helimagnets with B20 structure, namely, in (Co,Fe)Si [28] and FeGe [29] far from the ordering temperatures. To image the magnetic structure, the authors used Lorentz force microscopy, since the neutron scattering is inapplicable in the case of thin films and does not allow the direct identification of non-periodic structures like isolated skyrmions, for instance. In the applied magnetic field and with changing temperature, the authors observed condensed phases of helicoids and skyrmion lattices which were able to set free the isolated units (kinks or isolated skyrmions) as in a crystal- gas resublimation. The break-through of Japanese researchers on the first clear conformation of *axisymmetric chiral localized states*, that are stabilized by a complex interplay of nonlinear and chiral effects, can be hardly overrated. From one side the experimental results of Yu et al. [28, 29] confirm the theoretical ideas elaborated earlier [31, 69]. From another side, however, they provide a new arena for the investigation of surface-induced effects on the modulated states in non-centrosymmetric helimagnets. The thicknesses of the layers in these experiments range from 15 nm to 75 nm (less or roughly about the length of the spiral) and tune the region of skyrmion existence from a vast to a tiny area in the applied magnetic field which is much higher than fields used in bulk materials. The conical phase - the main "competitor" of chiral skyrmions - is effectively suppressed in these nanolayers. Surface-induced uniaxial anisotropy (which can be roughly estimated from the characteristic fields, i.e. field of transition between helices and skyrmions, and/or field of disappearance of skyrmion lattice) must play an important role in the skyrmion stabilization [73].

The microscopic observation of skyrmions in magnetic nanolayers far from the ordering temperatures in Refs. [28, 29] is not called into question. On the contrary, the experimental results on chiral helimagnets near Curie temperatures mainly using diffraction or indirect evidence by transport measurements [88], remain essentially inconclusive and have been contested (see, e.g., [89]). Moreover, the interpreta-

---

tion of the "high-temperature" experimental data has been based on approximate solutions [79, 90] to the Dzyaloshinskii's model by using variational approaches in terms of a *mode instability*. The corresponding results do not describe the properties of skyrmions and the phase transition behavior of chiral magnets, which is governed by the *nucleation* of a localized mesoscale entities [21, 41, 91]. From the "high-temperature" experimental results, the relation of the microscopically observed skyrmions [28, 29] with the "precursor effects" near magnetic ordering [79–81] is unclear. This has introduced a new controversy to the long-standing problem of "precursor anomalies" in chiral magnetism.

The second part of the thesis reports the main physical properties of chiral skyrmions, elucidates their physical nature, and discusses peculiarities of skyrmionic textures in different classes of non-centrosymmetric magnetic systems. The first thorough investigation on skyrmionic magnetic textures within the general phenomenology of chiral magnets is presented. The obtained results imply that a host of novel effects may be studied in these systems including filament-like multidimensional solitons in three-dimensional bulk systems and baby-skyrmion textures in two-dimensions. Some important predictions are made on the novel effects like soliton clustering, skyrmion confinement, and finally complex mesophase formation by unconventional phase transitions. The present thesis derives first numerically rigorous solutions for helical and skyrmionic modulations of non-centrosymmetric magnetic systems in a broad range of the external parameters, establishes novel chiral effects, and discusses some important physical relations with other condensed-matter chiral systems (in particular, with liquid crystals). I show in details that such systems own exotic skyrmionic phases being based on multidimensional solitons, which are unusual objects themselves. The problem of the thermodynamical stability of skyrmion states with respect to the one-dimensional helical modulations is the central issue of the present thesis. The circumstances of skyrmion stabilization by small anisotropic contributions are comprehensively investigated for "low"- and "high-temperature" chiral skyrmions.

### 0.0.1. Thesis outline

The thesis is organized as follows:

In **the first chapter** I give a short introduction into the theoretical background of micromagnetism and into the basic properties of modulated skyrmion and helical states - solutions of the micromagnetic equations. First, I present the free energy of a magnet followed by the detailed description of the essential energy terms. Then, as an example of solutions minimizing the energy functional, I consider one-dimensional distributions of the magnetization - Bloch and Néel domain walls. Making the analysis of the domain wall energy in the presence of Dzyaloshinskii-Moriya interactions, I show under which circumstances it can become negative which leads to a proliferation of domain walls, i.e. to the appearance of the helical states. The chapter ends with a brief discussion of the topological and structural properties of two-dimensional

---

skyrmion states. It summarizes the known essentials of skyrmions taken in the forthcoming chapters for granted.

**The second chapter** may be considered as auxiliary as far as the skyrmion states are concerned. This chapter provides the basic analysis of homogeneous states in magnets with competing anisotropies and is instrumental for the further investigations on the thermodynamical stability of skyrmion states in chapter 4. On the other hand, the results of the present chapter can be used independently in the analysis of the interplay between intrinsic and surface/interface-induced magnetic anisotropies influencing the magnetization processes in nanomagnetic systems. I calculate the spin configurations in competing phases and parameters of accompanying multidomain states as functions of the applied field and the magnetic anisotropies. I construct magnetic phase diagrams and on their basis classify different types of the magnetization reversal which provide detailed analysis of the switching processes in magnetic nanostructures. The calculated magnetization profiles of isolated domain walls show that the equilibrium parameters of such walls are extremely sensitive to the applied magnetic field and values of the competing anisotropies and can vary in a broad range. For nanolayers with perpendicular anisotropy I calculate the geometrical parameters of stripe domains as functions of a bias field. These results are applied to analyse the magnetization processes as observed in various nanosystems with competing anisotropies, mainly, in diluted magnetic semiconductor films (Ga,Mn)As. At the end of this chapter I derive the values of surface-induced uniaxial anisotropy for ellipsoidal magnetic nanoparticles as functions of aspect ratios and particle sizes. I show that this specific anisotropy can stabilize multiple magnetic states in the system, suppresses demagnetization effects and prevents superparamagnetism. The calculated phase diagrams indicate the stability regions of different phases and the transition fields between them. I demonstrate that, by tuning sizes, geometry and surface anisotropy of elongated particles, a well-defined sequence of magnetic switching transitions can be realized in prescribed magnetic fields. This can be used in magnetic recording and spin electronic technologies.

In **the third chapter** on the example of magnetic nanowires and nanotubes I give an introduction into the phenomenological theory of surface-induced uniaxial anisotropy. The phenomenology allows to model a gradual penetration of surface-induced interactions into the volume of magnetic nanostructures and to investigate the inhomogeneous magnetization states defined by the surface symmetry. For chiral modulations in magnetic nanostructures and chiral liquid crystals considered in chapter 5, surface/interface induced interactions produce additional stabilization effects. At the same time one has to consider different magnetic inhomogeneities generated by the surface interactions themselves. The phase diagrams in such systems become extremely rich. The results of the present chapter give the basic insight in the phenomenon of surface-induced uniaxial anisotropy. In nanowires and nanotubes with large aspect ratio of height to radius, large induced magnetic anisotropy from lateral surfaces may stabilize non-collinear vortex-like states with magnetization vector rotating either along or perpendicular to radial directions. I derive and

---

solve micromagnetic equations for these "Néel" and "Bloch" vortices, and then analyse magnetization profiles and simplified analytical solutions. Phase diagrams for the occurrence of the different vortex phases in nanowires are presented in dependence on the surface anisotropy constants, the radius, and the saturation magnetization of the material. It is found that the transitions between the vortices and the homogeneous magnetization state in nanowires take place via continuous rotation, whereas the transition between the different vortices is first order. The phase diagram for hollow cylindrical nanotubes displays the regions with planar magnetization structures and twisted phases that are transforming by various first-order processes. As a limiting case, I consider the surface-induced anisotropy within the Néel approach, i.e., the surface effect being essentially confined to the near surface region.

In **the fourth chapter** I overview some aspects of the two - dimensional skyrmion states with constant value of the magnetization modulus considered in early papers of A. N. Bogdanov [21, 69, 70]. On the contrary to the circular-cell approximation used in Refs. [21, 73], I derive numerically rigorous solutions for baby-skyrmions by using the direct energy minimization for a standard phenomenological Dzyaloshinskii model. It is the task of this chapter to compare quantitatively the skyrmion features obtained by both methods. *In the first half* of the chapter I consider modulated helical and skyrmion states within the isotropic model including only the primary energy contributions stabilizing the chiral modulations, namely, direct exchange, Dzyaloshinskii-Moriya coupling, and Zeeman energy. After the solutions for one-dimensional cones and helicoids have been determined, I focus on the properties of isolated skyrmions obtained by numerical and analytical means. I show that skyrmion textures are composed of these countable localized magnetic units manipulated and organized into lattices by tuning the competition between direct and chiral Dzyaloshinskii-Moriya exchange. The theoretical results provide a comprehensive description of skyrmion lattice evolution in an applied magnetic field. From the isotropic phenomenological model it follows that skyrmions are only metastable solutions with respect to helices, and the inclusion of small anisotropic contributions is vital for the thermodynamical stability of skyrmions. *In the second half* of the fourth chapter I investigate the influence of the additional anisotropic contributions on the structure and stability of skyrmion states. I demonstrate that *uniaxial distortions* suppress the helical and conical states, and the skyrmion lattice can be formed as thermodynamically stable state in a broad range of magnetic field. Cubic and exchange anisotropy may stabilize skyrmions over cones for particularly chosen directions of the applied magnetic field with respect to the easy anisotropic axes. The results of the present chapter are related to different classes of non-centrosymmetric ferromagnets and can be extended to multisublattice magnets (e.g. antiferromagnets).

In **the fifth chapter** I consider the interplay of volume and surface-induced energy contributions in the formation of specific axisymmetric order-parameter distributions, spherulites, in confined mesoscopic systems. The confined geometry opens up the perspectives to create new chiral architectures and put into practice control



---

over them. I demonstrate the numerical solutions for the double-twisted entities, which exist as smooth static solitonic textures and are extended into the third direction in accordance with the modulating effect of the surfaces. The processes of condensation of such peculiar skyrmionic states into the lattice (spherulitic matter) are strongly defined by the surface anchoring and the force moving localized isolated units together. The thermodynamic advantage of spherulitic extended matter with respect to one-dimensional spiral modulations can be achieved in the vast part of the constructed phase diagram for the appropriately chosen ratios between internal and induced interactions. I also argue that frustrated spherulite patterns which are commonly observed in liquid crystal systems can be transformed into nonsingular skyrmionic textures by adjusting the material and geometrical parameters of the cells. I briefly touch the question of dipole-dipole interactions in their influence on the parameters of skyrmion states in thin magnetic layers. Finally, I show how theoretical findings of this chapter can be applied for the explanation of modulated states experimentally observed in nanolayers of cubic helimagnets and liquid crystals.

In the **sixth chapter** I provide the analysis of skyrmion and helical states with the variable length of the magnetization modulus. The theoretical results on such modulated states belong to the main achievement of the present thesis. They allow to establish the link between the "low-temperature" skyrmions with constant modulus theoretically investigated by A. N. Bogdanov et. al. [21, 69, 70] and experimentally observed by Yu et al. [28, 29] with those "high-temperature" skyrmions responsible for a number of precursor effects in the vicinity of the ordering temperature [80, 81]. Analysing the properties of isolated skyrmions, I show that the interaction between the chiral skyrmions, being repulsive in a broad temperature range, changes into attraction at high temperatures. This leads to a remarkable *confinement* effect: near the ordering temperature skyrmions exist only as bound states, and skyrmion lattices are formed by an unusual instability-type nucleation transition. Numerical investigations on two-dimensional models demonstrate the confinement and the occurrence of different skyrmion lattice precursor states near the ordering transition that can become thermodynamically stable by anisotropy or longitudinal softness in cubic helimagnets. Particularly, a square half-skyrmion lattice having no analogue with smooth constant modulus solutions may develop and even become a stable phase. The theory and results from numerical simulations demonstrate why a multitude of different small pockets of different phases is generically expected in a distinct temperature interval, interleaved between paramagnetic and helix magnetic state in non-centrosymmetric helimagnets like MnSi and FeGe. I also introduce a new fundamental parameter, *confinement temperature*  $T_L$ , separating the peculiar region with "confined" chiral modulations from the main part of the phase diagram with regular helical and skyrmion states.

Finally, in the **seventh chapter** I apply the concept of skyrmionic textures in chiral magnetic systems developed in Ref. [92] to continuum models of glass-forming liquids. A field theory with a frozen gauge background describes the frustrated tiling of the whole space by incompatible locally preferred clusters. The elastic energy

---

term due to decurving the template into a flat space is linear in spatial derivatives of the local order parameter and is responsible for stabilization of skyrmion units. A softened version of the order parameter allows to replace the notion of localized defects as disclination lines by smooth but more complex geometrical adaptation of ordering with regions of suppressed order-parameter intensity. I show that the skyrmions in the simplest version of these frustration models are close, but soft relatives of the hedgehog solutions in Skyrme's original  $SU(2)$  symmetric model for nucleons. I also argue that stable skyrmions are formed at elevated temperatures in molecular liquids and that their condensation into frustrated textures underlies the stability of supercooled and glassy states, which may resemble the states in extended dense nuclear matter.

**Conclusion and outlook** on the problems of skyrmion states in condensed-matter systems presented in the thesis are given at the end.

# 1. The main principles of micromagnetism

This chapter introduces the main principles of micromagnetism (section 1.1) and outlines the range of questions which may be addressed with the micromagnetic calculations. In the section 1.2 I describe the energy terms of a ferromagnet, make a notice which energy terms have a significant influence on the realized distributions of the magnetization and which may be omitted. As an auxiliary example, I consider the classical micromagnetic calculations of the structure of the Bloch and Néel domain walls (section 1.3.1). After that I show that Dzyaloshinskii-Moriya interactions lead to the transformation of domain walls into the one-dimensional modulated spiral states with a fixed sense of rotation (1.3.2). I give a short introduction into the basic properties of these chiral helical states (section 1.3.2) stabilized by the Dzyaloshinskii-Moriya interaction. In section 1.4 I proceed with two-dimensional magnetic textures - skyrmions. I define their internal structure (section 1.4.1 *A*), mention the question of topological and physical stability (section 1.4.1 *B*), and then consider the mechanism of the lattice formation from separate molecular units - isolated skyrmions (section 1.4.2).

## 1.1. The purpose of micromagnetism

With the term "micromagnetism" I infer the family of theoretical problems in which the well-formed distributions of the magnetization vector  $\mathbf{M}$  (called microstructures) are analysed. Micromagnetism is a phenomenological theory with the continuum representation of the magnetization: such an approach is correct only if characteristic length of the problem (the size of the sample, the width of domains, the period of the modulated states) is larger than the parameter  $a$  of the crystallographic lattice. According to the hierarchy of descriptive levels of magnetically ordered materials introduced in the textbook of A. Hubert and R. Schäfer [24] (Fig.1.1), micromagnetism addresses the samples with characteristic length scales 1-1000 nm and occupies the second level just above Atomic Level Theory - statistical thermodynamics of elementary magnetic moments ( $<1$  nm). The third and fourth levels of the hierarchy are, correspondingly, domain theory (1-1000  $\mu\text{m}$ ) and phase analysis ( $>0.1$  mm). In the present thesis I focus mainly on the micromagnetism and its application to nanomagnetic objects, although in the Chapter 2 I argue that the phase theory can be adapted successfully for nanomagnets. As micromagnetism is a phenomenological theory, it does not reveal the nature of such fundamental properties of a magnet as the saturation magnetization, magnetic anisotropy, and magnetostriction. In this

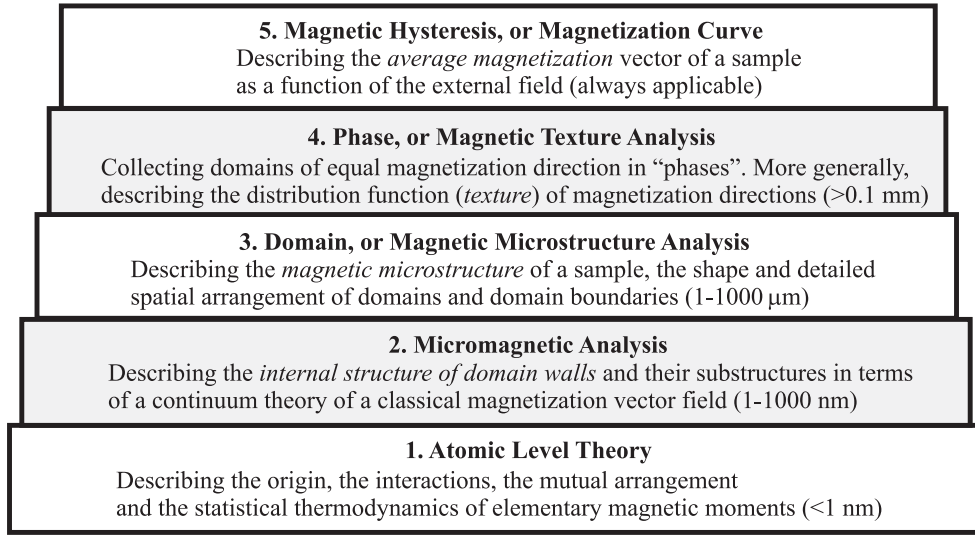


Figure 1.1.: The hierarchy of descriptive levels of magnetically ordered materials. The values in parenthesis indicate the sample dimensions for which the different concepts are applicable (adapted from [24]). The levels of the hierarchy considered in the present thesis are marked by grey color.

sense micromagnetism must not be confused with microscopical (quantum) theory of magnetically ordered materials. However, with respect to model domain theory micromagnetism considers magnetic crystals in a more detailed point of view and, for example, takes into account the internal structure of domain walls.

In micromagnetism the magnetization is represented as a vector function of spatial coordinates and time  $\mathbf{M}(x, y, z, t)$ . In the present thesis, however, effects related to the dynamics of the magnetization are not within the scope. In the following I consider the static magnetization distributions representing the globally stable or metastable states. The spatial dependence  $\mathbf{M}(x, y, z)$  can be obtained by minimizing the total free energy

$$W_{tot} = \int [w_{ex} + w_a + w_{DM} + w_H + w_m + w_{str} + w_{ms} + f_0 + w_s] dV \quad (1.1)$$

including exchange  $w_{ex}$ , anisotropy  $w_a$  (e.g., uniaxial  $w_u$  and cubic  $w_{cub}$  anisotropies), Dzyaloshinskii - Moriya  $w_{DM}$ , external field (Zeeman)  $w_H$ , and stray field  $w_m$  energy densities.  $w_{str}$  is the energy density of all stresses of non-magnetic origin,  $w_{ms}$  is a magnetostrictive energy density.  $f_0$  collects non-gradient terms of the magnetization and accounts for the effects related to the change of the modulus.  $w_s$  stands for the surface-induced energy contributions.

The free energy is the essence of micromagnetism: the interplay between different energy contributions determines the microstructure realized. In the subsequent sections I give an overview of energy terms defining the distributions of magnetic moments. I will present the energy terms as the continuum theoretical expressions which may be derived from symmetry considerations and by replacing the localized

spins  $\mathbf{S}_i$  in the corresponding quantum mechanical Hamiltonians of these energy terms. In this sense, the continuous micromagnetic approximation can be considered as a result of transition from an ensemble of discrete magnetic moments in atomistic models to a continuous vector field. Some energy terms, however, will be omitted in the following, for example, magnetostrictive effects and effects of non-magnetic stresses.

I start from the exchange interaction which is considered to be the strongest interaction in the hierarchy of magnetic energy terms.

## 1.2. Key Energy Terms of a Ferromagnet

### 1.2.1. Exchange interaction

#### *A. Isotropic exchange interaction*

Magnetic ordering in crystals is related to the exchange interaction due to which magnetic moments tend to align parallel (ferromagnets) or antiparallel (antiferromagnets) to each other. Such exchange interaction is isotropic with respect to rotation of the magnetization in the crystallographic lattice: exchange interaction only orders the magnetic moments, but does not chose preferable directions for them.

For electrons, the exchange interaction is the consequence of the Pauli principle, and the magnitude of exchange forces is determined by the overlap of wave function for neighbouring atoms (the details can be found in any book on magnetism, for example, in Ref. [93]). As it was discussed by Heisenberg in 1928, the exchange interaction originates from the quantum exchange term of the Coulomb interaction between electrons in orbitals on neighboring ions. The exchange energy of two neighboring spins making some non-zero angle is given by the Hamiltonian of exchange interaction:

$$H_e = -2J \mathbf{S}_i \mathbf{S}_j \quad (1.2)$$

where the coupling constant  $J$  is the exchange integral. The same expression can be derived by demanding the invariance of the Hamiltonian of particle interaction with respect to spatial rotations [94].

Equation (1.2) is relatively simple to derive for two electrons, but generalizing to a many-body system is far from trivial. Nevertheless, it was recognized in the early days of quantum mechanics that interactions such as that in Eq. (1.2) probably apply between all neighboring atoms. This motivates the Hamiltonian of the Heisenberg model which replaces the initial microscopic Hamiltonian by the sum:

$$H_e = - \sum_{ij} J_{ij} \mathbf{S}_i \mathbf{S}_j. \quad (1.3)$$

The factor 2 is included in the double counting within the sum. The exchange integral  $J_{ij}$  being the function of the radius-vector connecting  $i$ th and  $j$ th lattice sites decays exponentially with increasing the distance between adjacent atoms. There-

fore, often it is possible to take  $J_{ij}$  to be equal to a constant  $J$  for nearest neighbor spins and to be 0 otherwise. In the case of ferromagnets  $J > 0$  and  $J < 0$  for antiferromagnets.

A continuum theoretical expression used in the micromagnetism for exchange interaction may be obtained by an expansion of Eq. (1.3) into a Taylor series as described comprehensively, for instance, in the textbook of Chikazumi [93]:

$$W_{ex} = \int w_{ex} dV = A \int ((\nabla\alpha_1)^2 + (\nabla\alpha_2)^2 + (\nabla\alpha_3)^2) dV \quad (1.4)$$

Here,

$$A = \frac{2JS^2n}{a} \quad (1.5)$$

is the exchange stiffness constant with  $n$  being the number of atoms in a unit cell. Its zero-temperature value is related to the Curie point  $T_c$ :  $A(0) \approx kT_c/a$  [24].  $\alpha_i$  in Eq. (1.4) are direction cosines of the magnetization:

$$\alpha_1 = \sin\theta \cos\psi, \alpha_2 = \sin\theta \sin\psi, \alpha_3 = \cos\theta. \quad (1.6)$$

Even if the Heisenberg interaction between localized spins is not applicable (as in metallic ferromagnets), Eq. (1.4) still describes phenomenologically the stiffness effect to first order. Only the interpretation of the exchange constant has to be changed [24].

If the spin quantum number  $S$  is replaced by the local magnetization according to the relation,  $\mathbf{M}_s(\mathbf{r}) = g\mu_B\mathbf{S}_z(\mathbf{r})/\Omega(\mathbf{r})$  ( $S_z$  is the  $z$ -component of spin  $\mathbf{S}$  of the magnetic ion at position  $\mathbf{r}$ ,  $\Omega(\mathbf{r})$  is the atomic volume per magnetic ion,  $g$  is the Landé factor,  $\mu_B$  is the Bohr magneton), it can be obtained:

$$A = \frac{2JM_s^2n}{N^2g^2\mu_B^2a} \quad (1.7)$$

where  $N = 1/\Omega$ . According to Eq. (1.7) the temperature dependence of the exchange constant is given by that of  $M_s(T)$ . As well, the exchange integral  $J$  is related to the Curie temperature,  $T_c$ , within the framework of molecular field theory. The order of magnitude of the exchange constant  $A$  is about  $10^{-7} - 2 \times 10^{-6}$  erg/cm [ $10^{-12} - 2 \times 10^{-11}$  J/m]. The value of  $A$ , for example, for cobalt in thin layer is usually about  $2 \times 10^{-6}$  erg/cm [24].

The polar coordinates used for the magnetization in Eq. (1.6) allow to write Eq. (1.4) in another convenient form:

$$W_{ex} = A \int [(\mathbf{grad}\theta)^2 + \cos^2\theta(\mathbf{grad}\psi)^2] dV. \quad (1.8)$$

The exchange energy density can be expressed in a more general form by consider-

ing it phenomenologically as an energy of a magnetic inhomogeneity [94, 95]. As the components of the magnetization vector  $\mathbf{M}(\mathbf{r})$  change gradually from point to point for the states of a ferromagnet close to the homogeneously magnetized ground state, the energy density can be expanded into series of gradients of the magnetization. The coefficients of this expansion are tensors which possess the symmetry properties of a crystal. A systematic analysis of the stiffness term can be found in Döring's review of micromagnetics [95].

For magnets with the center of inversion the expansion starts from energy terms quadratic in gradients. Taking into account that the energy density does not depend on the direction of the magnetization, one can write a general expression for exchange energy density:

$$w_{ex} = \alpha_{ij} \frac{\partial \mathbf{M}}{\partial x_i} \cdot \frac{\partial \mathbf{M}}{\partial x_j} \quad (1.9)$$

where  $\alpha_{ij}$  are some tensors of second rank. For the ferromagnetic order to be stable, expression (1.9) must be positive definite [97], i.e. the principal values of tensor  $\alpha_{ij}$  must be positive. In uniaxial crystals tensor  $\alpha_{ij}$  has two independent components  $\alpha_{xx} = \alpha_{yy}, \alpha_{zz}$ . In cubic crystals,  $\alpha_{ij} = A\delta_{ij}$ .

### B. Asymmetric exchange interaction

In many magnetic crystals the magnetic properties may be strongly influenced by the asymmetric exchange interaction known also as the Dzyaloshinsky-Moriya interaction (DMI). When acting between two spins  $\mathbf{S}_i$  and  $\mathbf{S}_j$ , it leads to a term in the Hamiltonian which is generally described by a spin vector product:

$$H_{DM} = \mathbf{D}_{ij} \cdot (\mathbf{S}_i \times \mathbf{S}_j). \quad (1.10)$$

where  $\mathbf{D}_{ij}$  is the Dzyaloshinskii vector.

Dzyaloshinskii-Moriya interactions arise in certain groups of magnetic crystals with low symmetry where the effects of coupling (1.10) do not cancel. Their effect is to cant (i.e. slightly rotate) the spins by a small angle. In general,  $\mathbf{D}_{ij}$  may not vanish even in centrosymmetric crystals. Anisotropic exchange interaction occurs commonly in antiferromagnets and then results in a small ferromagnetic component of the moments which is produced perpendicularly to the spin-axis of the antiferromagnet. The effect is known as *weak ferromagnetism*. It is found, for example, in  $\alpha$ -Fe<sub>2</sub>O<sub>3</sub>, MnCO<sub>3</sub>, and CoCO<sub>3</sub>. To explain the phenomenon of weak ferromagnetism the interaction (1.10) was phenomenologically introduced by Dzyaloshinskii [98]. Moriya found a microscopic mechanism due to the spin-orbit coupling responsible for the interactions (1.10) [37].

Another fundamental macroscopic manifestation of the antisymmetric coupling (Eq. 1.10) takes place in non-centrosymmetric magnetic crystals. Dzyaloshinskii showed that in this case the interaction (1.10) stabilizes long-periodic spatially modulated structures with fixed sense of rotation of the vectors  $\mathbf{S}_i$ . Within a continuum approximation for magnetic properties, the interactions responsible for these modulations are expressed by inhomogeneous invariants. One calls these contributions

to the free magnetic energy, involving first derivatives of magnetization or staggered magnetization with respect to spatial coordinates, inhomogeneous Dzyaloshinskii-Moriya interactions. They are linear with respect to the first spatial derivatives of a magnetization  $\mathbf{M}$  of type [41]

$$\mathcal{L}_{ij}^{(k)} = M_i \left( \frac{\partial M_j}{\partial x_k} \right) - M_j \left( \frac{\partial M_i}{\partial x_k} \right). \quad (1.11)$$

where  $M_i$  and  $M_j$  are components of magnetization vectors that arise in certain combinations in expressions (1.11) depending on crystal symmetry, and  $x_k$  are spatial coordinates. Such antisymmetric mathematical forms were studied in the theory of phase transitions by E. M. Lifshitz and are known as *Lifshitz invariants* [97].

Depending on the crystal symmetry [41, 69], the Dzyaloshinskii-Moriya energy  $W_{\text{DM}}(\mathbf{M})$  includes certain combinations of Lifshitz invariants (1.11). Particularly, for important uniaxial crystallographic classes,  $(nmm)(C_{nv})$ ,  $\bar{4}2m(D_{2d})$ , and  $n22(D_n)$  functional  $W_{\text{DM}}$  can be written as

$$(nmm) : W_{\text{DM}} = \int w_{\text{DM}} dV = \int [D (\mathcal{L}_{xz}^{(x)} + \mathcal{L}_{yz}^{(y)})] dV, \quad (1.12)$$

$$(\bar{4}2m) : W_{\text{DM}} = \int [D (\mathcal{L}_{xz}^{(y)} + \mathcal{L}_{yz}^{(x)})] dV, \quad (1.13)$$

$$(n22) : W_{\text{DM}} = \int [D_1 (\mathcal{L}_{xz}^{(y)} - \mathcal{L}_{yz}^{(x)}) + D_2 \mathcal{L}_{xy}^{(z)}] dV. \quad (1.14)$$

where  $n = 3, 4, 6$ , and  $D_1, D_2, D$  are Dzyaloshinskii constants.

Lifshitz invariants for  $n$  ( $C_n$ ) and  $\bar{4}$  ( $S_4$ ) classes consist of terms with simultaneous presence of two Dzyaloshinskii constants related to directions  $x, y$  in the basal plane:

$$(n) : W_{\text{DM}} = \int [D_3 (\mathcal{L}_{xz}^{(x)} + \mathcal{L}_{yz}^{(y)}) + D_4 (\mathcal{L}_{xz}^{(y)} - \mathcal{L}_{yz}^{(x)})] dV, \quad (1.15)$$

$$(\bar{4}) : W_{\text{DM}} = \int [D_5 (\mathcal{L}_{xz}^{(x)} - \mathcal{L}_{yz}^{(y)}) + D_6 (\mathcal{L}_{xz}^{(y)} + \mathcal{L}_{yz}^{(x)})] dV. \quad (1.16)$$

For cubic helimagnets belonging to 23 (T) (as MnSi, FeGe, and other B20 compounds) and 432 (O) crystallographic classes Dzyaloshinskii-Moriya interactions are reduced to the following form:

$$W_{\text{DM}} = \int [D (\mathcal{L}_{yx}^{(z)} + \mathcal{L}_{xz}^{(y)} + \mathcal{L}_{zy}^{(x)})] dV = \int [D \mathbf{M} \cdot \text{rot} \mathbf{M}] dV. \quad (1.17)$$

Dzyaloshinskii-Moriya interactions stabilizing chiral magnetic states may be also induced by the symmetry breaking at the surface in confined systems as magnetic nanolayers, nanowires, and nanodots. As a genuine consequence of surface-induced DM couplings different types of chiral modulations have been observed [25, 27].



Therefore, thin film systems are appropriate candidate structures to study chiral magnetic skyrmions. In particular, micromagnetic analysis of the chirality selection for the vortex ground states of magnetic nanodisks shows that the sign and the strength of the DM coupling strongly influence their structures, magnetization profiles and core sizes [108]. The calculated relations between strength of the DM interactions and vortex-core sizes provide a method to determine the magnitude of surface-induced DM couplings in ultrathin magnetic films/film elements.

### *C. Anisotropic exchange interaction.*

MnSi with the DMI in the form (1.17) is one of the most investigated chiral helimagnets. The energy scales in this compound are well separated and allow to distinguish between different contributions to the ground state [99] (see also section 1.4.2 B). The isotropic exchange energy is the strongest energy contribution. It fixes the spins parallel to each other. The DMI are much weaker and induce the rotation of spins with the characteristic period of 18 nm (39 unit cells).

The symmetry analysis of the P2<sub>1</sub>3 structure of MnSi and FeGe was made by Bak and Jensen [99] and by Nakanishi [100]. The analysis showed that the expansion of the free energy in a slow-varying spin density  $\mathbf{S}(\mathbf{r})$  besides gradient terms of Eqs. (1.4) and (1.17) must be supplemented by the gradient term in the following form:

$$W_{\text{EA}} = B_{\text{EA}} \int \left[ \left( \frac{\partial \alpha_1}{\partial x} \right)^2 + \left( \frac{\partial \alpha_2}{\partial y} \right)^2 + \left( \frac{\partial \alpha_3}{\partial z} \right)^2 \right] dV. \quad (1.18)$$

which is called exchange anisotropy. The constant  $B_{\text{EA}}$  is reduced by order of magnitude with respect to the exchange stiffness  $A$ . The role of energy term (1.18) manifests itself in fixing the propagation directions of spiral states in MnSi [99] and may be considered as a third level of hierarchy of energy scales. As well, the anisotropic exchange can stabilize skyrmion states along particular crystallographic directions (section 4.9).

## **1.2.2. Anisotropy energy**

The tendency of the magnetization  $M$  to point along different fixed directions in space is described by the anisotropy energy  $W_a$ . Magnetic anisotropy arises from the spin-orbit interactions and demands additional energetic effort to turn the magnetization into any direction different from the preferred axes, called the easy axes. Generally, the magnetic anisotropy energy term has the same symmetry as the crystal structure of the material, and one calls it a magnetocrystalline anisotropy. The effects of deviations from ideal symmetry because of lattice imperfections are in turn described by the induced anisotropies.

In principle, the spin-orbit coupling underlying the magnetocrystalline anisotropy can be evaluated from basic principles. However, results of *ab initio* calculations are still restricted to the zero-temperature ground - state. Often these calculations are also very difficult or unreliable, in particular for high-symmetry systems like

cubic magnetic crystals. Therefore, it is easier to use phenomenological expressions (power series expansions that take into account the crystal symmetry) and determine the coefficients from the experiment. Magnetocrystalline anisotropy is usually small compared to the exchange energy.

### A. Uniaxial anisotropy

The simplest case of anisotropic contribution is uniaxial magnetic anisotropy. In hexagonal and tetragonal crystals an approximate expression for the anisotropy energy density is

$$\begin{aligned} W_u &= \int w_u dV = \int [K_{u1}\alpha_3^2 + K_{u2}\alpha_3^4] dV = \int [K_{u1}(\mathbf{a} \cdot \mathbf{m})^2 + K_{u2}(\mathbf{a} \cdot \mathbf{m})^4] dV = \\ &= \int [K_{u1} \cos^2 \theta + K_{u2} \cos^4 \theta] dV. \end{aligned} \quad (1.19)$$

where  $\mathbf{m} = M/|\mathbf{M}|$ . In these uniaxial systems the energy depends only on the angle between the magnetization  $\mathbf{m}$  and a coordinate axis parallel to the easy axis  $\mathbf{a}$ .

Usually, anisotropy energies are in the range  $10^2 - 10^7 \text{ J m}^{-3}$  what corresponds to an energy per atom about  $10^{-8} - 10^{-3} \text{ eV}$ . For example, hexagonal cobalt exhibits uniaxial anisotropy with  $K_{u1} = 4.53 \times 10^5 \text{ J m}^{-3}$ ,  $K_{u2} = 1.44 \times 10^5 \text{ J m}^{-3}$  at room temperature and the stable direction of spontaneous magnetization parallel to the  $c$ -axis. The values of higher-order terms are usually small and not reliably known. For large negative and positive values of  $K_{u1}$ , Eq. (1.19) describes an easy axis and easy plane, correspondingly. For intermediate values, i.e. under the condition  $-2 < K_{u1}/K_{u2} < 0$ , the easy direction lies on the surface of a cone with the angle  $\theta$  defined by the ratio between  $K_{u1}$  and  $K_{u2}$ :  $\sin \theta = -K_{u1}/2K_{u2}$ .

Sometimes a generalized second-order anisotropy has to be considered [24]. This applies to crystals of lower than tetragonal or hexagonal symmetry, or cases when several uniaxial anisotropies are superimposed. The energy density of this orthorhombic anisotropy is written as:

$$w_u = \sum_{ij} K_{ij} \alpha_i \alpha_j \quad (1.20)$$

where  $K_{ij}$  is a tensor of rank two.

In chapter 4 (section 4.7.4) I show that the simultaneous presence of easy-axis uniaxial anisotropy (Eq. (1.19)) and the applied magnetic field stabilizes skyrmion states in cubic helimagnets. The easy-plane anisotropy with negative  $K_{u1}$ , on the contrary, prefers only one-dimensional conical modulations of the magnetization (Fig. 4.16 (a)).

### B. Cubic anisotropy

For cubic crystals the basic expression for magnetic anisotropy is

$$W_{cub} = \int w_{cub} dV = \int [K_{c1}(\alpha_1^2\alpha_2^2 + \alpha_1^2\alpha_3^2 + \alpha_2^2\alpha_3^2) + K_{c2}\alpha_1^2\alpha_2^2\alpha_3^2 + \dots] dV. \quad (1.21)$$

Considering only the most important contribution  $K_{c1}$  one finds that the crystallographic directions  $\langle 001 \rangle$  and  $\langle 111 \rangle$  are easy axes for  $K_{c1} > 0$  and  $K_{c1} < 0$ , respectively. Taking into account the term with  $K_{c2}$  shows that for some values of cubic anisotropy constants easy axes along  $\langle 110 \rangle$  can be realised (see, for example, tables and phase diagrams of cubic magnets in [101]). For iron (at 20°C), for example,  $K_{c1} = 4.72 \times 10^4 \text{ J m}^{-3}$ ,  $K_{c2} = -0.075 \times 10^4 \text{ J m}^{-3}$ . For nickel (at 23°C),  $K_{c1} = -5.7 \times 10^3 \text{ J m}^{-3}$ ,  $K_{c2} = -2.3 \times 10^3 \text{ J m}^{-3}$  [93].

The Eq. (1.21) is written in the  $\langle 001 \rangle$ -based coordinate system. Very often, however, it is necessary to have the common expression for the cubic anisotropy in the coordinate system related to the direction of the applied magnetic field in a crystal:

$$w_{cub} = K_{ijkl}^{(1)} \alpha_i \alpha_j \alpha_k \alpha_l + K_{ijklmn}^{(2)} \alpha_i \alpha_j \alpha_k \alpha_l \alpha_m \alpha_n. \quad (1.22)$$

Here, the tensors  $K_{ijkl}^{(1)}$  and  $K_{ijklmn}^{(2)}$  are transformed to a new coordinate system with the help of transformation matrices  $\mathbf{T}$  [24]. Such a procedure used in this thesis to consider the skyrmion and helical states in the oblique magnetic fields (section 4.9).

More details about cubic, orthorhombic, and/or exchange anisotropy can be found in A. Hubert and R. Schäfer's textbook on magnetic domains [24].

In section 4.9 I consider orientational effect of cubic anisotropy on the propagation direction of helicoids in cubic helimagnets. Competition of cubic anisotropy with exchange anisotropy can induce reorientation transitions of helicoids from one preferable direction to another one. In chapter 2 I consider effect of competition between uniaxial and cubic anisotropies on the homogeneous states in magnetic nanolayers and nanoparticles.

### C. Surface-induced uniaxial anisotropy

Surface-induced anisotropy is a part of magnetic anisotropy arising due to the complex physical processes on surfaces/interfaces: symmetry breaking at the boundaries of the magnetic nanostructures itself, homogeneous and inhomogeneous strains created by lattice mismatch between substrate and magnetic layer, interdiffusion with nonmagnetic substrates and spacers. Such additional anisotropies being sensitive to the thickness of the sample and to the covering with different non-magnetic materials allow to vary the magnetic properties over a broad range, in particular, to fix the magnetization in desirable directions as in small particles or to stabilize different twisted phases of the magnetization.

In the simplest phenomenological model introduced by Néel about sixty years ago [102] the surface-induced anisotropy is treated as averaged over the thickness  $d$  of a magnetic thin layer. Then the effective anisotropy of the layer is written as

$$K_{eff} = K_V + \frac{K_s}{d} \quad (1.23)$$

where  $K_V$  is the volume anisotropy (per unit volume), and  $K_s$  is the surface contribution (per unit area, that is the dimension of the coefficient  $K_s$  is  $\text{J/m}^2$ ). If the influence of two surfaces is considered, factor 2 must be added to the second

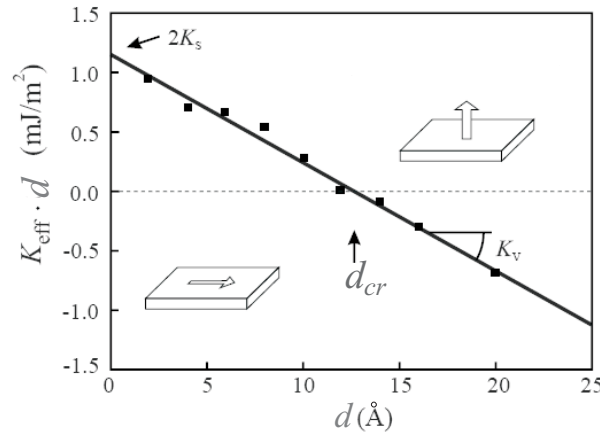


Figure 1.2.: Effective magnetic anisotropy of a Co layer in a Co/Pd multilayer as a function of the thickness  $d$ . The slope allows to determine  $K_V$ , the zero-crossing amounts to  $2K_s$  (adapted from [5]).

anisotropy term.

To illustrate the influence of the surface-induced anisotropy on the spin reorientation in magnetic layers I multiply Eq. (1.23) by  $d$ ,

$$K_{eff}d = K_Vd + K_s, \quad (1.24)$$

and plot dependence  $K_{eff}d$  versus  $d$ . The slope of the resulting curve allows to determine coefficient  $K_V$ , and the intersection of the curve with the ordinate axis - the surface anisotropy coefficient  $K_s$  (or  $2K_s$ ) [5]. As an example, Fig. 1.2 shows such a curve for a thin Co layer with variable thickness on the Pd substrate. Due to the negative slope of the curve the volume anisotropy  $K_V$  favours the in-plane orientation of the magnetization. The zero-crossing, however, occurs for a positive value of  $K_s$ , i.e. with the magnetization perpendicular to the film plane. Therefore, the critical thickness  $d_{cr}$  marks the reorientation transition from in-plane to out-of-plane orientation of the magnetization:

$$d_{cr} = -\frac{2K_s}{K_V}. \quad (1.25)$$

For the considered system  $d_{cr} = 13\text{Å}$ . Such behaviour is a general feature of all magnetic multilayers composed of Co/Pt(Pd), Co/Cu, Fe/Au or Ni/Cu bilayers.

It should be noted, however, that Néel model suffers from some shortcomings and cannot clarify some peculiarities of the layered systems. In particular, Eq. (1.24) does not explain an "anomalous" behaviour of the magnetic anisotropy with the non-linear character of the dependence  $K_{eff}d = f(d)$  (Fig. 1.3). To avoid these insufficiencies of the Néel's model, I will consider surface anisotropy in the framework of the phenomenological theory developed in Ref. [11] and proved to be successful in the explanation of different experimental phenomena. Within this model it is assumed that the surface-induced anisotropy extends into the depth of magnetic

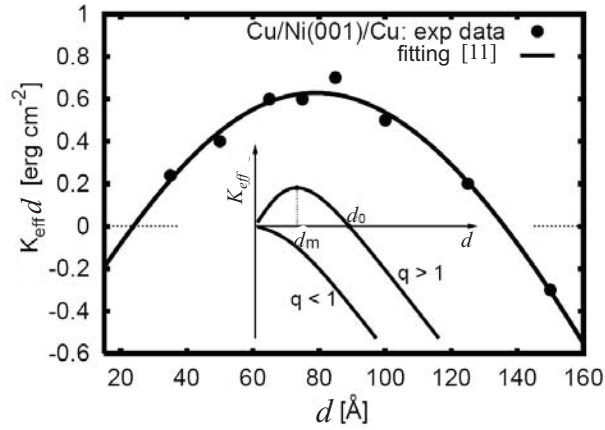


Figure 1.3.: Effective magnetic anisotropy in Cu/Ni/Cu sandwiches. Experimental data are taken from Ref. [103]. The fitting curve and the inset are taken from Ref. [11].  $q = (K_s^{(1)} + K_s^{(2)})/4\pi M$ .

layers, and the possible distributions of anisotropy coefficient  $K_s(\mathbf{r})$  are described by the general interaction functional:

$$\Phi_s = \int_V \left[ \alpha_s \sum_i \left( \frac{\partial K_s}{\partial x_i} \right)^2 + f(K_s) \right] d^3\mathbf{r}. \quad (1.26)$$

where the first term describes the stiffness of the field  $K_s(\mathbf{r})$  and  $f(K_s) = a_s K_s^2$  is a homogeneous function. The surface anisotropy has certain fixed values on the surfaces:

$$K_s \left( \frac{d}{2} \right) = K_s^{(1)}, \quad K_s \left( -\frac{d}{2} \right) = K_s^{(2)}. \quad (1.27)$$

Depending on the characteristic length

$$\lambda_s = \sqrt{\frac{\alpha_s}{a_s}}, \quad (1.28)$$

the present phenomenological model includes two limiting treatments of induced anisotropy as a pure boundary effect ( $\lambda_s/d \approx 0$ ) and the uniaxial anisotropy homogeneously distributed through the layer ( $\lambda_s/d \approx 1$ ). In Fig. 1.4 the profiles  $K_s = K_s(z)$  parametrized by the ratio  $\lambda_s/d$  are plotted. Here,  $z$  is a spatial coordinate across the layer.

Energy density of surface-induced interactions according to the proposed phenomenological theory [11] may be represented in the following generalized form:

$$w_s(\mathbf{r}) = \sum_i \eta_i(\mathbf{r}) \Xi_i(\mathbf{m}). \quad (1.29)$$

Here,  $\eta_i(\mathbf{r})$  are spatially inhomogeneous coefficients that are treated as internal variables similar to the field of the order parameter  $\mathbf{m}(\mathbf{r})$  (according to the functional

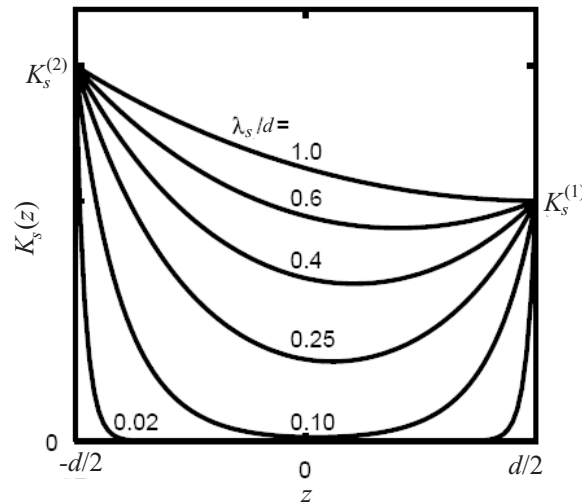


Figure 1.4.: Inhomogeneous distribution of the surface anisotropy coefficient  $K_s(z)$  in thin layered systems (taken from [11]). See text and Ref. [11] for details.

$\Phi_s$ , Eq. (1.26)).  $\Xi_i(\mathbf{m})$  are invariants describing induced interactions [20]. Energy of the surface-induced uniaxial anisotropy is written as

$$W_s = \int w_s dV = \int [K_s(\mathbf{r})(\mathbf{m} \cdot \mathbf{s})^2] dV \quad (1.30)$$

where  $\mathbf{s}$  is the unity vector perpendicular to the surface. Energy density of the surface-induced Dzyaloshinskii-Moriya interaction considered in Ref. [20] looks like

$$w_s = D(\mathbf{r})L(\mathbf{r}) \quad (1.31)$$

where  $D(\mathbf{r})$  is a spatially dependent Dzyaloshinskii-Moriya coefficient, and  $L(\mathbf{r})$  are the Lifshitz invariants (see Eqs. 1.11). In the present thesis, however, Dzyaloshinskii-Moriya interaction is supposed to be always homogeneous irrespective of the considered magnetic system - bulk or a nanoobject. Surface-induced uniaxial anisotropy, on the contrary, is treated as the energy contribution with the inhomogeneous coefficient  $K_s(\mathbf{r})$  including limiting cases. In the case of surface-induced uniaxial anisotropy constrained to the surface region with  $\lambda_s/d \rightarrow 0$ , the total magnetic energy (1.1) of a nanosystem can be simplified by reducing to a sum of the volume ( $w_v(\mathbf{r})$ ) and surface ( $w_s(\mathbf{r})$ ) contributions:

$$W_{tot} = \int_V w_v d\mathbf{r} + \int_S w_s d\mathbf{r}. \quad (1.32)$$

Then the equilibrium distributions of the magnetization  $\mathbf{M}(\mathbf{r})$  are derived by solving the Euler equations for the volume functional  $w_v(\mathbf{r})$  with the boundary conditions imposed by the surface energy  $w_s(\mathbf{r})$  (see e.g. [20, 223, 227]).

In chapter 3 I adapt the model of surface anisotropy for thin films with respect

to magnetic nanowires and nanotubes. Further, in chapter 5 I consider stabilization effect of surface anisotropy on skyrmion states in magnetic nanolayers. In chapter 2 (section 2.7) I show that the competition between intrinsic and induced anisotropies stabilizes different multiple magnetic states in elongated magnetic nanoparticles.

### 1.2.3. Zeeman energy

If a magnet is placed in an external magnetic field  $\mathbf{H}$ , then the elementary magnetic moments tend to align parallel to the field. The energy corresponding to this process is called Zeeman energy and is expressed in micromagnetism as:

$$W_H = - \int \mathbf{M} \cdot \mathbf{H} dV. \quad (1.33)$$

Zeeman energy as well as anisotropy energies (section 1.2.2) belongs to the local-energy terms, i.e. energy contributions defined only by the local values of the magnetization direction. The exchange energy (section 1.2.1) is also local in a sense, that it is calculated as a function of derivatives of the magnetization.

Zeeman energy (1.33) can be considered as the first part of the magnetic field energy. The second part is connected with the magnetic field generated by the magnetic body itself - stray field energy.

### 1.2.4. Stray field energy

Stray field energy is a consequence of the fact that all elementary magnetic moments interact with each other by the long-range classical dipole-dipole interactions. This energy contribution can be written as

$$W_m = -\frac{1}{2} \int \mathbf{M} \cdot \mathbf{H}_m dV. \quad (1.34)$$

The stray field  $\mathbf{H}_m$  is created by the surface and volume charges and obeys the magnetostatic equations

$$\text{rot } \mathbf{H}_m = 0, \text{div } (\mathbf{H}_m + 4\pi\mathbf{M}) = 0. \quad (1.35)$$

In the literature, different terms are used for the field  $\mathbf{H}_m$ . It is called either the magnetic stray field, the dipolar field, the demagnetizing field or the magnetostatic field.

For some particular cases the energy of stray fields has the form of effective uniaxial anisotropy. In chapter 4 I show that this treatment is valid for axisymmetric skyrmions and one-dimensional spirals in the bulk materials. Considering skyrmions in thin layers, the solution of the magnetostatic problem (Eq. (1.35)) is necessary. In section 5.6 I investigate the evolution of skyrmion solutions in the presence of demagnetizing fields on the surface.

Within the phase theory approximation [24] considered in chapter 2 the demagnetizing field is assumed to be uniform. This is justified for samples with "perfect" shape (ellipsoidal with limiting cases of plates and cylinders). Therefore, I will consider first homogeneous states in an effective internal field and then map them on the plane of external field components.

### 1.2.5. Energy contributions imposed by the variation of the magnetization modulus

$f_0$  in Eq. (1.1) comprises magnetic interactions imposed by variation of the magnetization modulus  $M \equiv |\mathbf{M}|$ . In a broad temperature range the magnetization vector practically does not change its length, and nonuniform magnetic states include only rotation of  $\mathbf{M}$ . Near the ordering temperature, however, the magnetization modulus becomes small ( $M \ll 1$ ) and strongly depends on the applied field and temperature. In this case the term  $f_0(\mathbf{M})$  represents energy expansion for small values of the magnetization according to Landau theory:

$$f_0(\mathbf{M}) = a_1 M^2 + a_2 M^4 \quad (1.36)$$

where  $a_1$  and  $a_2$  are corresponding coefficients of Landau expansion. The magnetic moment  $\mathbf{M}$  enters only in even powers because only even terms are invariant under a reversal in the sign of the magnetization (only for even powers of  $\mathbf{M}$  time reversal symmetry is preserved). The case  $a_1 = 0$  corresponds to the critical temperature where spontaneous magnetization appears. Therefore, one can write  $a_1$  in the form:

$$a_1 = J(T - T_c). \quad (1.37)$$

Effects imposed by spatial variation of the modulus  $M$  will be discussed in chapter 6 in application to modulated states near the ordering temperatures.

## 1.3. One-dimensional distributions of the magnetic vectors: domain walls and spirals

From the total free energy (1.1), variational calculus derives a set of complicated non-linear and non-local micromagnetic equations [24, 101]. The solution of these micromagnetic equations in general case is invoked to give the comprehensive description of different magnetic phenomena on nanoscale: magnetization processes, the appearance of domain structure of different types (or different inhomogeneous states), and evolution of magnetic structures under different circumstances etc.

Unfortunately, no generally applicable route for the solution of the generalized micromagnetic problem is available. Solving micromagnetic equations is difficult because they consist in a system of non - linear integro- differential equations. The magnetostatic problem requires solutions for the stray field  $H_m$ : this field originates from the distribution of magnetic vectors  $M(x, y, z)$  and, on the contrary, defines



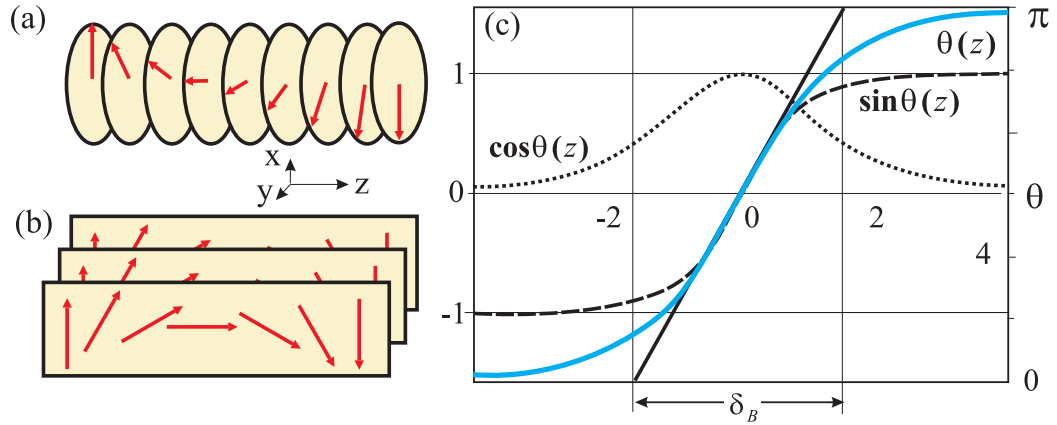


Figure 1.5.: The rotation of the magnetization vector from one domain to another through a  $180^\circ$  Bloch (a) and Neel (b) walls. Profiles  $\theta(z)$  (solid blue lines),  $\sin \theta(z)$  (dashed line), and  $\cos \theta(z)$  (dotted line) are plotted for the solution (1.42). Definition of the wall thickness  $\delta_B$  is shown. (Adopted from [24])

this distribution. Thus, one has to resort to some simplifications. The main focus of the thesis is the role of specific Dzyaloshinskii-Moriya interactions in stabilization of different modulated structures: spirals and skyrmions. As such structures represent one- and two-dimensional distributions of the magnetization, the micromagnetic equations can be handled numerically. The computer capabilities available nowadays make it possible to use numerical recipes to solve micromagnetic problems unsolved so far.

One-dimensional distributions of the magnetization are relatively easy to calculate using the methods of variational calculus, as first demonstrated by Landau and Lifshitz in their pioneering work [104]. The rotation of the magnetization  $\mathbf{M}$  from point to point depends only on one spatial coordinate, and the equilibrium distribution is accomplished as a result of competition between different energy contributions: in section 1.3.1 giving a short introduction into the classical theory of Bloch and Néel domain walls [104, 106] I show that the parameters of a domain wall are determined by the interplay of exchange and anisotropy energies; in section 1.3.2 I include Dzyaloshinskii-Moriya interaction into consideration of domain walls and show their transformations into spiral modulations with characteristic length defined by the stiffness  $A$  and Dzyaloshinskii constant  $D$ . In chapter 4 I consider the one-dimensional spiral modulations in more details and provide a comprehensive analysis of two-dimensional skyrmions in magnets with different crystallographic symmetry.

### 1.3.1. Domain walls in uniaxial magnets: Bloch and Néel walls

I start with the structure of classical Néel and Bloch domain walls. The calculation of the domain wall structure was one of the first achievements of the micromagnetism.

### A. Bloch wall

The first model of transitional layer between two magnetic domains was introduced by Bloch [105]. According to the model, the gradual change of the magnetization orientation in a domain wall is a result of competition between magnetic anisotropy trying to align the moments along the easy axis and to squeeze the wall, and exchange energy which expands the wall trying to reduce the misorientation of magnetic moments. Characteristic feature of the Bloch wall is absence of magnetic charges. This condition is fulfilled if the normal component of the magnetization is continuous, i.e.

$$\operatorname{div}\mathbf{M} = 0. \quad (1.38)$$

Bloch domain wall can be considered as a set of parallel planes perpendicular to the wall normal (for definiteness, I direct the normal to the wall along  $z$  direction, Fig. 1.5 (a)). Each of these planes is magnetized homogeneously while the neighboring planes differ by the orientation of the magnetization.

Components of the magnetization in the Bloch wall are functions only of the coordinate  $z$ :

$$M_x = M \cos \theta(z), M_y = M \sin \theta(z), M_z = 0, \quad (1.39)$$

and the boundary conditions for the angle  $\theta$  are

$$\theta(-\infty) = 0, \theta(\infty) = \pi. \quad (1.40)$$

By minimizing the energy functional one can obtain the Bloch wall energy:

$$\gamma_B = \int_{-\infty}^{\infty} \left[ K_u \sin^2 \theta + A \left( \frac{d\theta}{dz} \right)^2 \right] dV = 4\sqrt{A K_u}. \quad (1.41)$$

Analytical solution for the magnetization in the Bloch wall

$$\theta = \arccos \left( \tanh \left( \frac{z}{\sqrt{A/K_u}} \right) \right) \quad (1.42)$$

plotted in Fig. 1.5 (c) allows to introduce the commonly used notion of domain wall width (Lilley's definition) as a distance between the points at which the tangent at  $z = 0$  intersects the lines  $\theta = 0; \pi$ :

$$\delta_B = \pi \sqrt{\frac{A}{K_u}} \quad (1.43)$$

Such a definition will be also used while defining the characteristic size of isolated skyrmions in section 4.4.

### B. Néel wall

On the contrary to the Bloch wall, the magnetization in Néel wall rotates through the wall (Fig. 1.5 (b)). Magnetic charges arising within the wall lead to the intrinsic

magnetostatic field  $H_m$ , and

$$\operatorname{div} \mathbf{M} \neq 0. \quad (1.44)$$

From energetic point of view the existence of Néel walls in bulk materials is disadvantageous, but they can appear in thin films where the magnetostatic energy trying to keep the wall as narrow as possible competes with exchange energy trying to avoid strong inhomogeneities of the magnetization. For the same choice of coordinate axes as for Bloch wall (Fig. 1.5) the components of the magnetization for Neel wall are

$$M_x = M \cos \theta(z), \quad M_y = 0, \quad M_z = M \sin \theta(z), \quad (1.45)$$

Minimization of the energy functional

$$\gamma_N = \int_{-\infty}^{\infty} \left[ \left( \frac{d\theta}{dz} \right)^2 + 2\pi M_s^2 \cos^2 \theta(z) \right] dz \quad (1.46)$$

leads to the analytic solutions

$$\theta(z) = \arccos \left( \tanh \left( \frac{z}{\sqrt{A/2\pi M_s^2}} \right) \right). \quad (1.47)$$

The width of the Neel wall is expressed by the following equality

$$\delta_N = 4 \sqrt{\frac{A}{2\pi M_s^2}}. \quad (1.48)$$

which is very similar to the solution of Bloch wall (Eq. (1.43)). The stray field constant  $K_d = 2\pi M_s^2$  plays the same role for Néel walls as uniaxial anisotropy  $K_u$  - for Bloch walls.

In the next section I consider one-dimensional spiral modulations arising in non-centrosymmetric magnets with Dzyaloshinskii-Moriya interactions. On the contrary to domain walls where rotation sense is degenerate, spiral states permit only one rotational sense (left or right) defined by the sign of Dzyaloshinskii constant  $D$ . The type of realised spiral is specified by the crystallographic symmetry (for details see section 4.3).

### 1.3.2. One-dimensional spiral modulations

In the previous sections I considered the distribution of the magnetic vectors within the classical Bloch and Néel domain walls. Here, I show that Dzyaloshinskii-Moriya interaction can lead to the proliferation of domain walls, i.e. can destabilize the homogeneous state with respect to a modulated spiral state. To demonstrate this I direct the wave vector  $\mathbf{k}$  of such a helix along coordinate axis  $z$  as it was for Bloch wall (Fig. 1.5 (a)) and use spherical coordinates (1.39) for the magnetization vector  $\mathbf{M}$ . The Dzyaloshinskii-Moriya energy term in form of (1.17) is included into the

free energy. Then the energy functional in zero field and zero uniaxial anisotropy is reduced to the form

$$\gamma_{sp} = \int_0^{p_0} \left[ A \left( \frac{d\theta}{dz} \right)^2 + D \left( \frac{d\theta}{dz} \right) \right] dz \quad (1.49)$$

The competition of the counter-acting exchange and Dzyaloshinskii-Moriya interactions in energy (1.49) yields the ground state of the system in the form of a *single-harmonic* mode:

$$\theta(z) = \frac{z}{2L_D}, \quad L_D = \frac{A}{D}. \quad (1.50)$$

The period

$$p_0 = 4\pi L_D \quad (1.51)$$

and the sense of rotation of spiral modulations are determined by the sign and magnitude of the Dzyaloshinskii constant  $D$ . While the exchange stiffness in (1.49) is minimal in spatially homogeneous states, the Dzyaloshinskii-Moriya coupling favours a rotation of  $\mathbf{M}$ . Thus, winding of the magnetization with appropriate rotation sense and unlimiting reduction of the modulation period ( $(d\theta/dz) \rightarrow \infty$ ) leads to infinitely negative values of Dzyaloshinskii energy density.  $L_D$  proportional to the ratio of the counter-acting exchange and Dzyaloshinskii constants (1.50) introduces a fundamental *length* characterizing the magnitude of chiral modulations in non-centrosymmetric magnets.

It is important that for any sign of Dzyaloshinskii constant  $D$  there is such a rotation sense of  $\mathbf{M}$  which can lead to a negative energy  $\gamma_{sp}$ . To show this I follow the standard procedure (see section 2.6.1) and write the energy including Zeeman and anisotropy interactions in the form:

$$\gamma_{sp} = \gamma_0 \pm D |\theta_2 - \theta_1|, \quad \sigma_0 = 2\sqrt{AK} \int_{\theta_1}^{\theta_2} \sqrt{\Phi(\theta) - \Phi(\theta_{1,2})} d\theta \quad (1.52)$$

where  $\Phi(\theta) = -\mathbf{M} \cdot \mathbf{H} - K_u(\mathbf{m} \cdot \mathbf{a})^2$ . The first term  $\gamma_0$  depends on the exchange stiffness  $A$  and the barrier height

$$\Delta\Phi = [\Phi(\theta_{max}) - \Phi(\theta_{1,2})], \quad (1.53)$$

where  $\theta_{max}$  maximizes  $\Phi(\theta)$  along the wall,  $\theta_1$  and  $\theta_2$  determine magnetic states in two adjacent domains by minimizing functional  $\Phi(\theta)$ . This positive contribution can be written as

$$\gamma_0 = 2\zeta |\theta_2 - \theta_1| \sqrt{A\Delta\Phi} \quad (1.54)$$

where  $\zeta$  is a numerical factor determined by the average value of the integrand (1.52),  $0 < \zeta < 1$ . For one sense of rotation the energy contribution from the

Dzyaloshinskii-Moriya interaction decreases the domain wall energy. Thus, when

$$|D(\theta_2 - \theta_1)| > \gamma_0 \quad (1.55)$$

the domain wall energy becomes negative, resulting in an instability of the homogeneous phase with respect to chiral modulations. Finally,  $\gamma_{sp}$  can be expressed as

$$\gamma_{sp} = A |\theta_2 - \theta_1| \left( \frac{1}{L_0} - \frac{1}{L_D} \right). \quad (1.56)$$

where  $L_D$  (1.50) measures the energy gain due to the modulation, while the domain wall width

$$L_0 = \frac{\zeta}{2} \sqrt{\frac{A}{\Delta\Phi}} \quad (1.57)$$

measures energy losses. Thus modulated states are stable when the "rotating force"  $D$  overcomes the barriers  $\Delta\Phi$ , and the period  $4\pi L_D$  of free rotation is smaller than the domain wall width  $4\pi L_0$ . The critical values of the Dzyaloshinskii constants  $D_c$  for transitions between homogeneous ( $D < D_c$ ) and modulated chiral state ( $D > D_c$ ) vary strongly with an applied magnetic field and are given by the equation  $\gamma_{sp} = 0$ . Corresponding formulae for critical values of Dzyaloshinskii constant can be found in Refs. [45, 69, 71].

## 1.4. Two-dimensional distributions of the magnetic vectors - skyrmions

Dzyaloshinskii-Moriya interactions introduced in section 1.2.1  $B$  and shown to induce spiral states in magnets (section 1.3.2) may also lead to the appearance of the chiral skyrmions - particle-like twisted states with radial symmetry.

### 1.4.1. Chiral flux-lines as the building blocks of skyrmionic matter

In all the chapters related to skyrmions in chiral magnetic systems (chapters 4-6), I start the analysis of skyrmion states from the isolated skyrmions which may be considered as "bricks" for building the extended skyrmion textures (see sections 4.4, 5.3, 6.3). Isolated skyrmions are the solutions of the micromagnetic equations for chiral systems minimizing energy functional (1.1) (Fig. 0.1 (a) and Eqs. (4.1), (6.3)) and have distinctive features of topological solitons. Existence of chiral skyrmions in magnetism was predicted and investigated theoretically by A. Bogdanov et al. starting in 1989 [69].

#### *A. Internal structure of isolated skyrmions*

Isolated skyrmions can be thought of as isolated static solitonic textures localized in two spatial directions, which can be extended into the third direction as skyrmion

strings or Hopfions. The magnetization in the center of skyrmion pointing opposite to an applied magnetic field rotates smoothly and reaches the state along the field at the outskirts of skyrmion. The way the magnetization twists from the center to outskirts (i.e. the azimuthal angle of the magnetization in the polar system) depends on the symmetry of the underlying non-centrosymmetric helimagnet (see Fig. 4.3 and Eqs. (4.23)). In Fig. 0.1 (a) the magnetization performs Bloch-like type of rotation (see also the structure of Bloch domain wall in Fig. 1.5 (a)). Also the magnetization may have Néel-like rotational fashion or even more sophisticated types of rotation [69].

In the thesis I will use the spherical coordinates for the magnetization:

$$\mathbf{M} = M(\sin \theta(\rho) \cos \psi(\varphi), \sin \theta(\rho) \sin \psi(\varphi), \cos \theta(\rho)), \quad (1.58)$$

and cylindrical coordinates for the spatial variables [21, 22, 70]

$$\mathbf{r} = (\rho \cos \varphi, \rho \sin \varphi, z). \quad (1.59)$$

Therefore, the rotation of the magnetization in the isolated skyrmion is characterized by the dependence of the polar angle  $\theta$  on the radial coordinate  $\rho$  (in chapter 6 I consider also the dependence of the magnetization modulus  $M$  on  $\rho$ ).

Isolated skyrmions represent countable and smallest possible localized entities in a magnetization distribution. The nucleus in which most of the skyrmion energy is concentrated (see section 4.4.2) can be imaged as a two-dimensional elementary particle. The weak perturbation of the homogeneous state for  $\rho \rightarrow \infty$  is viewed as a "field" created by the particle. Two such elementary particles with the same sense of the magnetization rotation repel each other.

The characteristic size of the skyrmion is comparable with the width of the domain wall, and thus, is much smaller than the radius of a bubble domain stabilized by dipole-dipole interaction in the magnetic films with perpendicular anisotropy. But note, that in spite of the topological similarity between skyrmions and common bubble domains (the skyrmion may be naively visualized as a bubble without its core), they are different branches of solutions of micromagnetic equations as shown explicitly in sections 4.7.2 and 5.6. Bubble domains arise only as a result of the surface depolarization and the tension of ordinary domain walls and are intrinsically unstable. The skyrmions are stabilized by Dzyaloshinskii-Moriya interactions and exist even in very high fields without collapse (see for details [23]).

### *B. Topological and physical stability of isolated skyrmions*

Skyrmion states are classified as both topologically and physically stable.

The skyrmion "knots" are robust against small perturbations and cannot be continuously unwound. The chirality of a non-collinear structure can be measured from the strength of the twist or helical rotation of the magnetization,  $\mathbf{M} \cdot (\nabla \times \mathbf{M})$ . For

the radial skyrmion structure, the local twist is given by the expression

$$\tau = \left( \frac{d\theta}{d\rho} + \frac{1}{\rho} \cos \theta \sin \theta \right). \quad (1.60)$$

The sign of this expression measures the local and helical chirality in the structure. In particular, for  $0 \leq \theta \leq \pi/2$  and  $\theta_\rho > 0$  the local chirality of the helical structure is positive.

Alternatively, the field configuration can be characterized by a topological charge or skyrmion number  $Q$ :

$$Q = \frac{1}{4\pi} \int \mathbf{n} \left( \frac{\partial \mathbf{n}}{\partial x} \times \frac{\partial \mathbf{n}}{\partial y} \right) dx dy \quad (1.61)$$

where  $\mathbf{n}$  is a unit vector along the magnetization, and the integration is done over the inhomogeneous magnetization distribution. For trivial magnetization distributions  $Q = 0$ . For skyrmions  $Q$  has non-vanishing value.

Both the sign of  $\tau$  and the skyrmion number  $Q$  can be used to characterize the skyrmion structure.

Skyrmions are also physically stable: the physical size of the skyrmionic disk (Fig. 0.1) ranges from few lattice spacings up to microns depending on the balance between Dzyaloshinskii- Moriya interaction and the direct exchange. In centrosymmetric systems the size of skyrmions reduces to zero. Therefore, chiral couplings provide a unique mechanism to stabilize skyrmionic textures. This singles out chiral condensed matter systems with Lifshitz-type of invariants into a particular class of materials with skyrmionic states.

The influence of DMI on the stability of skyrmion states can be considered from general principles as it was comprehensively described in Ref. [233]. In the energy functional, one can separate energy terms quadratic ( $\phi_2(\theta)$ ) and linear ( $\phi_1(\theta)$ ) in the spatial derivatives of the configurational variable  $\theta$ .  $\phi_0(\theta)$  includes the terms which do not contain the spatial gradients. If the energy functional

$$\Phi = \int [\phi_2(\theta) + \phi_1(\theta) + \phi_0(\theta)] d^D x \quad (1.62)$$

is subject to the stretching-compression rescaling  $U(x) \rightarrow U(x/\lambda)$ , then

$$\Phi^D(\lambda) = \lambda^{D-2} \Omega_2^D + \lambda^{D-1} \Omega_1^D + \lambda^D \Omega_0^D \quad (1.63)$$

where

$$\Omega_k^D = \int [\phi_k(U)] d^D x. \quad (1.64)$$

$D$  is a dimensionality of modulated states. From Eq. (1.63) it clearly seen that DMI do not change the conditions of stability for one-dimensional spiral states with  $D = 1$ . However, for two-dimensional skyrmions with  $D = 2$  (or even for multidimensional magnetization distributions with  $D = 3$ ) DMI are extremely important.

Such solitonic textures can arise in different classes of non-centrosymmetric magnetic crystals [31,45,69,107], ferroelectrics, and multiferroics. Also described isolated skyrmions remind Abrikosov vortices in type II superconductors or thread-like textures in nematic liquid crystals [48]. However, contrary to these defected patterns with singularities in the core, the distribution of the order parameter in skyrmions is smooth.

### *C. Why skyrmion is called "skyrmion"?*

Localized solutions depicted in Fig. 0.1 (a) have been initially introduced under name *magnetic vortices* [69] because, to a certain extent, they are similar to 2D topological defects investigated in magnetism and known as "two-dimensional topological solitons" or "vortices" (e.g. well-known Belavin-Polyakov solutions for magnetic vortices [234]). On the other hand, the term *skyrmion* has been conceived in a field rather distant from condensed-matter physics and initially was related to the localized solutions derived by Skyrme within his model for low-energy dynamics of mesons and baryons [35]. In fact, the Skyrme model [35] comprises three spatial dimensions, and the name "baby-skyrmion" was used by some field theorists to distinguish two-dimensional localized states from "mature" three-dimensional solutions in the original Skyrme model [35], both types of them being topological static solitons. During the last decades the "skyrmion" has progressively won currency in general physics to designate *any* non-singular localized and topologically stable field configuration. Complying with this trend, in 2002 A. N. Bogdanov and coworkers renamed "chiral magnetic vortices" into "chiral skyrmions" [45].

Thus, the term *skyrmion* is an umbrella title for smooth localized structures to distinguish them from singular localized states, e.g., disclinations in liquid crystal textures [48]. This convention provides only a formal *label* for a large variety of very different solitonic states from many fields of physics [109]. In the context of the present thesis the label "chiral skyrmion" designates well-defined solutions of micromagnetic equations which are **(i) localized**, **(ii) axisymmetric**, and have **(iii) fixed rotation sense**.

### 1.4.2. Skyrmion lattices

Skyrmion strings (section 1.4.1) may condense into multiply modulated states. The extended skyrmionic textures are determined by the stability of the localized solitonic skyrmion cores and their geometrical incompatibility which frustrates regular space-filling. In chapters 4-6 I consider first circumstances under which isolated skyrmion entities condense into the lattice (sections 4.4.4, 5.4, 6.4.1), then properties of obtained skyrmion textures (sections 4.5, 6.4.2), and finally address the question of the energetic competition between one-dimensional helical modulations and skyrmions (sections 4.6, 5.5, 6.6).

#### *A. Condensation of isolated skyrmions into a lattice*

Under the influence of a sufficiently strong DM interactions isolated skyrmions



condense into lattices [21, 31, 69]. The process of condensation is ruled by two competing mechanisms: low-energy skyrmion cores trying to fill the whole space, and high-energy edge area responsible for the repulsion of isolated skyrmions. The transformation of skyrmions during the formation of the lattice has been investigated in Ref. [21]. Magnetic-field-driven evolution of the skyrmion lattice has similar features with the evolution of helical states investigated in [41] and bubble and stripe domain in uniaxial ferromagnets [24]. Despite a strong variation of the lattice periods isolated skyrmions preserve axisymmetric distribution of the magnetization in the central part of cells.

Mechanism of lattice formation through nucleation and condensation of isolated skyrmions follows a classification introduced by DeGennes [91] for (continuous) transitions into incommensurate modulated phases. According to DeGennes, the fully saturated ferromagnetic state is stable locally. However, it becomes unstable with respect to certain distortions of large amplitude - skyrmions: in practice, isolated skyrmions as excitations of ferromagnetic state nucleate near defects, and then condense into the lattice. Such nucleation-type phase transitions are rather frequent in the condensed matter physics: (a) the entry of magnetic flux in a type II superconductors involves nucleation of vortex lines; (b) an electric or magnetic field induces the transition between a cholesteric and a nematic liquid crystals; (c) the magnetic samples break up into domains with increasing role of demagnetizing field [48].

And vice versa, the magnetic state built up from skyrmions may be decomposed into an assembly of isolated skyrmions - molecular units, i.e. a transformation of condensed phases occurs by setting free the isolated skyrmion units as in a crystal-gas resublimation. Depending on small energy differences owing to additional effects, different extended textures with variable arrangements of the skyrmion cores may arise, just as in a molecular crystal.

#### *B. The problem of skyrmion thermodynamical stability*

The energetic advantage of skyrmion states over helicoids is due to rotation of the magnetization in two dimensions [21, 31] (see section 4.6). This (*double-twist*) grants a larger reduction of the Dzyaloshinskii-Moriya energy than a single-direction rotation in helical phases (section 1.3.2). Thus, the double-twist yields a lower energy density in the skyrmion cores compared to helical states. On the other hand, the incompatibility of spin configurations near the edges of the hexagonal cells (Fig. 0.1) leads to an excess of the energy density in this region [31] (Fig. 4.10 (a)). The analysis shows that at zero field this energy cost outweighs the energy gain in the skyrmion core. An increasing external magnetic field anti-parallel to the magnetization in the skyrmion center gradually decreases the total energy by suppressing the energy cost near the wall-like structure surrounding the skyrmion cores with the shape of a honeycomb. At a finite field the lattice has lower energy than the alternative helical states with the field perpendicular to the propagation direction - helicoids (see section 4.3.1). However, the skyrmions are still metastable states with respect to the helical states with the propagation vector along the field - conical phases (see section 4.3.2). And the problem of skyrmion thermodynamical

stability arises.

In the forthcoming micromagnetic calculations I will consider the energy functional (1.1) being comprised from three hierarchichally separated energy terms:

(i) Ferromagnetic exchange interaction (section (1.2.1) *A*) is supposed to be the strongest energy contribution aligning the spins parallel to each other;

(ii) Dzyaloshinskii-Moriya interactions (section (1.2.1) *B*) occupy the second level of the energetic hierarchy. These chiral energy contributions twist the magnetic vectors into a helix or skyrmions, but with a small angle between adjacent magnetic vectors that the characteristic length scales are large. Such a condition allows to exclude from the consideration discrete atomic-scale skyrmion lattices considered, for example, as the magnetic ground state of a hexagonal Fe monolayer on Ir(111) [25] and characterized by large angles between neighboring spins.

(iii) Different anisotropic energy contributions are assumed to be the weakest energy terms of functional (1.1). Nonetheless, these additional interactions are considered as playing the crucial role in the thermodynamical stability of skyrmions. From one side, the role of the additional energy contributions consists in suppressing the conical phase. This is achieved, for instance, by the uniaxial and cubic anisotropies. From the other side, additional interactions do not affect the cones, but change slightly the structure of skyrmions decreasing the energy penalty of boundary regions and thus making skyrmions thermodynamically stable.

## **Part I.**

# **Phenomenological theory of magnetization reversal in nanosystems with competing anisotropies**

---

## 2. Magnetization processes in magnetic nanolayers and nanoparticles with competing anisotropies

On the one hand, the results of the present chapter may be considered as having the significance in their own right in application to magnetic nanostructures. The skyrmion and spiral states introduced in chapter 1 are not even mentioned here. The main concern of the present chapter is an consequences of interplay between intrinsic cubic and surface/interface-induced uniaxial anisotropies in nanolayers of diluted magnetic semiconductors and magnetic nanoparticles. The calculated phase diagrams in components of external magnetic field provide suitable tools to classify and analyse a vast amount of experimental data on magnetization reversal in (Ga,Mn)As epitaxial layers and nanoparticles. The phase diagrams give comprehensive information and enable one to predict the spin configurations in coexisting phases and parameters of multidomain structures for various ratios of the competing magnetic anisotropies and for various relative orientations of the anisotropy axes with some angle between them.

On the other hand, however, the conventions of the present chapter, demonstrating the analysis of homogeneous states (section 2.3) in systems with competing cubic and uniaxial anisotropies (including limiting cases of uniaxial and cubic ferromagnets), are important for the study of the stabilizing effect of these two types of magnetic anisotropy on skyrmion and helical states in chiral magnets with Dzyaloshinskii-Moriya interactions (see chapter 4, sections 4.7, 4.9). The mechanisms defining the thermodynamical stability of skyrmions with respect to one-dimensional modulations in the presence of small anisotropic energy contributions are based entirely on the clear understanding of the energy landscape for equilibrium homogeneous states (see as an example Fig. 4.22). Therefore, the results of the present chapter are instrumental also for modulated states of chapters 4 - 6.

### 2.1. Introduction

In magnetic nanostructures complex physical processes on surfaces and interfaces give rise to enhanced uniaxial magnetic anisotropies [1, 2, 5, 110]. The interplay between these induced and intrinsic (magnetocrystalline) anisotropies strongly influences the magnetization processes in many important classes of nanoscale sys-

tems, such as ferromagnet - antiferromagnet bilayers [111–114], thin epilayers of diluted magnetic semiconductors [115–120] or in magnetic nanoparticles, [122–125][V] and is the reason of various remarkable effects involving complex spin reorientation [116, 120, 126–134] and the evolution of specific multidomain states [135–139].

Most theoretical studies in this field are restricted to the investigations of *Stoner-Wohlfarth* processes through coherent switching [140] in models with uniaxial and cubic anisotropies [141–147]. Such theories describe magnetization reversal in a limiting case of ideally hard magnetic materials. However, in real magnetic materials the reversal processes will usually take place by the formation of heterogeneous states consisting of the competing phases and their transformation under the influence of the applied field. The analysis of such *multidomain* states in systems with competing anisotropies and their influence on magnetization reversal is the subject of this chapter [VI,VII]. These investigations can be executed within a regular micro-magnetic theory [24, 148] (section 2.2), adapted to nanoscaled systems (see e. g. Refs. [11, 20, 149]) [VI,VII]. First, I plot phase diagrams of states in components of internal magnetic field (section 2.3), calculate stability limits of each possible magnetic configuration, and describe reorientation effects [148, 150, 151]. Then in section 2.4, I describe the procedure to map the obtained solutions onto the plane of external field components, I calculate the parameters of the multidomain states and analyse the magnetization processes [VI,VII].

In section 2.5 I apply the results to interpret reorientation effects and magnetization reversal as observed in experimental works on nanolayers of diluted magnetic semiconductors, FM/AFM bilayers, and thin films of Heusler alloys. In section 2.6 the calculated equilibrium parameters of the isolated domain walls and stripe domains are used to analyse recent experimental results in (Ga,Mn)As films with perpendicular anisotropy. Finally, in the section 2.7 I demonstrate stabilizing effect of surface-induced anisotropy on multiple magnetic states in elongated nanoparticles [V].

## 2.2. Phenomenological model

Within the standard phenomenological theory (see section 1.1) the magnetic energy of a nanoscale ferromagnetic sample can be written as a functional (1.1) with an energy density

$$w = A \sum_i \left( \frac{\partial \mathbf{m}}{\partial x_i} \right)^2 - \mathbf{M} \cdot \mathbf{H}^{(e)} - \frac{1}{2} \mathbf{M} \cdot \mathbf{H}_m + w_a, \quad (2.1)$$

including exchange interactions (Eq. (1.4)), Zeeman energy (Eq. (1.33)), and energy of stray fields (Eq. (1.34)). The anisotropy energy density  $w_a$  includes uniaxial anisotropy ( $K_u$ ) with the axis  $\mathbf{a}$  and cubic anisotropy ( $K_c$ ) with unity vectors  $\mathbf{n}_j$  along cubic axes (see sections 1.2.2  $A, B$ )

$$w_a(\mathbf{M}) = -K_u (\mathbf{m} \cdot \mathbf{a})^2 - \frac{1}{2} K_c \sum_{j=1}^3 (\mathbf{m} \cdot \mathbf{n}_j)^4. \quad (2.2)$$

The coefficients  $K_u$  and  $K_c$  are assumed to be *positive*. Hence,  $\mathbf{a}$  and  $\mathbf{n}_j$  directions are easy uniaxial and cubic magnetization axes, respectively. For the negative constant of cubic anisotropy the easy axes are of  $\langle 111 \rangle$ -type with angles  $70.5^\circ$  and  $109.5^\circ$  between them (in comparison with  $90^\circ$  for  $K_c > 0$ ). This geometry requires separate calculations. However, the procedure should be the same as described in details in the present chapter.

The equilibrium distribution of the magnetization  $\mathbf{M}(\mathbf{r})$  is generally spatially inhomogeneous. It can be derived directly by solving the equations minimizing the energy functional Eq. (2.1) together with the Maxwell equations (1.35). Thus, the micromagnetic problem is formulated as a set of non-linear integro-differential equations [24]. In many classes of magnetic systems a strongly pronounced hierarchy of magnetic interaction *scales* allows to reduce the micromagnetic problem to a set of auxiliary simplified problems [24, 148]. The procedure includes: (i) the calculation of spatially homogeneous equilibrium states by minimizing energy

$$w_0(\mathbf{M}) = -\mathbf{M} \cdot \mathbf{H} + w_a(\mathbf{M}) \quad (2.3)$$

in an (*internal*) magnetic field  $\mathbf{H}$  for fixed values of the material parameters in Eq. (2.3). The solutions of (i) are used to construct magnetic phase diagrams in components of the external magnetic field (ii) and to calculate the equilibrium parameters of multidomain patterns and the structure of domain walls (iii).

In the rest of the chapter, I apply this program to the model given by Eqs. (2.1) and (2.2). In order to make transparent the representation of internal homogeneous states and the phase diagrams, I restrict the discussion to the case of co-planar arrangements of easy axes and applied fields. Generalizations of this model are discussed to the end of the next section.

## 2.3. Reorientation transitions and metastable states. Phase diagrams in internal field components

In many cases of practical interest, the direction of the uniaxial anisotropy  $\mathbf{a}$  lies in the plane spanned by two of the cubic axes  $\mathbf{n}_j$  (see Eq. (2.2)). To be specific I define this plane as  $xOz$  plane assuming that  $z$  is directed along  $\mathbf{a}$ . In this case energy  $w_0$  from Eq. (2.3) can be written as a function of the angle  $\theta$  between  $\mathbf{M}$  and  $\mathbf{a}$ . Introducing the reduced energy

$$\Phi(\theta) = \frac{w_0}{K_c} + \frac{1}{8} \quad (2.4)$$

one obtains

$$\Phi(\theta) = -\frac{1}{8} \cos 4(\theta - \alpha) - \varkappa \cos^2 \theta - h \cos(\theta - \psi), \quad (2.5)$$

where

$$\varkappa = \frac{K_u}{K_c}, \quad h = \frac{H}{H_c}, \quad H_c = K_c M_0, \quad (2.6)$$

$\alpha$  is the angle between the uniaxial  $\mathbf{a}$  and cubic  $\mathbf{n}_1$  axis, the angle  $\psi$  defines the deviation of the magnetic field  $\mathbf{H}$  from the easy axis  $\mathbf{a}$  in the  $xOz$ -plane; correspondingly,  $h_z = h \cos \psi$  is the reduced field component along the uniaxial easy direction, and  $h_x = h \sin \psi$  is the perpendicular component.

Energy (2.5) is a function of variable  $\theta$  and includes four material (control) parameters, namely, angle  $\alpha$ , ratio  $\varkappa$  and reduced magnetic field components,  $h_x$ ,  $h_z$ . Model (2.5) has been introduced in 1964 by Torok et al. [141] for ferromagnetic films with misorientated uniaxial and biaxial easy magnetization directions. Previous investigations of (2.5) have been restricted to limiting cases of  $\alpha = 0$  and  $\alpha = \pi/4$  and were mostly concentrated on investigations of coherent rotation processes (Stoner-Wohlfarth regime) (see Ref. [140] and bibliography in Ref. [24]). Within this approach switching processes are identified with the boundaries of the metastable states (critical astroids). In this section I give a comprehensive analysis of model (2.5) in the full range of the control parameters  $(\alpha, \varkappa, h, \psi)$ . In particular, I show that the analysis of the metastable states only is not sufficient for the understanding of magnetization reversal in nanosystems with competing anisotropies. The peculiar evolution of the potential profile (2.5) under the influence of the applied field and specific reorientation effects are found to be crucial for the magnetization processes in this class of magnetic materials.

The stationary solutions with the equilibrium values of  $\theta$  are derived from the equation

$$\Phi_\theta = 0 \quad (2.7)$$

and are:

$$h \sin(\theta - \psi) = -\frac{1}{2} \sin 4(\theta - \alpha) - \varkappa \sin 2\theta \quad (2.8)$$

Here I introduce a common notation for derivatives

$$f(x)_{x \times k} \equiv \frac{d^k f}{dx^k}. \quad (2.9)$$

The equation for the lability lines of the solutions,

$$\Phi_{\theta\theta} = 0, \quad (2.10)$$

reads

$$h \cos(\theta - \psi) = -2 \cos 4(\theta - \alpha) - 2\varkappa \cos 2\theta \quad (2.11)$$

and determines the stability boundaries of the solutions together with Eq. (2.8).



Critical points of the transitions are determined by the set of equations

$$\Phi_{\theta \times k} = 0, k = 1, 2, 3. \quad (2.12)$$

The degeneracy of the solutions,  $\theta_i$  with  $i = 1 \dots L$ , that provide global energy minima in the system,

$$\Phi(\theta_1) = \Phi(\theta_2) = \dots = \Phi(\theta_L), \quad (2.13)$$

determines the coexistence regions between  $L$  magnetic phases and the conditions for first-order transitions in the magnetic phase diagrams. It is convenient to present the solutions  $\theta(h_x, h_z, \varkappa, \alpha)$  and critical regions for (2.5) in a set of phase planes  $(h_x, h_z)$  parametrized by the factors  $\alpha$  and  $\varkappa$ . I start the analysis from the limiting cases  $\alpha = 0$  and  $\pi/4$ , and after that highlight main features of the general model (2.5).

For symmetric cases with the easy-axes orientations along one the cubic axis ( $\alpha = 0$ ) and along the diagonals between them ( $\alpha = \pi/4$ ) the Eq. (2.5) can be written as

$$\Phi(\theta) = \mp \frac{1}{8} \cos(4\theta) - \varkappa \cos^2 \theta - h \cos(\theta - \psi), \quad (2.14)$$

with “−” for  $\alpha = 0$  and “+” for  $\alpha = \pi/4$ . Generally model (2.14) describes magnetic states in a planar ferromagnet with competing uniaxial (second-order) and biaxial (fourth-order) magnetic anisotropy. The model has been applied for many bulk and nanoscale magnetic systems, including reorientation effects in rare-earth orthoferrites [148,152][I-IV], several classes of intermetallic compounds [153], first-order magnetization processes in high-anisotropy materials [144], and for magnetic nanolayers with surface/interface-induced magnetic anisotropy [5, 110, 114, 145, 146, 149, 150]. The model from Eq. (2.14) has also proved to be valid for diluted magnetic semiconductors as a novel class of magnetic materials [115–117, 151].

The invariance of the potential Eq. (2.14) under the transformation

$$\varkappa \rightarrow -\varkappa, \quad \theta \rightarrow \theta + \frac{\pi}{2}, \quad \psi \rightarrow \psi + \frac{\pi}{2}, \quad (2.15)$$

means that the cases with different sign of  $\varkappa$  transform into each other by rotation of the reference system through an angle  $\pi/2$ . This invariance allows one to restrict the analysis to positive values of  $\varkappa$ . The analysis of (2.14) yields four topologically different types of  $(h_x, h_z)$ -phase diagrams depending on values  $\varkappa > 0$ , as shown in Fig. 2.1. Under transformation (2.15) the equations of equilibrium (2.8), (2.11) for the potential (2.14) with  $\alpha = 0$  are converted into those equations for  $\alpha = \pi/4$ . Thus, for the same values of  $\varkappa$  the lability lines for both cases transform into each other by a rotation through  $\pi/2$  (Fig. 2.1).

For  $\varkappa > 5$  the lability lines have a similar shape as the *Stoner-Wohlfarth* astroid [140]. In the limit of large  $\varkappa$ , the lability line asymptotically coincides with this astroid for simple uniaxial ferromagnets. As  $\varkappa$  decreases from 5 to zero the lability lines transform into an eight-cusp line with the shape of the classical wind rose. At the parameter value  $\varkappa = 5$ , a bifurcation takes place by the formation of so-

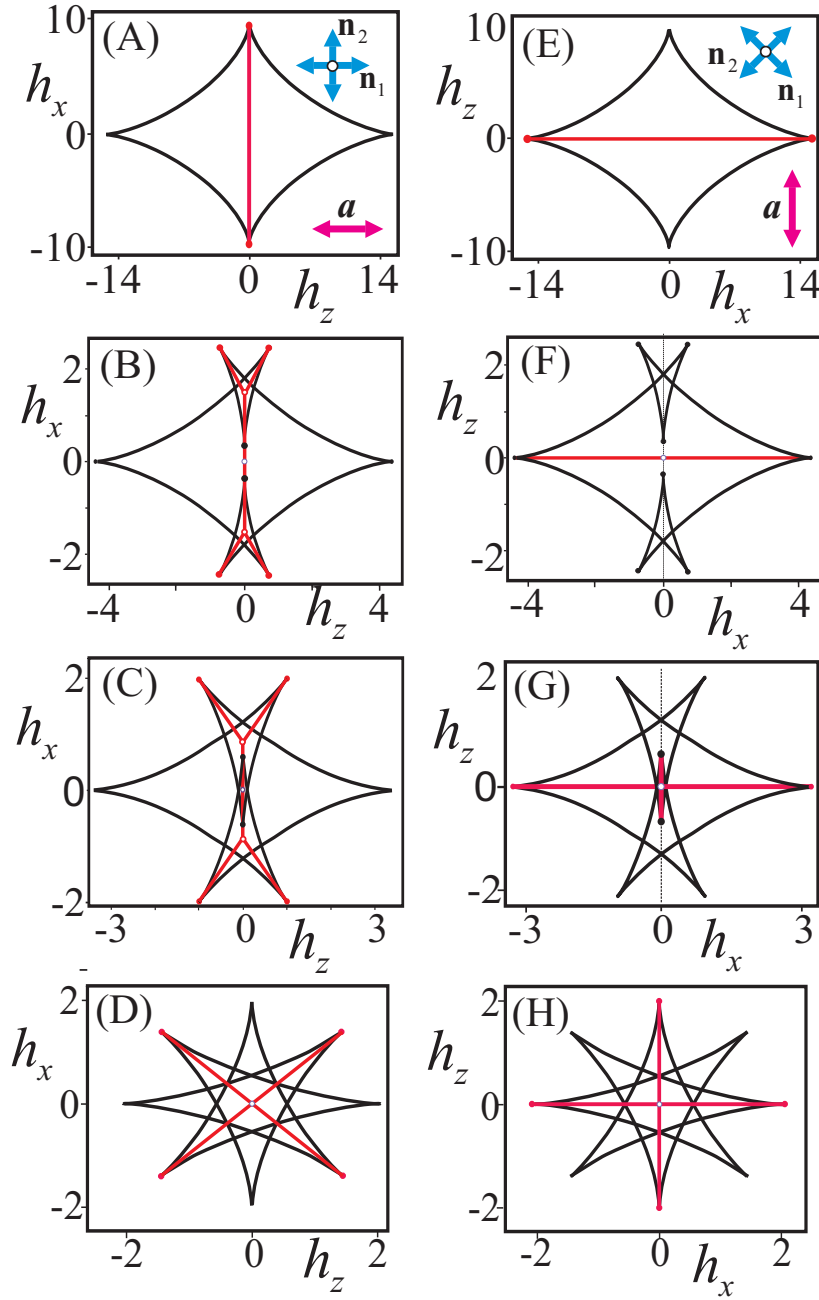


Figure 2.1.: The phase diagrams of magnetic states in components of the internal magnetic field ( $h_x$ ,  $h_z$ ) and different values of the parameter  $\kappa$  for the ratio of uniaxial and cubic anisotropy (Eq.2.6). The upper panel (A)-(D) is for systems with  $\alpha = 0$ , the bottom panel (E)-(H) is for systems with  $\alpha = \pi/4$ . Two-headed vectors show orientations of the uniaxial axis **a** and the cubic **n<sub>i</sub>** axes. The plots present the topologically different types of phase diagrams: (A), (E)  $\kappa > 5$ , (B), (F)  $5 > \kappa > 1$ , (C), (G)  $1 > \kappa > 0$ , (D), (H)  $\kappa = 0$ . Black lines indicate stability limits of metastable states. Red lines give the first-order transitions between different magnetic phases (see text for details).

called “swallow tails” [149] in one pair of opposite cusps (Fig. 2.1 (B), (F)). In the interval  $5 > \varkappa > 1$ , the swallow tails gradually widen, and at  $\varkappa = 1$  the lower cusp points reach the horizontal axis. In the interval  $1 > \varkappa > 0$  the phase diagrams have regions with overlapping swallow tails (Fig. 2.1 (C), (G)). Finally at  $\varkappa = 0$ , that is for zero uniaxial anisotropy, the lability line transforms into the wind rose with eight corners. For the two special orientations of the uniaxial anisotropy in Eq. (2.14) with  $\alpha = 0$  and  $\alpha = \pi/4$  the lability lines are identical. Still, the phase diagrams are fundamentally different as they pertain to different magnetic states and different coexistence regions of metastable magnetic states. Depending on the control parameters, there are regions with  $L = 2, 3$ , or 4 degenerate states, and, consequently, first-order transitions involving *two*, *three* and *four* phases.

For  $\varkappa > 5$  the first-order lines between *two* magnetic states are segments of straight lines connecting opposite cusp points (Fig. 2.1 (A), (E)) [149]:

$$h_z = 0, |h_x| \leq |h_x^c| = 2(\varkappa \mp 1). \quad (2.16)$$

At zero field the transitions occur between antiparallel magnetic states  $\theta_1 = 0$  and  $\theta_2 = \pi$ . For finite transversal magnetic fields  $|h_x| < h_x^c$  the solutions for coexisting phases are determined from Eq. (2.8) with  $h_z = 0$  and  $\alpha = 0 (\pi/4)$ ,

$$\sin^3 \theta - \frac{1 \pm \varkappa}{2} \sin \theta \pm \frac{h_x}{4} = 0. \quad (2.17)$$

These solutions describe a gradual decrease of the magnetization component  $m_z$ . In the endpoints of the first-order transitions  $h_x = \pm h_x^c$  the magnetization vectors in both phases are perpendicular to the easy direction.

For  $5 > \varkappa > 0$  the evolutions of the magnetic states within the swallow tails are different for the two models (see potential profiles in Fig. 2.2). For the model with  $\alpha = 0$ , the potential wells corresponding to the global energy minima are swapped within the swallow tails (Fig. 2.2 (A)). Hence, different canted states become degenerate in equilibrium along lines of first-order transitions (lines  $a_1 b_1$ ,  $a_1 b_2$ ,  $a_2 b_3$ ,  $a_2 b_4$  in Fig. 2.2 (A)). These lines meet the transition line  $a_1 a_2$  between symmetric phases,  $\theta_1, \theta_2 = \pi - \theta_1$ , in the points  $a_1$  and  $a_2$  where *three* phases coexist. The coordinates of points  $a_1$  and  $a_2$  are [149, 153]

$$\tilde{h}_x = \pm 2 \sin \tilde{\theta} (\cos 2\tilde{\theta} + \varkappa), \quad \tilde{h}_z = 0 \quad (2.18)$$

and the solutions for the coexisting phases read

$$\theta_1 = \pm \tilde{\theta}, \quad \theta_2 = \pi \mp \tilde{\theta}, \quad \theta_3 = \pm \frac{\pi}{2}, \quad (2.19)$$

where

$$\sin \tilde{\theta} = \frac{-1 + \sqrt{1 + 3\varkappa}}{3}. \quad (2.20)$$

For the model with  $\alpha = \pi/4$ , the minimum in the potential is unique for the swallow tails in the parameter range  $5 > \varkappa > 1$ . Hence, the transformation of the

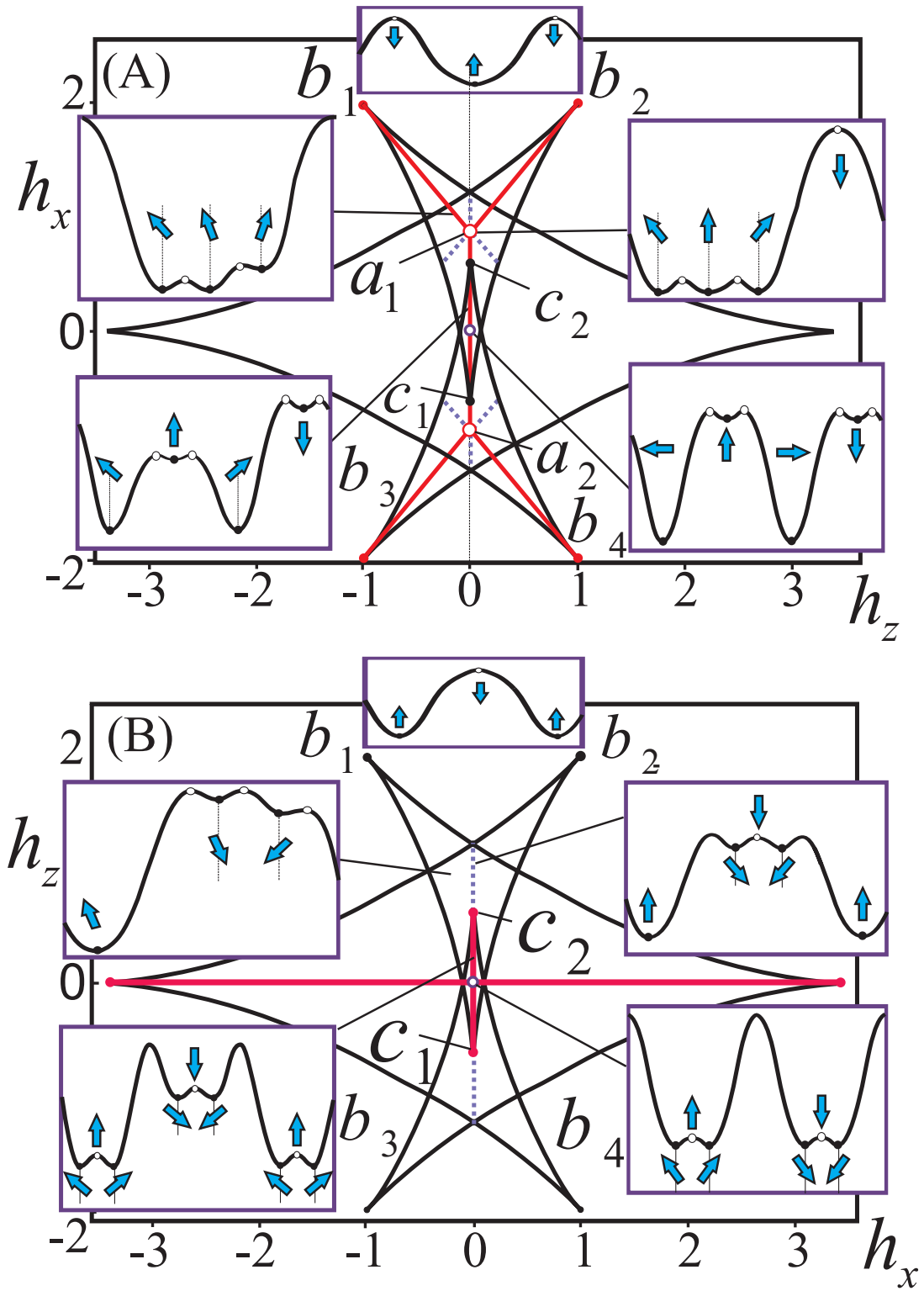


Figure 2.2.: The  $(h_x, h_z)$  phase diagrams for  $\varkappa = 0.7$ :  $\alpha = 0$  (A),  $\alpha = \pi/4$  (B). Potential profiles  $\Phi(\theta)$  are sketched for various points in the phase diagrams to illustrate the evolution of the magnetic states in both models.

energy profile involves only metastable states (Fig. 2.2 (B)). However, the particular transformation of the metastable states in these regions plays an important role in the evolution of the domain wall profiles (see Sec. VI). In the interval  $1 > \varkappa > 0$  the first order transitions arise within the region of the overlapping swallow tails. The transition line is a segment  $c_1 c_2$ , with the points

$$c_1 = (0; 2(\varkappa - 1)), c_2 = (0; -2(\varkappa - 1)). \quad (2.21)$$

Along this line segment *two* phases coexist with solutions  $\theta_1$  and  $\theta_2 = -\theta_1$ . The solutions  $\theta_1$  are given by the equation

$$\cos^3 \theta - \frac{1 + \varkappa}{2} \sin \theta - \frac{h_z}{4} = 0, \quad (2.22)$$

that can be derived from Eq. (2.8). The first-order transition line from  $c_1$  to  $c_2$  crosses the other transition line along  $(h_x; 0)$  in the origin. Hence, in this point *four* magnetic phases coexist with

$$\theta_1 = \frac{1}{2} \arccos \varkappa, \theta_2 = -\theta_1, \theta_3 = \pi - \theta_1, \theta_4 = \pi + \theta_1. \quad (2.23)$$

For  $\varkappa = 0$  (zero uniaxial anisotropy) both potentials (2.14) are converted into the model of a cubic ferromagnet. The corresponding phase diagrams (Fig. 2.1 (D) and (H)) are identical and include two lines of first-order phase transitions between symmetric states. In the origin four degenerate phases with magnetization along the cubic easy axes  $\mathbf{n}_1$  and  $\mathbf{n}_2$  coexist.

In the general case with a misalignment between uniaxial and cubic easy axes given by the parameter  $\alpha$  the potential  $\Phi$  (Eq. (2.5)) is a periodic function of  $\alpha$  with periodicity  $\pi/2$ . Thus an analysis in the range  $0 \leq \alpha \leq \pi/4$  covers all physically different states. Here I describe the evolution of the  $(h_x, h_z)$  diagrams when  $\alpha$  varies from zero to  $\pi/4$ . The sets of diagrams in Figs. 2.3 and 2.4 show the transformation of the transition and lability lines. The case with nonoverlapping swallow tails for the parameter range  $5 > \varkappa > 1$  is presented in Fig. 2.3. For small  $\alpha(\varkappa)$  two lines of the phase transitions between canted phases still exist (Fig. 2.3 (B)). With increasing  $\alpha$  the points  $a_1$  and  $a_2$  for the three-phase coexistence move to either of the cusp points  $b_2$  and  $b_3$  (Fig. 2.3 (C)). After these points have merged only two-phase transition lines exist in the system (line  $b_1 b_4$  in Fig. 2.3 (D), (E)). Thin (blue) lines in Fig. 2.3 (B)-(F) indicate the values of the magnetic fields where two metastable states have the same energy. They are not connected with any physical processes in the system but help to understand the transformation of the energy profiles.

The phase diagram with overlapping swallow tails for the parameter range  $1 > \varkappa > 0$  is shown in Fig. 2.4. In this case the transition lines between pairs of canted phases in the limit  $\alpha = 0$ , Fig. 2.4 (A), gradually transform into straight line segments for transitions between pairs of the symmetric phases in the limit  $\alpha = \pi/4$ , Fig. 2.4 (D). During this process the points of the three-phase coexistence  $a_1$  and

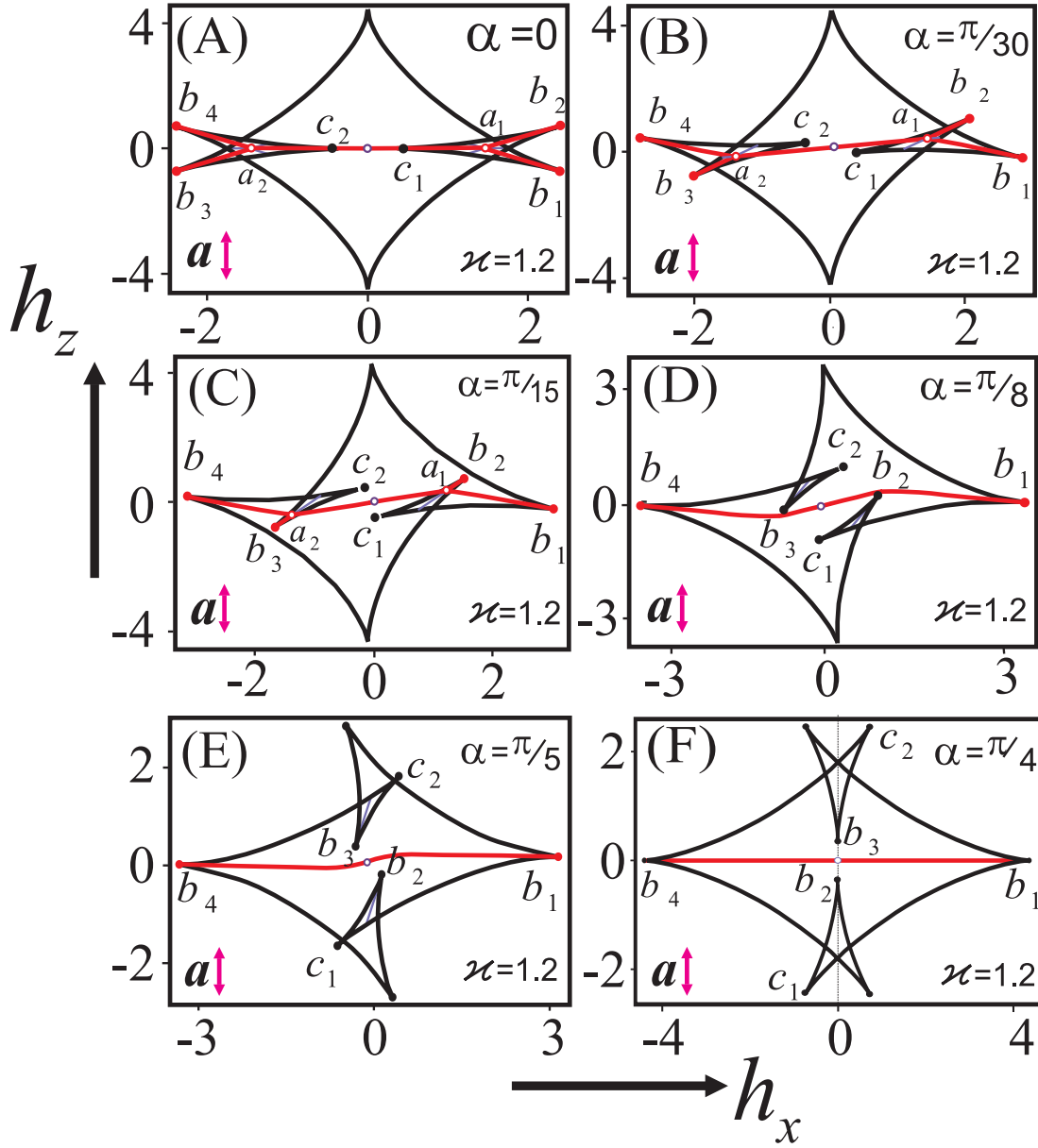


Figure 2.3.:  $(h_x, h_z)$  phase diagrams for  $\kappa = 1.2$  and different values of  $\alpha$  demonstrate the transformation between the two symmetric cases with  $\alpha = 0$  (A) and  $\alpha = \pi/4$  (F).

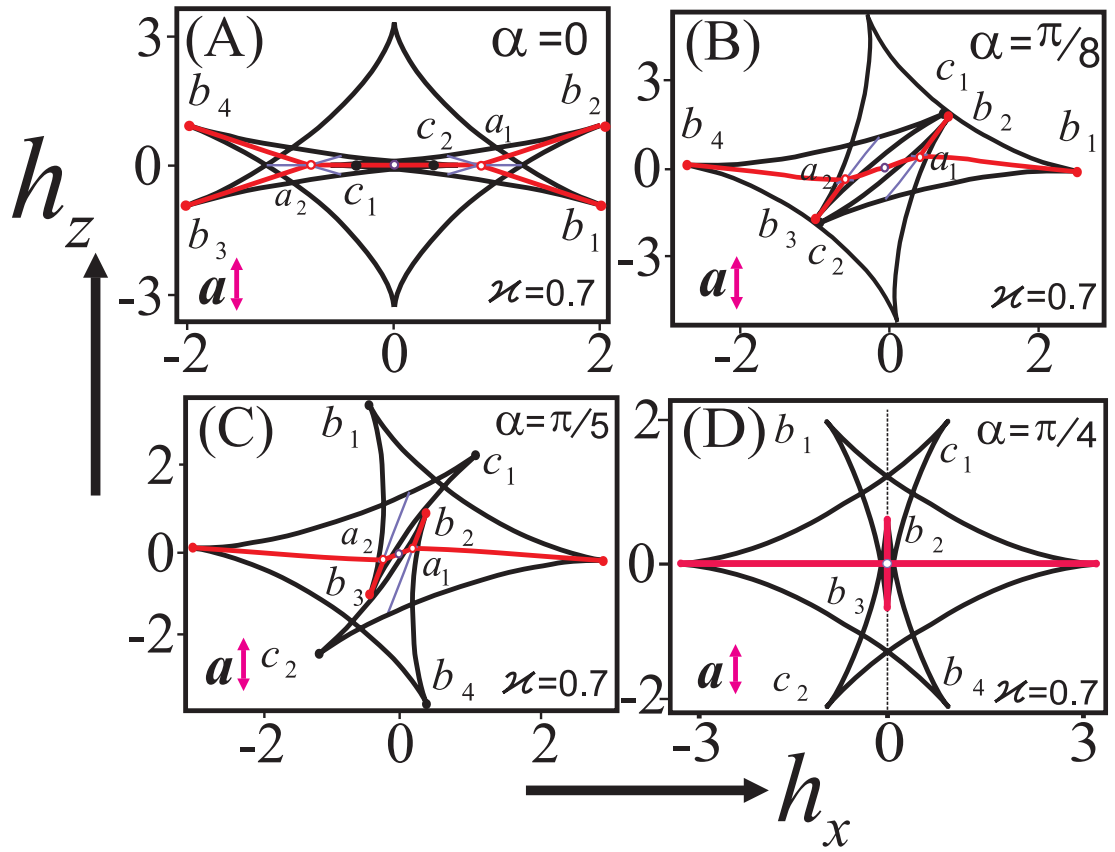


Figure 2.4.:  $(h_x, h_z)$  phase diagrams similar to that in the previous figure but for  $\kappa = 0.7$ .

$a_2$  move towards each other (Fig. 2.4 (B), (C)), and merge into the point with four-phase coexistence at the origin for  $\alpha = \pi/4$ , Fig. 2.4 (D).

The sets of modified astroids in Figs. 2.1 and 2.3 represent geometrical singularities studied by a special field in mathematics known as *catastrophe theory* [154]. It was found that for rather general form of potentials there exist only seven fundamental types of singularities referred to as *catastrophes* [154]. Four of them are realized in the lability lines of Figs. 2.1 and 2.3. The astroid lines, where one local minimum merges with a local maximum, are named *fold catastrophes*. The edge points where two folds meet have two minima merging with a maximum. These singularities are known as *cusp catastrophes*. By a characteristic discord in the terminology, the feature known in magnetics as “swallow tails” as shown in Fig. 2.1 (B), (F) are called *butterfly catastrophes* in mathematics, while the triangular regions, as those with the cusps  $c_1, b_2$  in Fig. 2.3 (D), are called *swallow tail catastrophes*. The lability lines in Fig. 2.1 belong to a family of *hypercycloids*. In present article I shall adhere to the terminology used in micromagnetism.

The transformation of the common Stoner-Wohlfarth astroid (as 4 - cusped hypercycloid - Fig. 2.1 (A), (E)), into the 8-cusped hypercycloid with the wind rose shape (Fig. 2.1 (D), (H)) occurs in many magnetic systems with competing anisotropies and has been investigated during the last forty years. To the best of our knowledge the 8-cusped hypercycloid has been firstly obtained in Refs. [141,155] (see also the remarks about earlier conference contributions in Ref. [141]). The transformation from the common astroids (Fig. 2.1) into a lability line with swallow tails, and the further evolution of these curves to the wind rose has been obtained in Ref. [141]. Torok et al. also demonstrated several diagrams of lability line for model with misorientated anisotropy axes (Eq.(2.14)). In many following papers (see, e.g. Refs. [142,143,156]) peculiarities of lability lines for the model (2.14) have been investigated. The coordinates of the critical points for (2.14) were calculated in Refs. [153,157–159]. The solutions for the first-order phase transition lines and the coexisting states have been carried out in Refs. [160,161] (see also Ref. [149])). In this chapter I have given an exhaustive summary of model (2.5).

## 2.4. Magnetic phase diagrams in external field components

In the previous section the solutions for possible magnetic states have been presented as functions of the internal field. For ellipsoidal magnets with a homogeneous magnetization  $\mathbf{M}(\mathbf{h})$  the equation [24]

$$\mathbf{h}^{(e)} = \mathbf{h} + 4\pi K_c^{-1} \hat{\mathbf{N}} \mathbf{m}(\mathbf{h}) \quad (2.24)$$

establishes the correspondence between magnetic phase diagrams in terms of the internal field  $\mathbf{h}$  and those in terms of the external field  $\mathbf{h}^{(e)}$  ( $\hat{\mathbf{N}}$  is the demagnetizing tensor). For phase diagrams in Figs. 2.1 and 2.3 the phase diagrams in external magnetic field components are plotted in Figs. 2.5 and 2.6, correspondingly. Thin



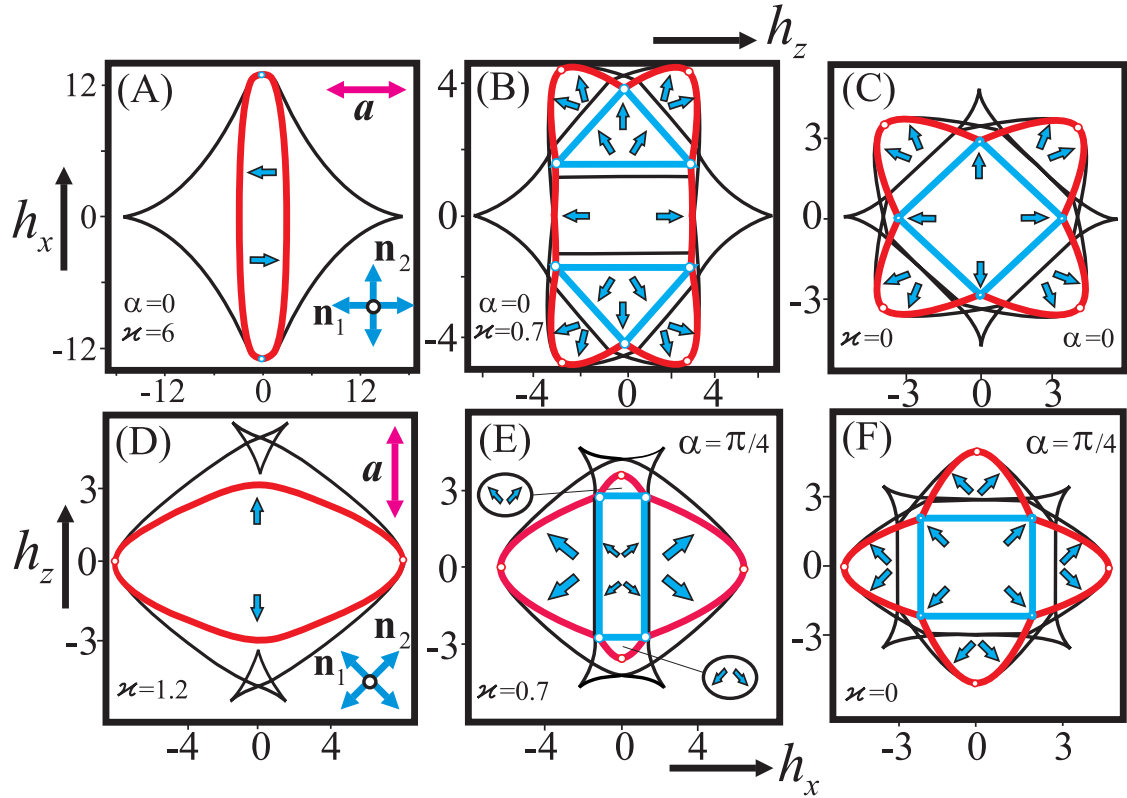


Figure 2.5.: Magnetic phase diagrams in the components of the external field  $h_x^{(e)}$ ,  $h_z^{(e)}$  for  $\alpha = 0$  ((A)- (C)) and  $\alpha = \pi/4$  ((D)- (F)). Thick lines limit regions of three- and four-phase (blue) and two-phase (red) multidomain states. Arrows show magnetic configurations in the (co-existing) domains. All calculations have been carried out for a spherical sample ( $N_{ii} = 1/3$ ).

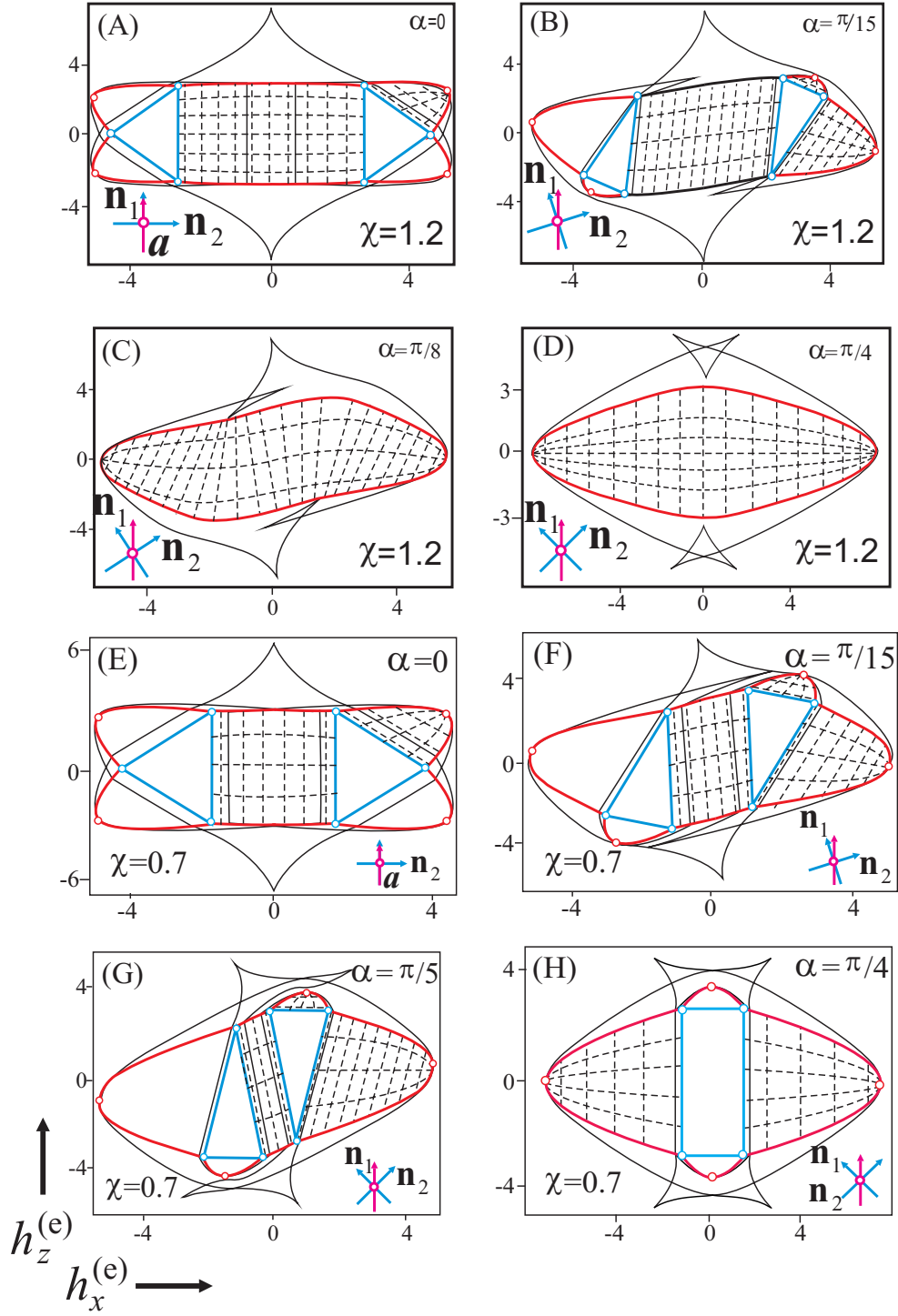


Figure 2.6.: Magnetic phase diagrams in the components of the external field  $h_x^{(e)}$ ,  $h_z^{(e)}$  for  $\chi = 1.2$ : (A)-  $\alpha = 0$ ; (B)-  $\alpha = \pi/15$ ; (C)-  $\alpha = \pi/8$ ; (D)-  $\alpha = \pi/4$  and  $\chi = 0.7$ : (E)-  $\alpha = 0$ ; (F)-  $\alpha = \pi/15$ ; (G)-  $\alpha = \pi/8$ ; (H)-  $\alpha = \pi/4$ . Thin dotted lines are the lines of the constant internal field and the constant phase fractions.

lines in Figs. 2.5, 2.6 define values of the external fields in which the internal field within the stable phases reaches the boundaries of the metastable region. The transition lines ( $\mathbf{h}_{tr}$ ) in Figs. 2.1, 2.3 transform into the areas bounded by thick (red) lines in Figs. 2.5, 2.6. These areas define maximum possible regions where thermodynamically stable multidomain states of the competing phases can exist [24, 148, 162].

For  $\varkappa > 5$  and  $\alpha = 0$  the  $(h_x, h_z)$  diagram in Fig. 2.1 (A) converts into that in Fig. 2.5 (A). The transition line in Fig. 2.1 (A) transforms into an area of a two-phase multidomain state that is bounded by an ellipse (red line). For  $|\varkappa| < 5$  and  $\alpha = 0$  the diagrams in the terms of external-field components become rather complicated: Fig. 2.5 (B) is obtained by mapping the phase diagram in Fig. 2.1 (B), and Fig. 2.5 (C) by mapping Fig. 2.1 (D). The lines of the two-phase transitions in Fig. 2.1 (B), (C) convert into areas of two-phase domain structures (DS); the points of three-phase coexistence (2.18) “swell” into the triangular regions of three-phase domain structure; and the point (0,0) in Fig. 2.1 (D), where four phase  $\theta_j = \pi j/4$  coexist, transforms into a rectangular area with a four-phase multidomain state.

The phase diagrams in Fig. 2.1 (F), (G), (H) for systems with  $\alpha = \pi/4$  are mapped into the phase diagrams in Fig. 2.5 (D), (E), (F), correspondingly. For  $\varkappa > 1$  the phase diagram in Fig. 2.5 (D) includes one region of two-phase multidomain states and two swallowtail pockets in the metastable region. For  $1 > \varkappa > 0$   $\mathbf{h}^{(e)}$ -phase diagrams include a rectangular area, where four-phase domain states are stable with spin configurations in the domains described by Eq. (2.23). Adjacent to this area, there are four regions in the phase diagrams with two-phase multidomain states (Fig. 2.5 (E)). Finally the  $\mathbf{h}^{(e)}$ - phase diagram for  $\varkappa = 0$  in Fig. 2.5 (F) becomes identical to that in Fig. 2.5 (C).

For  $\alpha$  varying from zero to  $\pi/4$  the phase diagrams are plotted in the case  $\varkappa = 1.2$  (Fig. 2.6 (A)-(D)) and  $\varkappa = 0.7$  (Fig. 2.6 (E)-(H)) and reflect the complex transformation of the regions of the DS existence. For  $\varkappa = 1.2$  the triangular areas of three phase DS and the regions of two phase DS deform (Fig. 2.6 (B)) and then disappear at all (Fig. 2.6 (C)) leading to a phase diagram with one distorted ellipse of two phase DS. The phase diagram for  $\varkappa = 0.7$  demonstrate another kind of transformation. Now, the regions of three-phase DS do not disappear (Fig. 2.6 (F), (G)) but, on the contrary, join to form a rectangular area of four phase DS (Fig. 2.6 (H)). Here in Fig. 2.6, the thin dashed lines denote the lines of constant internal field and constant phase fractions (in regions of stable two-phase DS). When an external magnetic field is varied following these lines, then either domain walls are displaced or the magnetization rotates in each domain, respectively.

In the next section I apply the diagrams of solutions in Figs. 2.1, 2.2, 2.3, 2.4 and the phase diagrams in Figs. 2.5, 2.6 to analyze the magnetization processes in nanosystems with competing anisotropies. I emphasize that those diagrams describe two limiting cases of ideally hard and ideally soft magnetic behavior. In ideally hard magnetic materials magnetization processes occur via evolution of metastable states. Magnetic phases exist everywhere in their stability regions up to their boundaries (*Stoner-Wohlfarth regime*). The corresponding magnetization curves (dotted lines in Fig. 4.16) are characterized by the widest possible hysteresis cycles, [24] and single

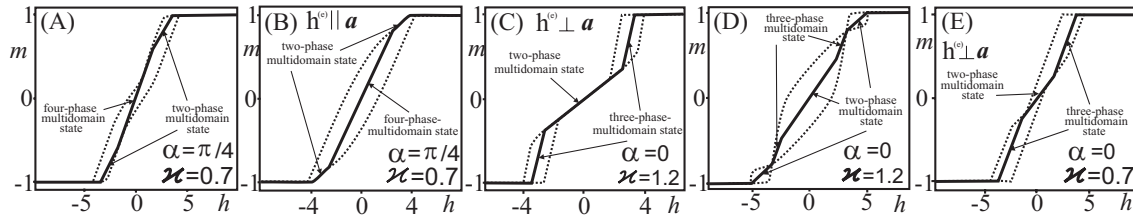


Figure 2.7.: Magnetization curves (schematically) for systems with two- and four-phase multidomain states (A),(B) and for those with two- and three-phase multidomain states (C)-(E).

domain states are realized in these systems. In the opposite case of ideally soft magnetic materials the magnetization reversal occurs via the evolution of *thermodynamically* stable states. Such *anhysteretic* processes involve the formation of multidomain patterns. These spatially inhomogeneous states are composed of domains formed by the competing phases of the magnetic-field induced first-order transition [24,148]. Extended regions of multidomain states have been observed during reorientation processes in several groups of bulk magnetic systems (e. g. orthoferrites and easy-axis antiferromagnets [148,163]). For these magnetically soft, low anisotropy systems the multidomain states are described by the phase theory equations [24,148]. The phase theory approximation strictly is valid only if the characteristic sizes of the sample are much larger than the sizes of domains, and transitional regions between domains are localized into narrow domain walls. [24] Both these requirements are met only in ideally soft, massive magnetic samples. Thus, in soft magnetic materials the magnetization processes are mainly determined by occurrence of the first-order phase transitions and the evolution of the magnetic states in the coexistence phases during these transitions (solid lines in Fig. 4.16). The magnetization processes in real materials are intermediate between these two limiting cases and include both evolution of the metastable and multidomain states. In magnetic nanolayers domain sizes usually exceed the layer thickness. In magnetic nanoparticles only few domain walls are observed, and in sufficiently small particles multidomain states are completely blocked. On the other hand, coercivity of the magnetic nanosystems prevents the formation of the equilibrium states and causes hysteretic magnetization reversal.

## 2.5. Comparison with experiment

The phase diagrams of solutions in Figs. 2.1-2.4 can be applied for explanation of magnetization processes in many nanomagnetic systems with competing anisotropies, for example, in thin films of diluted magnetic semiconductors (DMS), in ferromagnetic(FM) / antiferromagnetic(AFM) bilayers [114,129], Heusler alloys [164], and/or nanoparticles [150][V]. First, I consider the phase diagrams with symmetric arrangement of easy uniaxial and cubic anisotropy axes (Fig. 2.1, 2.2), as applied for nanolayers of DMS. And then I give examples of systems with different values of angle  $\alpha$  between anisotropy axes.

Layers of diluted magnetic semiconductors represent a new class of materials with

a strongly pronounced competing character of the magnetic anisotropy. In existing (Ga, Mn) As nanolayers the ratio  $\kappa$  of uniaxial and cubic anisotropy varies in a broad range and is controlled by strains, temperature and hole concentration [115–120,129]. The magnetization processes in  $\text{Ga}_{1-x}\text{Mn}_x\text{As}$  thin films grown by molecular beam epitaxy on GaAs(001) substrates are described by the diagrams of solutions for highly symmetric geometry,  $\alpha = 0; \pi/4$  (Fig. 2.1). The in-plane magnetization reversals in these systems are determined by the competition of cubic anisotropy with easy axes  $\langle 100 \rangle$  and uniaxial anisotropy favouring the directions of  $\langle 110 \rangle$  type. Thus, the solutions of (2.5) for  $\alpha = \pi/4$  are applicable in this case (Fig. 2.1 (E)-(H)). The main features of in-plane magnetization processes in such layers are summarized in Fig. 2.2 (B) and were experimentally investigated in a number of works [118,126,127,136].

In Ref. [136] the 300nm thick  $\text{Ga}_{1-x}\text{Mn}_x\text{As}$  ( $x = 0.03$ ) samples were studied combining direct imaging of magnetic domains and SQUID magnetometry. At temperatures above 30K the samples exhibit the uniaxial anisotropy with easy axis along [110], whereas for temperatures below 30K the magnetization vector deviates from this direction indicating the dominance of the fourfold symmetry. According to our phenomenology these magnetic films followed the temperature transition from the phase diagram in Fig. 2.1 (F) for dominating uniaxial anisotropy ( $\kappa > 1$ ) to that in Fig. 2.1 (G) with competing character of anisotropy ( $\kappa < 1$ ). The angle between the magnetization and the axis [110] is determined by the Eq. (2.23). For  $T=15\text{K}$  (the ratio  $\kappa = 0.42$  was obtained from fits of the hard-axis magnetization curves and calculating the easy-axis orientation from Eq.(2.14)) this angle is  $32^\circ$  which agrees with experimental results. The magnetization processes for high temperature ( $\kappa > 1$ , Fig. 2.1 (F), 2.5 (D)) proceed through the nucleation and expansion of domains with two orientations of the magnetization vector. In fields applied along the easy axis [110] the evolution of the DS is accompanied only by the  $180^\circ$  domain wall movement (Fig. 2.6 (D)), and the metastable states in swallow tails (see energy profiles in Fig. 2.2 (B)) can be considered as the nuclei of domains. During the magnetization processes along [100] axis the domains not only nucleate and expand but the magnetization rotates inside each domain of various phases (Fig. 2.6 (D)). The magnetization reversal for low temperature ( $\kappa = 0.42$ ) along one of the cubic easy axes proceeds in three stages [136] through the formation of intermediate domains (Fig. 2.1 (G), 2.5 (E)). In the first (and the last) stage a transversely magnetized domain nucleates indicating the entering into the area of two-phase DS in Fig. 2.5 (E). With field increasing the completely reversed domains nucleate and propagate rapidly through the sample indicating the beginning of the area with four phase DS in Fig. 2.5 (E) [136]. It is remarkable that the one stage switching processes are also possible and are accompanied by the transformation of four phase domain structure for some directions of magnetic field (blue open points in Fig. 2.5 (E)). The magnetization curves in Fig. 4.16 (A), (B) are typical for the in-plane geometry displaying biaxial character of the anisotropy. The successive switching of the magnetization in Fig. 4.16 (A) are caused by the redistribution of the metastable minima in the energy profiles for varying magnetic field (Fig. 2.2 (B)). The hysteresis loops of such a type are more pronounced for purely cubic anisotropy ( $\kappa = 0$ ) and were observed

for 603 nm-Ga<sub>0.957</sub>Mn<sub>0.043</sub>As films [126]. If the applied magnetic field makes the angle with the [100] axis in the range  $(0; \pi/4)$ , and initially spins are aligned along  $[\bar{1}00]$ , then the first incoherent reversal is related to the appearance of domains with [010] magnetization, whereas the second jump is due to the [100] domain (Fig. 2.1 (D)).

In Ref. [165] the character of in-plane magnetic anisotropy has been determined by means of transport measurements. All layers were patterned into 40-60  $\mu\text{m}$  wide Hall bar structures, and a strong anisotropic magnetoresistance effect provides a very convenient method to study the anisotropy at fixed temperature. The resistance polar plots of transport measurements for prevalent biaxial anisotropy [165] look similar to the phase diagram in Fig. 2.5 (C). The [110] uniaxial anisotropy leads to the narrowing and subsequent disappearance of the four phase DS area (Fig. 2.5 (D), (E), (F)). As well, it was shown that an additional uniaxial anisotropy with [010] easy axis is present in the system. This anisotropy results in the formation of a two phase DS region splitting the rectangle with four phases (Figs. 2.5 (B), (C)).

The solutions with  $\alpha = 0$  (Fig. 2.1 (A)-(D)). are realized for out-of-plane magnetic field and in-plane orientation of the magnetization [127, 130, 131]. The lability lines of phase diagrams for  $\alpha = 0$  (Figs. 2.1 (B), (F)) are similar to those for  $\alpha = \pi/4$  but the magnetization processes are quite different. The triple point with three coexisting phases inside the swallow tail (Fig. 2.1 (B)) has a crucial influence on the magnetization reversal and is the reason of specific double shifted hysteresis loops (Fig. 4.16 (C)) observed in many works [118, 120, 130].

In Ref. [130] Ga<sub>1-x</sub>Mn<sub>x</sub>As films grown on hybrid ZnSe/GaAs substrates with a low Mn concentration ( $x \approx 0.01$ ) were chosen to identify the role of both types of anisotropies in the magnetic reversal process. Varying the hole concentration  $p$  and temperature  $T$  the ratios  $\varkappa$  according to Figs. 2.1 (A)-(D) can be swept. For the hole concentration  $p = 8.5 \cdot 10^{19} \text{cm}^{-3}$  the temperature progression results in the succession of phase diagrams, namely, Fig. 2.1 (A) for  $T=20\text{K}$ , Fig. 2.1 (B) for  $T=7\text{K}$ , Fig. 2.1 (C) for  $T=3\text{K}$  and Fig. 2.1 (D) for  $T=1.5\text{K}$ . The switching processes for high temperature exhibit the typical behavior of a specimen magnetized along the hard direction (Fig. 2.1 (A)). In this case, a domain structure exists with magnetization vector tilted with respect to the magnetic field. As the temperature is lowered the triple point in Fig. 2.1 (B) denotes the existence of an additional stable magnetization state along the magnetic field direction. Thus, the subloops of the hysteresis curves (Fig. 4.16 (C)) reflect the jump of the magnetization into this minimum accompanied by the three phase domain structure. The variation of magnetic field in the region spanned by the swallow tails lead to various scenarios of the DS transformation (see energy profiles in Fig. 2.2 (A)). In particular, different cases (shown in Fig. 2.5 (B) by the red and blue open points) of the transition from multidomain states into a single domain state can be realized. For some directions of the magnetic field crossing regions with two- and three-phase DS one can observe even more complex hysteresis loops consisting of three subloops (Fig. 4.16 (D)). In our phenomenology the maximum hysteresis loops encircle the an-hysteretic magnetization curves with three and two phase DS. Experimentally that kind of magnetization processes was observed in Co<sub>2</sub>MnSi and Co<sub>2</sub>MnGe Heusler

alloys. [164] With the temperature decreasing the subloops in Fig. 4.16 (C) broaden around the two steps of the magnetization, and a hysteresis loop with only a weak double shift is observed (at  $T=1.5\text{K}$ , the experimentally measured value of  $\kappa \approx 0.26$  corresponds to phase diagram Fig.4.16 (E)). Note, that one should distinguish the hysteresis loops of such type for the cases with  $\alpha = \pi/4$  (Fig. 4.16 (A)) and  $\alpha = 0$  (Fig. 4.16 (E)) because the magnetization processes are fundamentally different. For (Ga,Mn)As systems with low hole concentration ( $p = 3.0 \cdot 10^{19}\text{cm}^{-3}$ ) uniaxial anisotropy is much larger than the cubic anisotropy [130]. This situation is described by model (2.5) with  $\kappa > 5$  (Fig. 2.1 (A), 2.5 (A)). If the magnetic field is applied along the easy axis of uniaxial anisotropy (Fig. 2.1 (B), 2.5 (B)) then the two phase DS transforms into a single phase state. As a remnant of the DS,  $360^\circ$  domain walls may remain in this state and can act as nuclei of new reverse domains when lowering or changing the external magnetic field. Experimentally such situations have been studied in magnetic field perpendicular to the film and for out-of-plane magnetization vector [139].

In FM/AFM bilayers of cubic materials the intrinsic cubic  $<100>$  anisotropy may compete with the uniaxial anisotropy induced by the exchange couplings between two layers. [129] To establish the exchange bias uniaxial anisotropy, the bilayer film is cooled in an in-plane magnetic field which determines the easy axis of induced anisotropy. In Ref. [129] the magnetization reversal has been studied in an exchange-biased  $\text{CaMnO}_3 / \text{La}_{0.67}\text{Sr}_{0.33}\text{MnO}_3$  bilayer film grown on vicinal  $\text{SrTiO}_3$   $<100>$  with the angle between cubic and uniaxial easy axes being  $\alpha = 30^\circ$ . With temperature decreasing the magnetic films followed the transition from the phase diagram of solutions in Figs. 2.3 (E) ( $T=160\text{K}$ ) to that in Fig. 2.4 (C) ( $T=5\text{K}$ ). The magnetization processes for high temperatures involve only the redistribution of a two phase DS (Fig. 2.6 (C)). The metastable states inside each swallow tail lead only to the slight deformation of energy profiles and do not influence significantly the magnetization reversal (Fig. 2.3 (E)). For low temperatures those metastable states become stable (Fig. 2.4 (C)) and alternatively a domain state can be realized. The three and two phase DS (Fig. 2.6 (F), (G)) in the system result in complex hysteresis loops with a hint of a double shift (Fig. 4.16 (E)) [129].

Double shifted magnetization curves with strongly pronounced subloops (Fig. 4.16 (C)) and the astroid with swallow tails (Fig. 2.3 (A)) were observed in Ref. [114] for metallic multilayersamples with the structure  $\text{Si}(100)/\text{Cu}(15\text{nm})/\text{Ni}_{80}\text{Fe}_{20}(35\text{nm})/\text{NiMn}(50\text{nm})/\text{Co}(\text{tnm})/\text{Pd}(15\text{nm})$  grown by an e-beam evaporation system. The thickness was varied between 5 nm and 25 nm. It was shown that the double-shifted hysteresis loops (and parameter  $\kappa$ ) could be tuned by several parameters, e.g., the variation of Co film thickness, and the field-annealed time.

In magnetic single-domain nanoparticles the competition of the uniaxial anisotropy due to the enhanced surface interactions and intrinsic magnetocrystalline anisotropy stabilizes different multiple magnetic states in the system with the possibility of switching between them (for details see Ref. [V]). Different geometries of relative easy axes alignment are realized in these nanoobjects. Phase diagrams with "swallow tails" (Fig. 2.6 (C)) for misaligned easy anisotropy axes have been obtained for Fe-Cu-B nanoparticles [122] and Co clusters. [123] Astroids with rounded corners (Fig.

2.5 (A)) have been observed in fcc-Co [124] and BaFeCoTiO nanoparticles [125].

In general, in many cases of practical interest the geometry with noncoplanar competing anisotropies is observed [129, 132, 133]. For example, in 50 nm thick  $\text{Ga}_{0.91}\text{Mn}_{0.09}\text{As}$  thin films grown on (311)A and (311)B substrates [129] the uniaxial anisotropies with  $[01\bar{1}]$  (or  $[\bar{2}33]$ ) and  $[311]$  easy axes compete with cubic anisotropy of  $\langle 100 \rangle$  type. In this case three dimensional phase diagrams, parametrized by the various ratios of anisotropy coefficients and magnetic field components, have to be constructed instead of 2D diagrams of solutions. Even for considered DMS films with (001) orientation, the out-of-plane magnetization processes can be considered as coplanar only with some restrictions. Indeed, for biaxial in-plane anisotropy and magnetic field perpendicular to the film one generally has a non-coplanar arrangement of the magnetization in domains. In that case, the phase diagram in Fig.2.5 (B) is only the cross-section of that more complex 3D phase diagram. But due to the degeneracy of in-plane cubic  $[100]$  and  $[010]$  axes with respect to the magnetic field the main peculiarities of the switching processes can be readily explained with the simple 2D phase diagram (Fig.2.1 (B)). Therefore, the magnetic anisotropy geometry and magnetic field orientation determine which phase diagrams of solutions (2D or 3D) is applicable in a particular case.

## 2.6. Multidomain patterns

Multidomain patterns have been observed in a number of systems with in-plane [136] and out-of-plane magnetization [135, 137–139, 166–169]. Particularly, isolated domain walls trapped in micropatterned constrictions of (Ga,Mn)As films demonstrate a number of remarkable properties [170–173] and can be used in different nanoelectronic devices (e. g. as magnetoresistive elements) [170]. The fine structure of the isolated domain wall is of prime importance when different types of domain walls are observed [174][I-IV]. Here in particular, I demonstrate that for the considered systems with competing anisotropies various types of domain walls exist with large sensitivity of their appearance on material parameters and external fields. Using the results of the two previous sections I calculate the equilibrium parameters of isolated planar domain walls and derive the equilibrium parameters of stripe domains in system with out-of-plane magnetization.

### 2.6.1. The structure of domain walls

For a planar isolated domain wall with energy density  $\Phi(\theta)$  (2.5) the structure is derived by optimization of the functional [I-IV]

$$w_{DW} = A\theta_x^2 + K_c\Delta\Phi(\theta) \quad (2.25)$$

with the boundary conditions

$$\theta_x(\pm\infty) = 0, \theta(+\infty) = \theta_1, \theta(-\infty) = \theta_2 \quad (2.26)$$



( $x$  is a spatial variable across the domain wall), and

$$\Delta\Phi(\theta) = \Phi(\theta) - \Phi_0, \quad (2.27)$$

where

$$\Phi_0 = \Phi(\theta_1) = \Phi(\theta_2) = \{\min\Phi\} \quad (2.28)$$

is the global minimum of the system. For such a one-dimensional problem (2.25) the Euler equation and the first integral can be written as [24]

$$2x_0^2\theta_{xx} = \Phi_\theta, \quad (2.29a)$$

$$x_0^2(\theta_x)^2 = \Delta\Phi(\theta) \quad (2.29b)$$

where  $x_0 = \sqrt{A/K_c}$  is a characteristic width of the domain wall.

The domain wall profiles  $\theta(x)$ , their energy and characteristic sizes can be readily derived by direct integration. However, Eqs. (2.29) allow to understand the main features of such solutions. The Eq. (2.29) shows that the *inflection* points of the domain wall profiles  $\theta(x)$  correspond to *stationary* points of potential (2.5) ( $\Phi_\theta = 0$ ). The second equation (2.29) shows that the larger the deviations of the energy from the minima  $\Delta\Phi(\theta)$  the larger the gradients of the profiles,  $\theta_x$ . Thus, the nucleation and further evolution of local minima in the metastable region causes complex reconstructions of the domain wall profiles. Transformations of the domain wall profiles have been earlier observed in easy-axis antiferromagnets and other magnetic crystals (see examples in Ref. [148]). Due to the remarkable lability of the potential profiles (2.5) (Fig. 2.2) this effect is expected to be strong in the systems with competing anisotropies. As an example, I derive the parameters of the domain walls for four-phase domains with the canted states (2.23) that are realized in the systems with  $\alpha = \pi/4$ ,  $1 > \varkappa > 0$  at zero fields.

In this case three types of domain walls can exist (Fig. 2.8 (A)): DWI between domains with  $\theta_1$ ,  $\theta_2$  and  $\theta_3$ ,  $\theta_4$

$$\Delta\theta_I = |\theta_1 - \theta_2| = |\theta_3 - \theta_4| = \arccos \varkappa, \quad (2.30)$$

DW II between  $\theta_1$ ,  $\theta_3$  and  $\theta_2$ ,  $\theta_4$

$$\Delta\theta_{II} = |\theta_1 - \theta_3| = |\theta_2 - \theta_4| = \pi - \Delta\theta_I, \quad (2.31)$$

and DWIII of  $180^\circ$  type between domains  $\theta_1$ ,  $\theta_4$  and  $\theta_2$ ,  $\theta_3$ . By integration of (2.29) the energy  $\sigma$  and the magnetization profiles for the DWI (upper signs) and DWII (lower signs) can be readily obtained as

$$\sigma = \delta_0 \left[ \sqrt{1 - \varkappa^2} \mp \varkappa \arccos(\pm \varkappa) \right] \quad (2.32)$$

$$x = \frac{x_0}{\sqrt{2(1 - \varkappa^2)}} \ln \left( \mp \frac{\tan \theta - \tan \theta_1}{\tan \theta + \tan \theta_1} \right), \quad (2.33)$$

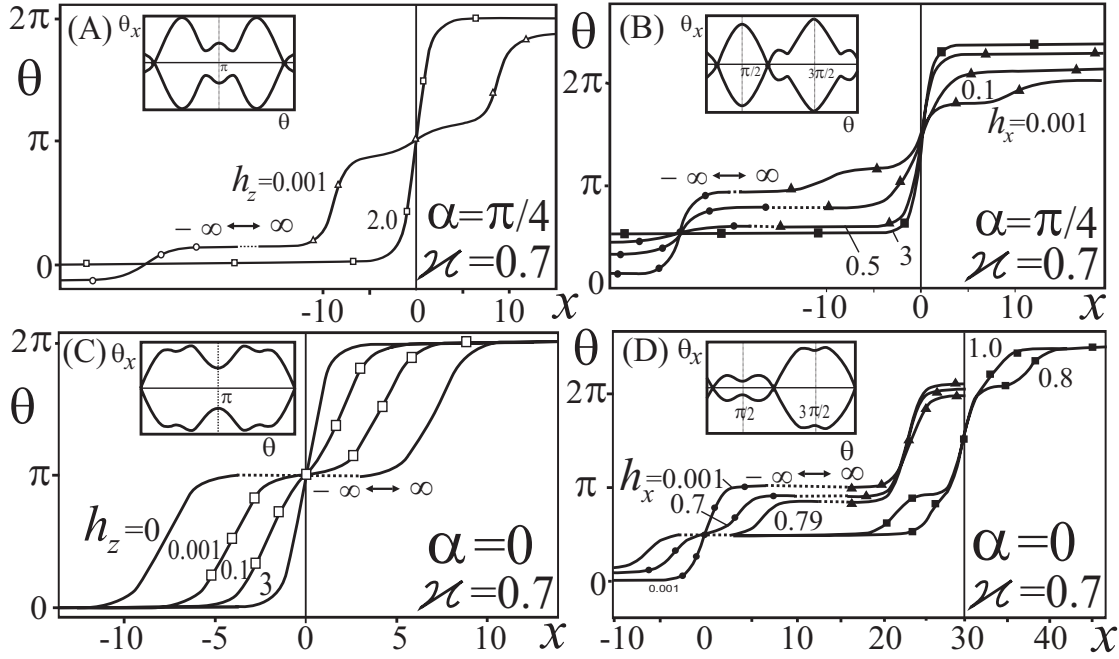


Figure 2.8.: Domain wall profiles for  $\varkappa = 0.7$ : (A), (B)-  $\alpha = \pi/4$ , (C), (D) -  $\alpha = 0$ . Corresponding energy profiles are plotted in Fig. 2.2. Insets show the phase plane  $(\theta; \theta_x)$  where  $\theta_x = d\theta/dx$  (See Eq.(2.29)).

where  $\delta_0 = \sqrt{A K_c}$ . Depending on the ratio  $1 > \varkappa > 0$  DWI with  $\Delta\theta_I < 90^\circ$  becomes more favourable than DWII with  $\Delta\theta_{II} > 90^\circ$  and should exhibit stronger contrast in experiment [174]. Such domain boundaries were experimentally observed in thin films of (Ga,Mn)As by Lorentz microscopy. [174] From Ref. [175] and using (2.33) I can evaluate the DW width. For DWI at the temperature  $T = 10$  (30)K I obtain  $\delta = 50$  (100)nm while for DWII  $\delta = 43$  (76)nm which is consistent with the experiment. Here,  $A = 0.4 \cdot 10^{-12} \text{Jm}^{-1}$ ,  $K_c = 1.18$  (0.32)  $\text{Jm}^{-3}$ ,  $K_u = 0.18$  (0.11)  $\text{Jm}^{-3}$ . For  $\varkappa > 1$  only DWIII exist.

These domain walls are characterized by strong variation of their parameters with the applied magnetic field. At magnetic field  $h_z$  or  $h_x$  domain walls of two types are present: walls where the magnetization vector rotates less or more than  $180^\circ$  (Fig. 2.8 (A), (B)). Note, that for magnetic field  $h_z > 2(1 - \varkappa)$  the metastable minima (Fig. 2.2 (B)) strongly influence the profile and energy of the domain. Such a remarkable modification of the structure should strongly influence magnetoresistance of domain walls (e. g. in nanoconstrictions).

In Fig. 2.8 (C), (D) domain wall profiles and typical phase portraits for the case  $\alpha = 0$  ( $\varkappa = 0.7$ ) are plotted. At applied magnetic field  $h_z$  only  $360^\circ$  domain walls exist. Within these walls, nuclei of the domain with  $\pi$  and  $\pm\pi/2$  are present (see phase portrait in Fig. 2.8 (C)). In a magnetic field strong enough these nuclei disappear. So, the energy of domain wall increases, although the width decreases. By application of magnetic fields perpendicular to the easy axis  $\mathbf{a}$  in the interval  $[0; a_1]$  there are walls of two types between upper and lower canted phases (Fig. 2.8

(D)). In each domain wall nuclei of domains with  $\pi/2$  and  $3\pi/2$ , correspondingly, are present. At  $h_x = h_x(a_1)$  these nuclei expand forming three-phase multidomain textures [130].

### 2.6.2. Parameters of stripe domains

Magnetic configurations in (Ga,Mn)As systems include a number of noncollinear two- and multi-phase states. These phases can create thermodynamically stable multidomain states [148]. For two coexisting phases with the magnetization  $\mathbf{M}^{(1)}$  and  $\mathbf{M}^{(2)}$  effective values of magnetization can be introduced [148]

$$M_{\perp} = \frac{(\mathbf{M}^{(1)} - \mathbf{M}^{(2)}) \cdot \mathbf{v}}{2}, \quad H = \frac{[\mathbf{H} - \mathbf{H}_{tr} - 4\pi(\mathbf{M}^{(1)} + \mathbf{M}^{(2)})] \cdot \mathbf{v}}{2}. \quad (2.34)$$

In particular, for perpendicular magnetized (Ga,Mn)As nanolayers with  $\kappa > 5$  the phase diagrams of magnetic states (Fig. 2.1, (A), (E)) are similar to those for uniaxial ferromagnets. In this case  $M_{\perp} = M_0$  and domains are separated by  $180^\circ$  domain walls [24]. According to Eq.(2.34) the problem of multidomain states for two-phase noncollinear states can be reduced to a ferromagnetic collinear domain structure with up and down magnetization  $M_{\perp}$  in a bias field  $H$  ( $\mathbf{v}$  is the unity vector perpendicular to the layer plane,  $\mathbf{H}_{tr}$  is the transition field between the phases  $\mathbf{M}^{(1)}$  and  $\mathbf{M}^{(2)}$ ) [148]. Similar multidomain texture are formed in the systems with a number of coexisting phases larger than two. For example, for  $-1 < \kappa < 1$ ,  $\alpha = 0$  the magnetic configurations (Eq. (2.23)) create four-phase multidomain states. In a layer with  $\mathbf{a} \parallel \mathbf{v}$  these textures can be described by a model of ferromagnetic domains with the magnetization (Fig. 2.9)

$$M_{\perp} = M \sqrt{\frac{1 + \kappa}{2}}. \quad (2.35)$$

With effective values of the magnetization  $M_{\perp}$  and bias field  $H$  (2.34) the energy density of a (Ga,Mn)As nanolayer with stripe domains can be reduced to the well-studied model of ferromagnetic stripes [24, 176, 177]

$$w = 2\pi M_{\perp}^2 \left[ w_m + \frac{2\Lambda p}{\pi^2} - \frac{Hq}{2\pi M_{\perp}} \right] \quad (2.36)$$

with the stray field energy density given by

$$w_m = 1 - \frac{2p}{\pi^2} \int_0^1 (1 - \tau) \ln \left[ 1 + \frac{\cos^2(\pi q/2)}{\sinh^2(p\tau/2)} \right] d\tau, \quad (2.37)$$

where

$$p = 2\pi \frac{t}{D}, q = \frac{(d_+ - d_-)}{D}, \quad (2.38)$$

$t$  is the layer of thickness  $t$ ,  $D = d_+ + d_-$  is the stripe period, and  $d_{\pm}$  are domain

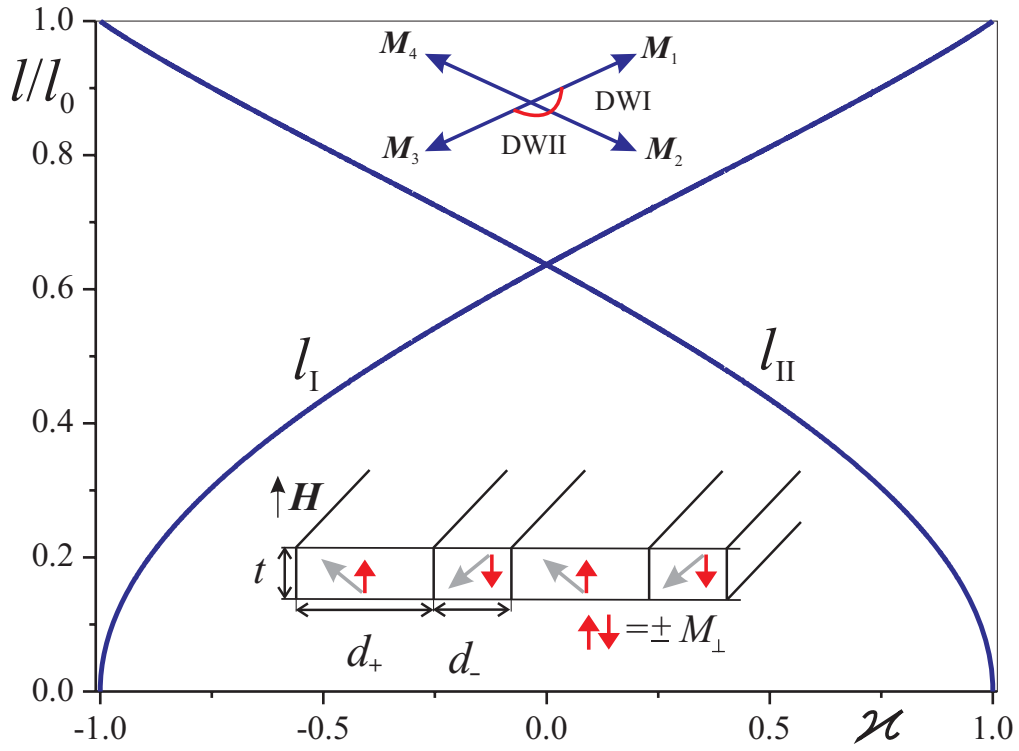


Figure 2.9.: Characteristic lengths  $l_{I(II)}$  for stripe domains with DWI(DWII) in four-phase state ( $l_0 = \pi\sqrt{AK_c}/(4M_0^2)$ ).

sizes with up and down magnetization (Fig. 2.9). The dimensionless parameter

$$\Lambda = \frac{\sigma(\kappa)}{4M_{\perp}(\kappa)^2 t} = \pi \frac{l(\kappa)}{t} \quad (2.39)$$

measures the ratio between the domain wall energy  $\sigma$  and the stray field energies. It scales with the *characteristic length*

$$l(\kappa) = \frac{\sigma}{4\pi M_{\perp}^2} \quad (2.40)$$

as the relevant material parameter [24]. Minimization of (2.36) with respect to  $p$  and  $q$  derives the solutions for the geometric parameters  $d_{\pm}$  as functions of three control parameters of model (2.37): the layer thickness  $t$ , the bias field  $H$ , and factor  $\Lambda$ . These solution have been investigated in detail (see Refs. [24,176,177] and bibliography in Ref. [24]). Particularly, it was shown that the solutions for stripes exist only below certain critical field [177]

$$H < H^*(\Lambda) < 4\pi M_{\perp}. \quad (2.41)$$

As the bias field approaches  $H^*$  the stripes gradually transform into the homogeneous state by unlimited growth of the period ( $D \rightarrow \infty$ ). However, at the critical field the domain of the minority phase preserves a finite size  $d_{-}(H^*) = d_{-}^*$ . At higher fields

$$H^* > H > 4\pi M_{\perp} \quad (2.42)$$

it exists as a metastable state gradually shrinking to zero size at the saturation field.

In perpendicular magnetized (Ga,Mn)As layers the period of multidomain patterns exceed their thicknesses [135,139,169]. For such large stripes ( $D \geq t$ ) the expansion of the integral (2.37) allows to simplify the problem [176]. After some algebra, the solutions for stripes can be derived in analytical form as a set of parametrical equations

$$D(H) = \frac{\pi u t}{\sqrt{1 - (H/H^*)^2}}, \quad d_{\pm} = \frac{D}{\pi} \arccos \left( \mp \frac{H}{H^*} \right), \quad (2.43)$$

$$H^*(u) = 4\pi M_{\perp} f(u), \quad 2\Lambda = g(u). \quad (2.44)$$

Here I introduce parameter

$$u = \frac{d_{-}^*}{t} \quad (2.45)$$

and functions

$$f(u) = \frac{2 \arctan \frac{1}{u} - u \ln \left( 1 + \frac{1}{u^2} \right)}{\pi}, \quad (2.46)$$

and

$$g(u) = (1 + u^2) \ln(1 + u^2) - u^2 \ln(u^2). \quad (2.47)$$

According to (2.43) at zero field

$$D(0) = D_0 = \pi t u, \quad (2.48)$$

thus, the ratio

$$\frac{D_0}{d_-^*} = \pi. \quad (2.49)$$

It means that at the transition field the domain of the minority phase becomes approximately six times narrower than the domain size at zero field ( $D_0/2$ ). Within this approximation the equilibrium magnetization in the stripe phase equals

$$\langle M \rangle = M_\perp q = \frac{2M_\perp}{\pi} \arccos \left( \frac{H}{H^*} \right). \quad (2.50)$$

Finally, in the limit of large domains  $D \gg t$ ,

$$D_0 = \pi t \exp(\Lambda - 1/2), \quad (2.51)$$

and the transition fields for stripe and bubble domains becomes exponentially small, e. g. transition field

$$H^* = 4M_\perp \exp(-\Lambda + 1/2), \quad (2.52)$$

the bubble collapse field

$$H_c = 16M_\perp \exp(-\Lambda - 1/2), \quad (2.53)$$

and ratio [176]

$$\frac{H^*}{H_c} = \frac{e}{4} = 0.6796. \quad (2.54)$$

These results show that the solutions of magnetic domains in (Ga,Mn)As layers should demonstrate general features similar to those in uniaxial ferromagnets. However, there is an important difference between these two systems. In uniaxial ferromagnets the characteristic length is expressed as a combination of basic magnetic parameters (constants of uniaxial anisotropy  $K_u$ , exchange stiffness  $A$  and saturation magnetization  $M$ ):

$$l_f = \frac{\sigma_f}{4\pi M^2} = \frac{\sqrt{AK_u}}{\pi M^2} \quad (2.55)$$

depends only on values of uniaxial anisotropy  $K_u$ . On the contrary, in the diluted magnetic semiconductors the characteristic length  $l(\varkappa)$  strongly depends on the values of competing magnetic anisotropies and varies in a broad range providing a complex behaviour of multidomain patterns in these materials. Eqs. (2.43), (2.44), (2.50) connect equilibrium parameters of stripe domains with material parameters of (Ga,Mn)As systems (2.5). For this model calculations of  $M_\perp$  and the domain wall

energy  $\sigma$  allow to express  $\Lambda$  as a function of  $\kappa$  and  $\alpha$ . For example, for four-phase domains (Eq. (2.23)) the magnetization and the domain wall energies (Eq. (2.32)) yield functions  $l_{I(II)}(\kappa)$  plotted in Fig. 2.9.

Stripe domains have been observed in a number of (Ga,Mn)As nanolayers [135, 137–139, 166–169]. In Table I I collect experimental data (indicated by bold) and the calculated stripe domains parameters (by solving Eqs. (2.43), (2.44), (2.50)) for (Ga,Mn)As layers (a-c), an yttrium-iron garnet film (d) and FePd nanolayers (e,f). For thin layers of (Ga<sub>0.957</sub>Mn<sub>0.043</sub>)As for  $T = 9$  K (1) and  $T = 80$  K (2) [135] I use the experimental values of  $t$  and  $D_0$  to calculate other parameters of stripes. For a layer (Ga<sub>0.93</sub>Mn<sub>0.07</sub>)As at  $T = 80$  K [169] I use  $t$  and a value of the transition field  $H^*/(4\pi M_\perp)$  to calculate  $l$ ,  $\Lambda$  and domain sizes  $D_0$  and  $d_-^*$ . For comparison I derive stripe domain parameters for an epitaxial garnet film Y<sub>1.88</sub>Lu<sub>0.2</sub>Ca<sub>0.92</sub>Ge<sub>0.92</sub>Fe<sub>4.08</sub>O<sub>12</sub> [178], and for FePd nanolayers [179]. According to [169] the saturation magnetization in (Ga<sub>0.93</sub>Mn<sub>0.07</sub>)As  $M_s = 28$  kA/m. Then, from the calculated value of the characteristic length I derive  $\sigma = 49.0$   $\mu\text{J}/\text{m}^2$  (for comparison, in the (Y,Fe) garnet film  $M_s = 13.6$  kA/m, and  $\sigma = 110$   $\mu\text{J}/\text{m}^2$  [178]).

In garnet films and other classical materials with perpendicular anisotropy regular stripe domains are observed, if the layer thickness is considerably larger than the characteristic length. In such systems the equilibrium domain sizes at zero field  $D_0$  do not exceed the layer thicknesses ( $D_0 \leq t$ ). When films become thinner than  $l$  (e.g. in the vicinity of the compensation temperature of ferrimagnets [176]) the demagnetization forces are too weak to overcome coercivity and the formation equilibrium domains is impeded. As a result such multidomain patterns consist of very large domains with irregular boundaries [24]. Similar disordered domains and strongly hysteretic behaviour have been observed in (Ga,Mn)As films with perpendicular anisotropy [135, 138, 167–169]. It means that the equilibrium multidomain state are hardly reached in these systems. For example, in (Ga<sub>0.93</sub>Mn<sub>0.07</sub>)As layers the observed width of the minority stripe at the critical field is  $d_-^* = 1.7 \pm 0.3$   $\mu\text{m}$  [169], and about one order larger than the calculated equilibrium value ( $d_-^* = 0.2$   $\mu\text{m}$ ). Up to now only few results on experimental investigations of multidomain states in perpendicularly magnetized (Ga,Mn)As nanolayers have been reported. New detailed investigations involving modern experimental methods developed in other fields of nanomagnetism (see e.g. Ref. [253]) are desirable. The results of this section establish important physical connections with multidomain states in other classes of perpendicular magnetized materials and provide a theoretical basis for future research.

## 2.7. Surface-induced anisotropy and multiple states in elongated magnetic nanoparticles

Magnetic nanoparticles play a vital role in modern magnetoelectronics, and are considered as very promising materials for various applications in nanophysics and biomedicine [181, 182]. Moreover, magnetic nanoparticles provide an ideal model sys-

Table 2.1.: Parameters of the stripe domains in (Ga,Mn)As layers (a-c) [135,169], a (Y,Fe) garnet film (d) [178] and FePd nanolayers (e,f) [179]. They include experimental values (bold) and the results derived from model (2.36). Here,  $t$  is the layer thickness,  $l$  is the characteristic length,  $\Lambda = \pi l/t$  is the dimensionless parameter measuring the ratio between the domain wall energy and the stray field energy (see Eqs. (22),(23)),  $D_0$  is the equilibrium period at zero field,  $d_-^*$  is the equilibrium size of the minority phase at  $H = H^*$ , the transition field into the homogeneous state, Eq. (25).

	$t, \mu\text{m}$	$l, \mu\text{m}$	$\Lambda$	$D_0, \mu\text{m}$	$d_-^*, \mu\text{m}$	$H^*/(4\pi M_\perp)$
(a) (Ga <sub>0.957</sub> Mn <sub>0.043</sub> )As	<b>0.2</b>	0.132	2.07	<b>3.0</b>	0.95	$6.6 \cdot 10^{-2}$
(b) (Ga <sub>0.957</sub> Mn <sub>0.043</sub> )As	<b>0.2</b>	0.220	3.45	<b>12.0</b>	3.82	$1.7 \cdot 10^{-2}$
(c) (Ga <sub>0.93</sub> Mn <sub>0.07</sub> )As	$5 \cdot 10^{-2}$	0.10	1.920	0.643	0.2038	<b><math>3.9 \cdot 10^{-2}</math></b>
(d) (Y,Fe) garnet film	<b>11.0</b>	<b>0.47</b>	0.1342	12.50	3.0	0.6
(e) FePd nanolayer	$3.6 \cdot 10^{-2}$	$9 \cdot 10^{-3}$	0.7526	<b>0.13</b>	$3.9 \cdot 10^{-2}$	0.2612
(f) FePd nanolayer	<b><math>1.15 \cdot 10^{-2}</math></b>	$9 \cdot 10^{-3}$	2.477	<b>0.26</b>	$8.3 \cdot 10^{-2}$	$4.4 \cdot 10^{-2}$

tem to study different aspects of surface magnetism and magnetization reversal [125]. Recently, the advances in nanometer scale fabrication technology lead to the synthesis of different types of *elongated* magnetic nanoparticles (e.g. spherical, ellipsoidal, spindle-shaped or "nanorice") [183,184]. In particular, magnetic nanoparticles with different aspect ratios and sizes (ranging from 5 nm to several micrometers) can be fabricated by a polyol process as demonstrated in Ref. [184]. In such aspherical systems the enhanced surface interactions [5] should result in sizable uniaxial magnetic anisotropy. In this section I show that the additional anisotropy contribution allows to vary the magnetic properties over a broad range, in particular, to fix the magnetization in desirable directions and prevent superparamagnetic effects in small particles.

### 2.7.1. "Shape factors" of surface-induced anisotropy

I consider a case important in practice, where the surface-induced uniaxial anisotropy is described by constant surface density  $K_s$  (Néel approach) [5] and is written as (see also section 1.2.2 C):

$$w_s = -\frac{1}{V} \int_S K_s(\mathbf{r})(\mathbf{m} \cdot \mathbf{n})^2 dS, \quad (2.56)$$



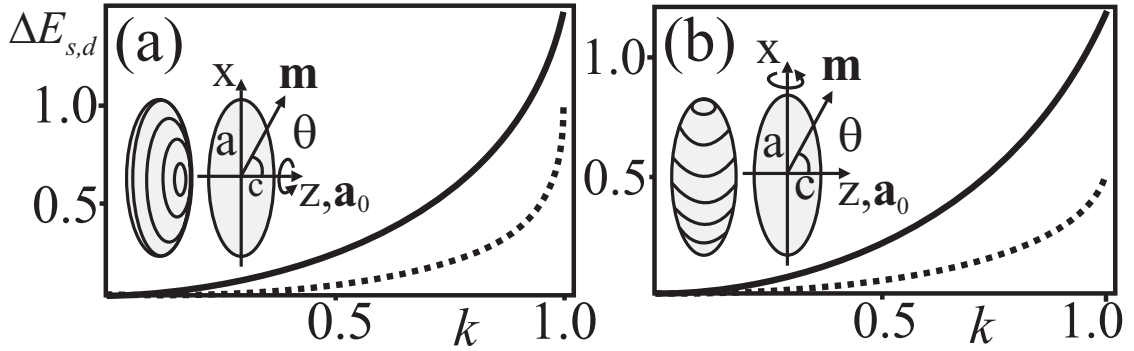


Figure 2.10.: Comparison of the demagnetization energy  $\Delta E_d$  (dotted line) and the induced anisotropy energy  $\Delta E_s$  (full line) for prolate (a) and oblate (b) ellipsoids

where  $\mathbf{n}$  is the unity vector normal to the particle surface. For ellipsoidal nanoparticles with the axes  $(2a, 2b, 2c)$  and a constant value of  $K_s$ , the surface energy  $w_s$  is reduced to a functional form of second-order anisotropy for an orthorhombic ferromagnet

$$W_s = K_v[\Lambda_1(\mathbf{m} \cdot \mathbf{a}_0)^2 + \Lambda_2(\mathbf{m} \cdot \mathbf{b}_0)^2 + \Lambda_3(\mathbf{m} \cdot \mathbf{c}_0)^2] \quad (2.57)$$

where  $\mathbf{a}_0, \mathbf{b}_0, \mathbf{c}_0$  are the unity vectors along the ellipsoid axes, and the "shape factors"  $\Lambda_i(a, b, c)$  can be written as elliptic functions of the ellipsoid sizes. For ellipsoids of revolution with eccentricity

$$k = \sqrt{1 - \frac{c^2}{a^2}} \quad (2.58)$$

the coefficients  $\Lambda_i$  can be expressed via elementary functions. For prolate shapes of the dimensions  $(2a, 2a, 2c)$  I get:

$$\begin{aligned} \Lambda_a &= \frac{3(1 - k^2)}{8k^3} \left( -2k - (1 + k^2) \log \frac{1 - k}{1 + k} \right), \\ \Lambda_c &= \frac{3}{4k^3} \left( 2k + (1 - k^2) \log \frac{1 - k}{1 + k} \right), \end{aligned} \quad (2.59)$$

and for oblate ellipsoids with the dimensions  $(2a, 2c, 2c)$  I receive:

$$\begin{aligned} \Lambda_a &= \frac{3(1 - k^2)}{2k^3} \left( -k\sqrt{1 - k^2} + \arcsin k \right) \\ \Lambda_c &= \frac{3}{4k^3} \left( k\sqrt{1 - k^2} + (2k^2 - 1) \arcsin k \right). \end{aligned} \quad (2.60)$$

Figure 2.10 shows a comparison of shape factors  $\Lambda_i$  and demagnetizing factors of an ellipsoid  $\hat{\mathbf{N}}$ :

$$\Delta E_d = (N_a - N_c), \Delta E_s = (\Lambda_a - \Lambda_c). \quad (2.61)$$

Both the demagnetizing factors  $N_i$  and the "shape factors"  $\Lambda_i (i = a, b, c)$  are geometrical factors, which depend only on the ratio of the ellipsoid geometrical axes. However, their impacts on the magnetic states are fundamentally different. The surface anisotropy energy  $w_s$  is imposed by short-range internal (local) magnetic interactions. On the contrary, the demagnetizing fields are produced by the sample magnetization and have long-range (non local) character. Note that for systems with locally out-of-plane surface anisotropy ( $K_s > 0$ ) the uniaxial anisotropy favours the magnetization orientation along the shorter ellipsoidal axis, while the demagnetization energy (so-called "shape anisotropy") reaches the minimum when the magnetization is along the longer axis. Thus, the uniaxial anisotropy weakens the demagnetization effects, and may even completely suppress them. According to numerous experiments on magnetic nanolayers, the surface anisotropy  $K_s$  can be strongly increased by covering the magnetic layers with different nonmagnetic materials [5]. Similar effects could be produced in coated magnetic nanoparticles.

### 2.7.2. Magnetization processes and multiple states in magnetic nanoparticles

The equilibrium magnetic states in the nanoparticle are formed as a result of the competition between applied magnetic field, cubic and uniaxial anisotropies [148–150]. Because the strength of these anisotropy contributions and the relative orientation of the easy axes can vary over a broad range, the system should possess a large variety of magnetic phases with different types of spontaneous and induced magnetic reorientation transitions.

Using Eq. (2.24) [V,VI] the phase diagram for the components of the internal field (Fig. 2.1) is transformed into those in external-field components (Fig. 2.11). The lability lines (full black lines) of these diagrams bound the regions of metastable states. The areas inside, which are marked by dotted/dashed lines (red and blue), include several stable states of  $\mathbf{m}$  with the possibility of switching from one stable homogeneous state to another. Regions confined by dotted red lines are obtained by transformation of the corresponding transition lines of Fig. 2.1. They include two stable orientations of  $\mathbf{m}$ . The critical points in Fig. 2.1 (a) "swell" into the triangular regions with three possible homogeneous states (blue dashed line in Fig. 2.11 (b)). The point in the origin of Fig. 2.1 (b) where four phases coexist is mapped into a rectangular area with four possible orientations of  $\mathbf{m}$ . (Fig. 2.11 (d)). One has to distinguish these regions from those of the multidomain structures considered in Fig. 2.5.

As an example, I consider magnetization processes in elongated nanoparticles influenced solely by the uniaxial surface anisotropy. The equilibrium homogeneous magnetic states in such a nanoparticle are formed as a result of the competition between applied magnetic field and surface anisotropy [V,VI]. In this case the reduced energy density from Eq. (2.3) of the system  $\Phi(\theta) = (w_0 \cdot c)/(K_s \Delta E_s)$  can be written as

$$\Phi(\theta) = -\cos^2 \theta - h \cos(\theta - \psi), \quad (2.62)$$

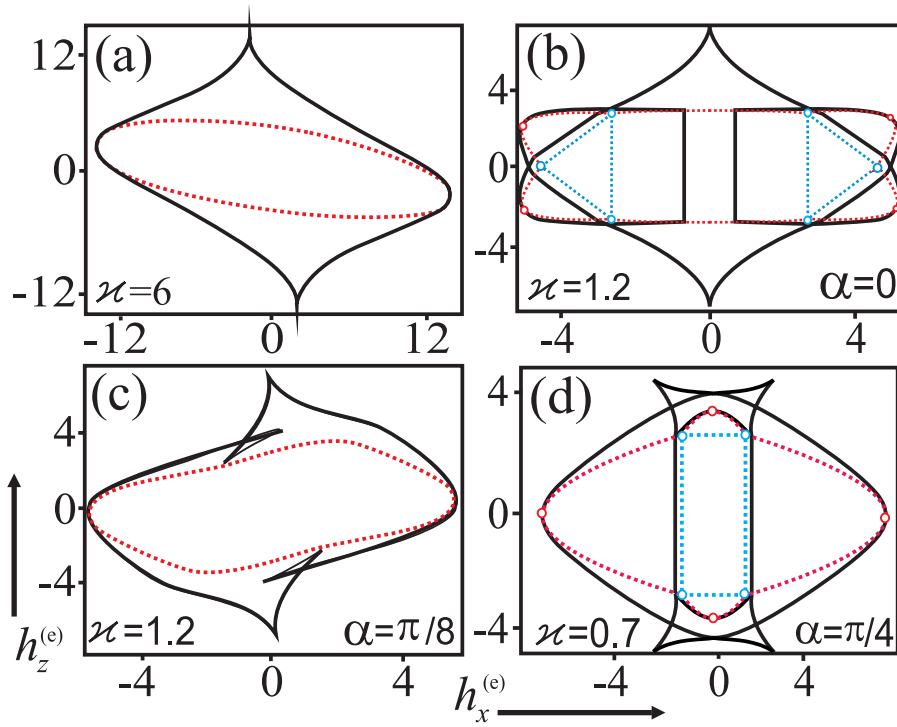


Figure 2.11.: Typical phase diagrams in the external field components for elongated magnetic nanoparticles: (a) large uniaxial anisotropy ( $\kappa = 6$ ) and misoriented anisotropy and ellipsoid axes ( $N_{xz} \neq 0$ ); (b) competing anisotropies with angle  $\alpha = 0$  between their easy axes and  $\kappa = 1.2$ ; (c) misaligned easy axes with  $\kappa = 1.2, \alpha = \pi/8$ ; (d) easy axis to be directed along diagonal between two cubic axes,  $\kappa = 0.7$ .

where  $h = H/H_c$  ( $H_c = K_s \Delta E_s / (cM_0)$ ). The solutions of  $\theta$  minimizing the potential  $\Phi(\theta)$  (2.62) compose a phase diagram in components of internal magnetic field  $(h_x, h_z)$  (the famous Stoner-Wohlfarth astroid [140], thick full line in Fig. 2.12 (a)). To map this critical line on the space spanned by the components of external magnetic field  $(h_x^{(e)}; h_z^{(e)})$  one has to use the following relation [V,VI]:

$$\mathbf{h}^{(e)} = \mathbf{h} + \frac{4\pi c}{K_s \Delta E_s} \hat{N} \mathbf{m}(\mathbf{h}). \quad (2.63)$$

It is possible to write analytic expressions for critical line  $\mathbf{h}^{(e)}$  (dashed line in Fig. 2.12 (a)):

$$h_z^{(e)} = (1 - h_x^{2/3})^{3/2} + 4\pi N_{zz} \cos \theta. \quad (2.64)$$

Overall the magnetic phase diagram in Fig. 2.12 (a) describes the main features of the model (2.62) as applied to single-domain nanoparticles and provides a basis for detailed analysis of the magnetization processes [V,VI]. In experiments on single nanoparticles, astroids  $h_z^{(e)}$  (Fig. 2.12 (a)) with rounding of their edges have been observed in fcc-Co [124] and BaFeCoTiO nanoparticles [185] (Fig. 2.12 (b)).

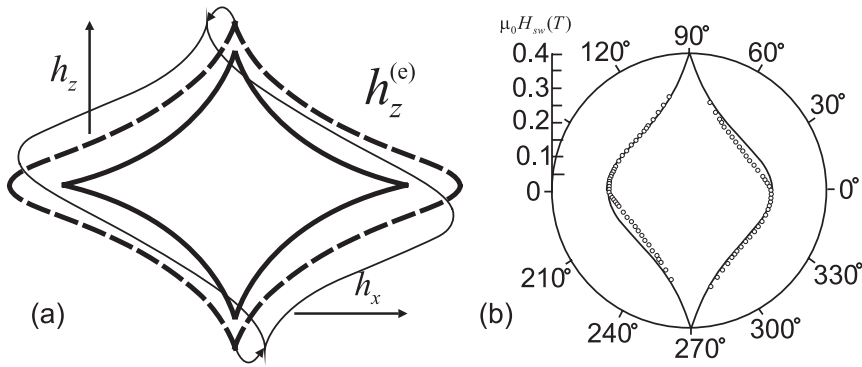


Figure 2.12.: (a) The mapping of the famous Stoner-Wohlfarth astroid (thick full line) onto the plane of external field components (dashed line). The thin full line is for the case  $N_{xz} \neq 0$  (read text for details). (b) The switching field  $H_{sw}$  of the BaFeCoTiO nanoparticle as a function of the angle  $\theta$  (Data are taken from W.Wernsdorfer et al. [185]).

Phase diagrams with "swallow tails" (Fig. 2.11 (c)) have been obtained for Fe-Cu-B nanoparticles [122] and Co clusters [123]. In nanoparticles with misorientated anisotropy and ellipsoid geometrical axes (i.e. when  $N_{xz} \neq 0$ ) the critical line  $h_z^{(e)}$  undergoes the deformation with oblique sharp edges (thin solid line in Fig. 2.12 (a)).

## 2.8. Summary and Conclusions

I have developed some micromagnetic methods [24, 148] which give a consistent description of magnetization processes and multidomain structures in systems with competing anisotropies such as diluted magnetic semiconductors.

Theoretically constructed phase diagrams in external field components in the limiting case of ideally soft magnetics allow to understand the creation of equilibrium domain structure [136], within anhysteretic magnetization reversal, and explain various parts of magnetization curves (Fig. 4.16). Thus, magnetic phase diagrams allow to put in good order and classify a vast amount of experimental data on reorientation effects, multidomain processes, and magnetization reversal in (Ga, Mn) As systems. These diagrams also give opportunity to predict changes of magnetic states of the system in zero magnetic field under influence of temperature [135, 137, 138] and in the case of arbitrary angle  $\alpha$  between competing anisotropy axes [132, 133].

It is also shown that the applied magnetic field causes drastic transformations of the domain wall profile and strongly influences its parameters. Domain walls can serve as nuclei of domains for a new phase. At certain values of the magnetic field a domain wall can be divided into domains of a new phase and two types of new domain walls. At certain critical endpoints of phase coexistence, domain walls can disappear by the rotation of the magnetization in adjacent domains towards each other.

For nanolayers with perpendicular anisotropy the geometrical parameters of stripe domains have been calculated as functions of a bias field.

For ellipsoidal magnetic particles I have shown the impact of surface anisotropy on the stabilization of multiple states and switching between them. I have calculated the shape factors of surface-induced anisotropy which can be considered as counterparts of demagnetizing coefficients. Our results are in accordance with the existing experimental data on switching processes in elongated magnetic particles [122, 124, 185].



# 3. Surface-induced anisotropy and vortex states in ferromagnetic nanowires and nanotubes

In the previous chapter I considered stabilizing effect of surface-induced anisotropy on multiple states in magnetic nanolayers and nanoparticles. Corresponding phase diagrams of states clearly demonstrate the sequence of transitions from one homogeneous state to another one with applied magnetic field and the dependence on competing anisotropies. In the present chapter I show that in nanowires and nanotubes with large aspect ratio of height to radius large induced magnetic anisotropy from lateral surfaces may stabilize non-collinear magnetization states. In section 3.2 a phenomenological model of surface-induced anisotropy is introduced that describes these effects within a micromagnetic calculation. The phenomenology allows to model a gradual penetration of surface-induced interactions into the volume of magnetic nanostructures. As a limiting case, the ansatz includes the Néel approach for a surface anisotropy that is essentially confined to the near surface region.

In section 3.3 I show that in cylindrical nanowires and nanotubes remanent states with magnetization vector rotating either along or perpendicular to radial directions are possible. Micromagnetic equations for these "Néel" or "Bloch" vortices are derived and solved. The main features of the vortex states are given, including a detailed analysis of magnetization profiles and simplified analytical solutions. Phase diagrams for the occurrence of the different vortex phases in nanowires are presented in dependence on the surface anisotropy constants, the radius, and the saturation magnetization of the material. The transitions between the vortices and the homogeneous magnetization state in nanowires take place via continuous rotation, whereas the transition between the different vortices is first order.

## 3.1. Introduction

There is a rising interest in the production and investigation of magnetic nanowires and nanotubes with a large aspect ratio of height/radius  $h/R$ . The shape of such elongated nanomagnetic structures may yield a rather effective magnetic anisotropy, which is required for applications. Regular arrays of nanowires may be used for future high-density magnetic recording [186, 187]. Bulk production of such magnetic wires may also allow one to assemble them as base units into permanent magnetic materials [188]. Single wires or tubes are investigated for applications in magnetoresistive spintronic devices [189], for actuation and manipulation in bi-

ological systems [190], or as field-sensitive probes, e.g. in scanning magnetic force microscopes (MFMs) [191]. To control and optimize the properties of such devices a detailed understanding and theoretical modelling of ferromagnetic wire-like or tube-like structures with width in the nanometer range is required.

A great number of magnetic nanowires and -tubes are currently produced by different methods and from different materials. Depending on production method, such as deposition along edges on surfaces [192], micropatterning [193], or deposition into different template films with a self-organized or etched arrangement of pores, in various polymer materials, microbiological substrates, mica, or alumina films [186, 194–197] the nanowires are placed in different matrices or environments. Also methods to produce magnetic nanotubes using various templates have recently been developed [186, 195, 198–200]. On the other hand, growth of ferromagnetic 3d metal wires has been achieved in single- or multiwall carbon nanotubes (CNTs) [201, 202]. Also magnetic oxides can be grown as nanowires and nanotubes or tubes [203–208].

As it is the shape of these ultrafine nanomagnetic structures that may determine their overall magnetic anisotropic behavior, their intrinsic and surface-induced magnetic anisotropy may be considered as a secondary effect. However, as it is known from magnetic films, a multitude of surface-related effects in nanoscale magnetic objects alters the intrinsic magnetic properties [5]. It also leads to an inhomogeneous spatial variation of magnetic parameters near the surfaces or throughout the whole nanoscale specimen. Experimental observations on the magnetic behavior of nanowire systems suggest in fact that additional magnetic anisotropy contributions can be sizeable and important. Intrinsic strong anisotropy in nanowires of hexagonal (hcp) Co causes effective easy magnetization directions perpendicular to the wire-axes [196]. However, similar magnetic properties have been observed also for finely polycrystalline Ni nanowires, where such strong anisotropy must be related to surface or interface effects [209, 210]. Noncollinear remanent states have been reported in Fe nanowires, which lead to high saturation fields in fields applied perpendicularly to the nanowire [211]. Anisotropic magnetoresistance measurements performed on nanowires embedded in the polymer membrane have been used as a probe of the magnetization orientation with respect to the current [186, 212, 213]. In Ni nanowires vortex-like non-collinear states are probably the reason of slight deviations of magnetoresistance from constant value in magnetic field along the nanowire axis [213]. The analysis of substructures in the ferromagnetic-resonance (FMR) lines of Ni nanowire indicate the presence of rather strong surface-anisotropies [214–216]. Reduced coordination number at the surfaces causes strong magnetic surface anisotropy as known for planar surfaces and ultrathin films [102, 217]. For nanotubes with thin walls, these effects may become very prominent and can be amplified by the curved surface structure. Ab initio calculations for thin wires show that both structural properties and electronic states are strongly changed in these systems because of the extended surface defects (see, e.g., recent calculations for 3d metal wires in CNT's in Ref. [218] and references there). Magnetoelastic effects due to the mechanic coupling with a surrounding matrix may alter the intrinsic magnetic anisotropy as observed for thicker wires, e.g., from temperature dependence of magnetic properties in Ni-wire



arrays [219–221]. However, due to surface effects, the inhomogeneous mechanical strains in these nanoobjects may also cause an inhomogeneity of the induced magnetoelastic anisotropy. In systems made from alloys and compounds, also surface segregation and termination effects may cause spatially inhomogeneous magnetic properties in a nanoobject.

In this chapter, the phenomenological theory for a micromagnetic treatment of distributed surface-induced anisotropies [11, 20] is extended and applied for nanowires and nanotubes with cylindrical symmetry. This additional energy contribution is due to induced orbital moments at the surface/interface [19] and may have significant influence on magnetic properties of magnetic nanostructures. In magnetic nanolayers according to depth-resolving experimental techniques the surface-induced interactions spread into the depth of the magnetic nanosystem [19, 20, 222] and favour magnetization orientations perpendicular to the surface. The same orientational effects should be attributed to cylindrical nanowires. Thus, I assume that there is an additional induced magnetic anisotropy related to the surface. This anisotropy energy may be spatially distributed throughout the nanostructure. The idealized shape of perfectly cylindrical wires or tubes allows to derive symmetry adapted models and analytical solutions of the profiles to describe inhomogeneous distribution of the surface anisotropy. Depending on the phenomenological parameter the surface anisotropy (SA) can be considered as either a mere surface effect (Néel approach [102, 223]) or a volume contribution. The induced anisotropy can stabilize vortex-like states by stabilizing a twisted magnetization structure in radial direction throughout the whole body of the nanowires. These are intrinsically non-collinear states in remanence. These vortices are not related to the usual surface vortex states in circular magnetic nanodots or nanocolumns [224], which are due to demagnetizing effects. Also, these states in remanence are not related to reversal modes, which appear as instabilities starting from a fully collinear saturated state in an infinite perfect wire without surface-induced anisotropy due to a reversing external field. I give the detailed analysis of magnetization profiles and present simplified analytical solutions to describe the main features of the vortex states. I construct the basic phase diagrams of remanent magnetic states in nanowires/nanotubes in dependence on surface anisotropy constants, which include homogeneous state and two vortex states of different type. For nanotubes I consider also the limiting cases of vortex states, namely, a *tangentially rotating* state with magnetization vector along concentric circles of the cross-section and a *radially rotating* state with magnetization along radial directions. In nanotubes, I show that the magnetic states combine the features of vortex states in nanocylinders [225, 226] and twisted phases in magnetic nanolayers [11].

## 3.2. Micromagnetic equations

Within standard micromagnetics [24] (chapter 1) the equilibrium (generally spatially inhomogeneous) distribution of the magnetization  $\mathbf{M}(\mathbf{r})$  in an infinite nanocylin-

der/nanotube is derived by variation of the energy functional per unit length  $W_m$ :

$$W_m = \int_V \left[ A \sum_i \left( \frac{\partial \mathbf{m}}{\partial x_i} \right)^2 - \mathbf{H} \cdot \mathbf{M} - \frac{1}{2} \mathbf{M} \cdot \mathbf{H}_m + w_a(\mathbf{m}) + \Omega_a(\mathbf{m}) \right] d\mathbf{r} \quad (3.1)$$

including exchange interactions (Eq. (1.4)), Zeeman energy (Eq. (1.33)), and energy of stray fields (Eq. (1.34)).

The homogeneous function  $w_a(\mathbf{m})$  is the density of the intrinsic magnetocrystalline anisotropy (section 1.2.2 *A, B*), and  $\Omega_a(\mathbf{m})$  is the surface anisotropy energy density (section 1.2.2 *C*).

As I consider infinite nanocylinders, thus, only lateral surfaces influence the magnetization state preserving cylindrical symmetry of the magnetization distributions. Then for the following calculations it is convenient to write the magnetization vector  $\mathbf{m}(\mathbf{r})$  in terms of spherical coordinates (1.58), and to use cylindrical coordinates (1.59) for the spatial variable  $\mathbf{r}$  as it was described in section 1.4.1 *A*. Moreover, the solutions of (3.1) are assumed to be homogeneous in the  $z$  direction and are expressed as [225, 226]

$$\theta = \theta(r), \psi = \varphi + \xi(r). \quad (3.2)$$

For magnetic nanotubes with internal radius  $R_1$  and external radius  $R_2$  I introduce the ratio

$$\eta = \frac{R_1}{R_2} \quad (3.3)$$

in order to treat filled cylindrical nanowires and hollow nanotubes by the same formalism. In the limit  $\eta \rightarrow 0$  one has magnetic nanowires, whereas for  $\eta \rightarrow 1$  a tubular thin film of vanishing thickness. Thus, by tuning the parameter  $\eta$ , one can achieve different modulated states of the magnetization appropriate either to limiting cases (cylindrical wires and curved films) or intermediate states between them.

The non-dimensional energy per unit length (3.1) for magnetic nanotubes after integration with respect to  $\varphi$  can be written as

$$\begin{aligned} \frac{W_m}{2\pi A} = & \int_{\eta}^1 [\theta_{\rho}^2 + \sin^2 \theta (\xi_{\rho}^2 + \rho^{-2}) - h \cos \theta + \\ & + (\beta_d - \sigma_2(\rho)) \sin^2 \theta \cdot \cos^2 \xi + \sigma_1(\rho) \cos^2 \theta] \rho d\rho. \end{aligned} \quad (3.4)$$

(Here  $\theta_{\rho} = d\theta/d\rho$ ,  $\xi_{\rho} = d\xi/d\rho$ ). To reduce the number of control parameters, I rescale the spatial variable

$$\rho = \frac{r}{R_2} \quad (3.5)$$

and use the following quantities for the demagnetization constant and applied magnetic field [24]

$$\beta_d = \frac{2\pi M^2 \cdot R_2^2}{A}, \quad h = \frac{H \cdot M R_2^2}{2A}. \quad (3.6)$$

In (5.1) contributions of intrinsic magnetocrystalline anisotropy  $w_a$  are not included.

The surface anisotropy has been decomposed into two independent contributions  $\sigma_{1(2)}(\rho)$  [225]:

$$\Omega_a(\mathbf{m}) = \sigma_1(\mathbf{r})(\mathbf{m} \cdot \hat{\mathbf{n}}_z)^2 - \sigma_2(\mathbf{r})(\mathbf{m} \cdot \hat{\mathbf{n}}_\rho)^2 = \sigma_1(\rho) \cos^2 \theta - \sigma_2(\rho) \sin^2 \theta \cos^2 \xi. \quad (3.7)$$

The first term  $\sigma_1(\rho)$  represents a uniaxial anisotropy along the cylinder axis and favors "easy plane" magnetization states in the cylinder cross-sections. The second term  $\sigma_2(\rho)$  favors states with magnetization directed outward or inward of the lateral surfaces and tends to suppress the demagnetizing effects.

In the framework of the phenomenological theory of Refs. [11, 20], the equilibrium distributions of surface-induced anisotropies are derived by the minimization of a general interaction functional [226] (see also section 1.2.2 *C* for details):

$$W = \int \left[ \left( \frac{d\sigma_{1(2)}(\rho)}{d\rho} \right)^2 + \sigma_{1(2)}^2(\rho) G(\rho) + \frac{\sigma_{1(2)}^2(\rho)}{\lambda_{1(2)}^2} \right] 2\pi\rho d\rho, \quad (3.8)$$

where

$$G(\rho) = 0 \quad (3.9)$$

for the uniaxial anisotropy  $\sigma_1(\rho)$  and

$$G(\rho) = \frac{1}{\rho^2} \quad (3.10)$$

for the radial contribution  $\sigma_2(\rho)$ . The parameters  $\lambda_{1(2)}$  are the characteristic lengths for this theory which characterize the resistance of the system against the surface-induced interactions. In principle values of  $\lambda_{1(2)}$  can be derived from *ab initio* calculations of induced spin-orbit coupling [218]. Experimentally these parameters can be obtained only indirectly, for example, from the radius dependences of the function  $\Phi(R) = K_{eff}R$  where  $K_{eff}$  is the effective anisotropy (Figs. 1.2, 1.3).

The minimization of (3.8) yields the solutions for penetration of surface anisotropy coefficients  $\sigma_1(\rho)$  and  $\sigma_2(\rho)$  into the depth of magnetic nanotube:

$$\sigma_{1(2)}(\rho) = A_{1(2)} J_{0(1)} \left( \frac{i\rho}{\lambda_{1(2)}} \right) + B_{1(2)} Y_{0(1)} \left( \frac{i\rho}{\lambda_{1(2)}} \right), \quad (3.11)$$

where

$$A_{1(2)} = \frac{a_{1(2)}}{c_{1(2)}}, B_{1(2)} = \frac{b_{1(2)}}{c_{1(2)}}, \quad (3.12)$$

and

$$\begin{aligned}
 a_{1(2)} &= \sigma_{1(2)}(\eta) Y_{0(1)} \left( \frac{i}{\lambda_{1(2)}} \right) - \sigma_{1(2)}(1) Y_{0(1)} \left( \frac{i\eta}{\lambda_{1(2)}} \right), \\
 b_{1(2)} &= \sigma_{1(2)}(1) J_{0(1)} \left( \frac{i\eta}{\lambda_{1(2)}} \right) - \sigma_{1(2)}(\eta) J_{0(1)} \left( \frac{i}{\lambda_{1(2)}} \right), \\
 c_{1(2)} &= Y_{0(1)} \left( \frac{i}{\lambda_{1(2)}} \right) J_{0(1)} \left( \frac{i\eta}{\lambda_{1(2)}} \right) - Y_{0(1)} \left( \frac{i\eta}{\lambda_{1(2)}} \right) J_{0(1)} \left( \frac{i}{\lambda_{1(2)}} \right), \quad (3.13)
 \end{aligned}$$

$J_{0(1)}$ ,  $Y_{0(1)}$  are the Bessel functions of first and second kind, respectively. Here  $\sigma_{1(2)}(\eta)$  and  $\sigma_{1(2)}(1)$  are coefficients of surface anisotropy on internal and external surfaces of nanotube.

For small characteristic lengths,  $\lambda_{1(2)}/(1 - \eta) \ll 1$ , the profiles (3.11) are essentially confined to the near surface region and decay exponentially within the volume of the wires/tubes (Fig. 3.1 (a)). In this case, the surface anisotropy can be consid-

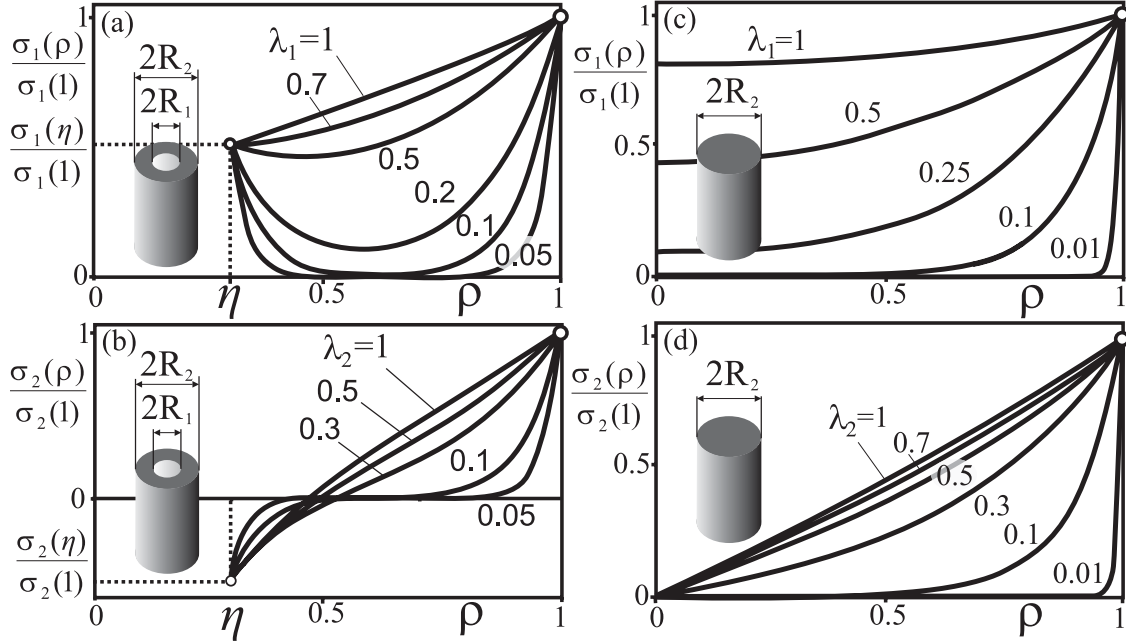


Figure 3.1.: Inhomogeneous distributions for the surface-induced anisotropies  $\sigma_{1(2)}(\rho)/\sigma_{1(2)}(1)$  within magnetic nanotubes (a), (b) and in nanowires (c), (d) for different characteristic lengths  $\lambda_{1(2)}$  according to the model Eq. (3.8) for infinitely long cylindrical objects. (a),(c) show the axial contribution of the surface anisotropy, whereas (b),(d) are the radial contribution. In (b) the distribution for a negative boundary coefficient  $\sigma_2(\eta)$  is shown.

ered as a mere surface effect. Phenomenologically, it is described as an additional surface energy contribution with constant anisotropy coefficient

$$\varkappa_{1(2)}(\eta) = \eta \lambda_{1(2)} \sigma_{1(2)}(\eta), \quad \varkappa_{1(2)}(1) = \lambda_{1(2)} \sigma_{1(2)}(1). \quad (3.14)$$

For larger characteristic lengths,  $\lambda_{1(2)}/(1 - \eta) \approx 1$ , the surface anisotropy profiles vary smoothly within the magnetic volume (Fig. 3.1 (a)).

For nanotubes the profiles of uniaxial and radial anisotropy are almost identical. The functions  $\sigma_{1(2)}(\rho)$  essentially depend on the ratios of the boundary anisotropy coefficients on the internal and external surfaces and on the parameter  $\eta$  (Fig. 3.1 (a)). Moreover, for opposite signs of boundary coefficients more complex situations may occur, which provide a large variability of possible magnetization states (Fig. 3.1 (b)). Experimentally the values of surface anisotropy constants on both surfaces  $\sigma_{1(2)}(\eta)$  and  $\sigma_{1(2)}(1)$  can be strongly increased by coverings with different nonmagnetic materials as it was done for magnetic layers [5].

For magnetic nanowires, as it was noticed before,  $\eta \rightarrow 0$ , thus distributions of surface-induced anisotropy can be obtained from (3.11):

$$\sigma_{1(2)}(\rho) = \sigma_{1(2)}(1) \frac{J_{0(1)}\left(\frac{i\rho}{\lambda_{1(2)}}\right)}{J_{0(1)}\left(\frac{i}{\lambda_{1(2)}}\right)}, \quad (3.15)$$

For  $\lambda_{1(2)} \ll 1$  I obtain merely surface anisotropy with coefficients

$$\varkappa_{1(2)}(1) = \lambda_{1(2)}\sigma_{1(2)}(1). \quad (3.16)$$

For  $\lambda_{1(2)} \approx 1$  the axial part of the surface anisotropy has a significant value in the cross-section center (Fig. 3.1 (c)) while the radial part is zero (Fig. 3.1 (d)) and almost linearly changes towards  $\sigma_2(1)$  at the boundary.

To obtain the equilibrium magnetization states in nanowires/nanotubes one has to minimize functional (5.1). In the case of distributed surface anisotropy coefficients  $\sigma_{1(2)}(\rho)$  are included in Euler equations:

$$\begin{aligned} \theta_{\rho\rho} + \frac{\theta_\rho}{\rho} - \frac{\sin\theta \cos\theta}{\rho^2} - \xi_\rho^2 \sin\theta \cos\theta + \sigma_1(\rho) \sin\theta \cos\theta - \frac{h}{2} \sin\theta \\ - (\beta_d - \sigma_2(\rho)) \sin\theta \cos\theta \cos^2\xi = 0, \\ \xi_{\rho\rho} \sin^2\theta + \frac{\xi_\rho \sin\theta}{\rho} + 2\xi_\rho\theta_\rho \sin\theta \cos\theta + (\beta_d - \sigma_2(\rho)) \sin^2\theta \sin\xi \cos\xi = 0. \end{aligned} \quad (3.17)$$

On surfaces one has free boundary conditions. For magnetic nanotubes

$$\theta_\rho|_{1(\eta)} = \xi_\rho|_{1(\eta)} = 0 \quad (3.18)$$

and for magnetic nanowires

$$\theta(0) = 0, \theta_\rho|_1 = \xi_\rho|_1 = 0. \quad (3.19)$$

In the Néel approach surface anisotropy coefficients  $\varkappa_{1(2)}$  are included in boundary conditions, derived from variation of (5.1) with the terms  $\Omega_a$  and an integration by

parts [225]. For nanotubes one has:

$$\theta_\rho|_{1(\eta)} - [\varkappa_1 + \varkappa_2 \cos^2 \xi] \sin \theta \cos \theta|_{1(\eta)} = 0, \quad \xi_\rho|_{1(\eta)} + \varkappa_2 \sin \xi \cos \xi|_{1(\eta)} = 0. \quad (3.20)$$

And for nanowires

$$\theta(0) = 0, \quad \theta_\rho|_1 - [\varkappa_1 + \varkappa_2 \cos^2 \xi] \sin \theta \cos \theta|_1 = 0, \quad \xi_\rho|_1 + \varkappa_2 \sin \xi \cos \xi|_1 = 0. \quad (3.21)$$

### 3.3. Solutions for vortex profiles

In the following, I calculate remanent states and zero-field phase diagrams for surface-induced anisotropy with positive boundary coefficients in the limit of the Néel approach. The approach is sufficient to describe the possible magnetization distributions and the structure of the phase diagrams for the different states driven by surface-induced anisotropies.

For *nanowires*, the simplest solutions with cylindrical symmetry among the many possible forms of vortex-like states are described by  $\xi = \text{const}$ . There are only two possible solutions of this kind [20, 225, 226]. In the first solution  $\xi = \pm\pi/2$  and the magnetization vector rotates in the plane perpendicular to the radial directions similar to the rotation in a Bloch domain wall. I call this stray-field-free structure a “Bloch vortex” (Fig. 3.2 (a)). In the second solution  $\xi = 0$  and the vector  $\mathbf{m}$  rotates along the radial directions as in a Néel domain wall. This “Néel vortex” possesses internal magnetic “charges” (Fig. 3.2 (b)).

The Euler equation for the tilted angle  $\theta$  in these two vortex states is given by

$$\theta_{\rho\rho} + \frac{\theta_\rho}{\rho} - \frac{\sin \theta \cos \theta}{\rho^2} - \frac{w_\theta}{2} = 0, \quad (3.22)$$

where

$$w = -h \cos \theta \quad (3.23)$$

for the Bloch vortex and

$$w = -h \cos \theta + \beta_d \sin^2 \theta \quad (3.24)$$

for the Néel vortex. Multiplying the Eq. (3.22) by  $2\rho^2\theta_\rho$  and integrating with respect to  $\rho$  from zero to unity one obtains an integral equation

$$(\rho\theta_\rho)^2 - \sin^2 \theta - \rho^2 w|_1 + 2 \int_0^1 w d\rho = 0. \quad (3.25)$$

For the Bloch vortex in zero field  $h = 0$  and with zero anisotropy  $\beta = 0$ , the function  $w = 0$ . The Eq. (3.25) yields analytical solutions (solid lines in Fig. 3.3 (a)) given by

$$\theta(\rho) = 2 \arctan(\kappa \rho), \quad \kappa = \sqrt{\frac{\varkappa_1(1) - 1}{\varkappa_1(1) + 1}}. \quad (3.26)$$

Then, the difference between the energy  $W_0$  for the homogeneous state with  $\theta \equiv 0$  and the energy  $W_v$  for the vortex state of the solutions Eq. (3.26)

$$\Delta W = W_0 - W_v = (\varkappa_1(1) - 1)^2 / \varkappa_1(1) \quad (3.27)$$

is positive in the complete existence range of these vortices,  $\varkappa_1(1) > 1$ . This range is shown by right inclined hatching in the phase diagram (Fig. 3.4). Therefore, the Bloch vortex is stable as soon as it arises by a continuous rotation of the magnetization vector from the homogeneous state.

The  $m_z$  component of the vortex

$$m_z(\rho) = \cos \theta = \frac{1 - (\kappa\rho)^2}{1 + (\kappa\rho)^2} \quad (3.28)$$

changes from unity on the nanowire axis toward its lowest value on the lateral surface (solid lines of Fig. 3.3 (b)). The average magnetization along the cylinder axis is derived by integrating  $m_z$  from Eq. (3.28) with respect to  $\rho$ ,

$$\langle m_z \rangle = \frac{2}{\pi} \int_0^{2\pi} d\varphi \int_0^1 m_z(\rho) \rho d\rho = 2 \left( \frac{\varkappa_1(1) + 1}{\varkappa_1(1) - 1} \right) \ln \left( \frac{\varkappa_1(1)}{1 + \varkappa_1(1)} \right) - 1. \quad (3.29)$$

The dependence of the remanent magnetization on wire radius could be used for an experimental determination of the parameter  $\varkappa_1(1)$ . In particular, the critical nanowire radius for the transformation into the homogeneous magnetization states may be observable (Fig. 3.5).

For the Néel vortex the profiles  $\theta(\rho)$ , magnetization distribution, average magnetization in  $z$ -direction and the magnetic energy have been determined by numerical integration of Eq. (3.25) with  $w = \beta_d \sin^2 \theta$  at various parameters  $\varkappa_1(1)$ ,  $\varkappa_2(1)$  and some value of  $\beta_d = 2$ . It should be emphasized that in the Néel vortex the surface anisotropy competes not only with the exchange as in the Bloch vortex but also with the demagnetization. This is the reason that the magnetization vector rotates less than in Bloch vortices for the same strength of the surface anisotropy (dotted lines in Fig. 3.3 (a), (b)). Also, the average magnetization  $\langle m_z \rangle$  for Néel vortices retains larger values in the whole range of anisotropy parameters (dotted lines in Fig. 3.5).

The area of existence for Néel vortices is shown in the phase-diagram (Fig. 3.4) by left-inclined hatching. One can see from this phase diagram that the Néel vortex arises from the homogeneous state (vertical hatching in Fig. 3.4) by a gradual rotation of the vector  $\mathbf{m}$ , i.e. this phase transition under influence of increasing surface anisotropy is continuous. On the other hand, the transformation between the Néel vortex and the Bloch vortex state is obtained by a first-order process (thick solid line in Fig. 3.4). Correspondingly, there are overlapping regions in the phase diagram, where these two vortex types may co-exist as metastable and stable phase, respectively. The existence ranges of the metastability regions are bounded by lability lines (given by thinner lines in Fig. 3.4). As a consequence, there can be various types

of multidomain states: (i) Pieces of Néel- and Bloch vortices can co-exist along the first-order line of the phase diagram (Fig. 3.4). (ii) Vortices of either type exist with net magnetization up and down, and these states always coexist in zero field. (iii) Bloch vortices can have different sense of rotation/chirality and with specific domain walls between them  $\theta = \theta(\rho), \xi = \xi(\rho)$ . Experimentally such domain walls can be observed directly using Lorentz microscopy. In Ref. [229] domain walls of different chirality were observed in a ferromagnetic  $\text{La}_{0.6}\text{Sr}_{0.4}\text{MnO}_3$  nanowire separating domains with the homogeneous magnetization along the nanowire axis.

The basic solutions of the vortex-like states, as calculated sofar, may be distorted by additional magnetic effects. In the case of distributed anisotropy, the characteristic length  $\lambda_{1(2)}$  provides an additional control parameter which strongly influences the magnetization profiles of vortices (Fig. 3.6). A uniaxial anisotropy as well as magnetic field  $h > 0$  along the nanowire axis forces the alignment of the spins along the cylinder axis. This will generally favour more homogeneous states in order to reduce the region of unaligned spins. A magnetocrystalline uniaxial anisotropy with inclined easy-axes or similarly cubic anisotropy breaks the cylindrical symmetry. These effects tend to destroy vortex states. The magnetic state splits into domains along the wire with magnetization oriented along easy axes of the corresponding anisotropies. Such effects have been observed, e.g., in polycrystalline Co nanowires where the hcp  $c$  axes were strongly deviating from the nanowire axis [196]).

For magnetic nanotubes, the considered vortex states are possible as well, but only for appropriate values of  $\kappa_{1(2)}(\eta)$  and  $\kappa_{1(2)}(1)$  determined within the Néel approach in Eq. (3.17). The limiting cases of the Néel vortex and Bloch vortex are a radially rotating state,  $\theta = \pi/2, \xi = 0$  (Fig. 3.2 (e)), and a tangentially rotating state,  $\theta = \pi/2, \xi = \pi/2$  (Fig. 3.2 (c)), correspondingly. However, the transitions from the vortex solutions into these planar states are first order. Particular twisted phases with  $\theta = \pi/2, \xi = \xi(\rho)$  [11, 223] are realized by first order phase transitions from the radially rotating state or by a continuous transition from the tangentially rotating state. As in the case of nanowires, the different coexisting magnetization states may form domain structures. In particular, the Néel vortex and the radially rotating state lead to the appearance of magnetostatic charges and concomitant demagnetization effects.

## 3.4. Conclusions

It was shown that in magnetic nanowires and nanotubes, surface-induced uniaxial anisotropy from lateral surfaces may have a dominating influence on magnetic properties of these nanostructures. Overcoming the stray-field energy, this anisotropy may cause spin-reorientation transitions from the homogeneous longitudinal magnetization state into two types of vortices.

Within a micromagnetic description, a general model for infinitely long cylindrical ferromagnetic wires/tubes under the influence of surface anisotropy has been formulated and specialized to solutions with cylindrical symmetry. An analytic solution describing a continuous transition into stray-field-free vortex-states due to



the axial part of the surface-anisotropy has been presented. General properties of vortex-states stabilized by surface-anisotropy in cylindrical wires have been briefly discussed.

The phase diagram of states on the plane of surface-anisotropy constants shows a characteristic sequence of phases that is due to a balance between demagnetization and a tendency of the positive surface-anisotropy to turn the magnetization into the radial directions. When Néel vortices can be stabilized, very interesting domain states may occur. Nanotubes with strong surface anisotropies and very thin walls may be best candidates to produce such states.

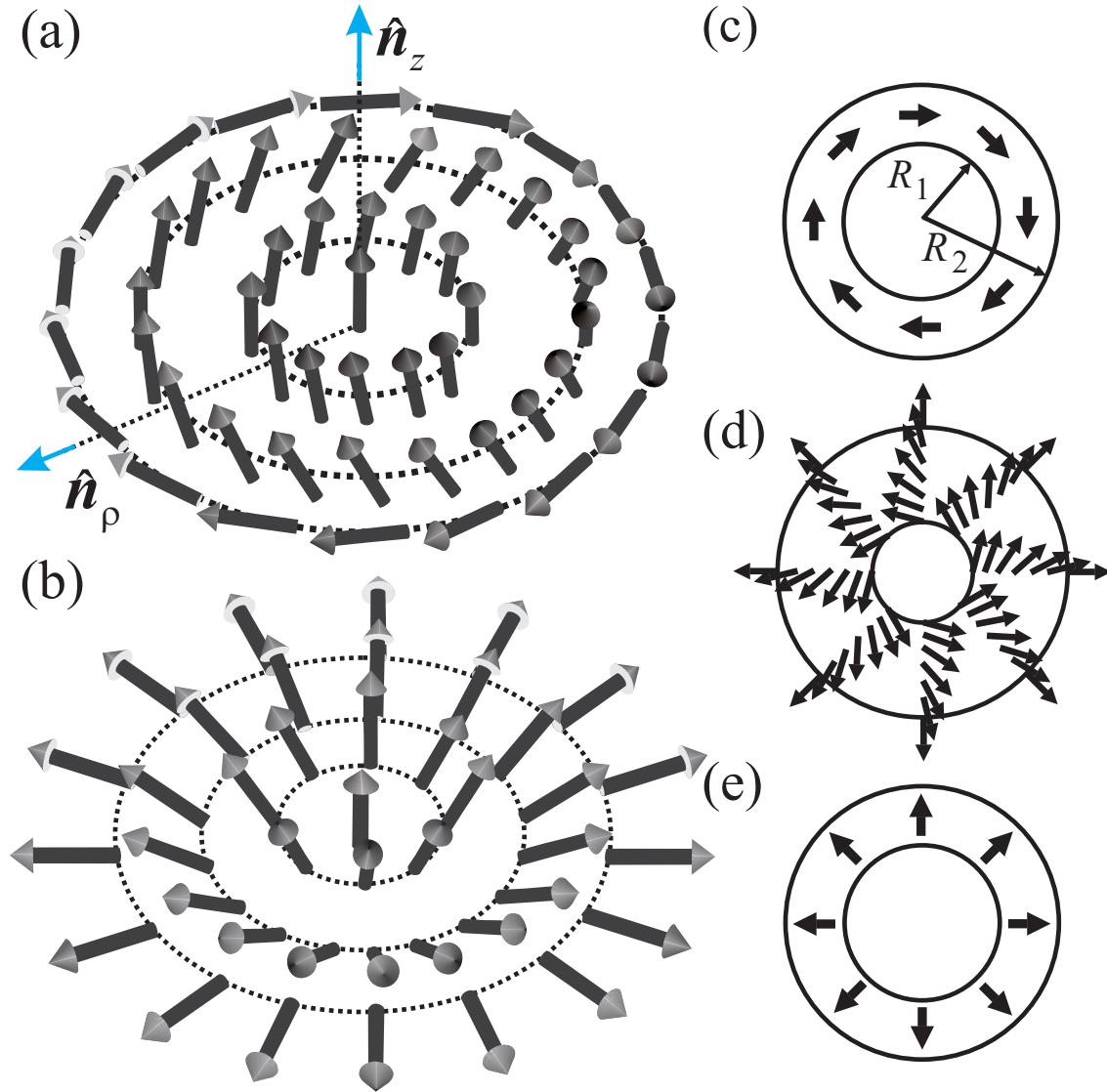


Figure 3.2.: Vortex magnetization states of an infinitely long cylinder (shown in cross-section): (a) "Bloch vortex"; (b) "Néel vortex". Magnetization states in hollow tubes: (c) tangentially rotating state; (d) twisted mode; (e) radially rotating state in the limit of dominating surface anisotropy.

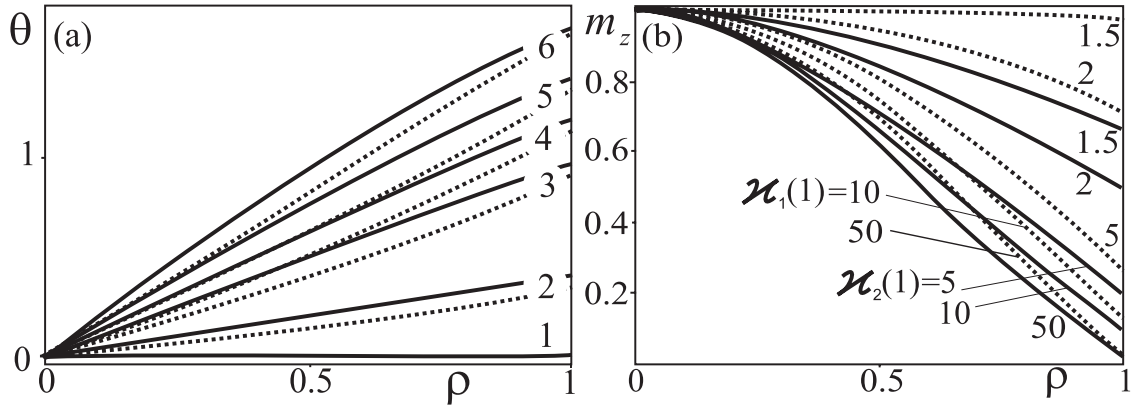


Figure 3.3.: Profiles  $\theta(\rho)$  (a) and  $m_z(\rho)$  (b) of Bloch (solid lines) and Néel vortices (dotted lines) at various parameters of surface anisotropy  $\kappa_1(1), \kappa_2(1)$ . In (a) pairs of curves for Bloch and Néel vortices correspond to the following sequence: 1- ( $\kappa_1(1) = 1, \kappa_2(1) = 0.46$ ); 2- ( $\kappa_1(1) = 1.05, \kappa_2(1) = 0.47$ ); 3- ( $\kappa_1(1) = 1.5, \kappa_2(1) = 0.53$ ); 4- ( $\kappa_1(1) = 2, \kappa_2(1) = 0.57$ ); 5- ( $\kappa_1(1) = 3, \kappa_2(1) = 0.61$ ); 6- ( $\kappa_1(1) = 10, \kappa_2(1) = 0.7$ ). These states correspond to points on the line of the first-order phase transition between the two vortices, see phase diagram in Fig. 3.4.

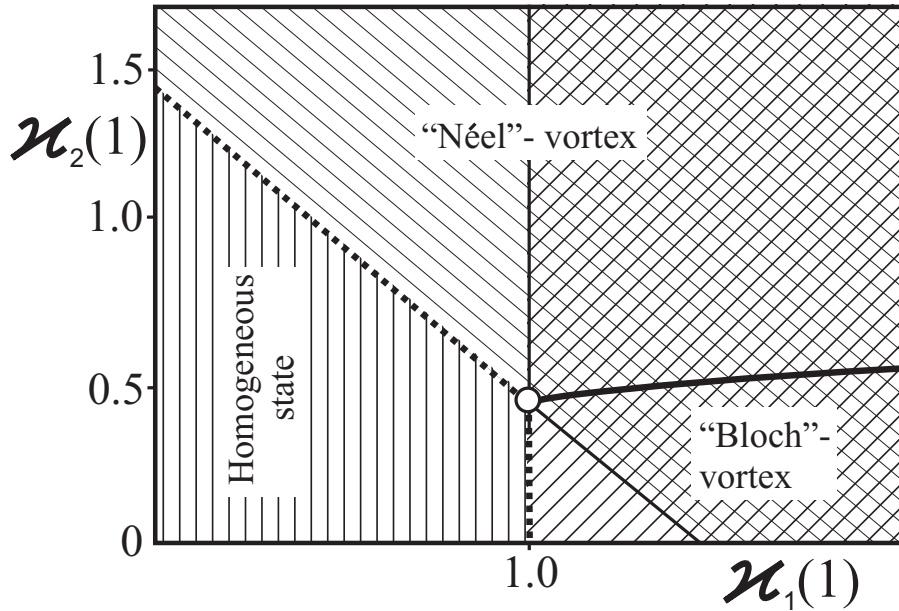


Figure 3.4.: Phase diagram of remanent magnetic states in infinitely long magnetic nanowires in dependence on surface-induced anisotropy and for zero magnetocrystalline anisotropy. Solid and dotted lines are lines of first order and continuous phase transitions, respectively. Thin full lines are the stability lines of corresponding phases.

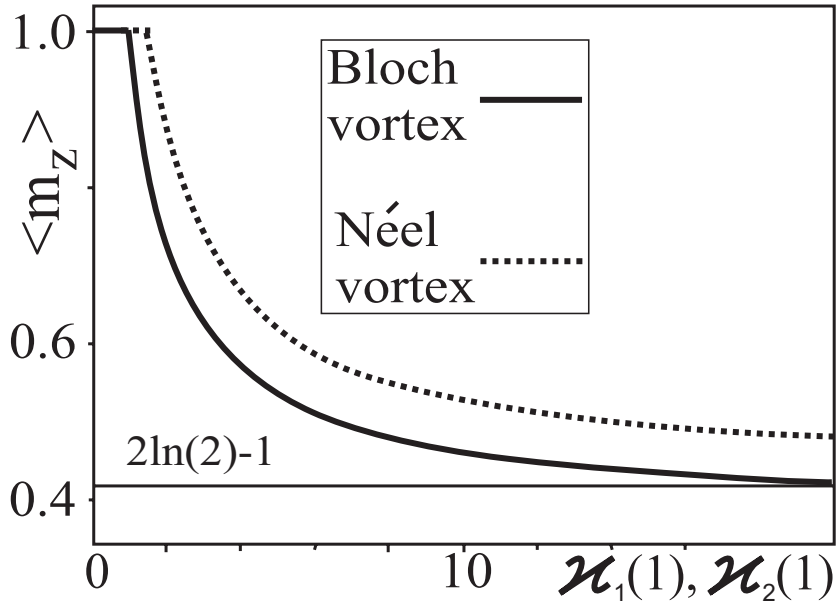


Figure 3.5.: Average magnetization of Bloch (solid line) and Néel vortices (dotted line) versus the surface-induced anisotropies  $\kappa_1(1), \kappa_2(1)$ . For the Néel vortex  $\kappa_1(1) = 0$ .

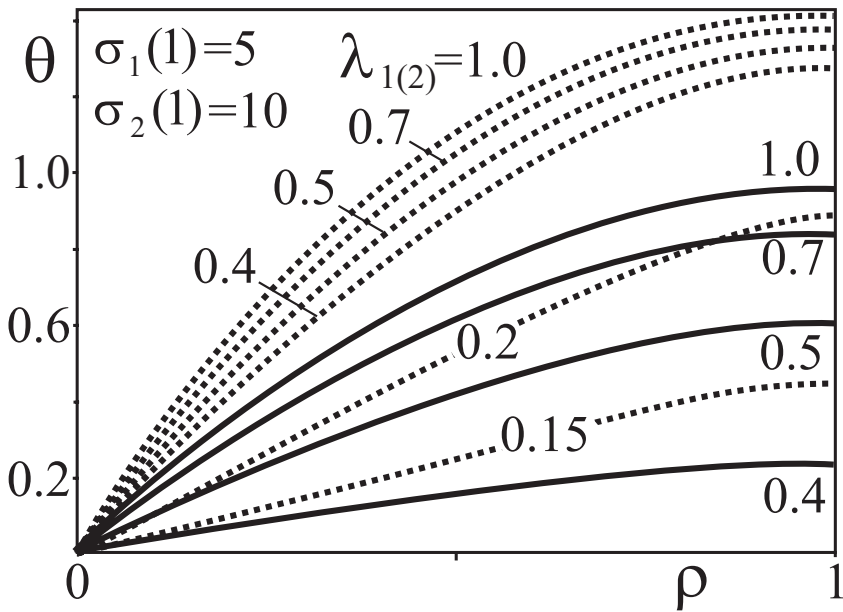


Figure 3.6.: Influence of the parameter  $\lambda_{1(2)}$  on profiles  $\theta(\rho)$  in the case of distributed anisotropy for  $\sigma_1(1) = 5, \sigma_2(1) = 10$ .

## **Part II.**

### **Phenomenological theory of skyrmion and helical states in magnets with intrinsic and induced chirality**

---

## 4. Chiral skyrmion states in non-centrosymmetric magnets

### 4.1. Introduction

Chiral skyrmion states exist in non-centrosymmetric magnetic crystals [21,22,31,69] as a consequence of the asymmetric exchange Dzyaloshinskii-Moriya interactions that destroy the homogeneous magnetic state and generally lead to twisted incommensurate magnetic spin-structures [41]).

Recently, microscopic observation of skyrmion lattices and free skyrmions in magnetic layers of the chiral helimagnets with the noncentrosymmetric cubic B20 crystal structure confirm the existence of these chiral topological spin-textures in otherwise rather simple magnetic metals [28, 29]. The stabilization of these states and their transformation properties impressively illustrate the theoretically predicted solitonic nature of these chiral two-dimensionally localized spin-states [21,22,31,69]. In particular, the experiments clearly show the ability of skyrmions to form densely packed two-dimensional arrangements and how the field-driven transformation process can decompose these lattices by setting free the constituent skyrmions as excitations. The stabilization of such skyrmion lattices against one-dimensionally modulated helices in these cubic helimagnets at low temperatures requires a subtle effect possibly combining uniaxial magnetic anisotropy (or cubic and exchange anisotropy) with the magnetic field [XI,XII]. However, both in magnetic films and in magnetic crystals, symmetry imposed restrictions on the chiral Dzyaloshinskii-Moriya interactions may allow to create skyrmion lattices with high perfection in applied fields because the competing conical helix state does not exist [21,69].

This chapter is mainly devoted to numerically rigorous solutions of hexagonal skyrmion lattices for cubic helimagnets. It justifies and extends previous approximate solutions that used a circular cell approximation (CCA) for the calculation of the free energy of skyrmion lattices [21,69][XI]. The theoretical results of the present chapter provide a comprehensive description of skyrmion lattice evolution in an applied magnetic field and/or in the presence of uniaxial, cubic, and exchange anisotropy. The low-temperature phenomenological theory with fixed modulus of magnetization,  $|M|=\text{const}$ , is applied to the magnetic states in chiral magnets.

## 4.2. Phenomenological theory of modulated states in chiral helimagnets

### 4.2.1. The general micromagnetic energy functional

Within the phenomenological theory introduced by Dzyaloshinskii [41] the magnetic energy density of a non-centrosymmetric ferromagnet with spatially dependent magnetization  $\mathbf{M}$  can be written as

$$W(\mathbf{M}) = \underbrace{A \sum_{i,j} \left( \frac{\partial m_j}{\partial x_i} \right)^2 + D w_D(\mathbf{M}) - \mathbf{M} \cdot \mathbf{H} + W_a(\mathbf{m})}_{W_0(\mathbf{M})} \quad (4.1)$$

where  $A > 0$  and  $D$  are coefficients of exchange and Dzyaloshinskii-Moriya interactions;  $\mathbf{H}$  is an applied magnetic field;  $x_i$  are the Cartesian components of the spatial variable.  $w_D$  is composed of Lifshitz invariants (section 1.2.1 *B*). Almost all calculations of the present chapter have been done for cubic helimagnets with  $w_D = \mathbf{m} \cdot \text{rot} \mathbf{m}$ .

$W_a(\mathbf{m})$  includes short-range anisotropic energies:

$$W_a(\mathbf{m}) = - \sum_{i=1}^3 \left[ B_{EA} \left( \frac{\partial m_i}{\partial x_i} \right)^2 + K_c (\mathbf{m} \cdot \mathbf{n}_i)^4 \right] - K_u (\mathbf{m} \cdot \mathbf{a})^2 \quad (4.2)$$

where  $B_{EA}$ ,  $K_c$ , and  $K_u$  are coefficients of exchange, cubic, and uniaxial magnetic anisotropies, correspondingly;  $\mathbf{a}$  and  $\mathbf{n}_i$  are unit vectors along easy uniaxial and cubic magnetization axes, respectively.

Functional  $W_0(\mathbf{M})$  includes only basic interactions essential to stabilize skyrmion and helical states. Solutions for chiral modulated phases and their most general features attributed to all chiral ferromagnets are determined by this functional. Generically, there are only small energy differences between various modulated states. On the other hand, weaker energy contributions (as magnetic anisotropies (4.2)) impose distortions on solutions of model (4.1) which reflect crystallographic symmetry and values of magnetic interactions in individual chiral magnets. It is essential to recognize that these weaker interactions determine the stability limits of the different modulated states. The fact that thermodynamical stability of individual phases and conditions of phase transformations between them are determined by magnetocrystalline anisotropy and other relativistic or weaker interactions means that (i) the basic theory only determines a set of different and unusual modulated phases, while (ii) the transitions between these modulated states, and their evolution in magnetization processes depends on symmetry and details of magnetic secondary effects in chiral magnets, in particular the strengths of relativistic magnetic interactions. Thus functional (4.1) is the *generic* model for a manifold of interaction functionals describing different groups of noncentrosymmetric magnetic crystals, because it allows to identify the basic modulated structures that may be found in them.



Dzyaloshinskii's phenomenology (4.1) is a main theoretical tool to analyze and interpret experimental results on chiral magnets. During last three decades of intensive investigations of chiral modulations in different classes of non-centrosymmetric magnetic systems a huge empirical material has been organized and systematized within the framework of this theory (see, for example, a review [44] and bibliography in papers [31, 45]). The Dzyaloshinskii interaction functional (4.1) plays in chiral magnetism a similar role as the Frank functional in liquid crystals [48] or Ginzburg-Landau functionals in physics of superconductivity [49, 50].

### 4.2.2. Reduced variables and characteristic lengths

For the forthcoming calculations I will use two ways of introducing non-dimensional variables.

In the first method, the length scales are reduced by the characteristic width of the Bloch domain wall (see Eq. (1.43)). This method is valuable in the situations where anisotropic magnetic materials are considered and the influence of "tunable" DM interactions on the solutions of micromagnetic equations is investigated. In particular in section 5.6, I consider the solutions for magnetic bubble domains stabilized by dipole-dipole interactions in the presence of induced DMI.

In the second method, the lengths are expressed in units of  $L_D$ , i.e. the length scales are related to the period of the spiral state in zero field (see section 1.3.2). Such a method is suitable for the calculations of the present chapter, as first I consider different modulated states as solutions of the isotropic energy functional  $W_0(\mathbf{M})$  and then "activate" additional small anisotropic contributions  $W_a(\mathbf{m})$ .

*A. Reduced variables with the length scales in units of the width of the Bloch domain wall*

Following Refs. [70] I introduce the non-dimensional variables based on the domain wall width

$$L_B = \sqrt{\frac{A}{K_u}}. \quad (4.3)$$

Then the energy functional (4.1) can be written in the reduced form as

$$w(\mathbf{m}) = \sum_{i,j} \left( \frac{\partial m_j}{\partial \tilde{x}_i} \right)^2 - \frac{4\kappa}{\pi} \mathbf{m} \cdot \text{rot} \mathbf{m} - 2\mathbf{m} \cdot \mathbf{h} - \sum_{i=1}^3 \left[ \frac{B_{EA}}{K_u} \left( \frac{\partial m_i}{\partial \tilde{x}_i} \right)^2 + \frac{K_c}{K_u} (\mathbf{m} \cdot \mathbf{n}_i)^4 \right] - (\mathbf{m} \cdot \mathbf{a})^2 \quad (4.4)$$

where

$$\mathbf{h} = \frac{\mathbf{H}}{H_a}, \quad \tilde{\mathbf{r}} = \frac{\mathbf{r}}{L_B}, \quad w(\mathbf{m}) = \frac{W(\mathbf{M})}{H_a M} \quad (4.5)$$

and

$$H_a = \frac{2K_u}{M} \quad (4.6)$$

is the anisotropy field.

The parameter

$$\varkappa = \frac{\pi D}{4\sqrt{A K_u}} \quad (4.7)$$

plays a similar role as the Ginzburg-Landau parameter in the theory of superconductivity. It describes the relative contribution of the Dzyaloshinsky energy term. In Refs. [22, 70] it was shown that modulated structures can be realized as thermodynamically stable states only if  $\varkappa$  exceeds the value of 1.

#### B. Reduced variables with the length scales in units of $L_D$

Following Refs. [21] I introduce the non-dimensional variables based on the period of the helical state in zero magnetic field. Then the energy functional (4.1) can be written in the reduced form as

$$w(\mathbf{m}) = \sum_{i,j} \left( \frac{\partial m_j}{\partial \tilde{x}_i} \right)^2 - \mathbf{m} \cdot \text{rot} \mathbf{m} - \mathbf{m} \cdot \mathbf{h} - \sum_{i=1}^3 \left[ b_{EA} \left( \frac{\partial m_i}{\partial \tilde{x}_i} \right)^2 + k_c (\mathbf{m} \cdot \mathbf{n}_i)^4 \right] - \beta_u (\mathbf{m} \cdot \mathbf{a})^2 \quad (4.8)$$

where

$$\mathbf{h} = \frac{\mathbf{H}}{H_D}, \quad \tilde{\mathbf{r}} = \frac{\mathbf{r}}{L_D}, \quad w(\mathbf{m}) = \frac{W(\mathbf{M})}{H_D M} \quad (4.9)$$

and

$$H_D = \frac{D^2}{AM}. \quad (4.10)$$

The reduced constants of exchange  $b_{EA}$ , cubic  $k_c$ , and uniaxial  $\beta_u$  anisotropies are defined as

$$b_{EA} = \frac{B_{EA}A}{D^2}, \quad k_c = \frac{K_c A}{D^2}, \quad \beta_u = \frac{K_u A}{D^2}. \quad (4.11)$$

### 4.3. One-dimensional chiral modulations

As it was shown in section 1.3.2, the Dzyaloshinskii-Moriya interactions (1.11) arising in non-centrosymmetric magnets play a crucial role in destabilizing the homogeneous ferromagnetic arrangement and twisting it into a helix (Fig. 4.1). At zero magnetic field such helices are single-harmonic modes forming the global minimum of the functional  $W_0(\mathbf{M})$  [41]:

$$\mathbf{M} = M_s [\mathbf{n}_1 \cos(\mathbf{k} \cdot \mathbf{r}) + \mathbf{n}_2 \sin(\mathbf{k} \cdot \mathbf{r})], \quad |\mathbf{k}| = \frac{1}{2L_D} \quad (4.12)$$

where  $\mathbf{n}_1, \mathbf{n}_2$  are the unit vectors in the plane of the magnetization rotation orthogonal to the wave vector  $\mathbf{k}$  ( $\mathbf{n}_1 \perp \mathbf{n}_2$ ;  $\mathbf{n}_1 \perp \mathbf{k}$ ;  $\mathbf{n}_2 \perp \mathbf{k}$ ).

The modulations (4.12) have a fixed rotation sense determined by the sign of Dzyaloshinskii-Moriya constant  $D$  and are continuously degenerate with respect to propagation directions in the space.

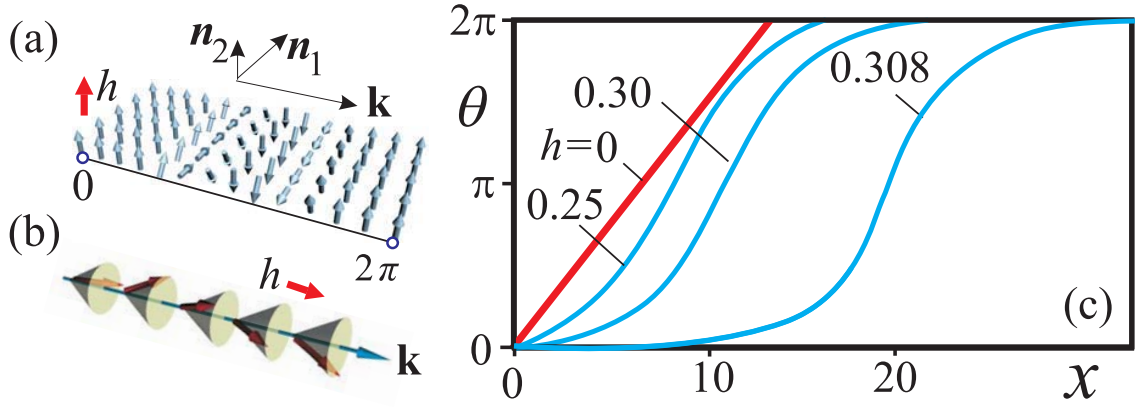


Figure 4.1.: One-dimensional chiral modulations in cubic helimagnets. In a helical "array" (a) the magnetization rotates in the plane spanned by the orthogonal unity vectors  $\mathbf{n}_1$  and  $\mathbf{n}_2$  and the rotation sense is determined by the sign of Dzyaloshinskii constant  $D$ . Under the influence of the magnetic field applied perpendicularly to the propagation direction the helix is transformed into a transversally distorted *helicoid* with non-linear profiles  $\theta(x)$  (c). Magnetic field applied along propagation direction stabilizes single-harmonic conical phase (b).

An applied magnetic field lifts the degeneracy of the helices (4.12) and stabilizes two types of one-dimensional modulations: cones and helicoids (Fig. 4.1 (a), (b)).

### 4.3.1. Helicoids

If the propagation vector  $\mathbf{k}$  of a spiral state is perpendicular to an applied magnetic field, I will call such a state *helicoid* (Fig. 4.1 (a)).

#### A. Solutions for the polar angle $\theta$ in the helicoid

Analytical solutions for the polar angle  $\theta(x)$  of the magnetization written in spherical coordinates,

$$\mathbf{M} = M_s (\sin \theta(x) \cos \psi, \sin \theta(x) \sin \psi, \cos \theta(x)), \quad (4.13)$$

are derived by solving a *pendulum* equation

$$A \frac{d^2 \theta}{dx^2} - H \cos \theta = 0. \quad (4.14)$$

Such solutions are expressed as a set of elliptical functions [41] and describe a gradual expansion of the helicoid period with increased magnetic field (see the set of angular profiles  $\theta(x)$  in Fig. 4.1 (c)). In a sufficiently high magnetic field  $H_H$  [21] [XI] the helicoid infinitely expands and transforms into a system of isolated non-interacting  $2\pi$ -domain walls (kinks) separating domains with the magnetization along the ap-

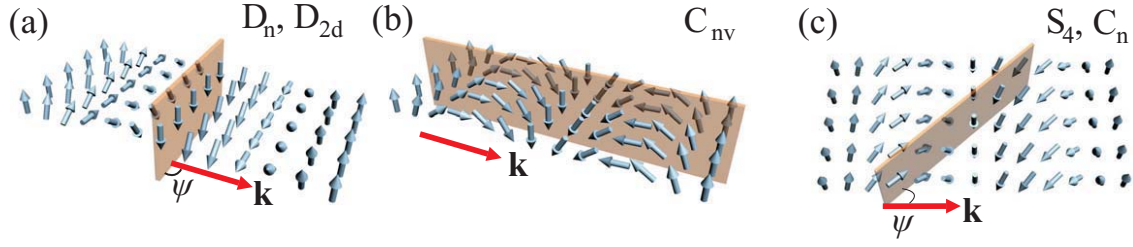


Figure 4.2.: Basic modulated structures: a) helicoid for systems with  $D_{2d}$  and  $D_n$  symmetry; b) cycloid for helimagnets with  $C_{nv}$  symmetry. The plane of magnetization rotation (shown by red color) makes angle  $\psi = \pi/2$  (a) and  $\psi = 0$  with the propagation direction  $\mathbf{k}$ . For the magnets of  $S_4$  and  $C_n$  crystallographic classes (c) angle  $\psi$  is specified by the ratio of Dzyaloshinsky constants (see text for details).

plied field [21, 41]. Non-dimensional value of this critical field is

$$h_H = \frac{H_H}{H_D} = \frac{\pi^2}{8} = 0.30843. \quad (4.15)$$

#### B. Solutions for the azimuthal angle $\psi$ in the helicoid

Distribution of the polar angle  $\theta(x)$  in magnetic field is common for helimagnets of all crystallographic classes. Azimuthal angle  $\psi$ , on the contrary, is fixed by the different forms of the Lifshitz invariants.

For cubic helimagnets (1.17) as well as for magnets belonging to the crystallographic classes  $D_{2d}$  (1.13) and  $D_n$  (1.14) the magnetization  $\mathbf{M}$  rotates in the plane perpendicular to the propagation direction like in a common Bloch wall (Fig. 4.2 (a)), i.e.  $\psi = \pi/2$ .

For helimagnets of  $C_{nv}$  symmetry, the magnetization vector undertakes Néel-type rotation along the propagation direction and comprises cycloid (Fig. 4.2 (b)), i.e.  $\psi = 0$ .

For helicoids with competing DM interactions, angle  $\psi$  is determined by the ratio of DM constants:  $\psi = \arctan(-D_\mu/D_\nu)$ ,  $\nu = 3, 5$ ;  $\mu = 4, 6$  (Fig. 4.2 (c)).

#### 4.3.2. Cone

A conical spiral is a solution of the functional  $W_0(\mathbf{M})$  with propagation direction along the magnetic field in which the magnetization rotation retains single-harmonic character:

$$\psi = \frac{z}{2L_D}, \quad \cos \theta = \frac{|\mathbf{H}|}{2H_D}. \quad (4.16)$$

In such a helix the magnetization component along the applied field has a fixed value

$$M_\perp = M \cos \theta = \frac{MH}{2H_D}, \quad (4.17)$$

and the magnetization vector  $\mathbf{M}$  rotates within a cone surface. The critical value

$$h_d = 2H_D \quad (4.18)$$

marks the saturation field of the cone phase.

The conical state combines properties of the homogeneous state and the flat spiral as a compromise between Zeeman and DM energies. This conical phase is the global minimum of functional  $W_0(\mathbf{M})$  (4.1).

Note, that a conical spiral will propagate along direction of an applied magnetic field, if corresponding Lifshitz invariants are present along this direction.

## 4.4. Chiral localized skyrmions: the building blocks for skyrmionic textures

### 4.4.1. Equations

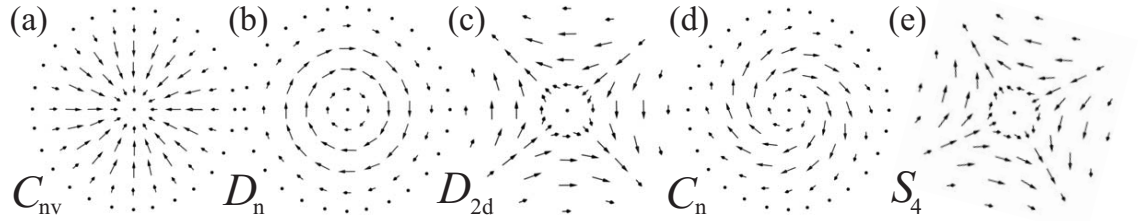


Figure 4.3.: Projections of the magnetization onto the basal plane for localized skyrmions of non-centrosymmetric magnets with  $C_{nv}$  (a),  $D_n$  (b),  $D_{2d}$  (c),  $C_n$  (d), and  $S_4$  (e) symmetry

The equations minimizing functional  $W_0(\mathbf{M})$  in (4.1) include solutions not only for one-dimensional helical states (section 4.3), but also for two-dimensional isolated skyrmions (IS) with magnetization written in spherical coordinates (1.58) and cylindrical coordinates used for the spatial variable (1.59).

The equilibrium solutions  $\theta = \theta(\rho)$  for isolated Skyrmions are common for heli-magnets of all crystallographic classes considered in section 1.2.1 *B*. The dependences  $\theta = \theta(\rho)$  are derived from the Euler equation [21, 22, 69, 70]:

$$\frac{d^2\theta}{d\rho^2} + \frac{1}{\rho} \frac{d\theta}{d\rho} - \frac{\sin 2\theta}{2\rho^2} - \frac{\sin^2 \theta}{\rho} - \frac{h}{2} \sin \theta = 0 \quad (4.19)$$

with the boundary conditions

$$\theta(0) = \pi, \theta(\infty) = 0. \quad (4.20)$$

The Euler equation (4.19) has been obtained by variation of  $W_0(\mathbf{M})$  after substituting (1.58) and (1.59). The non-dimensional units have been introduced in accordance

with the section 4.2.2 *B*. In the case of DM interactions with competing counterparts (1.15), (1.16), however, the spatial coordinates have to be normalized by

$$L_D = \frac{A}{\sqrt{D_\mu^2 + D_\nu^2}}, \nu = 3, 5; \mu = 4, 6. \quad (4.21)$$

Then DM energy contributions in reduced form can be parametrized by the relative ratios

$$d_\nu = \frac{D_\nu}{\sqrt{D_\nu^2 + D_\mu^2}}, d_\mu = \frac{D_\mu}{\sqrt{D_\nu^2 + D_\mu^2}}, \sqrt{d_\nu^2 + d_\mu^2} = 1. \quad (4.22)$$

Azimuthal angle  $\psi$ , as in the case of helicoids (see Fig. 4.2), depends on the symmetry class of the corresponding helimagnet (Fig. 4.3):

$$\begin{aligned} C_{nv} : \psi &= \varphi, \\ D_n : \psi &= \varphi - \pi/2, \\ D_{2d} : \psi &= -\varphi + \pi/2. \end{aligned} \quad (4.23)$$

For classes with competing DM interactions the functions  $\psi(\varphi)$  are specified by the ratio of DM constants [69]:

$$\psi(\varphi) = \varphi + \arctan\left(-\frac{d_\mu}{d_\nu}\right). \quad (4.24)$$

The total energy of an isolated skyrmion with respect to the homogeneous state can be written as

$$E = \int_0^\infty \varepsilon(\theta, \rho) d\rho, \quad \varepsilon(\theta, \rho) = 2\pi\rho \left[ \left( \frac{d\theta}{d\rho} \right)^2 + \frac{\sin^2 \theta}{\rho^2} + h(1 - \cos \theta) + \frac{d\theta}{d\rho} + \frac{\sin 2\theta}{2\rho} \right] \quad (4.25)$$

where  $\varepsilon(\theta, \rho)$  is an energy density.

#### 4.4.2. Methods

The most appropriate method to obtain solutions of (4.19) for isolated skyrmions is to solve the auxiliary Cauchy problems for these equations with the initial conditions [21]:

$$\theta(0) = \pi, \frac{d\theta}{d\rho}(0) = a_i. \quad (4.26)$$

For arbitrary values of  $a_i$  the lines  $\theta_\rho(\theta)$  normally end by spiraling around one of the attractors  $(\theta_i, 0)$  where  $\theta_i$  are specified by the magnetic field  $h$ . As an example in Fig. 4.4 (b) two lines with  $a_1 = 0.5$  and  $a_3 = 2$  are plotted.

The curves end in the points  $(2k\pi, 0)$  with  $k = 1, 2, \dots$  only for certain discrete values of initial derivatives  $a_i$ . Then these particular trajectories chosen among all possible trajectories in *phase space*  $(\theta, d\theta/d\rho)$  represent localized solutions of the boundary value problem (4.19).

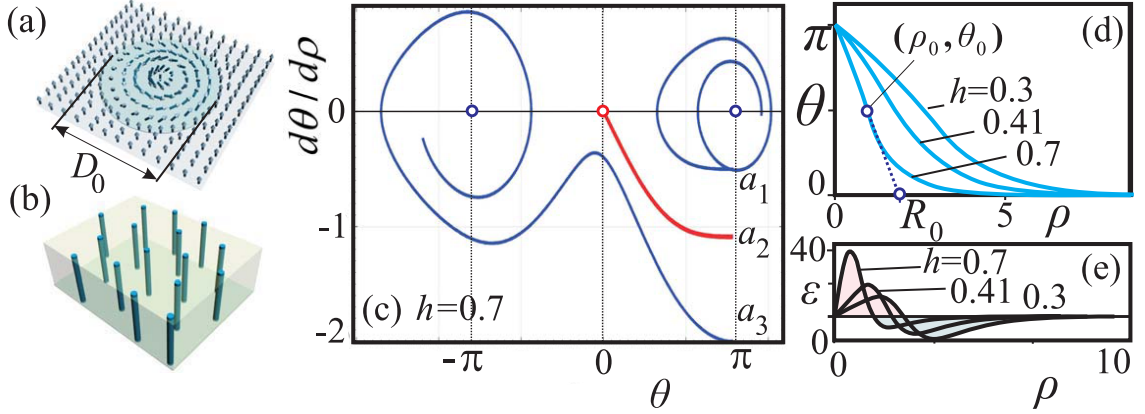


Figure 4.4.: Isolated skyrmions: (a) cross-section through an isolated skyrmion shows axisymmetric distribution of the magnetization (shaded area indicates the core with the diameter  $D_0$ ); (b) isolated skyrmions are homogeneously extended into the third dimension as skyrmionic filaments; typical solutions of Eq. (4.19) for isolated skyrmions are shown as phase portraits (c) on the plane  $((\theta, \theta_\rho))$  and magnetization profiles  $\theta(\rho)$  (d). (e) Energy densities  $\varepsilon(\theta, \rho)$  for different values of the applied magnetic field  $h$ .

In Fig. 4.4 (b) such a *separatrix* solution corresponds to  $(d\theta/d\rho)(0) = a_2 = 1.088$ . Note, that in magnetic fields applied opposite to the magnetization in the center of an isolated skyrmion, besides the ordinary skyrmions with  $\Delta\theta = \theta(0) - \theta(\infty) = \pi$ , also skyrmions with any odd number of half- turns  $\Delta\theta = 3\pi, 5\pi$  can exist [70].

The set of profiles  $\theta(\rho)$  for different values of the applied magnetic field is plotted in Fig. 4.4 (d). As these profiles bear strongly localized character, a skyrmion core diameter  $D_0$  can be defined in analogy to definitions for domain wall width [24] (section 1.3.1), i.e. as two times the value of  $R_0$ , which is the coordinate of the point where the tangent at the inflection point  $(\rho_0, \theta_0)$  intersects the  $\rho$ -axis (Fig. 4.4 (a), (d)):

$$D_0 = 2(\rho_0 - \theta_0(d\theta/d\rho)_{\rho=\rho_0}^{-1}). \quad (4.27)$$

According to conventions of Refs. [21, 22, 69] such arrow-like solutions will be decomposed into skyrmionic cores with linear dependence

$$\theta(\rho) = \pi(1 - \frac{\rho}{R}), \quad \rho \leq L_D \quad (4.28)$$

and exponential "tails" with

$$\theta \propto \exp[-\rho\sqrt{\frac{h}{2}}], \quad \rho \gg L_D. \quad (4.29)$$

The exponential character of skyrmion asymptotics has been derived by solving the

Euler equation (4.19) for  $\rho \rightarrow \infty$ :

$$\frac{d^2\theta}{d\rho^2} - \frac{h\theta}{2} = 0. \quad (4.30)$$

Therefore, a "nucleus" with a diameter  $2R$  can be considered as a two-dimensional particle-like state as it accumulates almost all energy of the isolated skyrmion. At the same time the asymptotic exponential tails will be viewed as the "field" generated by the particle [233].

From subdivision of the skyrmion structure general features of two-dimensional localized skyrmions can be revealed.

#### 4.4.3. Analytical results for the linear ansatz

Equilibrium radius  $R$  of the skyrmion core can be found from substituting the linear ansatz into (4.25) and minimizing with respect to  $R$ . The skyrmion energy (4.25) is reduced to a quadratic potential

$$E(R) = E_0 + \alpha R^2 - \frac{\pi}{2}R, \quad R_{min} = \frac{2.641}{h}, \quad E_{min} = E_0 - \frac{2.074}{h} \quad (4.31)$$

where

$$E_0 = 6.154 \quad (4.32)$$

is the "internal" energy of the skyrmions,

$$\alpha = 0.297 h, \quad (4.33)$$

and the parabola vertex point  $(R_{min}, E_{min})$  determines the minimum of energy (4.31).

This simplified model offers an important insight into physical mechanisms underlying the formation of the chiral skyrmions. The exchange energy  $E_0$  does not depend on the skyrmion size and presents an amount of positive energy "trapped" within the skyrmion (see red-shaded positive peak of energy for solutions  $\theta(\rho)$  in Fig. 4.4 (e)). The equilibrium skyrmion size arises as a result of the competition between chiral and Zeeman energies:

$$R_{min} \propto \frac{|D|}{H}. \quad (4.34)$$

In centrosymmetric systems with  $D = 0$  localized solutions are radially unstable and collapse spontaneously under the influence of applied magnetic field [21].



#### 4.4.4. Inter-skyrmion interaction and condensation of isolated skyrmions into the lattice

Asymptotic behaviour of the skyrmion solutions with  $\theta \propto \exp[-\rho\sqrt{h/2}]$ ,  $\rho \rightarrow \infty$  is determined by the Dzyaloshinskii-Moriya interactions. It can be considered as a specific "field" generated by the particle [233] which causes the repulsive character of the inter-skyrmion potential:

$$U(L) \propto \sqrt{L} \exp[-L\sqrt{\frac{h}{2}}] \quad (4.35)$$

where  $L \gg 1$  is the distance between skyrmion cores.

The ensemble of repulsive particle-like isolated skyrmions can condense into a lattice if the value of an applied magnetic field is smaller than the critical value  $h_S$ . In this case negative energy density associated with DM interactions (blue-shaded area of energy distribution  $\varepsilon(\theta, \rho)$ , Fig. 4.4 (e)) outweighs the positive exchange contribution (red-shaded area), and the skyrmion strings tend to fill the whole space with some equilibrium radius  $R_{min}$ . For equation (4.19),

$$h_S = 0.400659. \quad (4.36)$$

The mechanism of lattice formation through nucleation and condensation of isolated skyrmions follows a classification introduced by DeGennes [91] for (continuous) transitions into incommensurate modulated phases (see section 1.4 for details).

#### 4.4.5. Distinction of solutions for localized skyrmions from Belavin-Polyakov solitons

Note, that solitonic solutions with the same boundary conditions  $\theta(0) = \pi$ ,  $\theta(\infty) = 0$  as those for isolated skyrmions can be obtained also for isotropic centrosymmetric ferromagnets (well-known Belavin-Polyakov solutions for the nonlinear  $SO(3)$   $\sigma$ -model [234]). In this case for  $h = \beta = 0$  differential equation (4.19) has a manifold of analytical solutions:

$$\theta(\rho) = 2 \arctan \left( \frac{\rho}{\rho_0} \right)^N, \quad \psi(\varphi) = N\varphi + \alpha. \quad (4.37)$$

described by the angle  $\alpha$  and the parameter of integration  $\rho_0$ :

$$\alpha \in [0, \pi], \quad \rho_0 \in [0, \infty) \quad (4.38)$$

In spite of the seeming similarity with isolated skyrmions considered before, Belavin-Polyakov (BP) solitons represent a distinct branch of solutions.

First, the solutions of Eq. (4.37) are *achiral* localized structures with the energy

$$E_0 = 4\pi N \quad (4.39)$$

independent of the sense of rotation, i.e. angle  $\alpha$ . On the contrary, the sense of rotation and the exact value of angle  $\alpha$  in isolated skyrmions is dictated by the crystallographic symmetry and corresponding DM interactions (see formulas in section 4.4) and Fig. 4.3).

Second, solutions (4.37) have no definite size. Their energy is invariant under scale transformation of the profiles

$$\theta(\rho) \rightarrow \theta\left(\frac{\rho}{\lambda}\right), \lambda > 0. \quad (4.40)$$

The solutions (4.37) represent always separatrix lines in the phase portraits (Fig. 4.4 (c)) which for any value of initial derivatives hit the point  $\theta(\infty) = 0$ . Applied magnetic field and/or uniaxial anisotropy force Belavin-Polyakov solutions to end by spiraling around pole  $(\pi/2, 0)$  so that they never reach point  $(0, 0)$ . From the analysis of energy (4.31) it is seen that it has a parabolic dependence on size of the soliton with minimum for zero radius  $R$ . Thus applied magnetic field or internal anisotropic interactions lead to the spontaneous collapse of Belavin-Polyakov solutions. In chiral skyrmions the influence of DM interactions shifts the vertex of parabola describing the skyrmion energy (4.31) into the region of finite skyrmion radii. On the phase plane  $(\theta, d\theta/d\rho)$  only curves with appropriate initial derivatives will end in the point  $(0, 0)$  (Fig. 4.4 (c)).

Third, asymptotic behaviour of Belavin-Polyakov solutions has a  $1/\rho$ -character defined by the exchange energy. In isolated chiral skyrmions  $\theta \propto \exp[-\rho]$  which is caused by DM interactions. Moreover, energy density distributions  $\varepsilon(\rho)$  (Fig. 4.4 (e)) reveal two distinct regions: positive exchange-energy "bags" concentrated in the skyrmion center and extended areas with negative DM-energy density stretching up to infinity.

## 4.5. Properties of ideal skyrmion lattices: double twist versus compatibility

In early numerical approaches used in Refs. [21,22,70] the circular cell approximation (CCA) had been used to derive equilibrium parameters of skyrmion lattices. In this method the lattice cell is replaced by a circle (Fig. 4.5 (b)), and then Eq. (4.19) is integrated with boundary conditions

$$\theta(0) = \pi, \theta(R) = 0. \quad (4.41)$$

After that, the energy density of the lattice

$$W_{CCA} = \frac{1}{\pi R^2} \int_0^R \varepsilon(\theta, \rho) d\rho \quad (4.42)$$

is minimized with respect to the cell radius  $R$  (Fig. 4.5 (e)) and the equilibrium size  $R_{min}$  is found.

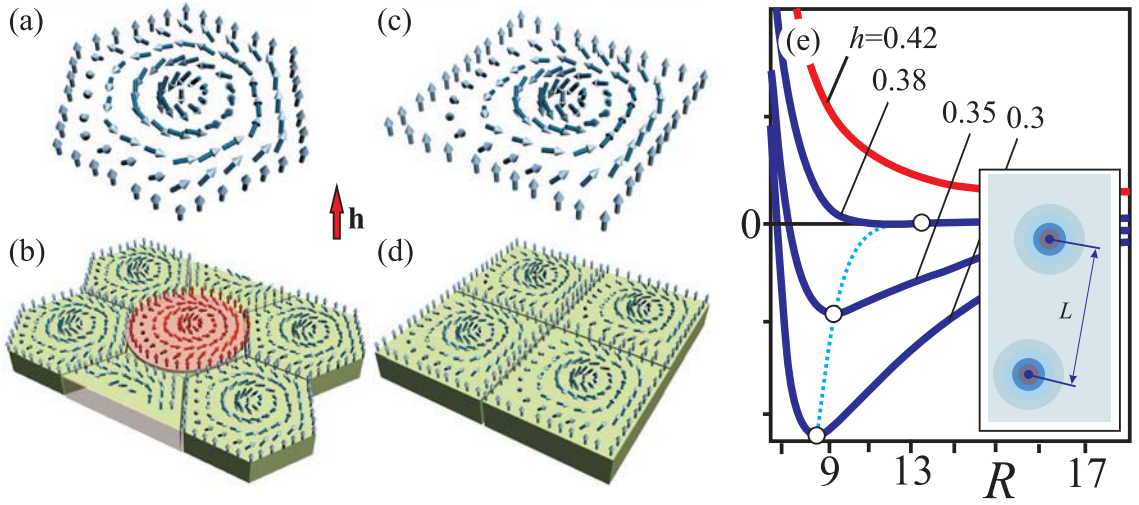


Figure 4.5.: Hexagonal (a),(b) and square (c),(d) skyrmion lattices: (a) and (c) are unit cells with axisymmetric distribution of the magnetization near the center; (b) and (d) are fragments of the lattices. In (b) the replacement of the cell in the skyrmion lattice by the circle according to the method of circular cell approximation is shown as outline. (e) Below the critical field  $h_s$  the energy of a skyrmion lattice has a minimum for some equilibrium cell size  $R_{min}$ .

In real hexagonal (Fig. 4.5 (a)) and/or square skyrmion lattices (Fig. 4.5 (c), (d)), the axisymmetric distribution of the magnetization is preserved only near the center of lattice cell while the overlapping solutions  $\theta(\rho)$  in the inter-skyrmion regions are distorted. Therefore, it is worthwhile to compare corresponding numerically rigorous solutions with those obtained from the circular-cell approximation.

#### 4.5.1. Methods: numerical recipes

For two-dimensional skyrmions the Euler-Lagrange equations derived from the energy functional (4.1) are non-linear partial differential equations. These equations have been solved by numerical energy minimization procedure using finite-difference discretization on rectangular grids with adjustable grid spacings and periodic boundary conditions. Components  $(m_x, m_y, m_z)$  of the magnetization vector  $\mathbf{m}$  have been evaluated in the knots of the grid, and for the calculation of the energy density (4.1) I used finite-difference approximation of derivatives with different precision up to eight points as neighbours. To check the stability of the numerical routines I refined and coarsened the grids from  $42 \times 72$  points up to  $168 \times 288$ . To avoid elliptical instability of the hexagonal skyrmion lattice I used grid spacings  $\Delta_y \approx \Delta_x$  so that grids are approximately square in order to reduce the artificial anisotropy incurred by the discretization. The final equilibrium structure for the 2D baby-skyrmion hexagonal lattice was obtained according to the following iterative procedure of the energy minimization using simulated annealing and a single- step Monte- Carlo dynamics with the Metropolis algorithm [235]:

(i) The initial configuration of magnetization vectors in the grid knots for Monte-Carlo annealing is specified by the solutions from circular-cell approximation.

(ii) A point  $(x_n, y_n)$  on a grid is chosen randomly. Then, the magnetization vector in the point is rotated without change of its length. If the energy change  $\Delta H_k$  associated with such a rotation is negative, the action is immediately accepted.

(iii) However, if the new state's energy is higher than the last, it is accepted probabilistically. The probability  $P$  depends upon the energy and a kinetic cycle temperature  $T_k$ :

$$P = \exp \left[ -\frac{\Delta H_k}{k_B T_k} \right], \quad (4.43)$$

where  $k_B$  is Boltzmann constant. Together with probability  $P$  a random number  $R_k \in [0, 1]$  is generated. If  $R_k < P$  new configuration accepted otherwise discarded (see, for example, [236]). Generally speaking, at high temperatures  $T_k$ , many states will be accepted, while at low temperatures, the majority of these probabilistic moves will be rejected. Therefore, one has to choose appropriate starting temperature for heating cycles to avoid transformation of metastable skyrmion textures into globally stable spiral states.

(iv) The characteristic spacings  $\Delta_x$  and  $\Delta_y$  are also adjusted to lead to the energy relaxation. The procedure is stopped when no further reduction of energy is observed.

#### 4.5.2. Features of ideal skyrmion lattices

While condensing into the lattice, isolated skyrmions can form either hexagonal or square skyrmion order (Fig. 4.5 (a)-(d)). Contour plots for the components  $m_x$ ,  $m_y$ , and  $m_z$  of the magnetization vector  $\mathbf{m}$  in both lattices are shown in Fig. 4.6 (a), (b). Separate isolated skyrmions preserve axisymmetric distribution of the magnetization near the cell center while the overlap of solutions  $\theta(\rho)$  (Fig. 4.4 (d)) distorts the inter-skyrmion regions.

*A. Comparison of energy densities and surface areas of the lattice cells from circular-cell approximation and numerical simulations.*

Figure 4.7 shows the distribution of the free-energy densities and magnetization profiles  $\theta(\rho)$  for equilibrium hexagonal skyrmion lattice in the circular-cell approximation and from numerical simulations. Due to the denser packing of individual skyrmions, hexagonal lattices provides smaller energy density in comparison with square lattice.

The difference of energy densities in hexagonal cell and CCA cell for  $h = 0$  is

$$\Delta W = \frac{W_{CCA} - W_{hexagon}}{W_{CCA}} = \frac{0.234 - 0.2312}{0.234} = 0.012. \quad (4.44)$$

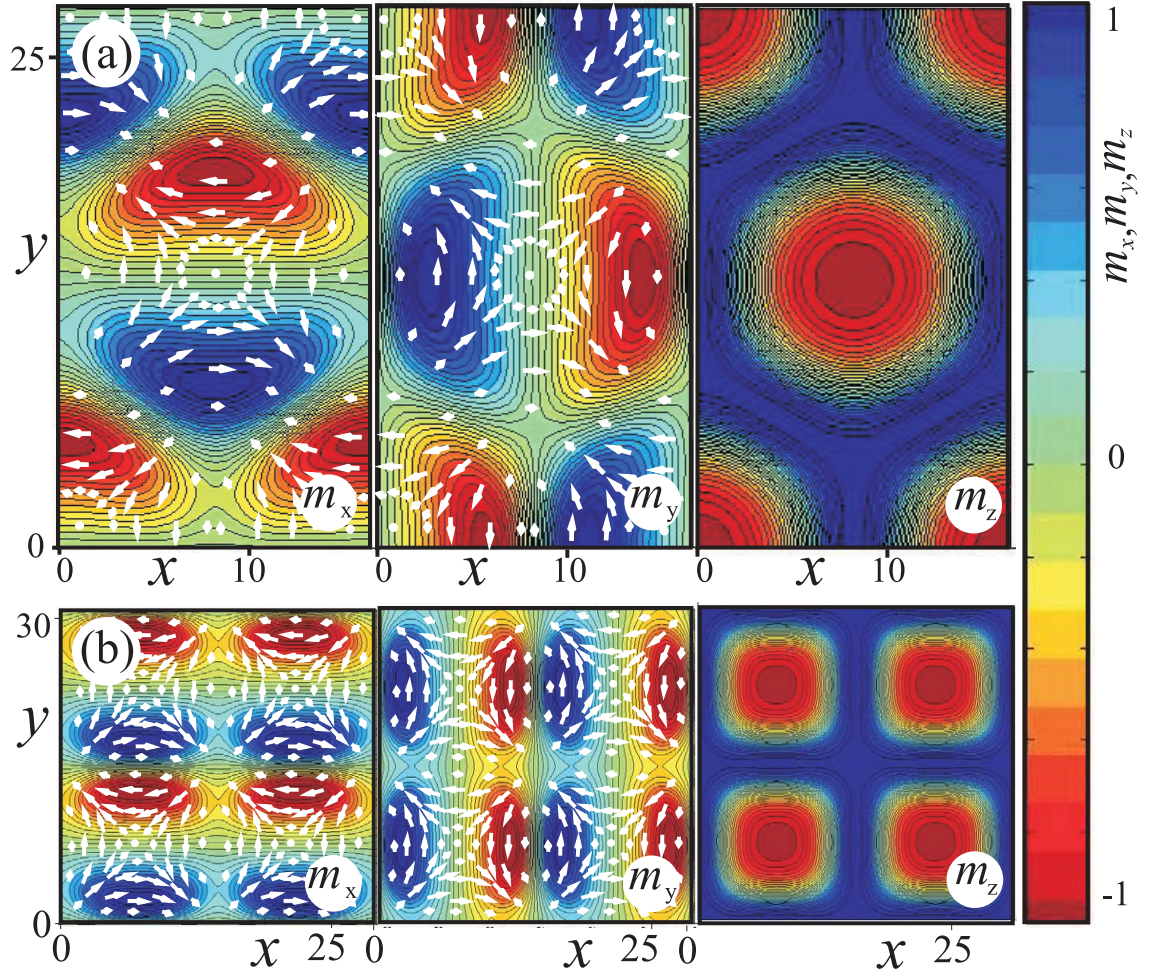


Figure 4.6.: Contour plots for  $m_x$ ,  $m_y$ , and  $m_z$  components of the magnetization on the plane  $(x, y)$  for the hexagonal (a) and square (b) skyrmion lattices of a helimagnet with  $D_{2d}$  symmetry. The white arrows show the corresponding distribution of the magnetization.

For the square cell the difference is larger,

$$\Delta W = \frac{W_{CCA} - W_{square}}{W_{CCA}} = \frac{0.234 - 0.2235}{0.234} = 0.0449. \quad (4.45)$$

The surface area of the cell in CCA is larger than the surface of the corresponding numerical hexagon,

$$\Delta S = \frac{S_{CCA} - S_{hexagon}}{S_{CCA}} = 0.0167, \quad (4.46)$$

whereas the surface area of square lattice cell is larger than the circle,

$$\Delta S = \frac{S_{square} - S_{CCA}}{S_{CCA}} = 0.0234. \quad (4.47)$$

Hence, the statement of the circular- cell approximation [21], that surface areas of a circle and a hexagonal cell must coincide, is basically erroneous. However, the smallness of all the differences between CCA and rigorous numerical simulations for model (4.1) allows to consider circular-cell approximation as an excellent approach for the global properties of the hexagonal skyrmion lattice. In particular, CCA yields an exact value of the upper critical field  $h_S$  as the skyrmions are located at big distances from each other and are independent on the detailed arrangement of individual filaments:  $h_S$  is the same for square and hexagonal lattices.

The distortions of angular solutions near the border of hexagon lead to corresponding redistribution of exchange and DM energy density (Fig. 4.7): due to the increase of exchange energy density along the apothem of the hexagon (dotted blue line), the total energy density (dotted black line) has also higher value than corresponding CCA energy density (thin black line).

*B. Expansion into the Fourier series of the  $m_z$ -component of the magnetization for the lattice from the rigorous calculations*

The Fourier expansion for  $z$ -component of the magnetization may be written as

$$m_z = \sum_{i,j=0}^{\infty} \lambda_{ij} [a_{ij} \cos(\frac{2\pi ix}{R_1}) \cos(\frac{2\pi jy}{R_2}) + b_{ij} \sin(\frac{2\pi ix}{R_1}) \cos(\frac{2\pi jy}{R_2}) + c_{ij} \cos(\frac{2\pi ix}{R_1}) \sin(\frac{2\pi jy}{R_2}) + d_{ij} \sin(\frac{2\pi ix}{R_1}) \sin(\frac{2\pi jy}{R_2})] \quad (4.48)$$

where

$$\lambda_{00} = 0.25, \lambda_{i0} = \lambda_{0j} = 0.5, \lambda_{ij} = 1, \quad (4.49)$$

$R_1$  and  $R_2$  are characteristic sizes of the elementary lattice cell (Fig. 4.6 (a)). With the present choice of origin of coordinates, coefficients

$$b_{ij} = c_{ij} = d_{ij} = 0. \quad (4.50)$$

The coefficients  $a_{ij}$  may be represented graphically for different values of the applied

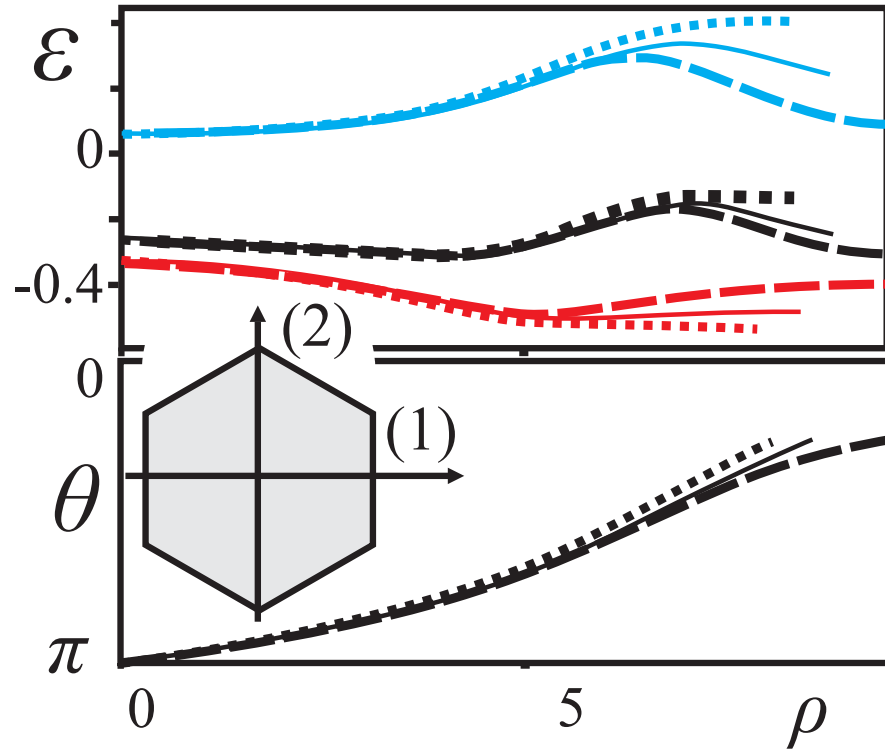


Figure 4.7.: Distributions of exchange (blue lines), DM (red lines), and  $\varepsilon_i(\rho)$  total energy densities in a hexagonal lattice for two particular directions  $i$  through the cell (dotted line along apothem, dashed line along the diagonal of the hexagon) plotted together with the corresponding dependences for circular-cell approximation (solid thin lines); profiles  $\theta_i(\rho)$  for circular-cell approximation (solid thin line) and numerical hexagon (dotted and dashed lines).

magnetic field (Fig. 4.8). Due to axial arrangement of the core the amplitudes of higher harmonics have comparable values with those of leading lattice harmonics. Positive coefficients  $c_{ij}$  of the expansion (4.48) are marked by red color, whereas negative coefficients - by blue. Multiplying the diameter of each circle by ten one can extract the value of the underlying coefficient.

In Ref. [79] a triple spin-spiral crystal is presented as a skeleton for such a skyrmion lattice in cubic chiral magnets. While the topology and rough geometry of these states is the same, this theoretical interpretation of the Skyrmion states of chiral magnets assumes that the skyrmionic states can be described by the first few harmonics of a hexagonal lattice. Skyrmions in this approach have triangular cores instead of radial cores. This point of view does not agree with the exact solutions and detailed demonstration of radial and localized solutions for skyrmions in the present chapter. The approach of [79] discounts the existence and relevance of the localized and radial nature of the skyrmion solutions. By virtue of the localized character of the skyrmion cores and its axial symmetry such an approximation by a number of Fourier modes is very poor as the convergence of the Fourier series is slow. Owing to the localization of the skyrmions their properties cannot be modeled, nor understood from a multi-Q ansatz with a finite number of Fourier components. In particular, the important transformation process of a Skyrmion lattice into an assembly of isolated skyrmion lines under an applied field cannot be described by the picture of a triple spin-spiral crystal.

Thus, the theoretical interpretation proposed in Ref. [79] is considered to be not correct.

#### *C. Rigorous solutions for skyrmion lattices with Dzyaloshinskii-Moriya interactions representing the weighted sum of Lifshitz invariants*

In the case of DM interactions (1.15), (1.16) with competing counterparts, the skyrmions have a more complicated structure as shown in Fig. 4.9 for particular case of  $C_n$  symmetry. For  $d_1 = 0.2$ ,  $d_2 = 0.9798$  angle  $\psi = \phi + 78^\circ$ , and the structure of skyrmions is slightly different from the "Bloch"-type skyrmion with  $D_n$  symmetry (Fig. 4.3 (b)). Note, that the cases  $d_1 = 1$ ,  $d_2 = 0$  and  $d_1 = 0$ ,  $d_2 = 1$  denote skyrmions with  $C_{nv}$  (Fig. 4.3 (a)) and  $D_n$  (Fig. 4.3 (b)) symmetry, correspondingly.

## **4.6. Competition of skyrmions with helicoids within the isotropic phenomenological model**

From the previous calculations it is known [31] [XI,XIV,XV], that "double-twisted" rotation of the magnetization as in skyrmions yields an energetic advantage only at small distances from the skyrmion axis in comparison with "single-twisted" spiral phases [31]. Conversely, the energy density is larger at the outskirts of the skyrmion which is the consequence of an inherent frustration built into models with chiral couplings: the system cannot fill the whole space with the ideal, energetically most favoured double-twisted motifs. The equilibrium energy of the skyrmion cell at zero



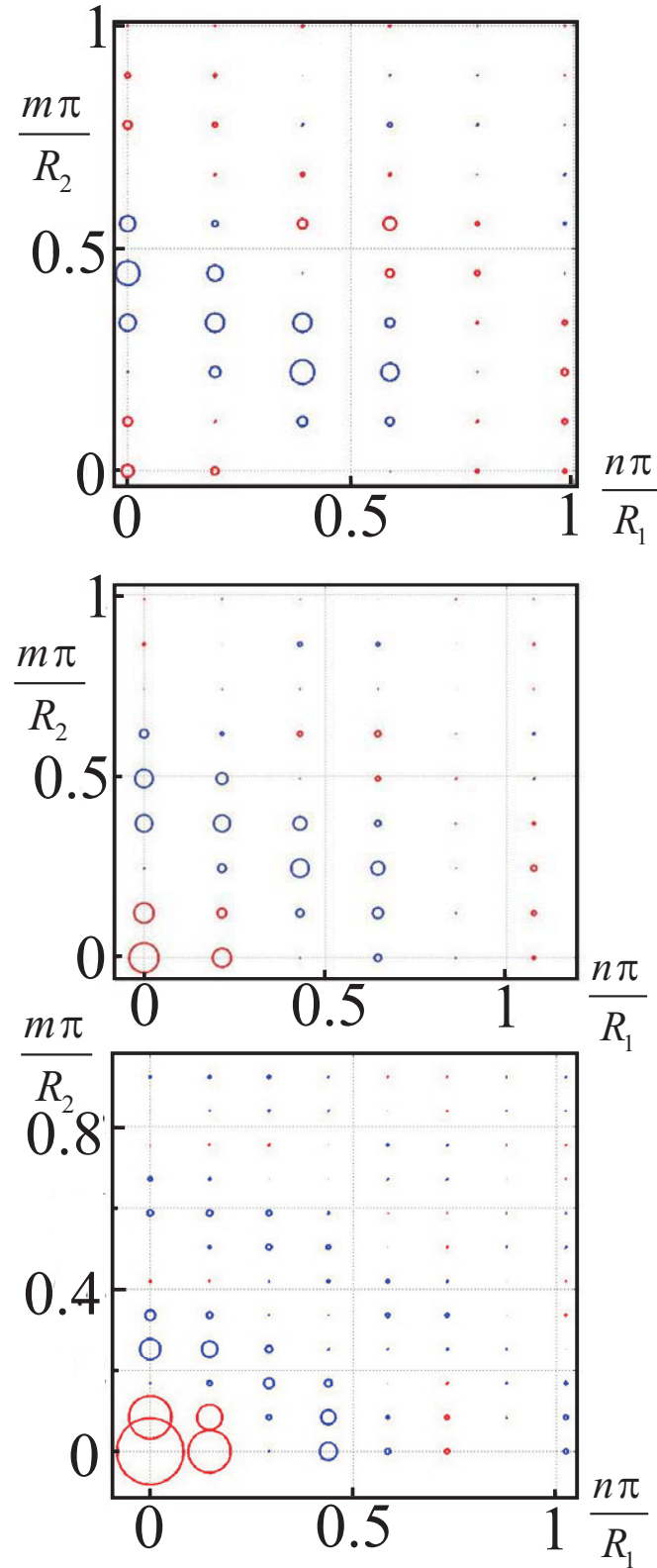


Figure 4.8.: Graphical representation of the coefficients of the Fourier expansion for  $z$ -component of the magnetization in the hexagonal skyrmion lattice for different values of the applied magnetic field  $h = 0$  (a),  $h = 0.2$  (b),  $h = 0.4$  (c). Positive coefficients are marked by red color, whereas negative - by blue.

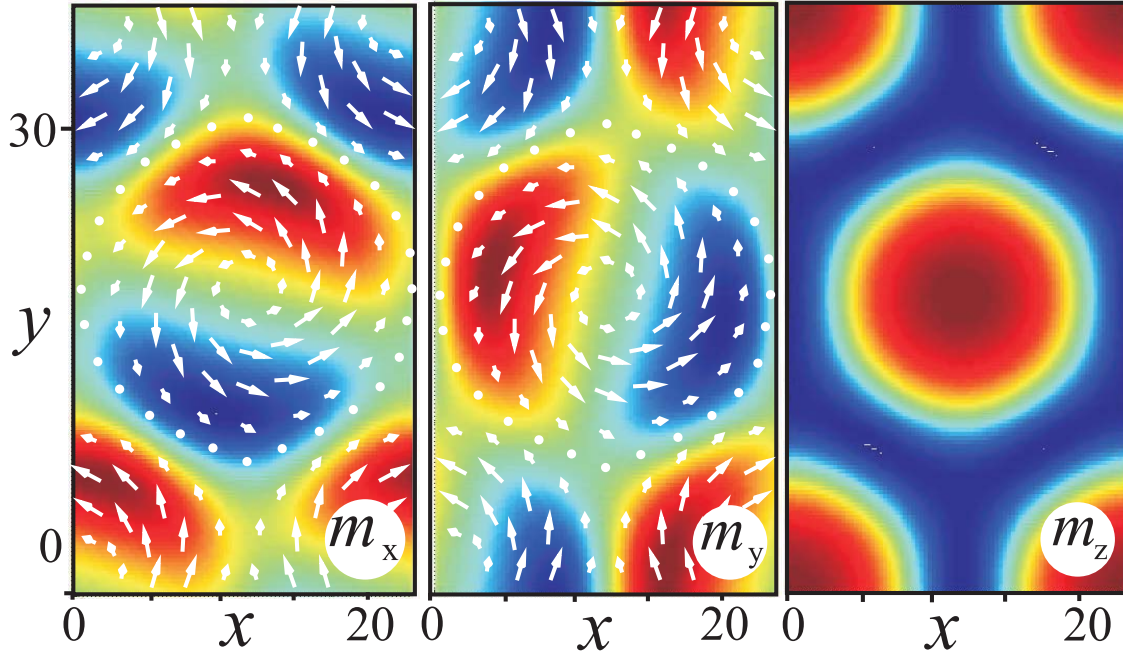


Figure 4.9.: Contour plots of  $m_x$ ,  $m_y$ , and  $m_z$  components of the magnetization for helimagnets with  $C_n$  symmetry ( $h = \beta = 0$ ,  $d_1 = 0.2$ ,  $d_2 = 0.9798$ ).

field

$$\tilde{w}_S(\zeta) = \frac{2}{\zeta^2} \int_0^\zeta \varepsilon(\rho) \rho d\rho \quad (4.51)$$

plotted as a function of the distance from the center  $\zeta$  (Fig. 4.10 (a)) shows that an energy excess near the border outweighs the energy gain at the skyrmion center. As a result, the skyrmion states are metastable states in comparison with lower-energy helical phases.

At higher magnetic fields, however, the skyrmion lattice has lower energy than the helicoid. The first order transition between these two modulated states occurs at [21]

$$H_1 = 0.1084H_D. \quad (4.52)$$

Properties of the skyrmion lattice solutions are collected in Fig. 4.10 and in Table 4.1. With increasing magnetic field, a gradual localization of the skyrmion core  $D_0$  is accompanied by the expansion of the lattice period. The lattice transforms into the homogeneous state by infinite expansion of the period at the critical field

$$H_S = 0.40066H_D. \quad (4.53)$$

Remarkably, the skyrmion core retains a finite size,  $D_0(H_S) = 0.920L_D$  and the lattice releases a set of *repulsive* isolated skyrmions at the transition field  $H_S$ , owing to their topological stability. These free skyrmions can exist far above  $H_S$ . On decreasing the field again below  $H_S$ , they can re-condense into a skyrmion lattice (Fig. 4.10 (b)). A similar type of sublimation and resublimation of particle-like

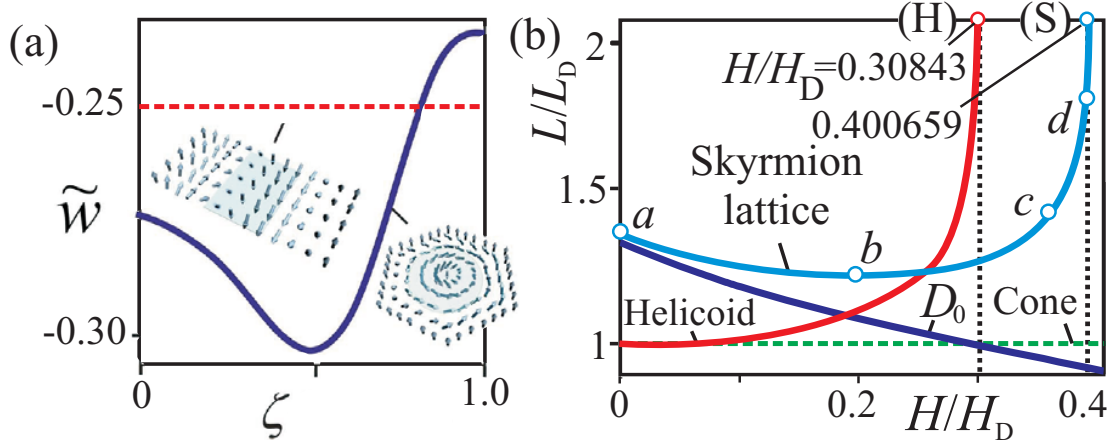


Figure 4.10.: (a) Local energies  $\tilde{w}(\zeta)$  of the skyrmion lattice and helicoid at zero field (reproduced from [31]); (b) equilibrium sizes of the cell core ( $D_0$ , Eq. (4.27)) and lattice period  $R$  compared to helicoid and cone periods.

textures occurs in helicoids at the critical field  $h_H$  (Eq. (4.15)): the period infinitely expands and the helicoid splits into a set of isolated  $2\pi$  domain walls or kinks [21, 41].

Table 4.1.: Critical fields and characteristic parameters of the hexagonal skyrmion lattice:  $H_1$  transition field between the helicoid and skyrmion lattice;  $H_S$  saturation field of the skyrmion lattice; last column gives properties of IS as excitations of the saturated state for an (arbitrary) high field  $H/H_D = 0.7$

		$H_1$	$H_S$	
Reduced magnetic field, $H/H_D$	0	0.1084	0.40066	0.7
Lattice cell period, $L/L_D$	1.376	1.270	$\infty$	-
Core diameter, $D_0/L_D$	1.362	1.226	0.920	0.461
Averaged magnetization, $m_S$	0.124	0.278	1	1

For a negative magnetic field applied along the magnetization in the center of skyrmion strings, both the skyrmion cores and the lattice cell size expand. Near the critical field  $h_H = -0.30843$  the vortex lattice consists of honeycomb-shaped cells separated from each other by narrow  $360^\circ$  domain walls (Fig. 4.11 (d)). Note, that for negative fields the honey-comb lattice is highly instable. It is hardly accessible and easily elongates into spiral state. For negative magnetic fields, isolated skyrmions do not exist.

Thus, it can be concluded that for functional  $W_0(\mathbf{M})$  (4.1) the cone phase is

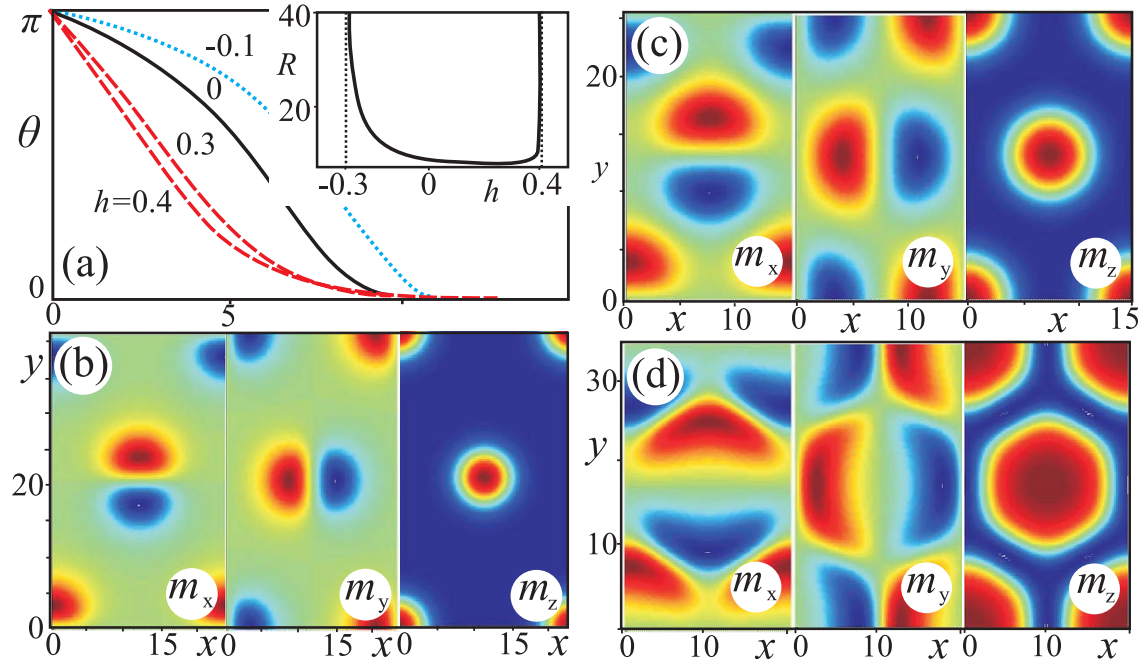


Figure 4.11.: Evolution of the hexagonal skyrmion lattice in magnetic field applied either opposite to the magnetization in the skyrmion center (b), (c) or parallel to it (d). The solutions are presented as angular profiles along diagonals of the hexagons (a), and contour plots for all components of the magnetization on the plane  $(x, y)$ : (b)  $h = 0.4$ , (c)  $h = 0.3$ , (d)  $h = -0.2$ . Inset of (a) shows the equilibrium characteristic size of the hexagonal lattice for both directions of the magnetic field: for positive values of the magnetic field the skyrmion lattice transforms into a system of isolated skyrmions with repulsive potential between them, whereas for negative magnetic field it turns into the homogeneous phase through a honeycomb structure with increasing lattice period (d).

the global minimum in the whole range of the applied fields where the modulated states exist ( $0 < h < h_d$ ). The helicoids and skyrmion lattices can exist only as metastable states. One has to look for additional energy contributions capable to stabilize skyrmion phase. In the next sections I consider some successful candidates for this role: uniaxial, cubic, and exchange anisotropy.

## 4.7. Stabilization of skyrmion textures by uniaxial distortions in non - centrosymmetric cubic helimagnets

From the numerical investigation of Eq. (4.1), I show now that a sufficiently strong magnetic anisotropy  $K_u$  (4.2) stabilizes skyrmionic textures in applied magnetic fields. The uniaxial anisotropy  $K_u$  in cubic helimagnets can be imposed, for example, by surface/interface interactions in thin films or nanolayers and tuned by covering the surface with different non-magnetic materials.

In sufficiently thick magnetic layers, such induced anisotropy can be considered as a pure surface effect which distorts the uniform prolongation of skyrmion filaments perpendicularly to the surface and transforms them into convex shaped spherulites. In details, such a case will be considered in chapter 5. In thin magnetic nanolayers surface-induced uniaxial anisotropy is uniformly distributed through the layer and can be considered as homogeneous uniaxial anisotropy with constant  $K_u$ . On the other side, the uniaxial anisotropy in cubic helimagnets may be induced by uniaxial strains in bulk systems.

By comparing the equilibrium energies of the conical phase, the helicoids, and the rigorous solutions for hexagonal skyrmion lattice, I have constructed the phase diagram of solutions (Fig. 4.12).

As in section 4.4, I start analysis of the phase diagram from isolated skyrmions.

### 4.7.1. Isolated skyrmions in chiral helimagnets with uniaxial anisotropy

In cubic helimagnets with uniaxial anisotropy, isolated skyrmions are solutions of the Euler equation written in the reduced form:

$$\frac{d^2\theta}{d\rho^2} + \frac{1}{\rho} \frac{d\theta}{d\rho} - \frac{\sin 2\theta}{2\rho^2} - \frac{\sin^2 \theta}{\rho} - \frac{h}{2} \sin \theta - \frac{\beta_u}{2} \sin 2\theta = 0 \quad (4.54)$$

with the boundary conditions

$$\theta(0) = \pi, \theta(\infty) = 0. \quad (4.55)$$

The region of metastable existence of simple  $\pi$ -skyrmions was calculated in Ref. [22]. On the phase diagram (Fig. 4.12) it is marked by white color and expands over large values of positive magnetic field and easy-axis uniaxial anisotropy.

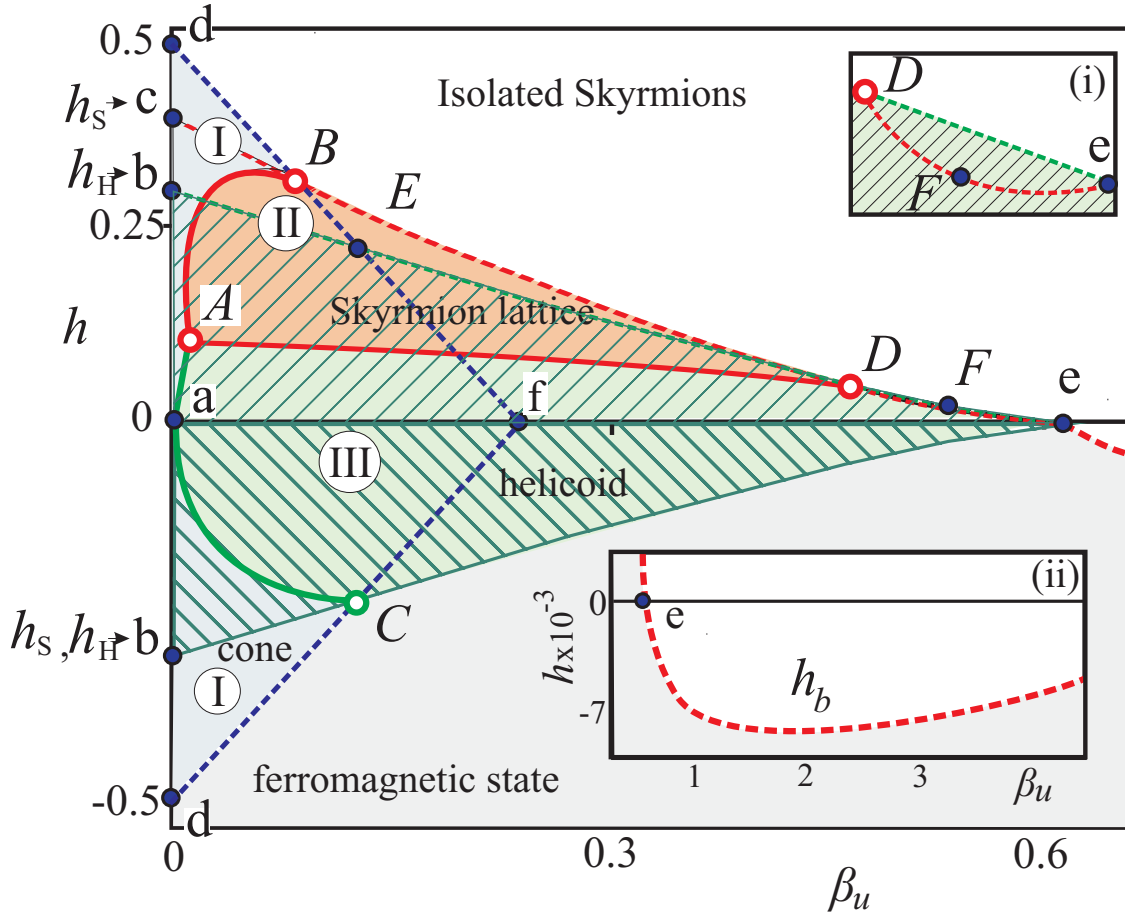


Figure 4.12.: Magnetic phase diagram of the solutions for model (4.1) including uniaxial anisotropy  $\beta_u$ . Filled areas designate the regions of thermodynamical stability of corresponding modulated phases: I - conical phase (blue shading); II - skyrmion phase (red shading); III - helicoid (green shading). White shading stands for the region of isolated skyrmions and kinks. In the region with grey shading no modulated states are available. Hatching shows the existence region of helicoids. The conical phase exists within the area (a-d-B-f). For  $\beta_u > 0.0166$  corresponding to the point A a skyrmion lattice can be stabilized in high magnetic fields. For  $\beta_u > 0.25$  corresponding to the point f only helicoids and skyrmions can be realized as thermodynamic phases. Two insets show the magnifications of particular parts of the phase diagram: inset (i) exhibits the region D – F – e where spiral state as only one modulated phase can exist; the inset (ii) shows the line (red dashed line) of skyrmion bursting  $h_b$  in negative fields (see text for details).

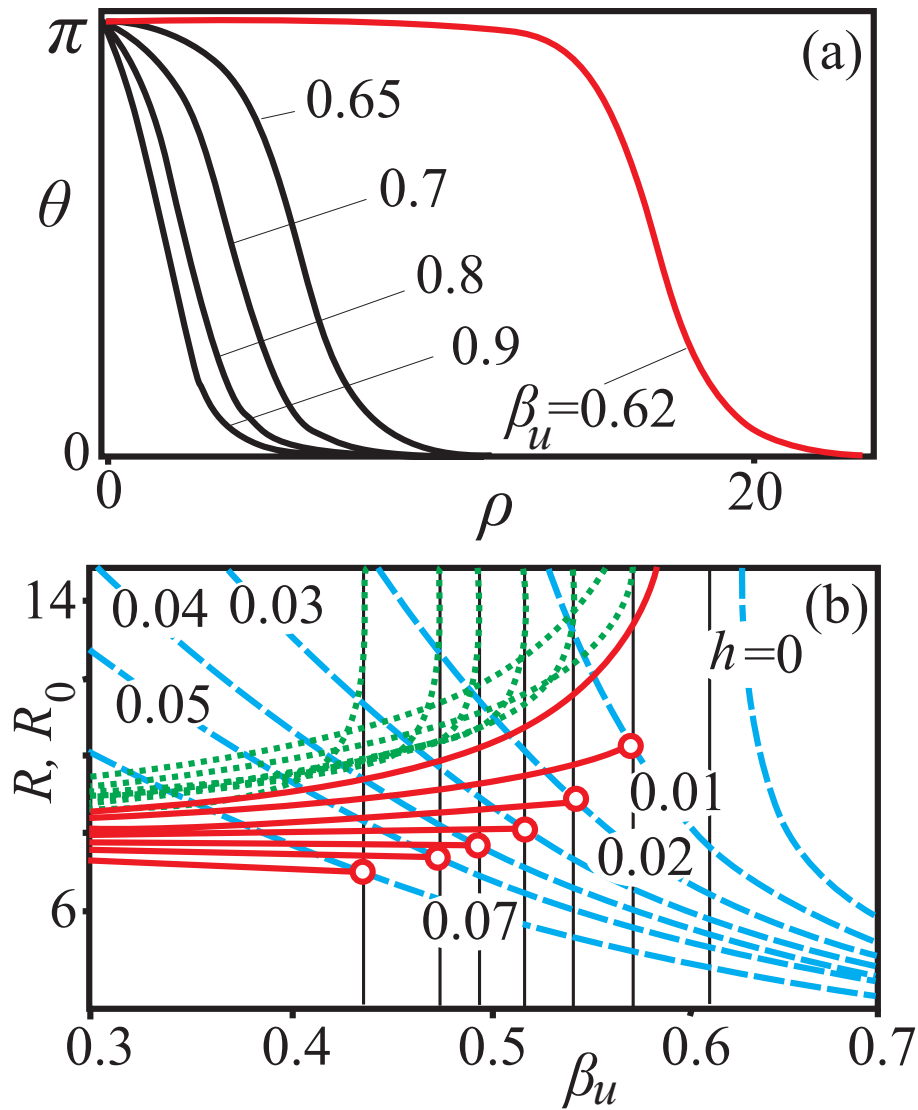


Figure 4.13.: (a) Angular profiles  $\theta(\rho)$  for isolated skyrmions in zero magnetic field and for different values of easy-axis uniaxial anisotropy  $\beta_u$  show the expansion of skyrmion cores while approaching the critical value of uniaxial anisotropy  $\beta_{cr} = 0.61685$ . In (b) the size of the core of isolated skyrmions determined according to the Lilley's definition (see section 4.4) is plotted in dependence on the uniaxial anisotropy constant  $\beta_u$  for different values of the applied magnetic field (dashed blue line). Red solid lines in (b) show the size of the skyrmion core in a skyrmion lattice, green dotted lines - the size of the lattice cell. For constant value of the applied magnetic field and variable constant of uniaxial anisotropy the lattice releases the isolated skyrmions for some critical value of  $\beta_u$ . This corresponds to the intersection point of red and blue lines; the green lines tend to infinity; the characteristic size of the core of the skyrmions undergoes a sudden change. For  $h = 0$  there is no connection between the skyrmion lattice and isolated skyrmions.



For  $h = 0$  and

$$\beta_u > \beta_{cr} = \frac{\pi^2}{16} \quad (4.56)$$

isolated skyrmions exist as a separate branch of skyrmion solutions [22]. With decreasing constant  $\beta_u$  the cores of isolated skyrmions expand, and the localized skyrmions disappear as a solution for the critical value  $\beta_{cr}$  (Fig. 4.13 (a)). The characteristic size  $R_0$  of the Skyrmion core determined according to the Lilley definition (blue dashed lines in Fig. 4.13 (b)) expands to infinity for  $\beta_u = \beta_{cr}$ .

In the applied magnetic field  $h > 0$ , the isolated skyrmions can condense into the lattice with decreasing constant of uniaxial anisotropy  $\beta_u$ . The solid red and dotted green lines in Fig. 4.13 (b) show dependences of the characteristic core and lattice cell sizes on the changing constant of uniaxial anisotropy  $\beta_u$ . In the point of intersection of red and blue lines, i.e. in the point of condensation of isolated skyrmions into the lattice, the skyrmion core undergoes a sudden leap, while the equilibrium lattice period expands unlimitedly.

For large values of uniaxial anisotropy  $\pi$ -skyrmions can exist even at negative fields (see inset (ii) of Fig. 4.12). The magnetization in the skyrmion core is then oriented along the field, while the surrounding matrix is magnetized in the opposite direction. Thus, the skyrmion size increases with increasing magnetic field. Finally, when  $h$  reaches a certain critical value  $h_b(\beta_u)$  (inset (ii) of Fig. 4.12) the skyrmion "bursts" into the homogeneous state with the magnetization parallel to the applied field. First such a behaviour of isolated skyrmions in a negative magnetic field was described in Ref. [70]. Also the technique to explore skyrmion stability was elaborated.

In the following I exploit the methods of Ref. [70] and present a comprehensive analysis of the structure and stability of all types of isolated skyrmions of the model (4.54).

#### 4.7.2. Localized skyrmions and the manifold of solutions of micromagnetic equations: the question of radial stability

In addition to skyrmion solution of Eq. (4.54) (Fig. 4.14 (a)) a family of specific vortex states with small values of derivative in the center  $d\theta/d\rho(\rho = 0)$  can be found.

The first vortex of this family is also of  $\pi$ -type, but has a larger core size (Fig. 4.14 (e)). The energy distribution in such a vortex (Fig. 4.14 (h)) looks qualitatively the same as for the common skyrmion (Fig. 4.14 (d)). This vortex can exist even for zero values of Dzyaloshinskii-Moriya interaction.

All other members of the vortex family (Fig. 4.14 (i), (m)) are characterized by the parts with a reverse rotation of the magnetization vector - nodes. Each sequential vortex has more nodes than preceding one and exhibits oscillations of the magnetization in the tail (Fig. 4.14 (i), (m)). The phase portraits for such vortices before hitting the point (0,0) round by turns the attractors in points  $(0, \pm\pi/2)$  (Fig. 4.14 (j), (n)).

The analysis of stability for all solutions of equation (4.54) shows that only the skyrmion solution (Fig. 4.14 (a)) is stable with respect to small perturbations of the



structure.

To check the stability of obtained skyrmion solutions I consider radial distortions of type  $\xi(\rho)$  with constraint

$$\xi(0) = \xi(\pi) = 0. \quad (4.57)$$

Such distortions are the relevant leading instabilities of radial skyrmion structures  $\theta(\rho)$ . By inserting  $\tilde{\theta}(\rho) = \theta(\rho) + \xi(\rho)$  into the energy functional (4.25) with uniaxial anisotropy I obtain the perturbation energy

$$E^{(2)} = \int_0^\infty \left[ \left( \frac{d\xi}{d\rho} \right)^2 + G(\rho)\xi^2 \right] \rho d\rho \quad (4.58)$$

with

$$G(\rho) = \cos(2\theta) \left( \frac{1}{\rho^2} + \beta \right) + \frac{h}{2} \cos \theta - \frac{\sin(2\theta)}{\rho}. \quad (4.59)$$

Radial stability of the function  $\theta(\rho)$  means that the functional  $E^{(2)}$  is positive for all functions  $\xi(\rho)$  which obey condition (4.57). Correspondingly, the solutions will be unstable, if there is a function  $\xi(\rho)$  that leads to a negative energy (4.58). Thus, the problem of radial stability is reduced to the solution of the spectral problem for functional (4.58). I solve it by expanding  $\xi(\rho)$  in a Fourier series:

$$\xi(\rho) = \sum_{k=1}^{\infty} b_k \sin(k\theta(\rho)) \quad (4.60)$$

Inserting this into Eq. (4.58) reduces the perturbation energy to the following quadratic form:

$$E^{(2)} = \sum_{l,k=1}^{\infty} A_{kl} b_k b_l \quad (4.61)$$

where

$$A_{kl} = \int_0^\infty \left[ kl \left( \frac{d\theta}{d\rho} \right)^2 \cos(k\theta) \cos(l\theta) + G(\rho) \sin(k\theta) \sin(l\theta) \right] \rho d\rho. \quad (4.62)$$

To establish radial stability of a solution, one has to determine the smallest eigenvalue  $\lambda_1$  of the symmetric matrix  $\mathbf{A}$  (4.62). If  $\lambda_1$  is positive, the solution  $\theta(\rho)$  is stable with respect to small radial perturbations. Otherwise it is unstable.

For our skyrmion solutions (Fig. 4.14 (c)) the eigenmode  $\xi_n(\rho)$  corresponding to the  $n$ th eigenvalue ( $\lambda_n$ ) consists mainly of the function  $\sin(n\theta(\rho))$ , with small admixtures of other harmonics. In particular, the eigenmode corresponding to the smallest eigenvalue  $\lambda_1$  can be written as

$$\xi_1(\rho) = \sin(\theta(\rho)) + \sum_{k=2}^{\infty} \varepsilon_k \sin(k\theta(\rho)), \quad (4.63)$$

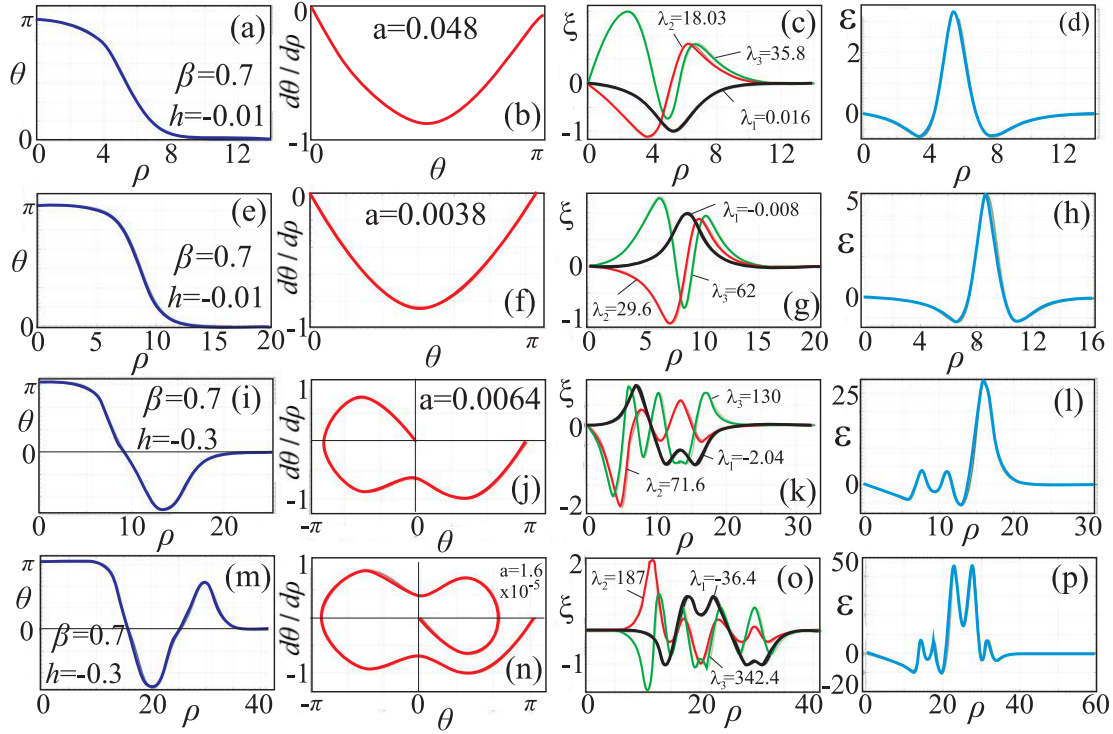


Figure 4.14.: Different types of isolated skyrmions which can be found among the solutions of the Euler equation (4.54) for negative magnetic field and easy axis uniaxial anisotropy. The first column (a), (e), (i), (m) shows the angular profiles  $\theta(\rho)$ . The second column (b), (f), (j), (n) exhibits the phase portraits. The eigenmodes plotted in the third column (c), (g), (k), (o) allow to deduce that all the solutions except skyrmions (c) are unstable. The distributions of the energy density for different types of localized solutions are plotted in the fourth column (d), (h), (l), (p).

where  $\varepsilon_k \ll 1$  in most cases. The function  $\xi_1(\rho)$  describes a displacement of the vortex front. Thus the lowest perturbation of the structure is connected with an expansion or compression of the profile. The calculations showed that in the region of existence of skyrmion solutions matrix (4.62) has only positive eigenvalues, and thus these solutions are radially stable.

The smallest eigenvalues of large  $\pi$ -vortices (Fig. 4.14 (e)) are always negative (Fig. 4.14 (g)). These vortices are unstable either with respect to infinite expansion of the core, or to a contraction into a common skyrmion [70]. The solutions of the spectral problem for vortices with nodes (Fig. 4.14 (k), (o)) reveals their instability with respect to perturbations that remove the energetically disadvantageous humps.

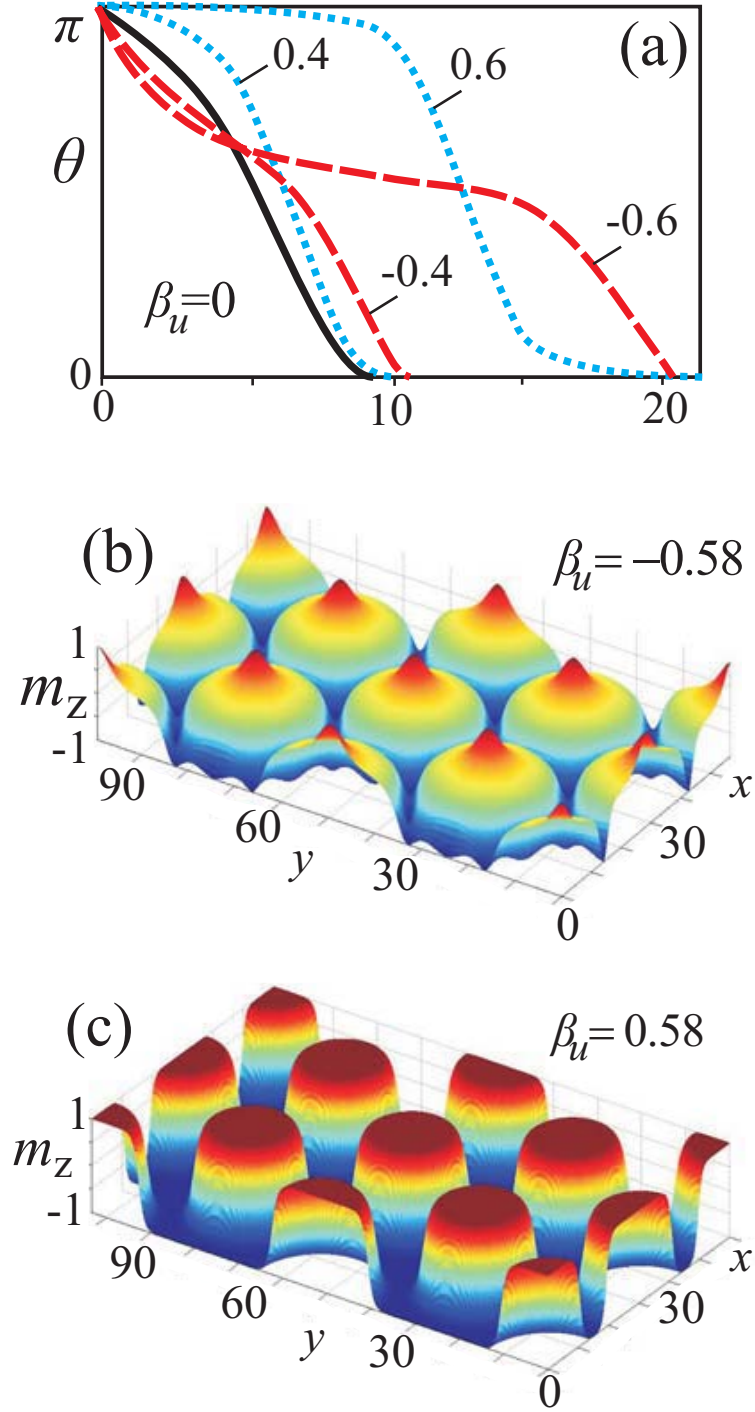


Figure 4.15.: Zero-field solutions of skyrmion lattices for easy-plane (b) and easy axis (c) uniaxial anisotropy shown as radial profiles  $\theta(\rho)$  (a) and surface plots of  $m_z$ -component of the magnetization.

### 4.7.3. Transformation of hexagonal skyrmion lattice under influence of uniaxial anisotropy

For  $h = 0$  the influence of uniaxial anisotropy on the skyrmion structure is rather weak for  $|\beta_u| < 0.25$ , but then it becomes pronounced up to the critical value  $|\beta_{cr}| = \pi^2/16$  where a second-order phase transition into the homogeneous state occurs.

Easy-plane type anisotropy,  $\beta_u < 0$ , leads to the compression of the regions close to the skyrmion core and boundary (Fig. 4.15 (a), red dashed lines in (c) and surface plot (b)). The easy-plane region of the lattice cell with  $\theta(x, y) = \pi/2$  grows rapidly approaching critical value  $\beta_{cr}$ .

Easy axis anisotropy,  $\beta_u > 0$ , on the contrary, expands the near-core region ( $\theta = 0$ ) and the skyrmionic outskirt with  $\theta = \pi$  (Fig. 4.15 (c), blue dotted lines in (a)).

### 4.7.4. Stabilization effect of uniaxial anisotropy on skyrmion states

For  $\beta_u = 0$  as it was noted in section 4.6, the conical phase is the globally stable state from zero field to the saturation field ( $0 < h < 0.5$ ), [99] (Fig. 4.12 interval  $(a - d)$ ). skyrmion lattices and helicoids are metastable solutions: skyrmions exist in the interval of magnetic fields from negative critical field with  $H_H/H_D = \pi^2/16 = 0.3084$  (Fig. 4.12 point  $b$ ) to positive critical field with  $H_S/H_D = 0.4006$  (Fig. 4.12 point  $c$ ); helicoids exist below the critical fields  $H_H/H_D$  (Fig. 4.12 point  $b$ ).

A sufficiently strong uniaxial anisotropy  $\beta_u$  suppresses the conical states. Cones can exist only in the triangular region  $(a - d - f)$ : within the region  $(a - d - B - A)$  they are thermodynamically stable and flip into the saturated state by the second-order phase transition at the critical line  $(d - B)$  when the conical structure closes. Within the region  $(a - A - B - f)$  the conical phase is a metastable state, at the lines  $(a - A)$  and  $(A - B)$  it discontinuously transforms into helicoids and skyrmions, respectively.

Modulated states with the propagation vectors perpendicular to the applied field (helicoids and skyrmion lattices) can exist even for larger values of uniaxial anisotropy (up to the point  $e$ ): helicoids occupy the area  $(a - b - D - e)$  with the line  $(b - D - e)$  of unwinding into homogeneous state, while skyrmions have the existing area  $(a - c - B - D - e)$  for positive fields and  $(a - b - e)$  for negative fields. The skyrmion lattice is the only modulated state that can exist in the triangular region  $(B - E - D)$ , and only helicoids exist in the region  $(D - F - e)$  (see inset (i) of Fig. 4.12).

By comparing energies of corresponding modulated phases (Fig. 4.16 (a)) one can conclude that skyrmions can be stabilized only with simultaneous influence of positive magnetic field and easy-axis uniaxial anisotropy. For easy-plane uniaxial anisotropy, the conical phase is always the global minimum of the system.

The skyrmion states are thermodynamically stable within a curvilinear triangle  $(A - B - D)$  with vertices  $(A) = (0.0166, 0.1197)$ ,  $(B) = (0.0907, 0.3187)$ , and  $(D) = (0.47, 0.05)$  (Fig. 4.12). The phase diagram from present rigorous solutions

very slightly differs from the calculations within the circular-cell approximation. Only point  $(A) = (0.0125, 0.1079)$  has the slightly different coordinates [XI].

The solutions for helicoids exist within area  $(a - A - D - e)$  with the line  $A - D$  of first-order phase transition into skyrmion lattice.

Thus, critical points  $A, B, D$  separate the phase diagram (Fig. 4.12) into three distinct regions with thermodynamical stability of each of considered phases. Moreover, one can introduce different regimes of uniaxial anisotropy:

(I) In the low anisotropy regime ( $\beta_u < \beta_{uA} = 0.0166$ ) only helical states are realized as thermodynamically stable phases: at the line  $a - A$  helicoids transform into cones;

(II) For  $\beta_{uA} < \beta_u < \beta_{uD} = 0.0907$  the skyrmion lattice becomes absolutely stable in a certain range of the applied field: at the line  $A - D$ , first, helicoid flips into skyrmion phase and then at the line  $A - B$  skyrmions transforms into cones;

(III) For  $\beta_{uD} < \beta_u < \beta_{ue} = 0.47$  there is only phase transition between helicoids and skyrmions at the line  $A - D$ ;

(IV) Finally for ( $\beta_{ue} < \beta_u < \beta_{cr}$ ) the helicoids are thermodynamically stable in the whole region where modulated states exist.

#### 4.7.5. Magnetization curves

Fig. 4.16 (b) shows the magnetization curves of all considered modulated structures for different values of uniaxial anisotropy.

For conical and helical phases, magnetization curves represent anhysteretic lines symmetric with respect to the field direction. In the region of helicoid existence, the magnetization changes linearly almost for all values of the applied magnetic field (except drastic increase near the field of saturation), but remains smaller in comparison to the linear magnetization increase of the conical phase.

Magnetization curves for skyrmion lattices bear pronounced hysteretic character with the mutual conversion of two critical fields  $h_H$  and  $h_S$  (points  $b$  and  $c$  in the Fig. 4.12). For instance, in large negative magnetic fields far beyond the disappearance of the honeycomb skyrmion texture, isolated skyrmions with the magnetization along  $z$  axis (with  $\theta(0) = 0$ ) can be nucleated. These skyrmions condense into a lattice in accordance with the physical principles described previously. In positive magnetic field this skyrmion lattice becomes a honeycomb structure and transforms into the homogeneous state. Thus, exemplified magnetization curve is composed from three subloops with remanent magnetization in zero magnetic field (Fig. 4.16 (b), inset).

### 4.8. Stabilization effect of exchange anisotropy on skyrmion states. Phase diagram of states

From the numerical investigation of Eq. (4.1) with an exchange anisotropy (Eq. (4.2)) I now show that skyrmion textures can be stabilized over conical phases even for relatively small values of  $b_{EA}$ .

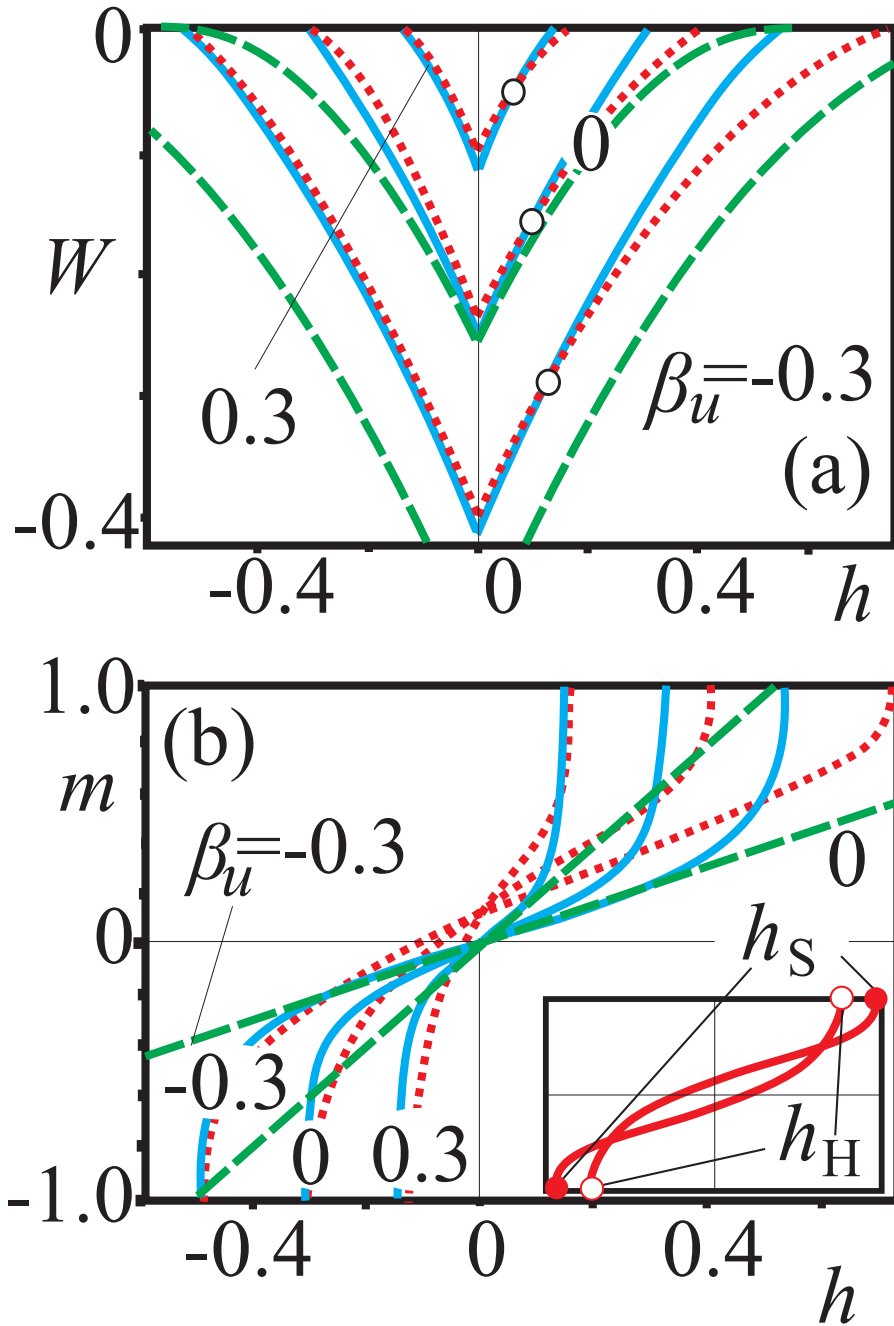


Figure 4.16.: (a) The energies of the skyrmion lattice (red dotted line), cone (dashed green lines), and helicoid (solid blue lines) with respect to the homogeneous state plotted as functions of magnetic field for different values of uniaxial anisotropy  $\beta$ . For  $\beta > 0.25$  only helicoids and skyrmions can be realized. (b) Magnetization curves of all modulated states for different values of uniaxial distortions  $\beta$ : green dashed lines for conical phase, red dotted lines for skyrmion lattice, and blue solid lines for helicoid. Inset shows hysteretic magnetization process for skyrmion lattice (see text for details).

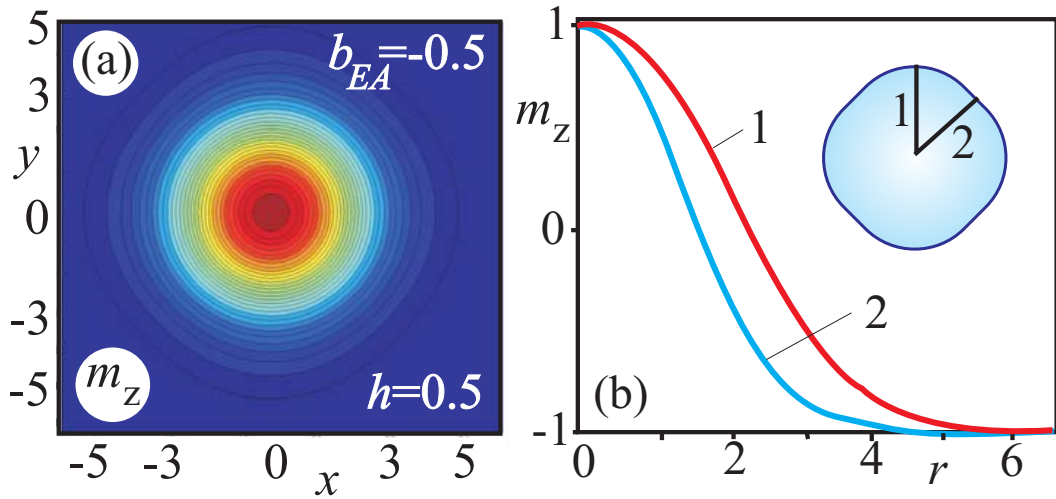


Figure 4.17.: (a) The contour plot for  $m_z$ -component of the magnetization in the isolated skyrmion for  $h = 0.5$ ,  $b_{EA} = -0.5$ . The isolated skyrmion acquires a square shape under influence of cubic exchange anisotropy. (b) Profiles  $m_z$  plotted in dependence on the spatial coordinate  $r$  in two cross-sections of the isolated skyrmion shown in inset.

The exchange anisotropy (see also section 1.2.1, Eq. (1.18)), on the contrary to uniaxial anisotropy (section 4.7.4), does not affect the one-dimensional conical phase, but deforms significantly the skyrmion states. With

$$b_{EA} < 0 \quad (4.64)$$

it supplies the skyrmions with additional negative energy density. For some critical value of  $b_{EA}^{(crit)}$  (I will distinguish between two values:  $b_{EA}^{(crit1)}$  is the critical value of exchange anisotropy when the skyrmion lattice can be stabilized in an applied magnetic field;  $b_{EA}^{(crit2)}$  is the value of EA when even in zero field the skyrmion lattice is the global minimum of the system; see phase diagram in Fig. 4.19) the amount of the additional energy is sufficient to make the skyrmions the global minimum of the system. In the following I will consider exactly this mentioned situation. The cones and skyrmions will be considered in the field applied along  $\langle 001 \rangle$  crystallographic direction.

Isolated skyrmions in the presence of exchange anisotropy assume a special character of the magnetization distribution: the double-twisted core retains its circular symmetry, but the boundary region is distorted into a square shape. It is clear that the numerical method in those cases, by the restriction to rectangular unit cells, is unable to reproduce the correct energy minimum if the lattice cell undergoes a distortion into parallelogram shape. I neglect this effect in the numerical calculations, because it is small. Thus, the solutions in Figs. 4.17, 4.18 and phase diagram in Fig. 4.19 have to be considered as semi-quantitative approximations. In Fig. 4.17 (a) such a square-like distribution of the magnetization is shown by contour plot of  $z$ -component of the magnetization for  $b_{EA} = -0.5$ ,  $h = 0.5$ . In Fig. 4.17 (b) the

profiles  $m_z = m_z(r)$  are clearly different along the two cuts of the isolated skyrmions (see inset in Fig. 4.17 (b)).

When isolated skyrmions condense into the lattice with the decreasing magnetic field, they are subject to the influence of two opposite mechanisms: from one side, they tend to form the densely packed lattice, from the other side however, the skyrmions try to keep this square symmetry imposed by the exchange anisotropy. As a result, the lattice of skyrmions is highly distorted. Rectangular lattices of this type have been calculated and relaxed according to the principles of section 4.5.1.

In Fig. 4.18 (b) I plotted the ratio  $R_1/R_2$  ( $R_1$  and  $R_2$  are the sizes of the elementary cell along two perpendicular directions  $x$  and  $y$  shown in Fig. 4.18 (a)) versus magnetic field for different values of the constant  $b_{EA}$ . As for perfect hexagonal lattice

$$\frac{R_1}{R_2} = 0.5773 \quad (4.65)$$

(Fig. 4.18 (b) stright line), the skyrmion lattice in the applied magnetic field shows the tendency of the deformation toward the square lattice with

$$\frac{R_1}{R_2} = 1 \quad (4.66)$$

(especially for large values of  $b_{EA}$ , see the last curve in Fig. 4.18 (b)). With increasing constant of exchange anisotropy the saturation field of the skyrmion lattice (that is the field when the lattice releases the free isolated skyrmions) also increases (dotted line in Fig. 4.18 (b) and the line  $h_S$  in Fig. 4.19).

In Fig. 4.19 I plotted the phase diagram for cones and skyrmions depending on the constant of exchange anisotropy  $b_{EA}$ . For

$$b_{EA} < b_{EA}^{(crit1)} = -0.13 \quad (4.67)$$

the spacious pocket shows up in the applied magnetic field with the thermodynamically stable skyrmions. For

$$b_{EA} < b_{EA}^{(crit2)} = -0.45 \quad (4.68)$$

even in zero magnetic field the skyrmions have the lowest energy of all modulated phases considered in this chapter.

## 4.9. Stabilization of skyrmion textures by cubic anisotropy

In the present section I explicitly refer to the cubic anisotropy that can favour skyrmions over conical phases for suitable orientation of the applied magnetic field and skyrmion axes (as well as propagation direction of the cones and helicoids) with respect to the easy anisotropy axes. Results of this section give straightforward recommendations how to make skyrmionic spin textures the thermodynamically sta-



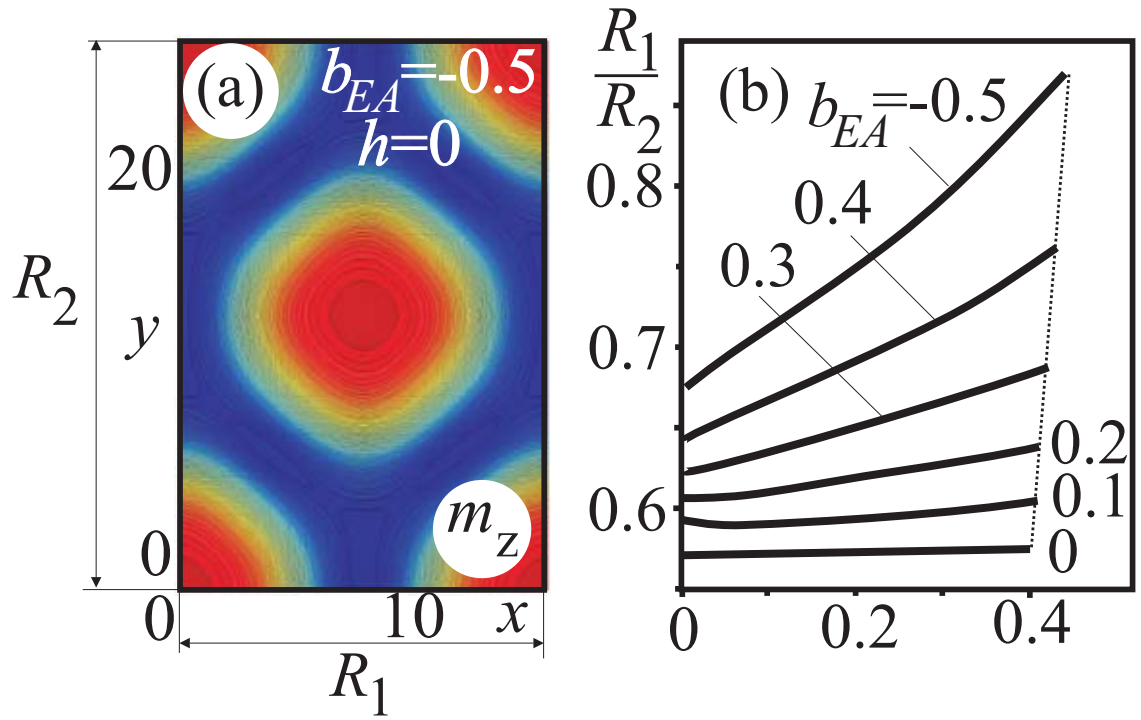


Figure 4.18.: (a) The contour plot for  $m_z$ -component of the magnetization in the skyrmion lattice for  $h = 0$ ,  $b_{EA} = -0.5$ . (b) The dependences of the ratios  $R_1/R_2$  on the applied magnetic field for different values of the exchange anisotropy  $b_{EA}$ . The perfect hexagonal lattice corresponds to the ratio  $R_1/R_2 = 0.5773$  (as for example for  $b_{EA} = 0$ ). The square lattice is characterized by  $R_1/R_2$  and can be realized for large values of  $b_{EA}$  in the field (as for example for  $b_{EA} = -0.5$ ).



ble state of the system. Calculations for all modulated phases have been obtained rigorously using methods of section 4.5.1.

The detailed analysis of chiral modulations in the presence of cubic anisotropy offers also practical recommendations to experimentalists under which circumstances to look for stable skyrmion states in bulk cubic helimagnets.

#### 4.9.1. Distorted conical phase in the presence of cubic anisotropy

As it was noted in section 4.7, uniaxial anisotropy along the propagation direction suppresses the conical phase for the values of the anisotropy coefficient  $\beta_u$  much smaller than it does for the skyrmion and helical phases (Fig. 4.12). After cones have been suppressed, skyrmions may become the thermodynamically stable state of the system in the applied magnetic field [XI].

Uniaxial anisotropy does not affect the ideal single-harmonic type of the magnetization rotation in the cone state, but just leads to the gradual closing of the cone. Cubic anisotropy, on the contrary, violates the ideal spin configuration of the conical phases: the magnetization deviates from the ideal conical surface trying to embrace the easy axes and to avoid the hard directions (Fig. 4.20).

Depending on the mutual arrangement of easy anisotropy axes and propagation direction of the cone the cubic anisotropy can either increase the energy of this phase or decrease it. Therefore, the rotation of the magnetization in the conical phase must be in tune with a complex landscape of the cubic anisotropy with various global and local minima.

The homogeneous states in a system with the cubic anisotropy in the applied magnetic field are described by the behaviour of the following energy functional (see also section 1.2.2 *B*):

$$\Phi(\Theta, \Psi) = k_c(m_x^2 m_y^2 + m_x^2 m_z^2 + m_y^2 m_z^2) - \mathbf{h} \cdot \mathbf{m}, \quad \mathbf{m} = (\sin \Theta \cos \Psi, \sin \Theta \sin \Psi, \cos \Theta) \quad (4.69)$$

where angles  $\Theta$  and  $\Psi$  define the orientation of the magnetization in the spherical coordinate system. I introduce angles  $\Theta$  and  $\Psi$  for the magnetization in the homogeneous state to distinguish them from the angles  $\theta$  and  $\psi$  characterizing the distribution of the magnetization in skyrmion states.

Depending on the values of the coefficient  $k_c$  and the components of magnetic fields different spatially homogeneous phases can be realized in the system. The basic principles how to handle such a type of functionals and to define the manifold of extrema in the applied magnetic field are given explicitly in chapter 2. Here, I will refer to the results of that chapter, while dealing with the modulated phases.

In the forthcoming calculations, the magnetic field  $h$  is considered to be applied along [001] crystallographic direction. The cases with  $k_c > 0$  and  $k_c < 0$  are discussed separately. Certainly, these two examples cannot address the problem of skyrmion stabilization over cones for random orientation of the magnetic field. But they represent the auxiliary cases consideration of which is instructive in the following.

#### A. Solutions for conical phase with $k_c > 0$ , $h||[001]$ .

In Fig. 4.22 I have plotted the energy density  $\Phi$  of Eq. (4.69) for some values of the applied magnetic field as surfaces in dependence on the angles  $\Theta$  and  $\Psi$  (Fig. 4.22 panel (a)), three-dimensional polar plots (Fig. 4.22 panel (b)), and their two-dimensional cuts (Fig. 4.22 panel (c)). Two-dimensional cuts of energy surfaces of panel Fig. 4.22 (a) are plotted in Fig. 4.21 (b), (c) as  $\Phi = \Phi(\Theta)$  for  $\Psi = 0$  and  $h = 0, 0.2$ . Fig. 4.21 (a) represents the astroid plotted according to the conventions of the chapter 2. The lability (orange) lines have been obtained by solving the system of equation,  $\Phi_\Theta = 0$ ,  $\Phi_{\Theta\Theta} = 0$  (see also Eqs. (2.8), (2.11)). The red lines are the lines of first-order phase transitions - the solutions with different orientations of the magnetization (global minima of the functional (4.69)) have equal energies along these lines (see also Eq. (2.13)). The present astroid corresponds to the two-dimensional case with  $\Psi = 0$ . The field applied along  $[001]$  crystallographic direction has only  $z$ -component, i.e. in the following  $h = h_z$ . Although, any other directions of the applied magnetic field can be considered. From all these graphs the comprehensive analysis of the magnetization rotation in the conical phase can be carried out.

For  $k_c > 0$  and  $h = 0$  the equilibrium states of the magnetization correspond to the easy axes of cubic anisotropy oriented along  $\langle 001 \rangle$  crystallographic directions (green arrows in Fig. 4.20 (a) and blue circle in Fig. 4.21 (b) marking the global minimum of  $\Phi(\Theta, \Psi)$ ). Maxima of the functional (4.69) are  $\langle 111 \rangle$  directions - the hard axes of cubic anisotropy (red arrows in Fig. 4.20 (a)). The equilibrium states of the magnetization in the homogeneous state have the orientations with  $\Theta = k\pi/2$ ,  $k = 0, 1, 2, \dots$ . In Fig. 4.22 (a), (b) these minima are marked by the yellow circles. In the panel (c) of Fig. 4.22 the orientations of the magnetization are shown by the blue arrows.

For  $h = 0$  the magnetization in the conical phase rotates in the plane (001) (brown plane in Fig. 4.20 (a)). While rotating, the magnetization leaves one energy minimum corresponding to  $\langle 001 \rangle$  directions and, rotating through the saddle point between hard axes  $\langle 111 \rangle$ , gets into another energy minimum with  $\langle 001 \rangle$  direction. The trace of the magnetization in the conical phase is shown by thick yellow line in Fig. 4.22 (a),(b).

In the applied magnetic field  $h||[001]$  the energy functional (4.69) has a global minimum corresponding to the state along the field and local minima for the states of the magnetization deflected from the plane (001). These minima disappear in the point  $A_1$  of the astroid (Fig. 4.21 (a)). The local minimum for the magnetization pointing against the field,  $\Theta = \pi$ , vanishes in the point  $A_2$ .

Rotation of the magnetization in the conical phase around the field sweeps the metastable states of Eq. (4.69) for  $h < h(A_1)$  and saddle points for  $h > h(A_1)$ . The conical phase becomes the metastable solution in comparison with the skyrmion lattice (see the phase diagram of states in Fig. 4.30 (a)). In a critical field the conical phase by a first-order phase transition flips into the homogeneous state. In Fig. 4.23 (a) I plotted the energy density of conical spiral with respect to the homogeneous state. The line  $\varepsilon$  in Fig. 4.30 (a) signifies the first-order phase transition when

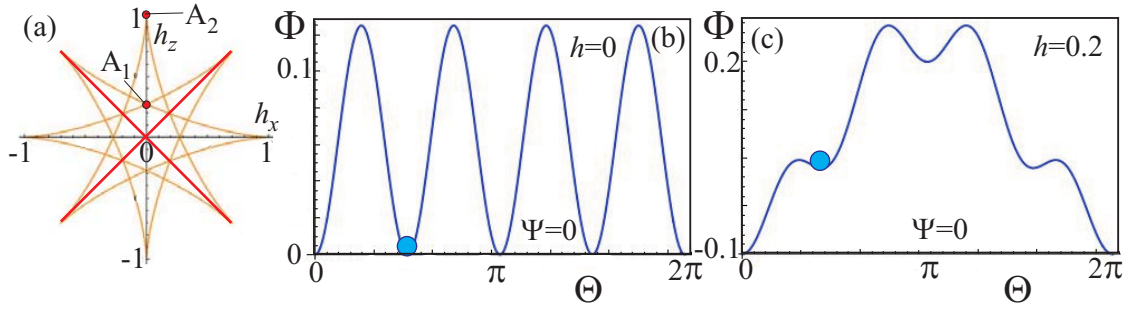


Figure 4.21.:  $k_c > 0$ ,  $h \parallel [001]$ . (a) The phase diagram in internal field components obtained according to the conventions of chapter 2. The orange lines are the lability lines bounding the region with plenty of local minima of energy functional (4.69). On the red lines two different angular phases have the same energy density, i.e. these are lines of the first-order phase transitions. (b), (c) show the energy density  $\Phi = \Phi(\Theta)$  (4.69) for fixed value of the azimuthal angle  $\Psi = 0$  and different values of the applied magnetic field  $h$ .

the energy difference of two phases is zero. The fields corresponding to jump of metastable conical phase with positive energy into homogeneous state are not shown on the phase diagram.

The magnetization curves for conical phase are depicted in Fig. 4.23 (b). From the behavior of all components of the magnetization (Fig. 4.23 (c)) in the applied magnetic field it can be concluded that the cones become more distorted in the high magnetic fields - the rotating magnetization tries to avoid the hard anisotropy axes  $\langle 111 \rangle$ .

#### B. Solutions for conical phase with $k_c < 0$ , $h \parallel [001]$ .

For  $k_c < 0$  and  $h = 0$  the equilibrium states of the energy functional (4.69) correspond to the easy axes of cubic anisotropy oriented along  $\langle 111 \rangle$  crystallographic directions (green arrows in Fig. 4.20 (b)). The angle of these easy direction with respect to the field  $h \parallel [001]$  is  $70.5^\circ$ . Maxima of the functional (4.69) are  $\langle 001 \rangle$  directions - the hard axes of cubic anisotropy (red arrows in Fig. 4.20 (b)).

The magnetization in the conical phase performs such a rotation to sweep the easy directions  $\langle 111 \rangle$  (Fig. 4.25 (a), (b)). Even in zero field the conical phase has non-zero component of the magnetization along the field (Fig. 4.20 (b)).

In the applied magnetic field the global minima of Eq. (4.69) gradually approach the field direction. For  $h > h(B_2)$  (see the astroid in Fig. 4.24 (a)) only the states with the magnetization along the field can exist. In the intermediate point  $B_1$  the local minima of those  $\langle 111 \rangle$  axes disappear that make angles more than  $90^\circ$  with the field, i.e. the easy axes under the brown plane in Fig. 4.20 (b).

In Fig. 4.26 (a) I plotted the energy density of the conical phase with respect to the homogeneous state for different values of cubic anisotropy  $k_c$  in dependence on the field  $h$ . The magnetization curves for conical phase (Fig. 4.26 (b)) display the

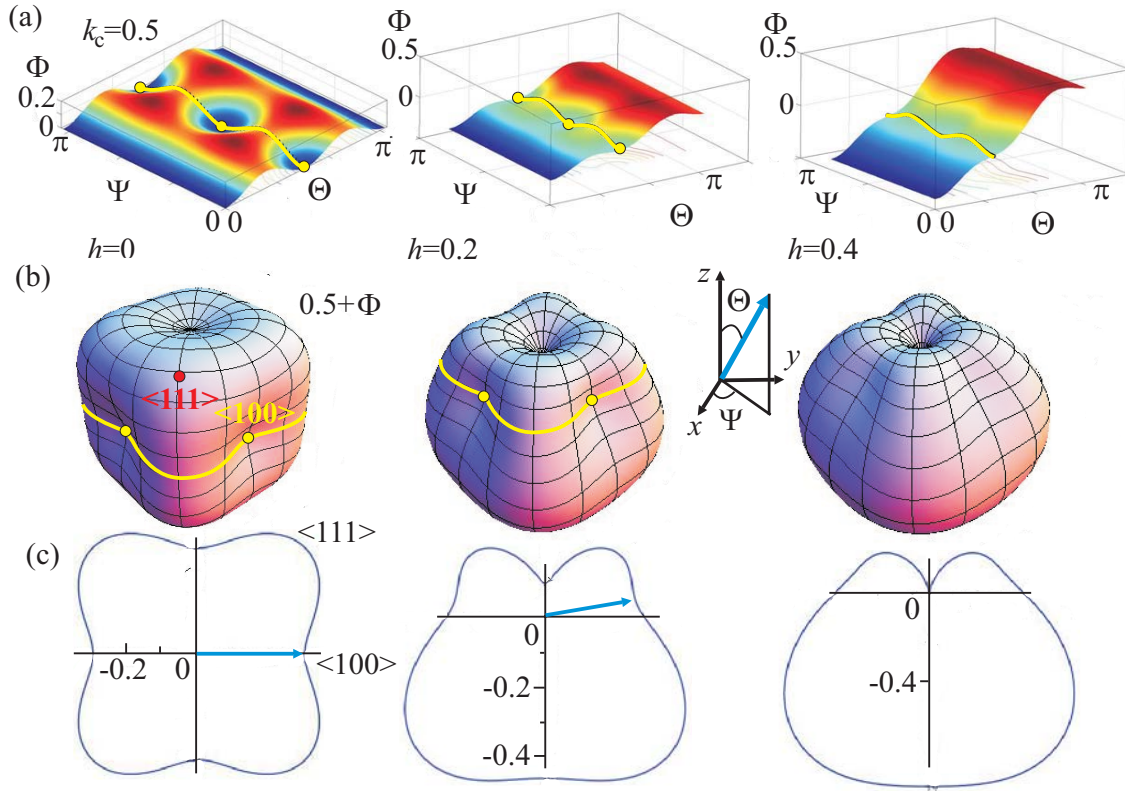


Figure 4.22.:  $k_c > 0$ ,  $h \parallel [001]$ . The energy density  $\Phi$  (4.69) plotted as two-dimensional surfaces in dependence on the angles  $\Theta$  and  $\Psi$  (a) and three-dimensional polar plots  $A + B\Phi$  (b) where  $A$  and  $B$  are suitable scaling factors. In the present case  $A = 0.5$ ,  $B = 1$ . The cuts of graphs in panel (b) with  $\Psi = 0$  are shown in panel (c). Path of the rotating magnetization in the conical phase is imaged by the yellow lines with yellow circles being the minima of Eq. (4.69). In the applied magnetic field the states of the magnetization in the cone correspond only to the local minima.

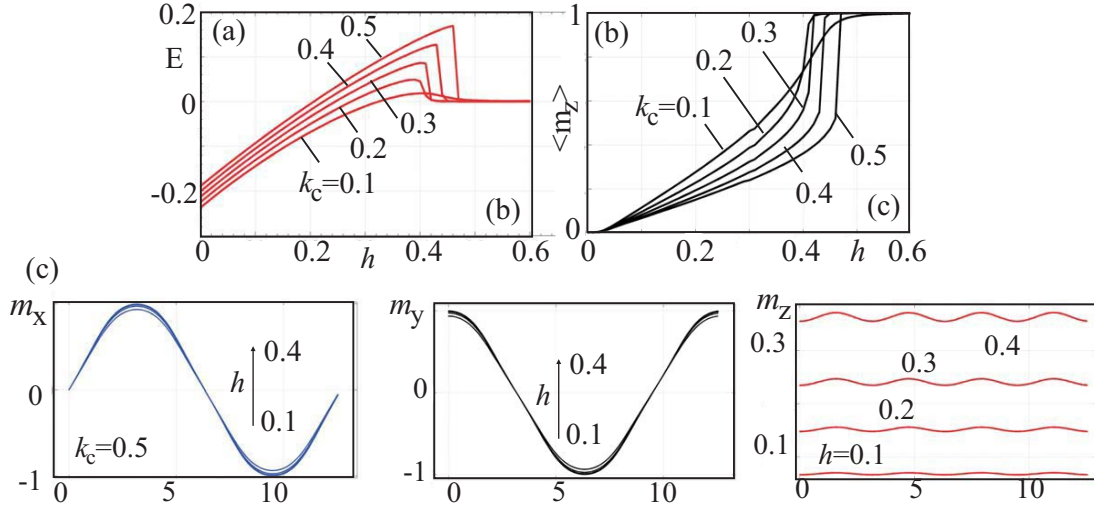


Figure 4.23.:  $k_c > 0$ ,  $h \parallel [001]$ . Solutions for the conical phase: (a) energy density of the conical phase with respect to the homogeneous state in dependence on the applied magnetic field  $h$  for different values  $k_c$  of the cubic anisotropy; (b) magnetization curves showing the component of the magnetization along the field,  $m_z$ . After reaching the hard cubic axes  $\langle 111 \rangle$  the magnetization jumps into the homogeneous state. (c) the components of the magnetization plotted along the propagation direction for different values of the applied magnetic field.

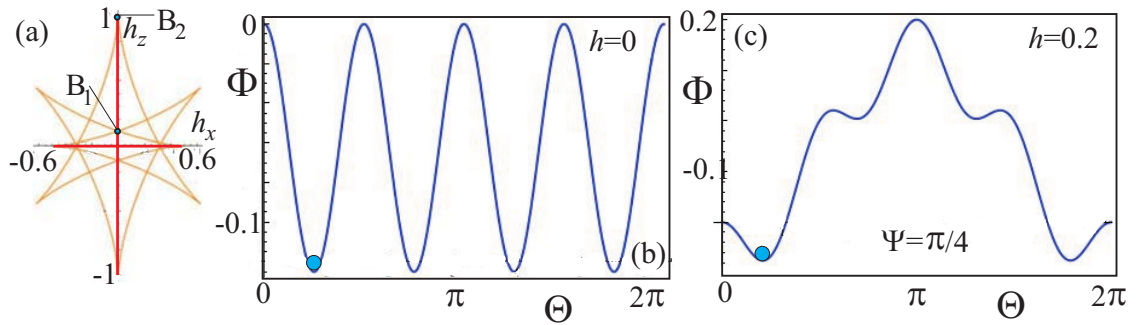


Figure 4.24.:  $k_c < 0$ ,  $h \parallel [001]$ . (a) Astroid obtained according to the rules of chapter 2. The red lines are the lines of the first-order phase transitions. The orange lines (lability lines) bound the region with a multitude of local minima. Magnetic field is applied along  $z$ -direction, i.e.  $h = h_z$ . (b), (c) functional  $\Phi = \Phi(\Theta)$  plotted with fixed azimuthal angle  $\Psi = \pi/4$ . The homogeneous states (global minima of Eq. (4.69)) swept by the rotating magnetization in the conical state are marked by blue circles in (b) and (c).



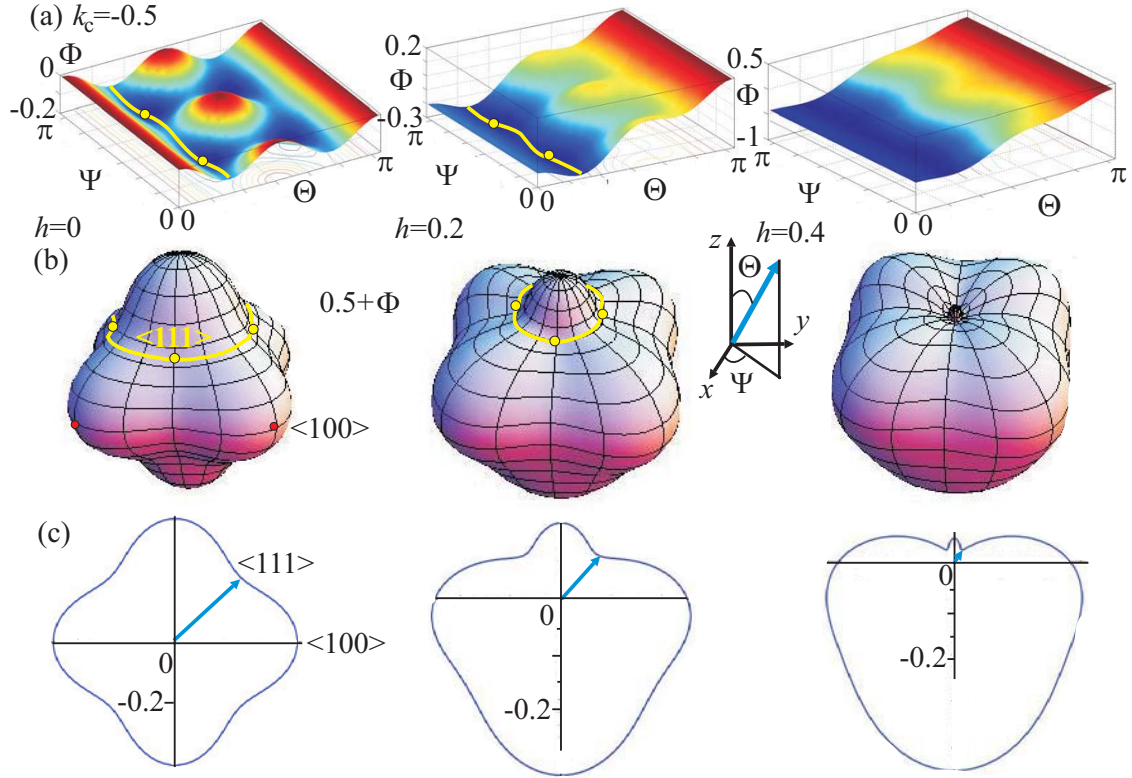


Figure 4.25.:  $k_c < 0$ ,  $h \parallel [001]$ . The energy density (4.69) plotted as two-dimensional surfaces in dependence on the angles  $\Theta$  and  $\Psi$  (a) and three-dimensional polar plots (b). The cuts of panel (a) with  $\Psi = \pi/4$  are shown in panel (c). Path of the rotating magnetization in the conical phase is shown by the yellow lines with yellow circles being the minima of Eq. (4.69). In the applied magnetic field the magnetization in the cones rotates to sweep the global minima of Eq. (4.69).



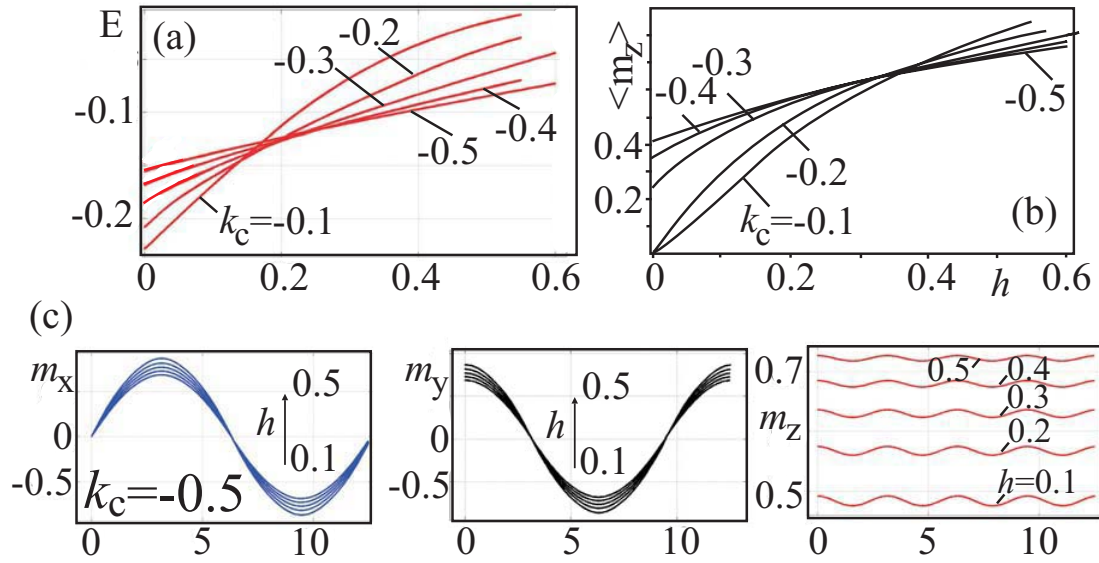


Figure 4.26.:  $k_c < 0$ ,  $h \parallel [001]$ . Solutions for the conical phase: (a) energy density of the conical phase with respect to the homogeneous state in dependence on the applied magnetic field  $h$  for different values  $k_c$  of the cubic anisotropy; by the second-order phase transitions cones transform into the homogeneous state with the magnetization along the field. (b) Magnetization curves showing the component of the magnetization along the field,  $m_z$ . Even in zero magnetic field the magnetization has non-zero  $z$ -components. (c) The components of the magnetization plotted along the propagation direction for different values of the applied magnetic field.

non-zero  $m_z$ -component of the magnetization in zero field as described earlier. From the behavior of all components of the magnetization (Fig. 4.26 (c)) in the applied magnetic field it can be concluded that the cones undergo the greatest deformation of their  $m_z$ -component in zero magnetic field.

#### 4.9.2. Distorted helicoid in the presence of cubic anisotropy

In the section 4.3.1 I introduced the following definition for the helicoid: helicoid is a spiral state with the propagation direction perpendicular to the applied magnetic field. (Fig. 4.1 (a)). In the presence of cubic anisotropy such a definition must be generalized to include arbitrary orientations of the applied magnetic field and propagation directions of helicoids.

Both the spin arrangements and the corresponding propagation directions in the helicoid are found to be extremely sensitive to the orientation and strength of the applied magnetic field as well as to the sign and value of the anisotropic constant  $k_c$ . Perturbations of the uniform rotation for the helicoid are related to the shape of potential profiles of homogeneous states (Figs. 4.22, 4.24, 4.25).

In a general case, there is a multitude of solutions for helicoids characterized by

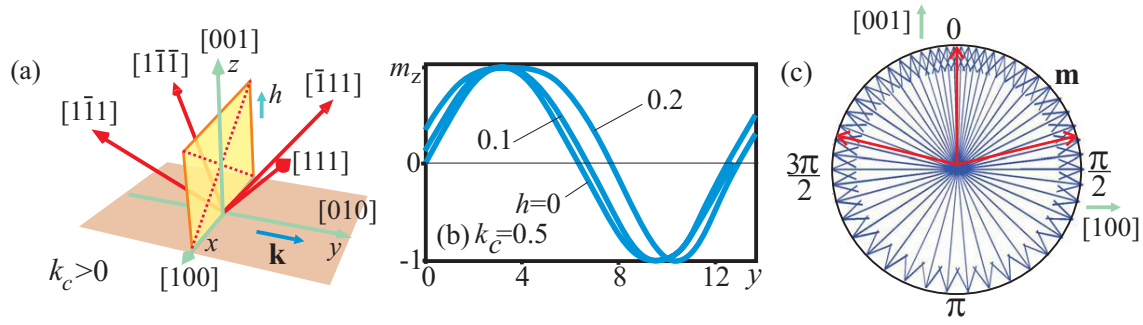


Figure 4.27.:  $k_c > 0$ ,  $h \parallel [001]$ . Solutions for the helicoid: (a) sketch showing the plane of the magnetization rotation (yellow plane), easy (green arrows) and hard (red arrows) directions of the cubic anisotropy, the directions of the applied magnetic field  $h$  and the helicoid propagation direction  $\mathbf{k}$ . The projections of hard anisotropy axes onto the plane of rotation are shown by dotted red lines. (b)  $m_z$ -component of the magnetization in dependence on the coordinate  $y$  for different values of the field. With increasing magnetic field parts of the curves with the magnetization along the field widen. (c) Polar plot for the component of the magnetization perpendicular to  $\mathbf{k}$  for  $h = 0.2$ . The densest distribution of the magnetic vectors corresponds to  $\theta = 0$  although the local minima can be distinguished also for  $\theta = \pm\pi/2$ .

variable directions of propagation vectors. In the following, helicoids are defined as states with vectors  $\mathbf{k}$  oblique to the field. Conical phase (see section 4.9.1) in the present definition can be considered as one of the helicoids with the propagation direction along the field.

#### A. Solutions for helicoids with $k_c > 0$ , $h \parallel [001]$ .

For the case with  $k_c > 0$ ,  $h \parallel [001]$  the helicoids propagate in the plane  $(001)$  along one of the easy axes  $\langle 001 \rangle$  of cubic anisotropy (Fig. 4.27). Magnetic field is applied perpendicularly to the vector  $\mathbf{k}$  as it was considered for helicoids of isotropic functional  $W_0$  (section 4.3.1). Deviation of the propagation direction from the plane  $(001)$  as well as from the easy cubic axis in the plane increases the energy of the helicoid.

The plane of the magnetization rotation in the helicoid contains the easy anisotropy axes  $\langle 001 \rangle$  (green arrows in Fig. 4.27 (a) including the easy axis  $[001] \parallel h$ ) and the projections of the hard anisotropy direction  $\langle 111 \rangle$  onto this plane (red dotted lines in Fig. 4.27 (a)). Already for  $h = 0$  the helicoid accomplishes an inhomogeneous rotation disturbed by anisotropic interactions.

Increasing magnetic field leads to slow rotation of the magnetization in the vicinity of the axis  $[001]$  and acceleration of the rotation for the directions opposite to the field. In Fig. 4.27 (c) the polar plot is shown for the component of the magnetization perpendicular to the vector  $\mathbf{k}$ . Distribution of the magnetic moments is densest for  $\theta = 0$ . The angular phases obtained by deflecting the inplane magnetization

with  $\theta = \pm\pi/2$  correspond to the local minima of Eq. (4.69) and also lead to the denser distribution of the magnetic moments (see Fig. 4.22). Described solutions are depicted in Fig. 4.27 (c) by red arrows.

In Fig. 4.27 (b) I have plotted  $m_z$  component of the helicoid in dependence on the spatial coordinate  $y$  along the propagation direction for different values of the applied magnetic field. For some critical value of the field the helicoid transforms into the homogeneous state with the magnetization along the field. This transition is signalled by an unlimited growth of the period for the helicoid and leads to the set of isolated domain walls with infinite separation between them. The line of these critical fields on the phase diagram (Fig. 4.30 (a)) has a label  $\eta$  (green dashed line). The energy density of the helicoid with respect to the homogeneous state is shown in Fig. 4.30 (b) (solid blue line).

#### *B. Solutions for helicoids with $k_c < 0$ , $h||[001]$ .*

For the case  $k_c < 0$ ,  $h|| < 001 >$  the energy of the helicoid must be minimized with respect to the orientation of the wave vector  $\mathbf{k}$  relative to the applied magnetic field. The equilibrium solutions for helicoids are directly related to the energy landscape of cubic anisotropy (see Fig. 4.25).

For  $h = 0$ , the propagation direction of a helicoid was found to point to  $<111>$  crystallographic directions. For definiteness in the following calculations, I assume  $\mathbf{k}||[111]$ ,  $\mathbf{h}||[00\bar{1}]$  (see sketch in Fig. 4.28 (a)). The magnetization in the helicoid rotates in the plane  $(11\bar{2})$  (grey shaded triangle in Fig. 4.28 (a)). The plane of the magnetization rotation contains the projections of easy anisotropy axes  $<111>$ . I marked the easy directions under the plane of rotation by blue color and above the plane - by red. Also all easy directions have been numbered. Rotating magnetization deviates from the plane  $(11\bar{2})$  and sweeps these easy axes. The  $m_z$ -component of the magnetization shown in Fig. 4.28 (b) is negative for the crystallographic directions  $[\bar{1}\bar{1}\bar{1}]$  (marked as 1),  $[1\bar{1}\bar{1}]$  (3),  $[\bar{1}\bar{1}1]$  (5), and positive for  $[11\bar{1}]$  (2),  $[\bar{1}11]$  (4),  $[\bar{1}1\bar{1}]$  (6).

For  $h = 0$  the helicoid has lower energy in comparison with the cones with  $\mathbf{k}||[00\bar{1}]$ . While conical phase is able to sweep four easy anisotropy axes (see section 4.9.1 *B*), the rotating magnetization in the helicoid meets six easy anisotropy directions on its way (Fig. 4.28 (a)).

Applied magnetic field  $\mathbf{h}||[00\bar{1}]$  leads to the significant distortions of the helicoid structure. The field destroys the degeneracy of energy minima of cubic anisotropy: easy axes 1,2, and 3 have lower energy in comparison with metastable directions 4, 5, and 6. During this complex magnetization process the wave vector  $\mathbf{k}$  of the helicoid is directed along the metastable minimum  $[111]$  with slight change of its orientation in the applied magnetic field. The distribution of the magnetic vectors in the plane perpendicular to the propagation direction becomes denser in the lower part of the polar plot in Fig. 4.28 (d).

In Fig. 4.30 (d) I plotted the energy density of the cone (blue line) and helicoid (green line) versus  $h$ . For some critical value of the magnetic field (point  $\beta$  in Fig. 4.30 (d)) conical phase becomes energetically more favourable than the helicoid.

This point indicates the first-order phase transition between these one-dimensional modulated phases. The critical fields have been plotted in the phase diagram (Fig. 4.30 (c)) for different values of the cubic anisotropy constant  $k_c$ . Note, that in the present geometry the cone sweeps easy axes 1,2,3 as well as the axis  $[111]$  perpendicular to the plane of rotation of the helicoid. As soon as the metastable minima 4,5,6 disappear, the helicoid transforms into the conical phase (see the third plot in panel (a) of Fig. 4.28).

### 4.9.3. Transformation of the hexagonal skyrmion lattice in the presence of cubic anisotropy

Alongside with the drastic influence on the conical phases and helicoids (see sections 4.9.1 and 4.9.2), cubic anisotropy distorts significantly skyrmion states: the symmetry of the skyrmion cores reflects the underlying energy landscape of the cubic anisotropy (Figs. 4.22, 4.25) and undergoes the respective transformation (Fig. 4.29).

In the calculations according to the methods of section 4.5.1, the direction of the skyrmion axes have been tuned with respect to the field and easy anisotropy axes in the search of the states with the lowest energy (the same minimization of the energy had been done in the section 4.9.2 *B* for helicoids). For  $k_c > 0$  the equilibrium position of the skyrmion axis is codirectional with the applied magnetic field. For  $k_c < 0$  the skyrmion axis has been found to follow the global minimum of the cubic anisotropy (Eq. (4.69)), i.e. for  $h = 0$  the skyrmion axis is directed along the easy cubic axes  $\langle 111 \rangle$ , but in the field it starts to move toward the field.

In Fig. 4.29 (a)-(c) I have plotted the contour plots for  $m_z$ -components of the magnetization in skyrmion lattices for both signs of the cubic anisotropy  $k_c$ . In Fig. 4.29 (a) and (b) the axes of skyrmion lattices are directed along the field; the cores of skyrmions become square shaped with the tendency either to elongate or to shorten along particular directions.

The skyrmion lattice of Fig. 4.29 (a) can be stabilized only in the applied magnetic field. The field localizes the skyrmion cores and prevents skyrmions from the transformation into helicoids. For the field lower than some critical value (in Fig. 4.30 (b) this field is marked by  $\gamma_0$ ) the easy axes of the cubic anisotropy in the plane of the skyrmion lattice induce the instability of skyrmions with respect to helicoids. By numerical means used in the present thesis it is hardly possible to obtain the solutions of the skyrmion lattice for zero and small magnetic fields. The easy directions of the cubic anisotropy are shown by the white arrows in Fig. 4.29 (a).

For another critical value of the field the skyrmion lattice releases the free isolated skyrmions. In Fig. 4.30 (a) these fields are depicted as the line  $\gamma$  (dashed red line). The energy density of skyrmion lattice is plotted in Fig. 4.30 (b) (red solid line for  $k_c = 0.5$ ). With increasing value of the constant  $k_c$  the interval between two critical fields (i.e. between the points  $\gamma_0$  and  $\gamma$ ) decreases. For the constants  $k_c > k_c(E)$  (Fig. 4.30 (a)) the skyrmion lattice is highly unstable.

The skyrmion lattice plotted in Fig. 4.29 (b) has the larger energy in comparison

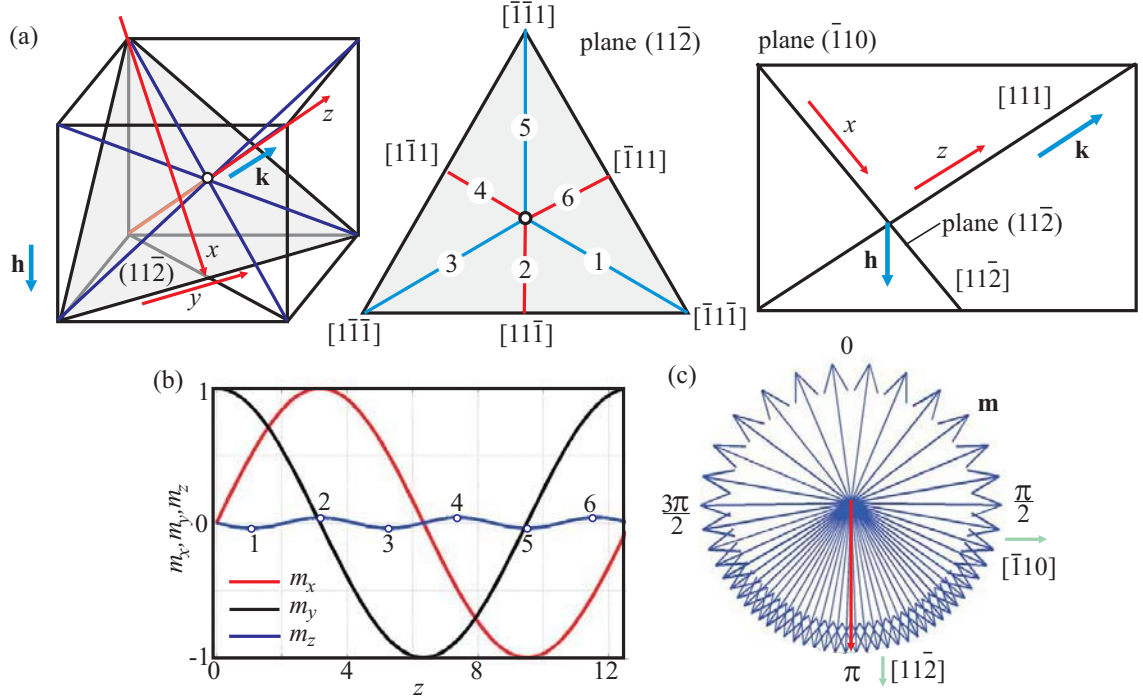


Figure 4.28.:  $k_c < 0$ ,  $h \parallel [00\bar{1}]$ . Solutions for the helicoid with  $\mathbf{k} \parallel [111]$ : (a) sketch showing the plane of the magnetization rotation (grey triangular plane), easy directions of the cubic anisotropy (blue straight lines), the directions of the applied magnetic field  $\mathbf{h}$  and the helicoid propagation direction  $\mathbf{k}$ , and the coordinate axes (red arrows) related to the helicoid. The projections of the easy anisotropy axes onto the plane of the magnetization rotation are numbered and marked by blue (the axes are above the plane) and red (the axes are under the plane) color. (b)  $m_x$  (red line),  $m_y$  (black line), and  $m_z$  (blue line) components of the magnetization in dependence on the coordinate  $z \parallel \mathbf{k}$  for  $h = 0$ . The maxima and minima of the  $m_z$ -component correspond to the deviations toward easy anisotropy directions. (c) Polar plot for the component of the magnetization perpendicular to  $\mathbf{k}$  for  $h = 0.2$ . The densest distribution of the magnetic vectors corresponds to the lower part of the plot: the rotating magnetization spans the easy direction in the direct vicinity of the applied magnetic field.



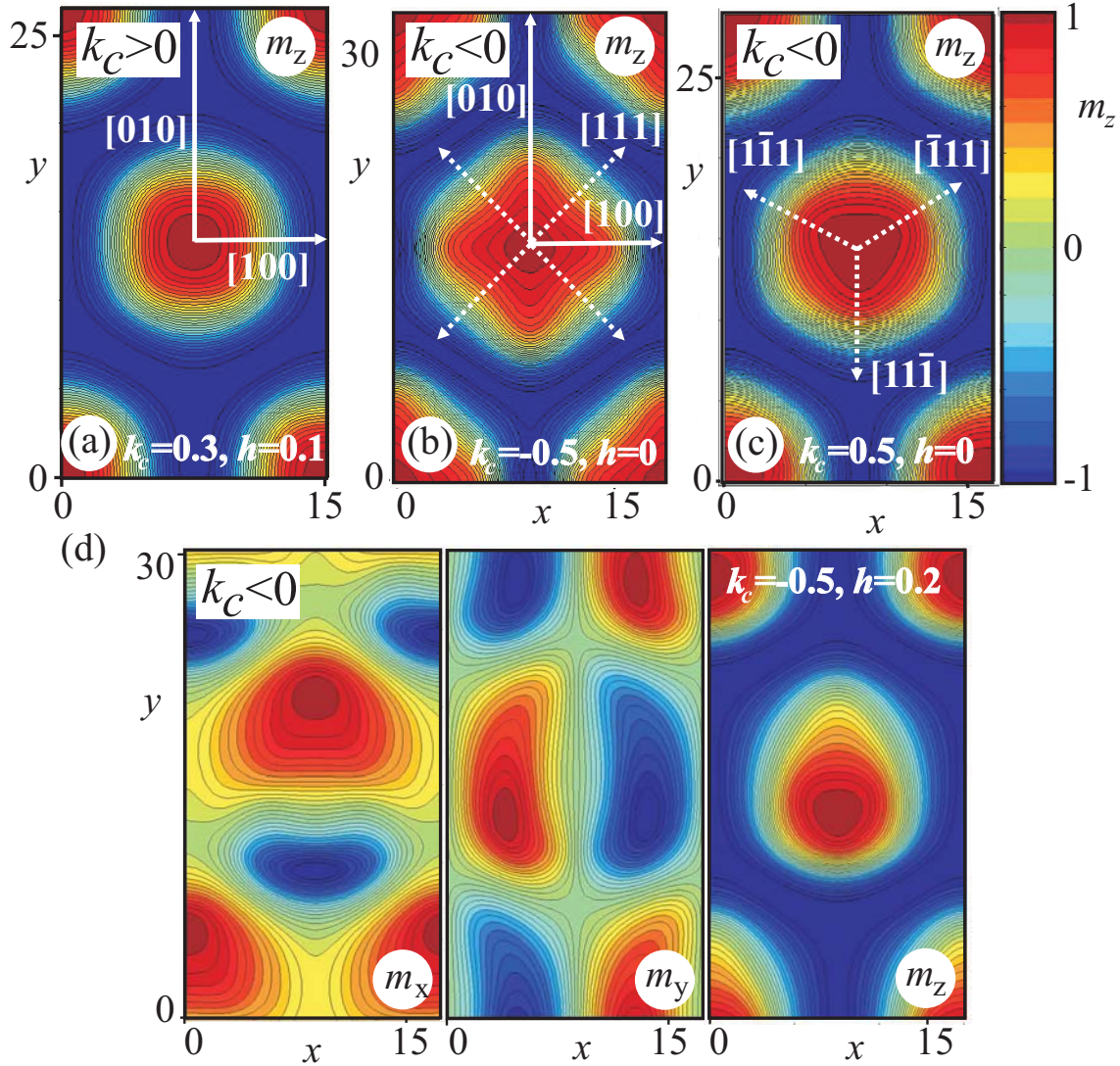


Figure 4.29.: Contour plots for components of the magnetization in skyrmion lattices for both signs of the cubic anisotropy constant  $k_c$ : (a), (b) contour plots for  $m_z$ -components of the magnetization with the axis of the skyrmion lattices directed along the field, i.e. along  $[001]$ . Axes  $\langle 100 \rangle$  of cubic anisotropy are shown as white arrows. In (a) with  $k_c > 0$ , these axes are easy directions, whereas in (b) with  $k_c < 0$  - they are hard anisotropy axes. (c) Contour plot for  $m_z$ -component of the magnetization in the skyrmion lattice with the axis along  $[111]$  crystallographic direction. Dotted white arrows indicate the projections of anisotropy axes  $\langle 111 \rangle$  onto the plane of skyrmion lattice. (d) Contour plots for  $m_x$ ,  $m_y$ , and  $m_z$  components of the magnetization in a case when axes of skyrmions do not point to the equilibrium state of the functional (4.69). The cores of the skyrmions are shifted from the center of the lattice cell, but the lattice retains the stability against transformation into helicoids.

with the lattice directed along the  $\langle 111 \rangle$  crystallographic directions (Fig. 4.29 (c)). White (solid) arrows in this case with  $k_c < 0$  indicate hard axes of the cubic anisotropy. White dotted arrows are projections of the easy axes  $\langle 111 \rangle$  onto the plane (001) of the skyrmion lattice. In the present calculations such a lattice was used as a cross-check of calculations: the energies of two skyrmion lattices coincide, when the angular phases of the functional (4.69) are aligned along the field.

In Fig. 4.29 (c) the axis of the skyrmion lattice points to the crystallographic direction  $[111]$ . In this case the dotted white arrows show the projections of the cubic easy axes  $\langle 111 \rangle$  onto the plane  $(11\bar{2})$ . The core of the lattice acquires the shape of a curvilinear triangle. With increasing magnetic field such a lattice gradually rotates keeping its axis parallel to an equilibrium state of the energy functional (4.69). In the panel (d) of Fig. 4.29 I plotted the skyrmion lattice in the applied magnetic field, but with the axis directed along  $[111]$  axis. The figure shows that the skyrmion lattice is essentially robust against the transformation into the helicoid even if its core is displaced from the central position in the lattice cell. Energy density of the skyrmion lattice is plotted in Fig. 4.30 (d) (red solid line). The skyrmions are only metastable states in comparison with cones and helicoids.

#### 4.9.4. The phase diagrams of states in the presence of magnetocrystalline cubic anisotropy

The phase diagrams of states for both signs of cubic anisotropy constant  $k_c$  and the field applied along  $[001]$  are plotted in Figs. 4.30 (a), (c). Further, I analyse each of these phase diagrams and give some qualitative recommendations as far the thermodynamical stability of skyrmions with respect to conical phases is concerned.

##### *A. Phase diagram of states for $k_c > 0$ , $\mathbf{h} \parallel [001]$ .*

Cones as modulated states with negative energy relative to the homogeneous state exist below the line d-A-B-C (dashed blue line  $\varepsilon$  in Fig. 4.30 (a)). At this line cones flip into the saturated state by a first-order phase transition as described in section 4.9.1 A. Nevertheless, above this line cones still exist as states with positive energy. Only within the region filled with a blue color (0-d-A-D or region I) they are thermodynamically stable. In the remaining part the cones are metastable states. At the lines  $\nu$  (red solid line A-D in Fig. 4.30 (a)) and  $\kappa$  (green solid line) cones transform discontinuously into skyrmions (red-colored area II) and helicoids (green colored region III), respectively. Dotted lines mark the phase transitions between the metastable states:  $\delta$  is the line of first-order phase transition between skyrmions and helicoids (blue line a-D), for  $k_c = 0$  the point 'a' corresponds to this transition in the isotropic case; line D-B (green dotted line) stands for the transition between metastable cones and helicoids in the region where skyrmions are thermodynamically stable states; line D-C (dotted red line) is the line of the first-order phase transition between skyrmions and cones in the region of stability of helicoids.

As it is seen from the phase diagram (Fig. 4.30 (a)), the skyrmion states are thermodynamically stable within a curvilinear triangle (A - D - E) with vertices

(A) = (0.047, 0.379), (D) = (0.233, 0.264), and (E) = (0.613, 0.203)). At the line D-E they transform into helicoids, and at c-A-E-C (red dashed line  $\gamma$ ) - into the homogeneous state with the magnetization along the field. (C)=(0.651,0.176) is the point of intersection of the lability lines for cones (blue dashed lines) and skyrmions; in the point E the lability lines for skyrmions and helicoids cross each other. Point B has the coordinates (0.269,0.253). For  $k_c > k_c(C)$  helicoids and cones can exist for much larger values of the applied magnetic field than skyrmions; skyrmions undergo the elongation into the helicoids in this region (see also section 4.9.3).

The solutions for helicoids exist below the line b-B-E (green dashed line) where they turn into the homogeneous state. In the region III of the phase diagram (Fig. 4.30 (a)) helicoids are the thermodynamically stable states of the system. Due to the strong influence of the cubic anisotropy on the conical phase, helicoids can exist in higher fields than cones for  $k_c > k_c(B)$ .

The present phase diagram has been built by comparing energies of corresponding modulated phases. In Fig. 4.30 (b) the energies of the skyrmion lattice (red line), helicoid (green line), and cone (blue line) are plotted in dependence on the applied magnetic field  $h$  for  $k_c = 0.4$ . In zero field the conical phase is the state with the minimal energy. Then, in the point  $\kappa$  the cone transforms into the helicoid. Points  $\delta$  and  $\nu$  indicate the transitions to skyrmions from helicoids and to skyrmions from cones, respectively. These transitions demand the closer look at them. For  $k_c = 0.3$ ,  $h(\delta) < h(\nu)$ , but for  $k_c = 0.4$ ,  $h(\delta) < h(\nu)$  (see inset of Fig. 4.30 (b)). For  $h < h(\gamma_0)$  the skyrmion lattice may elongate into the helicoid (see section 4.9.3 for details). The skyrmion cores become instable with respect to elliptic distortions. Numerically, such a transformation is accompanied by the drastic increase of the grid spacings ( $\Delta_y \gg \Delta_x$  or  $\Delta_x \gg \Delta_y$ ) along one of the spatial directions  $y$  or  $x$  (see section 4.5.1 for the introduction into the numerical recipes of the present calculations).

#### B. Phase diagram of states for $k_c < 0$ , $\mathbf{h}||[001]$ .

For  $k_c < 0$  and the field  $\mathbf{h}||[001]$  only one-dimensional chiral modulations are present in the phase diagram as thermodynamically stable states of the system (Fig. 4.30 (c)). At zero field the helicoid (green line) has lower energy in comparison with the cone (blue line in Fig. 4.30 (d)). The reason of this is explicitly explained in the section 4.9.2 B: rotating magnetization in the helicoid sweeps 6 easy axes of cubic anisotropy, while the conical phase - only 4. The situation is drastically changed in the applied magnetic field: point  $\beta$  signifies transformation of the helicoid into the cone by the first-order phase transition.

Skyrmions are metastable solutions. Points  $\alpha_1$  and  $\alpha_2$  of the transitions to skyrmions from cones and to skyrmions from helicoids are characterized by the higher energy densities comparing with the energy of the global helical and conical phases, respectively. Therefore, these transitions are hidden. In this connection the influence of the higher-order anisotropy terms may have significant influence on the skyrmion states.

#### C. General remarks how to stabilize skyrmion states in the presence of cubic



### *anisotropy*

Considered phase diagrams of states (Figs. 4.30 (a), (c)) allow to deduce some qualitative recommendations how to stabilize skyrmions over conical phases in the presence of cubic anisotropy. Such phase diagrams, however, cannot be considered as complete, since I did not consider possible three-dimensional states realized in the system. Moreover, competition of different small anisotropic contributions will also distort the stability regions of different modulated phases.

(i) As it was concluded in section 4.9.1, cubic anisotropy effectively suppresses conical phases for  $k_c > 0$  and  $\mathbf{h}||[001]$ . Rotating magnetization of the conical phase in this case sweeps the metastable directions of the energy functional (4.69). The same effect may be achieved for the field  $\mathbf{h}|| < 111 >$  and  $k_c < 0$ . In this case, the hard axes  $< 100 >$  of the cubic anisotropy impair the ideal harmonic rotation of the magnetization in the conical phase. The phase diagram of states looks qualitatively similar to the phase diagram in Fig. 4.30 (a), but with slightly different coordinates for all critical points. Therefore, the suppression of the cone depends on the sign of the cubic anisotropy constant  $k_c$ : for  $k_c > 0$  the field must be applied along  $< 001 >$ , for  $k_c < 0$  - along  $< 111 >$ . The cubic anisotropy  $k_c$  must be larger than some threshold value corresponding to the point A in Fig. 4.30 (a).

For  $k_c < 0$ ,  $\mathbf{h}||[001]$ , and  $h > h(\beta)$ , the conical phase is the thermodynamically stable state of the system (Fig. 4.30 (c)). The rotating magnetization in a cone sweeps the global minima of energy functional (4.69). The same situation will be also realized for  $k_c > 0$  and  $\mathbf{h}|| < 111 >$ , when the magnetization spans easy anisotropy axes  $< 100 >$ . The skyrmions will form only metastable states in these situations.

(ii) At the same time the constant  $k_c$  of cubic anisotropy must not be larger than the critical value  $k_c(E)$ . Otherwise, the skyrmions will tend to elongate into spirals (see for details section 4.9.3). Such an instability of skyrmions is related to the easy anisotropy axes  $< 100 >$  in the plane of the skyrmion lattice (Fig. 4.29 (a)). Skyrmions can be stabilized only in the applied magnetic field  $h > h(\gamma_0)$  (Fig. 4.30 (b)). For  $k_c < 0$ ,  $\mathbf{h}|| < 111 >$  the skyrmions will suffer from instability toward helicoids with  $\mathbf{k}|| < 111 >$  as easy cubic axes  $< 111 >$  make some angle with the skyrmion plane.

## 4.10. Candidate materials for experimental observation of skyrmion textures

From the general phenomenological point of view, the choice of materials that will show skyrmion lattices as low-temperature states in applied fields is dictated only by symmetry requirements and a magnetic ordering transition. Therefore, many different magnetic crystals from classes  $D_{2d}$  and  $C_{nv}$  could be listed as promising objects of pointed searches for skyrmion lattice phases in their magnetic phase diagrams. Here, I mention only very few of them, where clear indications of non-collinear magnetic states are known from early experiments.

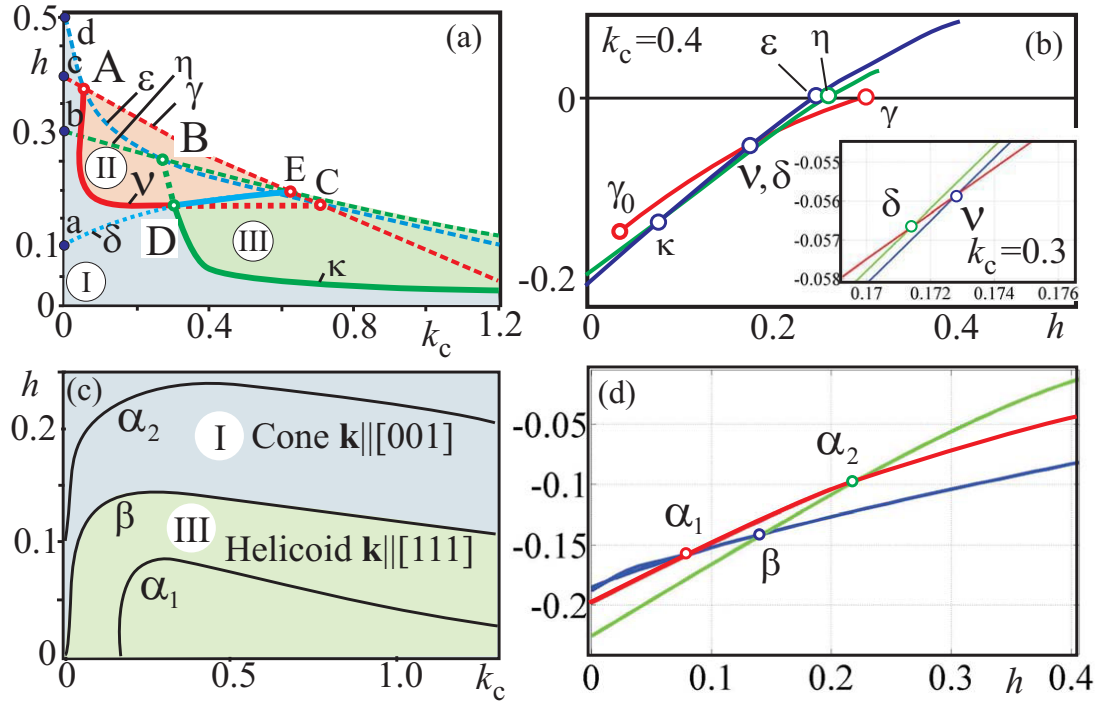


Figure 4.30.: Phase diagrams of states for  $k_c > 0$  (a) and  $k_c < 0$  (c). Magnetic field  $\mathbf{h}$  is applied along  $[001]$ . The regions of the thermodynamical stability are colored by red (skyrmions), blue (cones), and green (helicoids). The detailed description of the phase transitions between modulated phases is given explicitly in the text. (b), (d) The energy densities of the modulated phases in dependence on the field for fixed value of  $k_c$  (see section 4.9.4 for details).

*Defect spinel structure magnets*  $\text{GaM}_4\text{X}_8$ . The magnetic phase diagram of  $\text{GaMo}_4\text{X}_8$  shows a clear intermediate phase between ground-state and field saturated state [237]. The material behaves as almost a ferromagnet, and Rastogi and Wohlfahrt [237] pointed out the similarity with the behavior of  $\text{MnSi}$  and the possibility of a twisted non-collinear spin-structure.

*CeTMSn magnets.* The exemplary  $\text{CeCuSn}$  exists in two modifications,  $\alpha$ - and  $\beta$ - $\text{CeCuSn}$ . Only the  $\beta$ -variant is non-centrosymmetric with space-group  $\text{P6}_3\text{mc}$  belonging to Laue class  $\text{C}_{6v}$  and displays a series of marked anomalies in the magnetization data  $M(H)$ , while the centrosymmetric variant behaves apparently as a simpler magnetic systems. The direct comparison of the two different crystallographic states suggests an important role of chiral DM interactions [238].

In Ref. [21] two tetragonal materials  $\text{Tb}_3\text{Al}_2$  and  $\text{Dy}_3\text{Al}_3$  were proposed as suitable candidates for the observation of chiral skyrmions and spiral structures. Both crystals belong to the space group  $\text{C}_{4v}^4$ ;  $\text{Tb}_3\text{Al}_2$  has a Curie temperature  $T_C = 100$  K, and for  $\text{Dy}_3\text{Al}_3$ ,  $T_C = 190$  K has been measured [239,240]. At high temperatures they have rather complicated easy-axis type magnetic structures. At a transition temperature  $T_t$  they seem to switch to an easy-plane structure. This transition was found at  $T_t = 10$  K for  $\text{Tb}_3\text{Al}_2$  and at  $T_t = 20$  K for  $\text{Dy}_3\text{Al}_3$ . Up to now modulated magnetic structures have not been identified in these materials, but in view of the magnetic symmetry they could be present, particularly near  $T_t$ , where the uniaxial anisotropy constant is small and conditions for the realization of a magnetic mixed state are favourable.

The cubic materials  $\text{MnSi}$ ,  $\text{FeGe}$ ,  $\text{Fe}_x\text{Co}_{1-x}\text{Si}$ , and  $\text{Co}_x\text{Mn}_{1-x}\text{Si}$  belong to another group where skyrmions are believed to induce anomalies of phase diagram near the ordering transition (see chapter 6). In these compounds spiral structures related to the Dzyaloshinsky-Moriya interactions are well known [64, 87, 241]. The helix pitch  $L_D = 2\pi/|\mathbf{k}|$  is in general large in these compounds: it is 18 nm in the case of  $\text{MnSi}$  or even larger ( $>230$  nm) for  $\text{Fe}_{0.8}\text{Co}_{0.2}\text{Si}$  (see also some examples in the Table 4.2).

Table 4.2.: Néel temperatures ( $T_N$ ), helix periods ( $L_D$ ), and saturation fields ( $H_D$ ) for some cubic helimagnets, data from Ref. [51].

Compound	MnSi	FeGe	$\text{Fe}_{0.3}\text{Co}_{0.7}\text{Si}$	$\text{Fe}_{0.5}\text{Co}_{0.5}\text{Si}$	$\text{Fe}_{0.8}\text{Co}_{0.2}\text{Si}$
$T_N$ [K]	29.5	278.7	8.8	43.5	32.2
$L_D$ [nm]	18.0	68.3- 70.0	230	90.0	29.5
$H_D$ [T]	0.62	0.2	$(6.0 \pm 1.5) \cdot 10^{-3}$	$(4.0 \pm 0.5) \cdot 10^{-2}$	0.18

The skyrmion states in the present magnets can be easily stabilized by the small cubic anisotropy with easy axes along  $\langle 001 \rangle$  crystallographic directions and the applied magnetic field directed along  $\langle 001 \rangle$  as shown in section 4.9. The main effect of the cubic anisotropy in this case is suppression of the conical phase. The

phase diagram depicted in Fig. 4.30 (a) will be qualitatively the same for easy axes of cubic anisotropy along  $\langle 111 \rangle$  and the field parallel to one of these directions.

The skyrmion states may be stabilized over cones and helicoids also by the uniaxial anisotropy. The results of section 4.7.4 may help to clarify the role of small uniaxial distortions in high-pressure experiments in MnSi - an important and unsolved problem, which continues to attract widespread attention. For example for MnSi, earlier experiments [242] and analysis [243] of magnetoelastic couplings allow a quantitative estimate of strain-induced uniaxial anisotropy. The magnetoelastic coupling with uniaxial strains  $u_{zz}$  is given by  $w_{me} = b u_{zz} (M_z/M_S)^2$ , where  $M_S = 50.9$  A/m is the saturation magnetization [244] and  $b = 7.4$  GPa is a magnetoelastic coefficient derived from the magnetostriction data in Ref. [242]. Using exchange constant  $A = 0.11$  pJ/m, as estimated from the spin-wave stiffness reported in Ref. [245], and  $D = 2 q_0 A = 0.86$   $\mu$ J/m<sup>2</sup> for MnSi [31] one has  $K_0 \simeq 17$  kJ/m<sup>3</sup> and a dimensionless scale  $b/K_0 \simeq 44$  for the induced anisotropy. Thus, a modest strain  $u_{zz} = 0.0024$  is sufficient to reach an induced anisotropy  $K/K_0 = 0.1$  which is enough to stabilize the skyrmion lattice in magnetic field. This strain corresponds to a tensile stress  $\sigma_{zz} = 680$  MPa for MnSi by using the elastic constant  $c_{11} = 283$  GPa. [85] The rather low uniaxial stress necessary to stabilize the skyrmion lattice is particularly relevant for pressure experiments with a uniaxial disbalance of the applied stresses, but it could also be achieved in epitaxial films.

Additional uniaxial anisotropy may be also of surface-induced nature. In magnetic nanosystems surface/interface interactions provide additional stabilization mechanism of skyrmion states. As recently the skyrmion states were observed in thin magnetic layers of  $\text{Fe}_{1-x}\text{Co}_x\text{Si}$  and FeGe [28, 29], this might have the significant contribution (for the details see chapter 5 and particularly the section 5.7).

## 4.11. Conclusions

In non-centrosymmetric magnetic materials, Dzyaloshinskii-Moriya exchange based on the relativistic spin-orbit couplings stabilizes helical one- dimensional modulations, as well as solitonic textures, i.e., localized topologically non- trivial baby-skyrmions - repulsive particle-like spin textures imbedded into homogeneously magnetized "parental" state. These isolated skyrmion excitations can be manipulated as particle-like entities. Their relevant length scale can be tuned by the competition between direct and chiral DM exchange and may range from few atomic spacings up to microns. Theoretical results for the basic phenomenological continuum theory of chiral magnets demonstrate that localized spin-textures with constant value of the magnetization modulus may form extended regular states. The formation of skyrmionic textures is determined by the stability of the localized solitonic cores and their geometrical incompatibility that frustrates homogeneous space-filling. On the contrary to the circular-cell approximation, used as a method of choice to obtain approximate solutions for skyrmion lattices in early papers of A. N. Bogdanov et al. [21, 22, 70], the rigorous solution for skyrmion states in this chapter are derived by the direct energy minimization for phenomenological models of non-centrosymmetric

helimagnets from different crystallographic classes. These numerical results provide a comprehensive description of the structure of the skyrmion lattice and its evolution in the applied magnetic field directed either opposite or along the magnetization in the center of the skyrmion cell. Differences of lattice parameters from circular-cell approximation and from numerical calculations lie within 2% and, therefore, demonstrate that CCA is a good approximation.

It is shown that for crystals from Laue classes  $D_{2d}$  and  $C_{nv}$  skyrmion lattices are stable with respect to one-dimensional helices in the applied magnetic field. As the transition between spiral and skyrmion states is a first-order phase transition, domains of coexisting phases may be formed. For cubic helimagnets and other systems with Lifshitz invariants attached to three spatial directions, additional anisotropic contributions suppressing conical phase must be considered. Skyrmion lattices can be stabilized in a broad range of thermodynamical parameters in the presence of uniaxial anisotropy. Skyrmion stability demands the combined effect of uniaxial anisotropy and magnetic field. These findings demonstrate that distorted cubic helimagnets are very promising objects for investigations of skyrmion states. On the other hand, skyrmion states may be stabilized over cones by small cubic anisotropy itself. To achieve this goal the applied magnetic field must point along particular crystallographic directions strongly deforming the conical state.



# 5. Skyrmion and helical states in thin layers of magnets and liquid crystals

## 5.1. Introduction

As shown in chapter 4, specific chiral interactions in *bulk* non - centrosymmetric helimagnets provide a unique mechanism for stabilization of the localized and modulated structures with fixed sense of the magnetization rotation in one (spirals) or in two (baby-skyrmion) dimensions. Twisted modulations of such a type arise as a result of the competition between the exchange stiffness and chiral interactions, whereas Zeeman energy in accordance with smaller energy contributions rules the thermodynamical stability of the corresponding modulated phases. Currently however, the scope of material science interest has been shifted to the *confined* artificial systems in which the structural inversion asymmetry of the surface gives rise to qualitatively new phenomena. The new aspects of the physics in reduced dimensions include Rashba effect [246, 247], chiral Dzyaloshinskii-Moriya interactions [20, 27], surface/interface induced anisotropy [102, 227], and/or anchoring in liquid crystals. Understanding of these effects opens up the perspectives to create chiral architectures in nanosystems and put into practice control over them.

Surface-induced uniaxial anisotropy is a key factor that can influence chiral modulated states in magnetic nanosystems. Its interplay with volume energy contributions leads to the formation of specific axisymmetric distributions of the magnetization, spherulites, which exist as smooth static solitonic textures and are extended into the third direction in accordance with the modulating effect of the surfaces. As a starting point for investigations of this phenomenon I have calculated the equilibrium structures of skyrmions in a nanolayer with the induced uniaxial anisotropy for a case of "thick" layers when the induced magnetic anisotropy is strongly localized to the layer surfaces (a rigorous criterion of "thick" layer can be found in Ref. [227]; see also section 1.2.2 *C* for details). In this limiting case the induced anisotropy can be treated as a mere surface effect (according to Néel's theory of surface anisotropy [102]) and is included into the corresponding micromagnetic equations only through boundary conditions (section 5.2, section 1.2.2 *C*). In section 5.3-5.5 I give a comprehensive analysis of the spherulitic states in confined nanolayers.

Dipolar stray fields appearing on the surface of confined layers are another important factor having a sizable effect on modulated states. Due to the strong magnetodipole interaction chiral helices and skyrmion lattices can be significantly de-

formed. In section 5.6 I address this practically unexplored problem of the interplay between short-range energy contributions stabilizing modulated phases, skyrmions and helices, and the long-range magnetostatic forces.

## 5.2. Phenomenological model of modulated states in thin magnetic films

As it was shown in section 1.2.2 *C* on the example of thin magnetic layers and in the chapter 3 on the example of magnetic nanowires and nanotubes, generally the surface-induced anisotropy must be considered as inhomogeneously distributed through the volume of the nanosystem. However, the case with the induced anisotropy constrained to the surface region represents the practically most important situation. When the penetration length  $\lambda_s$  (see section 1.2.2 *C*) is much smaller then the characteristic sizes of the system, the surface-induced interactions influence the magnetization distributions only through the boundary conditions for the energy functional (Eq. (1.32)). In Refs. [227, 228], for instance, the corresponding estimates led to  $\lambda = 1.9 \text{ \AA}$  for Co/Au films and  $\lambda = 26.4; 31.9 \text{ \AA}$  for Ni/Cu multilayer systems.

In the present chapter I consider a magnetic nanolayer infinite in  $x$ - and  $y$ -directions and confined by parallel planar surfaces at  $z = \pm T/2$ . The volume energy density  $w_v$  (Eq. (1.32)) is taken from Eq. (4.1) including uniaxial anisotropy  $K_u$  (third energy term in (4.2)). Surface part of the Eq. (1.32) is written as

$$w_s = -K_s(\mathbf{m} \cdot \mathbf{s})^2 \quad (5.1)$$

with constant coefficient  $K_s = \text{const}$  of surface anisotropy (general case is expressed by Eq. (1.30)).

Importantly, such a model allows to describe also thin layers of chiral nematic liquid crystals sandwiched between two glass plates. The possible distributions of the director  $\mathbf{n}(\mathbf{r})$  in a bulk cholesteric liquid crystal placed in an electric field  $\mathbf{E} = E\mathbf{e}$  are determined by the minimization of the Frank free energy [48, 248]:

$$f_v = \frac{K_1}{2}(\text{div } \mathbf{n})^2 + \frac{K_2}{2}(\mathbf{n} \cdot \text{rot } \mathbf{n} - q_0)^2 + \frac{K_3}{2}(\mathbf{n} \times \text{rot } \mathbf{n})^2 - \frac{\varepsilon_0}{2}(\mathbf{n} \cdot \mathbf{E})^2. \quad (5.2)$$

Here,  $K_i$  ( $i = 1, 2, 3$ ) and  $q_0$  are elastic constants;  $\varepsilon_a$  is the dielectric anisotropic constant (we consider only materials with  $\varepsilon_a > 0$ );  $p = 2\pi/|q_0|$  determines the pitch of a helical structure in the ground state (at  $E = 0$ ). For the one elastic constant approximation,  $K_1 = K_2 = K_3 = K$ , the Frank energy density (5.2) can be reduced to the form:

$$f_v = K(\text{grad } \mathbf{n})^2 + 2Kq_0\mathbf{n} \cdot \text{rot } \mathbf{n} - \varepsilon_0 E^2(\mathbf{n} \cdot \mathbf{e})^2. \quad (5.3)$$

For  $\mathbf{H} = 0$  the energy density  $w_v$  coincides functionally with  $f_v(\mathbf{n})$  (Eq. 5.3). This allows to investigate skyrmionic states in chiral ferromagnets and liquid crystals within a common mathematical framework. The surface energy  $w_s$  for liquid crystals (Eq. (5.1)) describes a homeotropic anchoring of glass surfaces with  $K_s > 0$  [48]. In



the experiments with liquid crystals, such glass surfaces confine a thin layer of a liquid crystal and anchor the molecules perpendicularly to the surfaces. Phenomenological model (Eq. (5.3)) allows to obtain continuous distributions of the director  $\mathbf{n}$  for liquid crystals.

### 5.3. Isolated skyrmionic states

To investigate the structure of isolated skyrmions in thin magnetic layers one has to introduce cylindrical coordinates for the spatial variable  $\mathbf{r} = (r, \phi, z)$ , and the spherical coordinates for the order parameters  $\mathbf{m}$  and  $\mathbf{n}$ :  $\mathbf{m}, \mathbf{n} = (\sin \theta \cos \psi, \sin \theta \sin \psi, \cos \theta)$  (see section 4.4 for the details). On the contrary to the isolated skyrmions in bulk systems which are characterized by the dependence  $\theta = \theta(r)$  in the cross-section of a skyrmion filament (section 4.4) and are homogeneously extended into the third direction ( $z$ ), the localized skyrmions in confined media are solutions of the following boundary value problem with  $\theta = \theta(r, z)$ :

$$\begin{aligned} \theta_{ZZ} + \theta_{\rho\rho} + \frac{\theta_\rho}{\rho} - \frac{\sin \theta \cos \theta}{\rho^2} - \frac{\sin^2 \theta}{\rho} - \gamma \sin 2\theta + h \sin \theta &= 0, \\ (\theta_Z + \beta \sin \theta \cos \theta)|_{Z=\pm t/2} &= 0, \\ \theta(0, Z) = \pi, \theta(\infty, Z) &= 0. \end{aligned} \quad (5.4)$$

Skyrmionic strings in such systems are distorted into specific 3D textures in accordance with the anchoring effect of the surfaces, but the topology remains the same [249].

In Eq. (5.4) I introduced the new length scales for magnets:

$$\rho_0 = \frac{A}{D} \quad (5.5)$$

and liquid crystals

$$\rho_0 = \frac{1}{2q_0}. \quad (5.6)$$

Then  $\rho = r/\rho_0, Z = z/\rho_0$ . Four control parameters in Eq. (5.4),  $\gamma, h, \beta$ , and  $t$ , are expressed as combinations of material parameters of the model functional (5.1) and (5.3). For magnetic layers:

$$\gamma = \frac{AK_u}{D^2}, \quad h = \frac{HM_s A}{D^2}, \quad \beta = \frac{K_s}{D}, \quad t = \frac{TD}{A}, \quad (5.7)$$

For liquid crystals:

$$\gamma = \frac{\varepsilon \varepsilon_0 E^2}{K q_0^2}, \quad h = 0, \quad \beta = \frac{K_s}{2K q_0}, \quad t = 2T q_0. \quad (5.8)$$

Invariance of Eq. (5.4) under a scaling transformation:

$$t \rightarrow kt, \quad \gamma \rightarrow \gamma k^2, \quad h \rightarrow hk^2, \quad \beta \rightarrow \beta k. \quad (5.9)$$

allows to investigate solutions of Eq. (5.4) for a fixed reduced layer thickness  $t$  ( $t=1$  in the present chapter). For the liquid crystals it is convenient to redefine anisotropy parameter  $\gamma$  and to write it in the units of  $\varkappa$ :

$$\gamma = \frac{\pi^2}{16\varkappa^2}, \quad \varkappa = \frac{E_0}{E}, \quad E_0 = \pi q_0 \sqrt{\frac{K}{4\varepsilon_0}}. \quad (5.10)$$

The critical field  $E_0$  [249] marks the crossover between localized and modulated skyrmion states for bulk chiral helimagnets.

Boundary value problem (5.1) has been solved by a standard finite-difference method with discretization on rectangular grids with adjustable grid spacings. As initial guess for the iterative procedure according to Seidel method with Chebishev acceleration [250] I used the known solutions of Eq. (5.1) for bulk chiral systems [21], i.e. I started from the solutions with  $\beta = 0$  (see section 4.4).

Solutions for isolated skyrmions may be represented as a set of profiles  $\theta(\rho)$  for fixed coordinates  $Z$ . The profiles are strongly modified by the anchoring  $\beta$  from bell-like type in the center of the layer to arrow-like at the surface (blue lines in Fig. 5.1 (a)). The thickness-dependent radii  $R(Z)$  for each angular profile  $\theta(\rho)$  are defined as shown by red tangent lines in Fig. 5.1 (a), i.e. according to the Lilley definition (see section 1.3.1). The function  $R(Z)$  reproduces the convex shape of solutions with the largest value in the center of the layer ( $Z = 0$ ) and the smallest value corresponding to the layer surfaces ( $Z = \pm t/2$ ) (Fig. 5.1 (a), inset, and (b)-(e)). With increasing anchoring parameter  $\beta$  angular profiles  $\theta(\rho)$  near the surfaces become strongly localized (Fig. 5.1 (b)) with the characteristic sizes comparable to the molecular length; in this case the elastic approach of Eq. (5.4) is inapplicable, and the isolated skyrmions collapse into the homogeneous state.

The influence of the surface anchoring may lead not only to the compression of ideally cylindrical filament into convex-shaped spherulite, but also to the specific skyrmionic states with "necks" when the minimal value of  $R(Z)$  is reached not at the surface of the layer, but at some coordinate  $Z$  in the volume (Fig. 5.1 (c)). Such a peculiar shape of an isolated spherulite is a result of complex interplay between surface and volume energy contributions. It cannot be an artefact of the proposed method to define the function  $R(Z)$  since the lines with constant angle  $\theta$  show the same behaviour near the surface (see inset in Fig. 5.1 (a)).

The decrease of the film thickness  $t$  results in the same effects as increase of the anchoring parameter  $\beta$  (Fig. 5.1 (d), (e)) as it can be concluded from the equation (5.9) of the scale transformation. The set of profiles  $R(Z)$  for the fixed value of anchoring parameter  $\beta = 3$  and variable thicknesses  $t$  of the layer displays the change of the spherulite shape from that with "necks" for thin layers to the convex shape for thick films (Fig. 5.1 (d), (e)).

Still for the wide range of control parameters all angular profiles  $\theta(\rho)$  are of arrow-

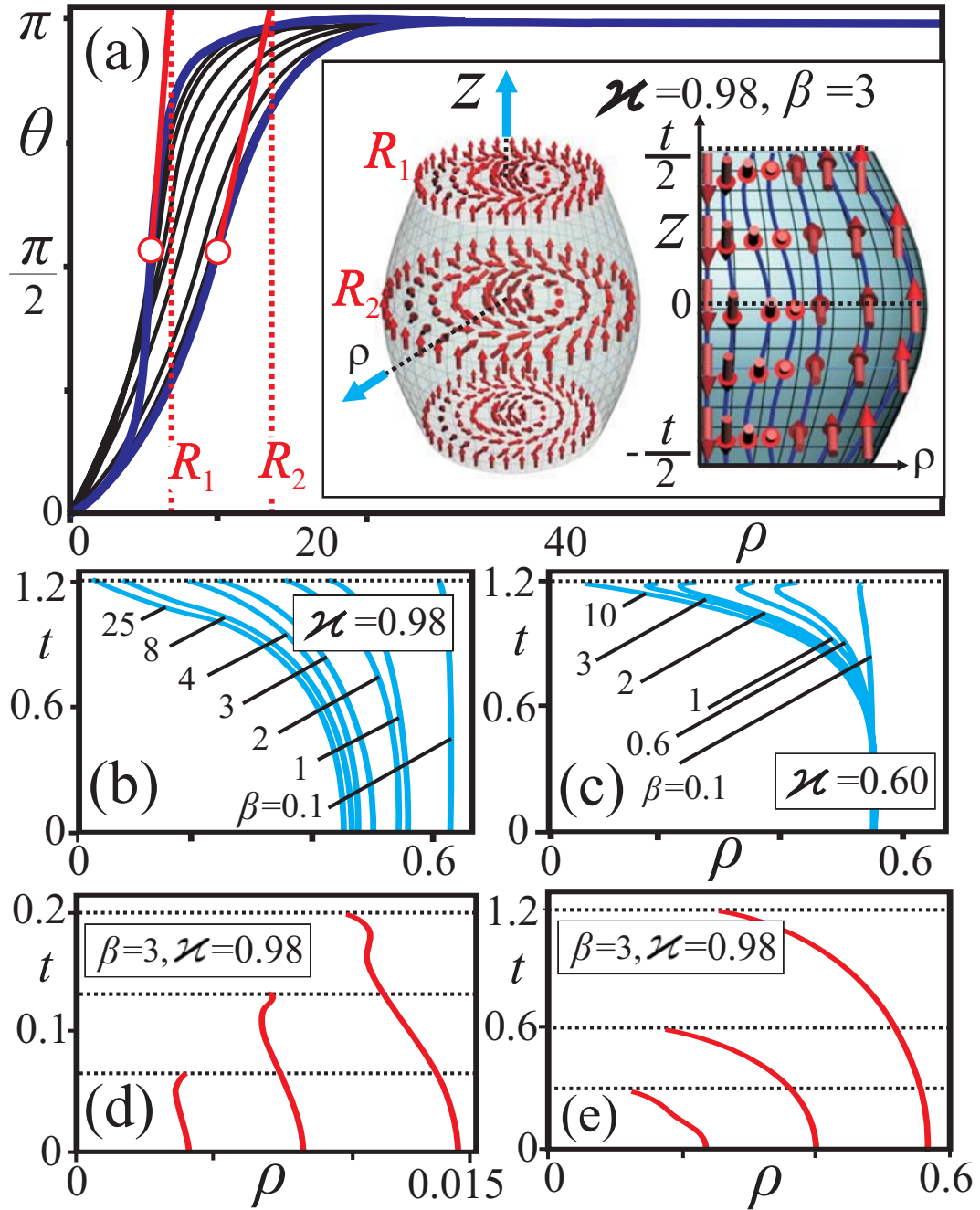


Figure 5.1.: (a) Equilibrium solutions of isolated spherulitic domains, shown as a set of profiles  $\theta(\rho)$  for fixed coordinate  $Z$  through the layer. Bold blue lines mark the profiles at the surface and in the center of the layer. Inset schematically displays the distribution of the order parameter vector field with  $\psi = \varphi - \pi/2$ . The effect of anchoring is imaged by its influence on the boundary surface of the spherulite as shown in (a) by red lines for each angular profile: (b), (c) represent shapes of the localized spherulites for different values of surface anchoring  $\beta$ ; (d), (e) - for different film thicknesses  $t$ .

like type squeezed along the sample thickness by anchoring. Such a type of angular profiles permits the use of the ansatz [249]:

$$\theta(\rho, Z) = \pi \frac{\rho}{R(Z)}. \quad (5.11)$$

The function  $R(Z)$  describes the compression of angular profile  $\theta(\rho)$  for  $R > 1$  and its expansion with  $R < 1$ . Integrating (5.4) with the ansatz (5.11) with respect to  $\rho$ , results in

$$\int_{-t/2}^{t/2} \left[ I_0 \left( \frac{dR}{dZ} \right)^2 + I_1 R^2 \left( \frac{\pi^2}{16\kappa^2} \right) - I_2 R - I_3 h R^2 \right] dZ \quad (5.12)$$

where

$$\begin{aligned} I_0 &= \int_0^1 t^3 \left( \frac{d\theta}{dt} \right)^2 dt = \frac{\pi^2}{4}, I_1 = \int_0^1 t \sin^2 \theta dt = \frac{1}{4}, \\ I_2 &= \int_0^1 t \left( \frac{d\theta}{dt} \right) dt = \frac{\pi}{2}, I_3 = \int_0^1 \left( \frac{t}{2} \right) \cos(\theta) dt = -\frac{1}{\pi^2} \end{aligned} \quad (5.13)$$

The Euler equation for the functional (5.12) with the boundary conditions

$$\left( \frac{dR}{dZ} \right)_{Z=\pm t/2} = R(Z) \beta \frac{I_1}{I_0} \quad (5.14)$$

has an analytical solution [249]:

$$R(Z) = \frac{1}{\pi A} \left( 1 - \frac{\beta \cosh(Z\sqrt{A})}{\beta \cosh(\frac{t\sqrt{A}}{2}) + \pi^2 \sqrt{A} \sinh(\frac{t\sqrt{A}}{2})} \right), \quad A = \frac{1}{16\kappa^2} + \frac{4h}{\pi^4}. \quad (5.15)$$

Considered analytical approach for arrow-like angular profiles describes numerically obtained solutions with a good accuracy, and can be generally applied for other appropriately chosen initial functions  $\theta(\rho/R(z))$ .

## 5.4. Condensation of repulsive skyrmions into a lattice

In the *bulk* helimagnets the inter-skyrmion interaction is known to be repulsive and screened at large distances  $L$  (see section 4.4.4). In thin confined layers the standard interaction of skyrmions (Eq. 4.35) is modified, and related to the exponential decay of the polar angle. The solution of the linearized Euler equation (5.4) for  $\rho \rightarrow \infty$  has the asymptotic decay with

$$\theta(\rho, Z) \propto \cos(\lambda Z) \exp(-\alpha \rho). \quad (5.16)$$

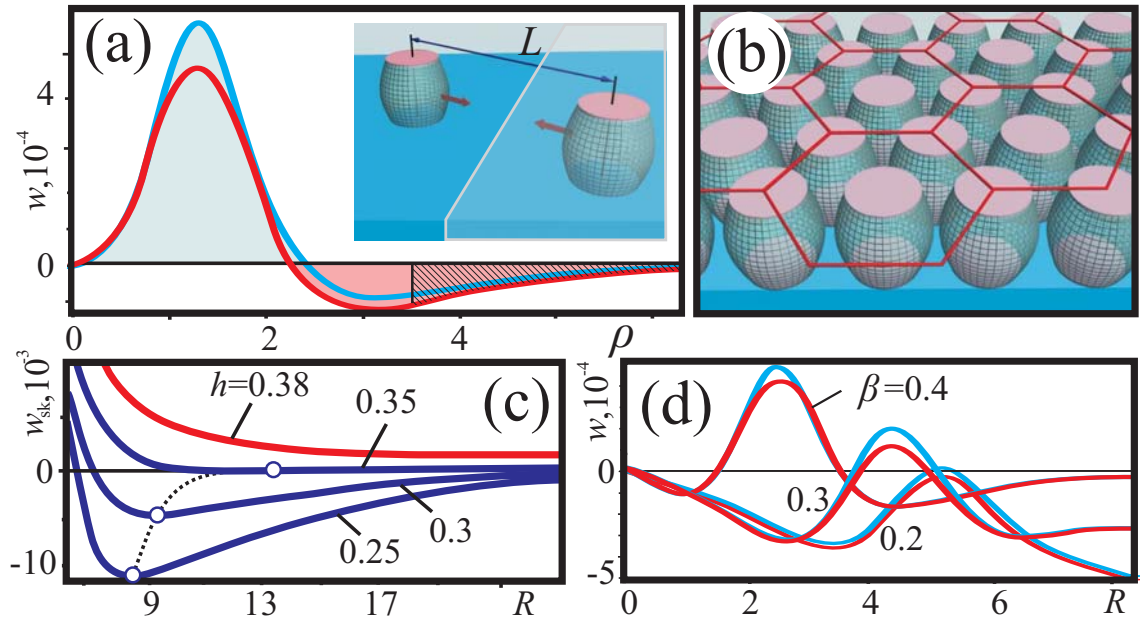


Figure 5.2.: Distribution of energy density in the isolated skyrmion state ( $\beta = 0.5$ ) (a) and in the skyrmion lattice ( $\beta = 0.2$ ) (d) for the profiles  $\theta(\rho)$  at the surface (blue line) and in the central film plane (red line) ( $\kappa = 3, h = 0$ ); (b) schematic representation of the hexagonal skyrmion lattice in the circular cell approximation; (c) dependence of the skyrmion energy on the radius of lattice cell  $R$  for different values of the applied magnetic field ( $\kappa = 3, \beta = 0.1$ ). Above the threshold field (red line) only isolated skyrmions can exist.

Here,  $\alpha = (\pi/4\kappa)^2 - h + \lambda^2$ , and  $\lambda$  are the roots of the transcendental equation,  $\lambda \tan \lambda Z = \beta$  (Fig. 5.2 (a), inset). The energy density underlying such a slow rotation is negative and depends on the distance from the center of the layer. In Fig. 5.2 (a) I plotted the energy density distribution in the profile at the surface (blue line) and in the center of the layer (red line). The interaction energy of two vortices has the expression:

$$U(L, \beta) = \sqrt{\frac{2\pi L}{\alpha^3}} \exp(-\alpha L). \quad (5.17)$$

The parameter  $\lambda$  due to the anchoring effect of the surfaces modifies this inter-skyrmion potential in comparison with Eq. (4.35). The lattice will be established from isolated skyrmions when the DM energy contribution (red-shaded area of energy distribution  $w_{sk}(\rho)$ , Fig. 5.2 (a)) of *all* profiles  $\theta(\rho, Z)$  outweighs the exchange energy contribution (blue-shaded area). Since the exchange part of the energy density is much larger for the surface profiles  $\theta(\rho, \pm t/2)$  (blue line in Fig. 5.2 (a)), the field of lattice formation will be smaller for larger values of parameter  $\beta$  (see, for instance, the second plot in Fig. 5.3 (d),  $\kappa$  here is fixed). This explains the shape of the lability surface for the lattice of spherulites in Fig. 5.3 (a). For Skyrmionic states in the lattice I used the circular-cell approximation [50] and solved Eq. (5.1) with boundary conditions  $\theta(0, Z) = \pi, \theta(R(Z)) = 0$  (Fig. 5.2 (b)).

## 5.5. Skyrmion lattices versus helicoids. Phase diagram of solutions

Alternative to the two-dimensional skyrmion state is the one-dimensional helicoid (Fig. 5.3 (a), inset) with propagation vector along  $Y$ -axis, parallel to the surfaces. Angle  $\theta$  of the magnetization with respect to  $Z$  axis in the helicoid can be obtained from the Euler equation with boundary conditions:

$$\begin{aligned} \theta_{ZZ} + \theta_{YY} - \gamma \sin \theta \cos \theta &= 0, \\ \theta(0) = \pi, \theta(p) &= 0, \\ \left(\frac{\partial \theta}{\partial Z} + \beta \sin \theta \cos \theta\right)|_{Z=\pm t/2} &= 0 \end{aligned} \quad (5.18)$$

where  $p$  is a period of the helicoid.

In the distorted helicoid propagating in the magnetic layer, angle  $\theta$  is a function of two coordinates,  $Y$  and  $Z$ . This distinguishes the solutions  $\theta(Y, Z)$  from those considered in chapter 4 with the dependence of the angle only on one spatial coordinate [21],  $\theta = \theta(Y)$  (see section 4.3.1). In the plane  $XZ$  (see inset in Fig. 5.3 (a)) the solutions for helicoids have convex shape as it was noted also for spherulites. I have plotted the dependences  $\theta = \theta(Z)$  in equidistant planes with fixed coordinate  $Y$  (thin black lines in Fig. 5.3 (b)). Such profiles have the most distorted shape in the vicinity of the point  $Y = p/2$ . Note that profiles for  $Y = p/2$  are straight lines

with  $\theta = \pi/2$ : the magnetization is balanced by the two anchoring surface planes. Dependence of the angle  $\theta$  along coordinate  $Y$  is also strongly distorted by the anchoring effect of the surfaces: the order parameters  $\mathbf{m}$  (or  $\mathbf{n}$ ) point up ( $\theta = 0$ ) and down ( $\theta = \pi$ ) in the wide regions (domains) and rotate rapidly in the interstitial regions (domain walls). Such a behavior of the spiral state may be also deduced from the densest localization of lines  $\theta(Z)$  in the vicinity of  $\theta = 0; \pi$  (thin black lines in Fig. 5.3 (b)).

The distribution of the energy density in the helicoid along the propagation direction  $Y$  is plotted in Fig. 5.3 (b) for the profiles at the surface  $\theta(Y, t/2)$  (blue line) and in the center of the layer  $\theta(Y, 0)$  (red line). The largest loss of the rotational energy occurs for the planes with  $\theta = \pi/2$  (Fig. 5.3 (b)).

On the phase diagram the regions of modulated skyrmion matter and helicoidal state are bounded by the surfaces with red and black lability lines, respectively (Fig. 5.3 (a)). Corresponding two-dimensional cuts of this three-dimensional phase diagram are shown in Fig. 5.3 (d). For  $h = 0$  (i.e. in the plane  $(\kappa, \beta)$ ) the energy density of the helicoid is always lower than that for skyrmion lattice (Fig. 5.3 (c)), i.e. skyrmions are metastable states with respect to helicoids for all possible values of the anchoring parameter  $\beta$ . The region of the thermodynamical stability of the helical state is marked by blue color in Fig. 5.3 (d). According to the phase diagram of Fig. 5.3 (d), increasing parameter  $\beta$  (for fixed value of  $\kappa$ ) leads to the suppression of skyrmions (red line) for much lower values than the suppression of helical states (black line). If the skyrmion lattice as metastable state has been formed for  $\beta = 0$ , then on the lability (black) line it releases free isolated skyrmions. But since the helicoids are the global minimum of the system above the lability line of the skyrmion lattice, the isolated skyrmions must undergo elongation into the helices.

For  $\kappa \rightarrow \infty$  (meaning zero uniaxial anisotropy [70]), i.e. on the plane  $(\beta, h)$  (Fig. 5.3 (d)), the thermodynamical stability of skyrmions can be achieved in the applied magnetic field only for relatively small values of the anchoring parameter  $\beta$  - in the triangular region marked by red color in Fig. 5.3 (d). For values of  $\beta$  larger than some threshold  $\beta_{th}$  (Fig. 5.3 (d)), the helicoids are the thermodynamically stable state. On the basis of competing Zeeman energy and surface-induced uniaxial anisotropy the anchoring can be classified as weak (favouring skyrmion lattice in the field for  $\beta < \beta_{th}$ ), intermediate (favouring helical state in zero and the applied magnetic field for  $\beta_{th} < \beta < \beta_0$ ), and strong (only isolated domain walls and localized skyrmions can exist,  $\beta > \beta_0$ ).

## 5.6. Magnetostatic problem for isolated skyrmions

In previous sections I discussed characteristic features of modulated states arising as a result of competing internal short-range interactions (as the exchange interactions, the Dzyaloshinskii-Moriya coupling, different types of intrinsic and induced magnetic anisotropy) and ignored the effects imposed by magnetodipole forces. In many magnetic nanostructures this assumption is justified by weakness of stray field effects as compared to the internal magnetic interactions (e.g. nanosystems with in-plane

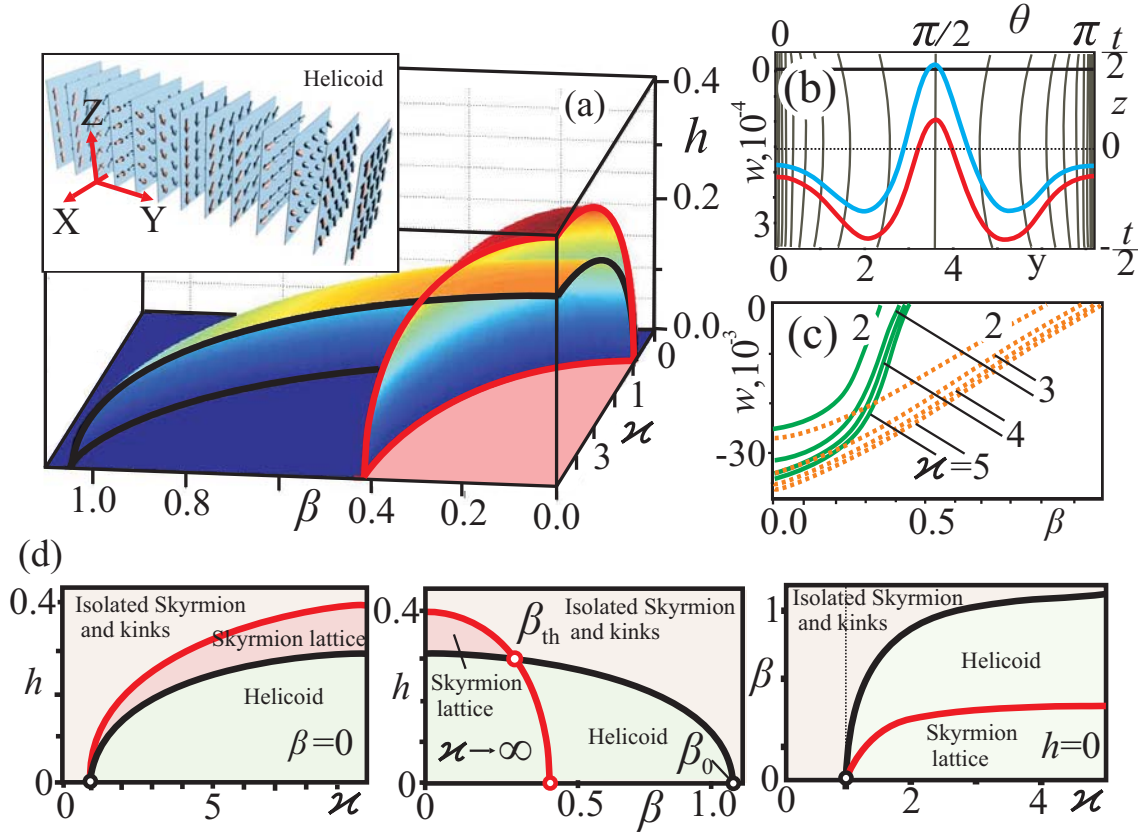


Figure 5.3.: (a) Phase diagram of solutions in the space of control parameters  $(\kappa, \beta, h)$ . Surfaces with red and black lines bound the regions of skyrmion lattice and helical state stability, respectively. (b) Distribution of the energy density in the helicoid ( $\beta = 0.5$ ) for the profiles  $\theta(Y)$  (see inset in (a) for schematic representation of distorted helicoid) at the surface (blue line) and in the central film plane (red line) ( $\kappa = 3, h = 0$ ); thin black lines show the dependences  $\theta(Z)$  in equidistant planes  $ZX$ . (c) Energy dependence of equilibrium skyrmion lattice (green lines) and spiral state (dotted orange lines) on the changed parameter of surface anchoring  $\beta$  ( $h = 0$ ). (d) The two-dimensional cuts of the three-dimensional phase diagram (a).



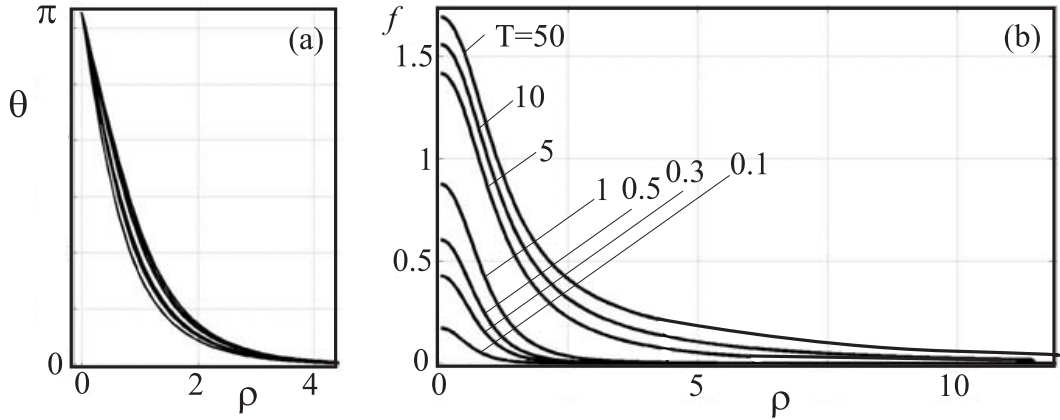


Figure 5.4.: (a) Equilibrium angular profiles  $\theta(\rho)$  for skyrmion solutions of Eq. (5.19) plotted for different values of film thickness  $T$ ,  $h = -0.05$ ,  $\kappa = 0.5$ ,  $Q = 5$ ; (b) function  $f(\rho)$  (5.20) for corresponding skyrmion solutions.

magnetization). However, in a large group of nanostructures with perpendicular anisotropy the magnetodipole coupling play an important role to stabilize specific multidomain patterns and topological defects [251–255]. Generally in nanolayers and multilayers with perpendicular magnetization the stray fields can also strongly modify chiral patterns - helices and skyrmions [23]. In this section I investigate the influence of long-range magnetostatic interactions on the characteristic features of isolated skyrmion states. It is only the first step to address the problem of the formation of the equilibrium modulated patterns under the competing influence of the Dzyaloshinskii-Moriya and magnetostatic interactions.

The total energy  $W$  of the skyrmion filament in the layer of thickness  $T$  can be written in the following reduced form:

$$\begin{aligned} \frac{WL_B}{2K_u} = & 2\pi T \int_0^\infty \left[ \left( \frac{d\theta}{d\rho} \right)^2 + \frac{\sin^2 \theta}{\rho^2} + \sin^2 \theta + \left( 2h - \frac{1}{Q} \right) (1 - \cos \theta) + \right. \\ & \left. + \frac{4\kappa}{\pi} \left( \frac{d\theta}{d\rho} + \frac{\sin \theta \cos \theta}{\rho} \right) - \frac{f(\rho)}{QT} \cos \theta \right] \rho d\rho \end{aligned} \quad (5.19)$$

where  $L_B = \sqrt{A/K_u}$  serves as a scale of the non-dimensional radial variable  $\rho$ , and  $Q = K_u/2\pi M^2$  is a quality factor,  $\kappa = \pi D/4\sqrt{AK_u}$ .

The stray-field energy of the skyrmion string had been derived by solving the corresponding magnetostatic problem as shown in Ref. [256,257] for magnetic bubble domains. Here, in Eq. (5.19)

$$f(\rho) = \int_0^\infty \int_0^\infty (1 - \cos \theta(\rho')) (1 - e^{-\xi T}) J_0[\xi \rho'] J_0[\xi \rho] \rho' d\rho' d\xi \quad (5.20)$$

$J_0$  is a Bessel function of zero order.

I solve the magnetostatic problem for two types of localized solutions (Fig. 4.14

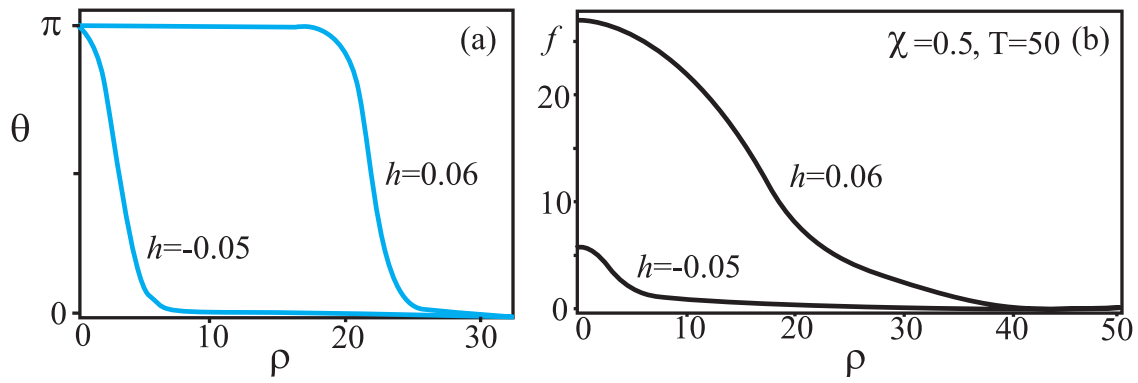


Figure 5.5.: (a) Equilibrium angular profiles  $\theta(\rho)$  for magnetic bubble domains (Eq. (5.19)) plotted for  $h = -0.05$  and  $h = 0.06$ , and  $\varkappa = 0.5, Q = 5$ ; (b) function  $f(\rho)$  (5.20).

(a), (e)). In the absence of demagnetizing fields the first localized solution (Fig. 4.14 (a)) represents skyrmion stabilized by the DM interactions. The second type of localized solution (Fig. 4.14 (e)) is unstable and can exist only in the field applied along the magnetization in the center. In the presence of dipole-dipole interactions this second type of the localized solution becomes stable, it is the solution for the famous magnetic bubble domain [23].

Typical solutions  $\theta(\rho)$  for localized skyrmions are shown in Fig. 5.4. For quality factor  $Q = 5$  and  $\varkappa = 0.5$  I plot the set of solutions parametrized by the film thickness  $T$ . With the decrease of the thickness the angular profiles become more localized. The solutions for skyrmions can exist in very strong positive field: they are protected from the collapse by DM interaction.

Solutions for magnetic bubble domains shown in Fig. 5.5 are characterized by much larger radial sizes in comparison with skyrmions. Such solutions are stable only in the narrow interval of magnetic field applied against the magnetization in the center. Any slight deviation of the control parameters  $T$ ,  $\varkappa$ ,  $Q$ , and  $h$  leads to the instability of these magnetic domains, although as a solution of the Euler equation bubble domains can exist even in the absence of dipole-dipole interaction (as it is seen from Fig. 4.14 (e)-(h)).

Bubble domains and skyrmions are two fundamentally different types of solutions of micromagnetic functional. As bubble domains are stabilized only in the narrow region of applied magnetic fields and film thicknesses [24], the skyrmions look more preferable for the possible applications.

## 5.7. Observations of skyrmionic and helical textures in $\text{Fe}_{0.5}\text{Co}_{0.5}\text{Si}$ nanolayers: theoretical analysis

Real-space images of skyrmion states in a thin layer of cubic helimagnet  $\text{Fe}_{0.5}\text{Co}_{0.5}\text{Si}$  have recently been obtained by using Lorentz transmission electron microscopy [28].

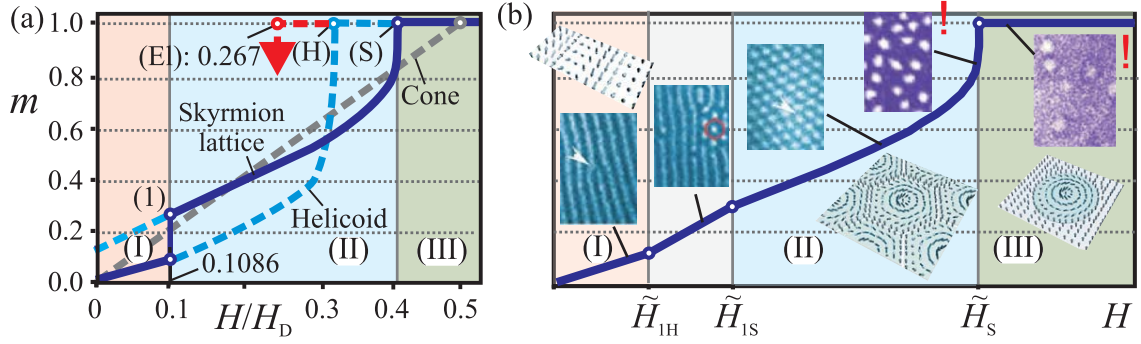


Figure 5.6.: The ideal magnetization curves for a bulk sample (based on results of [21]) (a) and for a thin layer (b) of a cubic helimagnet with suppressed cone phases. Solid lines indicate the thermodynamically stable states; dashed lines in Fig. (a), metastable configurations. The transition field  $H_1$  in the thin layer "spreads" into a region of multidomain states. Fragments of experimentally observed images [28] demonstrate excellent agreement with theoretically calculated magnetization curves. The patterns indicated with sign (!) contain images of isolated chiral skyrmions.

This is the first clear experimental manifestation of *chiral skyrmion states* in a non-centrosymmetric magnetic crystal. The first-order transition of a helicoid into a skyrmion lattice and its subsequent transformation into a system of isolated skyrmions observed in bias magnetic fields (Figs. 1, d-f, 2, 3 (a-d) in [28]) are in excellent agreement with the theoretical predictions on the behavior of skyrmions and the field-driven transitions into densely packed skyrmion lattices according to the magnetic phase diagrams calculated earlier [21, 31] (Fig. 5.6).

In the experiments, the thickness 20 nm of the magnetic layer  $\text{Fe}_{0.5}\text{Co}_{0.5}\text{Si}$  is much smaller than the helix period  $L_D = 90$  nm [28]. But, even for such a small thickness, the conical state propagating only for a fraction of a period perpendicularly through the layer has lower energy than a skyrmion lattice, absent additional effects that stabilize it in applied fields. Usually in magnetic nanolayers strong perpendicular uniaxial anisotropy arises, either as a result of surface effects [5] or of lattice strains. Thus, induced anisotropies give a possible explanation for the experimental observation of the skyrmions in these  $\text{Fe}_{0.5}\text{Co}_{0.5}\text{Si}$  layers, in accordance with the phase diagram for cubic helimagnets with uniaxial distortions (Fig. 4.12) [XI].

Fig. 5.6 presents the magnetization curve for a bulk isotropic helimagnet (a) (based on results of [21], Fig. 12) and the corresponding magnetization curve for a thin layer involving demagnetization effects [24] (b). Compared to theoretically calculated values in a bulk material ( $H_S$ ,  $H_H$ ) the corresponding critical fields in a thin layer are shifted, and their values can be estimated as  $\tilde{H}_{S(H)} = H_{S(H)} + 4\pi M$ . Due to demagnetization effects multidomain states can be stabilized in the vicinity of the transition field  $H_1$  [21]. The boundaries of these regions with coexisting phases can be estimated as  $\tilde{H}_{1H} = H_1 + 4\pi M m_H(H_1)$ ,  $\tilde{H}_{1S} = H_1 + 4\pi M m_H(H_1)$ . The magnetizations of the competing phases at the transition field equal  $m_H(H_1) =$

0.111 and  $m_S(H_1) = 0.278$ . The jump of the magnetization at the transition equals  $\Delta M = [m_S(H_1) - m_H(H_1)]M = 0.167M$ , i.e., it reaches about 17 % of the saturation value.

The magnetization curves in Fig. 5.6 are constructed for ideally soft magnetic material under the condition that only the equilibrium states are realized in the magnetic sample. In real materials the formation of the equilibrium states is often hindered (especially during the phase transitions), and evolution of metastable states and hysteresis effects play an important role in the magnetization processes. Particularly, the formation of the skyrmion lattice below  $H_S$  can be suppressed. Then isolated skyrmions exist below this critical field. At a critical field  $H_{El}$  the skyrmions become unstable with respect to elliptical deformations and "strip-out" into isolated  $2\pi$  domain walls. In a bulk material  $H_{El} = 0.267 H_D$  (indicated in Fig. 5.6 with a red arrow). In a thin layer, one estimates  $\tilde{H}_{El} = H_{El} + 4\pi M$ . As discussed earlier [21, 31, 69] the evolution of chiral skyrmions in magnetic fields has many features in common with that of bubble domains in perpendicular magnetized films, [24] and with Abrikosov vortices in superconductors [72].

The images from Ref. [28] (Fig. 5.6 (b)) reflect in details theoretically predicted evolution of the chiral modulations in the applied magnetic field: the helicoid phase is realized at low fields (region (I)); at higher field this transforms into the skyrmion lattice (region (II)) via an intermediate state ( $\tilde{H}_{1H} < H < \tilde{H}_{1S}$ ); finally the skyrmion lattice by extension of the period transforms into the homogeneous phase where isolated skyrmions still exist as topologically stable 2D solitons.

Two patterns indicated in Fig. 5.6 (b) with exclamation mark manifest the main result of Ref. [28]: the first images of *static two-dimensional localized states* aka *chiral skyrmions*! In Ref. [28] this result has been overlooked and misinterpreted as a coexisting ferromagnetic and skyrmion lattice phases. As it was expounded in the previous section, the transition of the skyrmion lattice into the homogeneous state is a *continuous* transition, but of the particular *nucleation* type. Such transitions exclude the formation of coexisting states.

The condensed skyrmion phases in the micrograph of Ref. [28] also appear as heavily distorted densely packed two-dimensional lattice configurations. This is expected for skyrmionic matter. As these mesophases are composed from elastically coupled radial strings, dense skyrmion configurations generally do not form ideal crystalline lattices but various kinds of partially ordered states, e.g. hexatic ordering implying only orientational order of bonds without positional long-range order, or other glassy arrangement following standard arguments put forth for the similar vortex matter in type-II superconductors [72]. The observation derives from the particle-like (or string-like) nature of skyrmions and suggests that skyrmionic mesophases may display rich phase diagrams.

## 5.8. Observation of skyrmion states in chiral liquid crystals

As it was noted in section 5.2, the phenomenological energy of cholesterics (5.3) has an identical mathematical form as that of cubic helimagnets (4.1). This implies close relations between chiral textures in both condensed matter systems. However, in contrast to magnetic systems favoring smooth distributions of the order parameter, liquid crystals usually form patterns composed of various types of singularities. Defects in liquid crystals are of various dimensionalities, not only line defects, but also points and walls, and appear due to the prevalence of orientational order over positional in the applied magnetic or electric fields. In the defects the director  $\mathbf{n}$  is said to be undefined and the properties of defects are often not well controlled. For many years the investigations of liquid crystal textures have been mostly concentrated on the processes related to the formation and evolution of these topological defects [38, 248, 258]. Only during the last decade physical analogies between liquid crystal and magnetic systems have been utilized to find new skyrmionic textures in these systems [31, 249, 259, 260]. Particularly, the analogy with cholesteric blue phases [258] has been used to establish the skyrmionic ground state in chiral magnetic metals near the ordering temperature [31]. The results on observations of specific skyrmion states (spherulitics) in confined cholesteric systems (Fig. 5.7 (b) [248]) can help to investigate similar structures in magnetic nanolayers [28, 29]. Liquid crystals have several advantages over magnetic systems for the modelling and investigation of various inhomogeneous structures. The system parameters can be varied over wide limits to establish necessary conditions for a given experiment; as a rule experiments are conducted at room temperature and are comparatively simple; the results of investigations are easily visualized, to a degree not usually attainable in the investigation of magnetic nanolayers.

Fig. 5.7 shows modulated patterns in chiral magnets (c,d) in comparison with those in chiral liquid crystals (a,b). Under non-restricted conditions, chiral-nematic LC molecules, which are characterized by an antisymmetric center in the molecule, organize themselves by following a helicoidal director alignment (Fig. 5.7 (a)). However, more exotic ground states are possible (for example, cholesteric fingers [261] and/or triple-twist torons [262]), in particular, spherulites (Fig. 5.7 (b)).

Such circular objects, called bubble domains or spherulites, can be formed as isolated entities or arranged in a hexagonal array (Fig. 5.7 (b)). For the first time, they have been observed in 1974 simultaneously by Kawachi and Kogure [263] and Haas and Adams [264] in materials of negative dielectric anisotropy. The spherulites were generated by applying pulses of DC or AC low frequency electric field strong enough to induce electrodynamic turbulence. Two years later, Bhide et al. [265] studied the optical properties of this pattern by laser diffraction and proposed that the bubble domain was a cholesteric pocket with oblate spheroid shape. This model was replaced by a more convincing model in papers of Akahane et al. [266, 267]. In this model which was inspired by the paper of Cladis and Kleman [268], two looped disclinations were assumed to exist near the glass plates. Another model

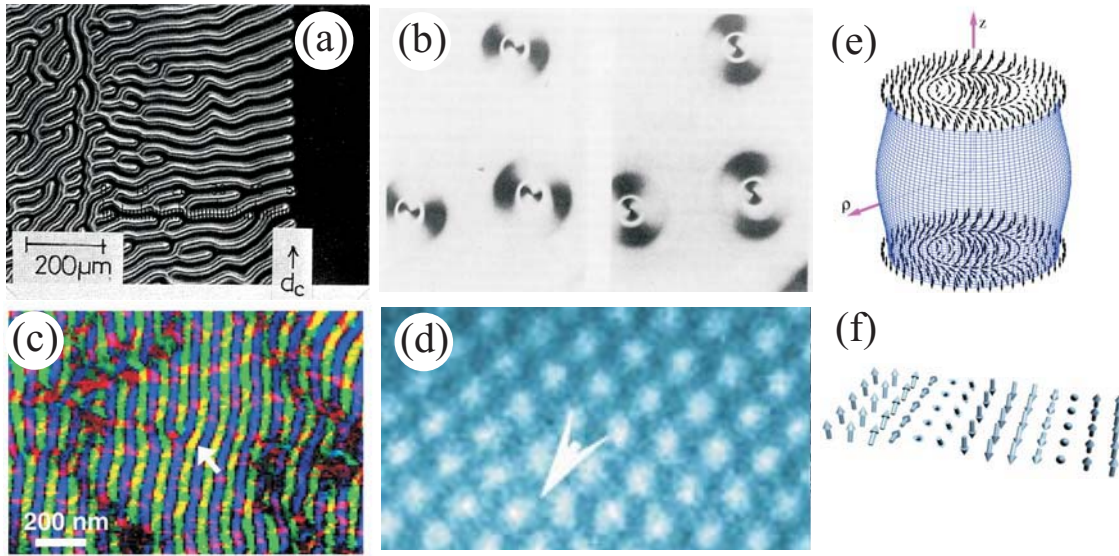


Figure 5.7.: Modulated phases in liquid crystals (a),(b) and their analogues in magnetic systems (c),(d): (a), (c) helical modulations in cholesterics [248] and in cubic helimagnets [271] with the distribution of the order parameters shown as a sketch in (f); (b), (d) isolated spherulites in a chiral liquid crystal [269] and hexagonal lattice of chiral skyrmions in (Fe,Co)Si [28]. (e) shows schematically the structure of a spherulite.

of Stieb [269] suggested that only one singular line is located along the axis of spherulite (Fig. 5.7 (b)). As well, according to the experiments of Pirkel et al. [270] the bubble domains can be formed from the looped finger in the cholesterics with positive dielectric anisotropy. In the present chapter I have shown that a non-singular model with a continuous distribution of the director field in the spherulite is among the solutions of the equations minimizing the Frank functional for the cholesteric layer with the homeotropic boundary alignment. Thus, the spherulitic bubbles in anchored chiral liquid crystal films [263–265] may be skyrmion textures.

## 5.9. Conclusions

In this chapter I investigated some effects imposed by the confined geometry of magnetic nanolayers on skyrmion states, namely, the influence of surface-induced anisotropy and demagnetizing fields on the stability and the structure of localized skyrmions. I showed that the surface-induced anisotropy produces pinning (anchoring) effect on magnetic states. It suppresses very effectively modulated skyrmion states and distorts the tubular structure of skyrmion filaments making them of convex-like shape with narrow "necks" near the surface. The similarity of phenomenological models for nonsingular spherulitics in liquid crystals and skyrmions in chiral magnetic materials offers new prospects for investigations of these solitonic states within a common theoretical approach. The rich experimental material on observation of spherulitic patterns in liquid crystals [248] in this sense can be used

as guidelines for investigations of skyrmion states in chiral magnetic layer systems.

Also in this section I addressed the problem of the influence of demagnetizing effects on the skyrmion solutions. I showed that skyrmions and magnetic bubble domains are two different branches of cylindrical magnetization structure with different mechanism of internal stabilization.





## 6. Confinement of skyrmion states in non-centrosymmetric magnets near ordering temperatures

In this chapter I consider skyrmionic states in non-centrosymmetric magnets near the ordering temperatures. I show that the interaction between the chiral skyrmions, being repulsive in a broad temperature range, changes into attraction at high temperatures. This leads to a remarkable *confinement* effect: near the ordering temperature skyrmions exist only as bound states. The confined skyrmions as discernible units may arrange in different mesophases. The confinement of multiple skyrmions is a consequence of the coupling between the magnitude and the angular part of the order parameter. Thus, near the ordering transitions, I consider the local magnetization not only as multiply twisted but also longitudinally modulated. From numerical investigations on 2D models of isotropic chiral ferromagnets, a staggered half-skyrmion square lattice at zero and low fields and a hexagonal skyrmion lattice at larger fields are found in overlapping regions of the phase diagram near the transition temperature. The creation of skyrmions as stable units and their condensation into different extended textures occurs simultaneously through a rare case of an instability-type nucleation transition [272]. As well, I introduce a new fundamental parameter, *confinement temperature*  $T_L$  separating the peculiar region with "confined" chiral modulations from the main part of the phase diagram with regular helical and skyrmion states.

### 6.1. Introduction

The peculiarities of the paramagnetic to helimagnetic transition in the intermetallic compounds MnSi and cubic polymorph FeGe have been investigated experimentally since a long time and seem to be related to the specific frustration introduced by the chiral Dzyaloshinskii-Moriya interactions. These compounds represent only two examples from the rich family of B20 magnets. The literature on the experiment in MnSi is overwhelming, this compound may be considered as a laboratory for investigation of chiral magnetic modulations near the ordering temperatures. The experiments on FeGe are still scarce. In the following I briefly summarize the main experimental results on the chiral magnetic properties of these compounds.

MnSi and FeGe crystallize in the B20 structure with the space group  $P2_13$  possessing no inversion symmetry and containing 3-fold axes along the  $\langle 111 \rangle$  space diagonals and 2-fold screw axes parallel to the cube axes. MnSi [80, 273] orders

magnetically at 29K and forms the helical modulation with the period of 18 nm. In another P2<sub>1</sub>3-compound FeGe [51] the ordered phase is observed below 280K: the propagation directions of the spirals point to  $\langle 100 \rangle$  crystallographic axes and change to  $\langle 111 \rangle$  with decreasing the temperature below 220K; the period of the spiral with 70 nm is much larger than in MnSi.

Intensive long-term experimental investigations of the chiral helimagnet MnSi and new experiments on FeGe report numerous physical anomalies along the magnetic ordering transition, and particularly, indicate the existence of a small closed area in  $(H, T)$  phase diagram, the so-called "A-phase" [78–80, 273–279, 281, 282]. As the modulation period is of the order of several hundred unit cells, the small angle neutron scattering is an appropriate tool to reveal different precursor anomalies. The first neutron scattering experiments on MnSi have been performed by Ishikawa [87] in 1976. In 1984 Ishikawa and Arai [279] interpreted the A-phase in MnSi as a paramagnetic state as no magnetic satellites around the nuclear peak were observed. Later, Lebech and Harris [273] revealed that the system in the A-pocket is still in a modulated state with the propagation direction perpendicular to the field. The magnetic phase diagram of MnSi close to the ordering temperature has been studied by different techniques, and the results were summarized by Kadowaki [80] (Fig. 6.1). Such a phase diagram based on ultrasound attenuation [274], ESR [283], magnetization and magnetoresistance [80] suggest the subdivision of the A-phase in different phases with phase separation lines between them. At least two subregions, A<sub>1</sub> and A<sub>2</sub>, can be singled out within the A-phase. Recent neutron scattering experiments revealed the six-spot pattern within the A-pocket [79] due to magnetic modulations transversal to the applied field and rather independent on the field direction. However, such "six spots" patterns as well as the Hall effect measurements [88] do not give the direct evidence for the existence of skyrmion states in the A-phase of MnSi. Note, that direct observation of skyrmions in nanolayers of FeGe [29] and (Fe,Co)Si [28] (see chapter 5, section 5.7) have been performed at temperatures far below the Curie ferromagnetic temperature and is not relevant to the A-phase. The phase diagram of FeGe near the ordering temperature also displays a complex structure of A-pockets with a complex succession of temperature- and field-driven crossovers and phase transitions [XIII].

In zero magnetic field the precursor effects have been observed above  $T_C$  as a ring of diffuse scattering in small angle neutron scattering on MnSi [78, 279, 280] and FeGe [51]. In both cases the radius of the ring is equal to the ordering wave vector. By doing neutron spin-echo spectroscopy [81] in MnSi such precursor effects were attributed to a non-trivial "spin-liquid phase" appearing in a limited temperature range just above  $T_C$ .

Described experiments show that the modulated phases mediating between paramagnetic and helical state in zero field or with applied magnetic field (the A-phase region) cannot be associated with a distinct simple phase. The A-phase must be explained by certain different mesophases. In this sense the current theoretical attempts to explain the A-phase by the formation of a specific modulated phase either with a one-dimensional (1D) modulation ("single"- $q$  helicoids) [89, 281, 282] or as "triple- $q$ " modulated textures [79] are considered to contradict the experimental



description of the inhomogeneous twisted magnetic structure in these mesophases.

## 6.2. Phenomenological theory and equations

Near the ordering temperatures the magnetization amplitude varies under the influence of the applied field and temperature. Commonly this process is described by supplementing the magnetic energy (4.1) with an additional term  $f_0(\mathbf{M})$  [99] (see Eq. (1.36)). By rescaling the spatial variable, the magnetic field, and the magnetization in (4.1)

$$\mathbf{x} = \frac{\mathbf{r}}{L_D}, \quad \mathbf{h} = \frac{\mathbf{H}}{H_0}, \quad \mathbf{m} = \frac{\mathbf{M}}{M_0} \quad (6.1)$$

where

$$L_D = \frac{A}{D}, \quad H_0 = \kappa M_0, \quad M_0 = \sqrt{\frac{\kappa}{a_2}}, \quad \kappa = \frac{D^2}{2A}, \quad (6.2)$$

energy density  $w_0(\mathbf{M})$  (4.1) can be written in the following reduced form

$$\Phi = (\mathbf{grad} \mathbf{m})^2 - w_D(\mathbf{m}) - \mathbf{h} \cdot \mathbf{m} + am^2 + m^4. \quad (6.3)$$

Coefficient  $a$  is expressed as

$$a = \frac{a_1}{\kappa} = \frac{J(T - T_c)}{\kappa}. \quad (6.4)$$

Alongwith three internal variables (components of the magnetization vector  $\mathbf{m}$ ) functional (6.3) includes only two control parameters, the reduced magnetic field amplitude,  $h$ , and the "effective" temperature  $a(T)$  (6.4). By direct minimization of Eq. (6.3) one can derive one-dimensional (helicooids and conical helices) and two-dimensional skyrmions (isolated and bound states) for arbitrary values of the control parameters. As in the chapter 4, I analyse first solutions for localized isolated skyrmions.

## 6.3. Solutions for high-temperature isolated skyrmions

The structure of isolated skyrmions near the ordering temperature is characterized by the dependence of the polar angle  $\theta(\rho)$  and modulus  $m(\rho)$  on the radial coordinate  $\rho$  (in chapter 4 only angular order parameter  $\theta(\rho)$  has been considered). The total energy  $E$  of such a skyrmion (per unit length along  $z$ ) after substituting  $\psi(\phi)$  (see dependences  $\psi(\phi)$  corresponding to different crystallographic classes in section 4.4 and Fig. 4.3) is as follows:

$$E = 2\pi \int_0^\infty \Phi(m, \theta) \rho d\rho \quad (6.5)$$

where energy density is

$$\Phi = m_\rho^2 + m^2 \left[ \theta_\rho^2 + \frac{\sin^2 \theta}{\rho^2} - \theta_\rho - \frac{\sin \theta \cos \theta}{\rho} \right] + am^2 + m^4 - hm \cos \theta \quad (6.6)$$

with a common convention  $\partial f / \partial x \equiv f_x$ . The Euler equations for the functional (6.3)

$$\begin{aligned} m^2 \left[ \theta_{\rho\rho} + \frac{\theta_\rho}{\rho} + \frac{\sin \theta \cos \theta}{\rho^2} + \frac{2 \sin^2 \theta}{\rho} - h \sin(\theta) \right] + 2(\theta_\rho - 1)m_\rho &= 0, \\ m_{\rho\rho} + \frac{m_\rho}{\rho} + m \left[ \theta_\rho^2 + \frac{\sin^2 \theta}{\rho^2} + \theta_\rho + \frac{\sin \theta \cos \theta}{\rho} \right] + 2am + \\ &+ 4m^3 - h \cos(\theta) = 0 \end{aligned} \quad (6.7)$$

with boundary conditions

$$\theta(0) = \pi, \theta(\infty) = 0, m(\infty) = m_0, m(0) = m_1 \quad (6.8)$$

describe the structure of isolated skyrmions. The magnetization of the homogeneous phase  $m_0$  is derived from equation:

$$2am_0 + 4m_0^3 - h = 0. \quad (6.9)$$

Eq. (6.7) can be solved numerically. But before to consider typical solutions  $\theta(\rho)$ ,  $m(\rho)$  of Eqs. (6.7) I consider the asymptotic behaviour of skyrmion solutions and some remarkable results that can be obtained by simple means. For 1D kinks such an analysis was done in Refs. [284, 285].

### 6.3.1. Crossover of skyrmion-skyrmion interactions

As it was determined in sect. 4.4, the asymptotic behaviour of isolated skyrmions bears exponential character [21]:

$$\Delta m = (m - m_0) \propto \exp(-\alpha\rho), \theta \propto \exp(-\alpha\rho). \quad (6.10)$$

By substituting these to the linearized Euler equations (6.7) for  $\rho \rightarrow \infty$

$$\begin{aligned} \Delta m_{\rho\rho} - m_0 \theta_\rho - \frac{1}{2} f_{mm}(m_0) \Delta m &= 0, \\ m_0^2 \theta_{\rho\rho} - \frac{h\theta}{2} m_0 + m_0 \Delta m_\rho &= 0 \end{aligned} \quad (6.11)$$

one finds three distinct regions in the magnetic phase diagram on the plane  $(a, h)$  with different character of skyrmion-skyrmion interactions (Fig.6.2): *repulsive* interactions between isolated skyrmions occur in a broad temperature range (area (I)) and is characterized by real values of parameter  $\alpha \in \Re$ , the magnetization in such skyrmions has always "right" rotation sense; at higher temperatures (area (II)) the skyrmion-skyrmion interaction changes to *attractive* character with  $\alpha \in C$ ; finally, in

area (III) near the ordering temperature,  $a_N = 0.25$ , only strictly confined skyrmions exist with  $\alpha \in \mathfrak{S}$ .

Equation for parameter  $\alpha$  obtained from (6.11)

$$\alpha^4 + \alpha^2[-2a - 8m_0^2 + 1] + (a + 6m_0^2)(a + 2m_0^2) = 0 \quad (6.12)$$

allows to write the equation for the line separating different regions:

$$\left(f_{mm}(m_0) - \frac{f_m(m_0)}{m_0}\right)^2 - 4\left(f_{mm}(m_0) + \frac{f_m(m_0)}{m_0}\right) + 4 = 0, \\ h = f_m(m_0). \quad (6.13)$$

For the particular case of Landau expansion (1.36) the separating line looks like

$$h^* = \sqrt{2 \pm P(a)}(a + 1 \pm P(a)/2), \quad P(a) = \sqrt{3 + 4a} \quad (6.14)$$

with turning points  $p$   $(-0.75, \sqrt{2}/4)$ ,  $q$   $(0.06, 0.032\sqrt{5})$ , and  $u$   $(-0.5, 0)$  (dashed line in Fig. 6.2 (a)).

The typical solutions as profiles  $\theta(\rho)$ ,  $m(\rho)$  for isolated skyrmions in each region are plotted in Fig. 6.2 (b)-(c). As in the region II the exponents  $\alpha$  are complex numbers, the profiles display antiphase oscillations (Fig. 6.2 (c)). Rotation of the magnetization in such an isolated skyrmion contains two types of rotation since: if rotation has "right" sense, the modulus increases, and otherwise, modulus decreases in parts of the skyrmion with "wrong" rotation sense. Such a unique rotational behaviour of the magnetization is a consequence of the strong coupling between two order parameters of Eq. (6.7) - modulus  $m$  and angle  $\theta$ .

### 6.3.2. Collapse of skyrmions at high fields

The solutions of Eqs. (6.7) exist only below a critical line  $h_0(T)$  (Fig. 6.2 (a)). As the applied field approaches this line, the magnetization in the skyrmion center  $m_1$  (Eq. (6.8)) gradually shrinks (Fig. 6.3 (b)), and as  $m_1$  becomes zero, the skyrmion collapses. This is in contrast to low-temperature skyrmions which exist without collapse even at very large magnetic fields [21] and are protected by the stiffness of the magnetization modulus which maintains topological stability of skyrmions. At high temperatures the softness of the magnetization amplitude allows to destroy the core of the skyrmion by "forcing" through the magnetization vector  $m_1$  along the applied field. The angle  $\theta$  nevertheless undergoes strong localization as it was also noted for "low-temperature" skyrmions (Fig. 6.3 (a)). As an example, I illustrated the magnetization process for an isolated skyrmion for  $a = -0.5$  (Fig. 6.3).

### 6.3.3. Phenomenon of confinement

The coupling of angular and longitudinal order parameters may be so strong, that oscillations in the asymptotics of isolated skyrmions do not diminish. The purely

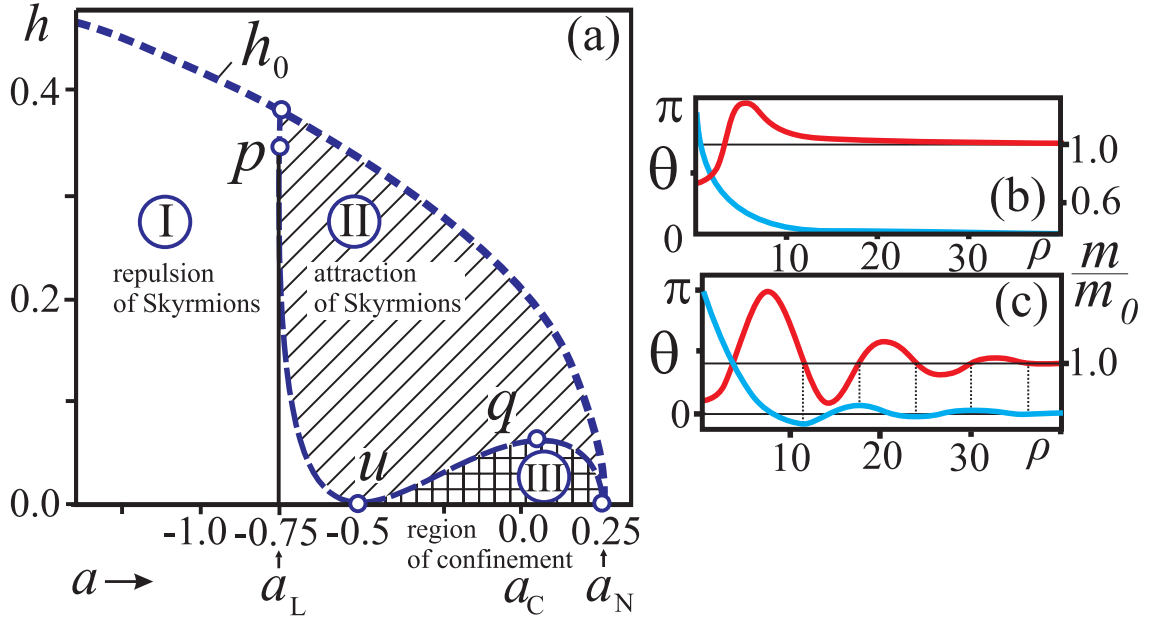


Figure 6.2.: The diagram on plane  $(a, h)$  showing the regions with different types of skyrmion-skyrmion interaction: I - repulsive interaction between isolated skyrmions; II - attractive inter-skyrmion interaction; III - the region of skyrmion confinement. Dashed line is defined by the Eq. (6.14): the turning points have the following coordinates -  $p$   $(-0.75, \sqrt{2}/4)$ ,  $q$   $(0.06, 0.032\sqrt{5})$ , and  $u$   $(-0.5, 0)$ . Above the line  $h_0$  no isolated skyrmions can exist. (b) Dependences of angular  $\theta$  and longitudinal  $m$  order parameters on polar coordinate  $\rho$  for isolated skyrmion in region I ( $a = -1, h = 0.4$ ). (c)  $\theta(\rho)$  and  $m(\rho)$  for isolated skyrmion in region II ( $a = 0.21, h = 0.05$ ).

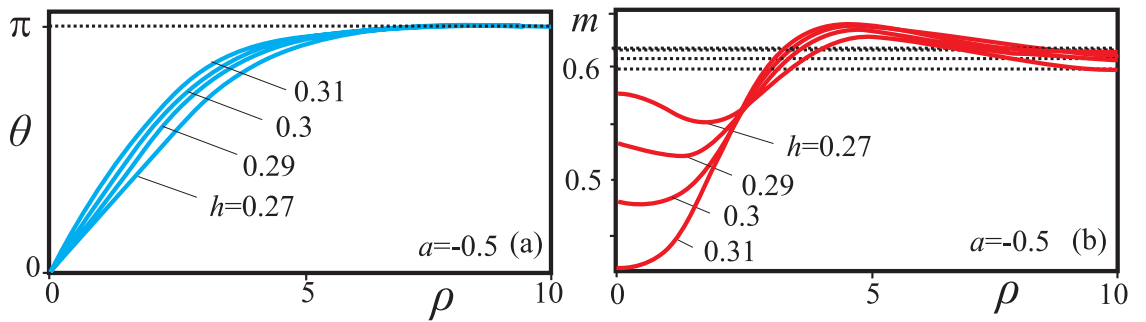


Figure 6.3.: Increasing magnetic field applied to isolated skyrmion ( $a = -0.5$ ) localizes profiles  $\theta(\rho)$  (a) and leads to the disappearance of isolated skyrmions by squeezing out modulus  $m_1$  in the center (b).

imaginary exponent  $\alpha$  then reflects the region of strict confinement. For  $-0.5 < a < 0.25$  line (6.14) delimits a small pocket (III) in the vicinity of the ordering temperature. Within this region skyrmions can exist only as bound states and drastically differ from those in the main part of the phase diagram.

The confinement temperature  $a_L = -0.75$  subdivides the temperature interval in low- and high-temperature parts: (i) in the main part ( $a < a_L = -0.75$ ) the rotation of the local magnetization vector determines the chiral modulation, while the magnetization amplitude remains constant; (ii) at high temperatures ( $a_L = -0.75 < a < a_N = 0.25$ ) spatial variation of the magnetization modulus becomes a sizeable effect, and strong interplay between longitudinal and angular variables is the main factor in the formation and peculiar behaviour of chiral modulations in this region.

The *confinement temperature*  $a_L$  [XII,XIV,XV] provides the scale that delineates the border between these two regimes in the phase diagram. The characteristic temperature  $a_L$  is of fundamental importance for chiral magnets. It is of the same order of magnitude as the temperature interval

$$(a_N - a_c) \propto \frac{D^2}{A} \quad (6.15)$$

(Fig. 6.2 (a)), where chiral couplings cause inhomogeneous precursor states around the magnetic order temperature (for details see Ref. [31]). Here,  $a_c$  is the conventional Curie temperature for centrosymmetric systems. When the temperature drops below  $a_c$ , the energy density of a ferromagnetically spin-aligned state is the lowest one. Dzyaloshinskii-Moriya interactions with negative energy density favour the rotation of the moments. Therefore, the transition to the ferromagnetic state is preceded by a transition to modulated states at the temperature  $a_N$ . Due to the relativistic origin and corresponding weakness of the DM exchange the shift

$$\Delta a_1 = a_N - a_c, \quad (6.16)$$

as well as

$$\Delta a_2 = a_N - a_L, \quad (6.17)$$

is small. For MnSi  $\Delta a_1$  is estimated to be 0.9 K [31]. The shift  $\Delta a_2$  must be three times as large as  $\Delta a_1$  [XII,XIV,XV].

The crossover and confinement effects arise as a generic property of the asymptotic behavior of chiral solitons at large distances from the core. These effects also apply to kinks [284, 285] and Hopfions [286].

## 6.4. The structure and properties of confined skyrmions

Isolated skyrmions condense into a hexagonal lattice below a field  $h_c$  (red line in Fig. 6.5), which marks the transition between the  $-\pi$ -skyrmion lattice (Fig. 6.4 (a)) and



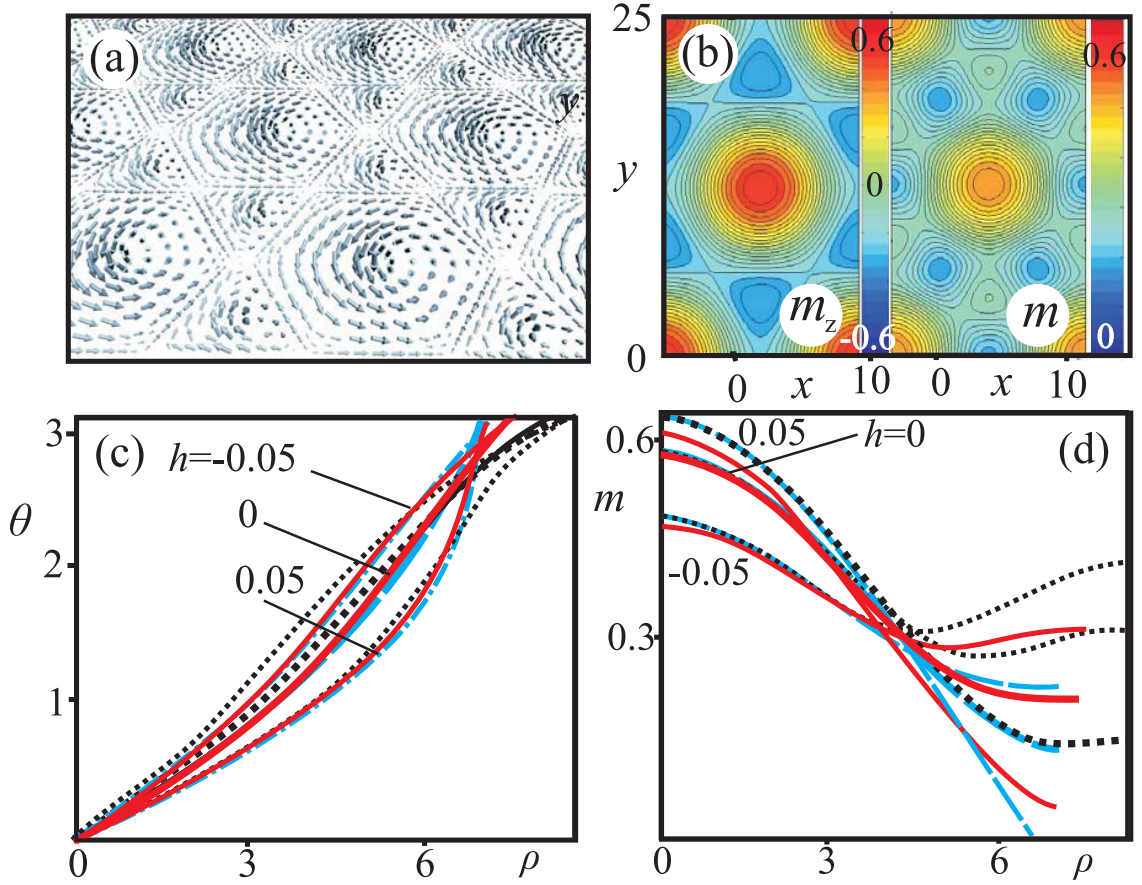


Figure 6.4.: The structure of the hexagonal skyrmion lattice near the ordering temperature  $a_N$  ( $a = 0.23$ ,  $h = 0$ ) shown as a sketch with the distribution of the magnetization vectors (a) and the contour plots of the  $m_z$ -component of the magnetization and its length  $m$  (b). In spite of the triangular region with the magnetization opposite to the magnetization in the "main" hexagon which are invoked to reduce the heightened energy density along the apothem of the hexagon (for details see Fig. 4.7 and the explanation in the section 6.4), the circular-cell approximation is a good approach to describe the field- and temperature-driven processes of such a lattice. (c), (d) Profiles  $\theta(\rho)$  and  $m(\rho)$  in the hexagonal cell for two different perpendicular directions through the core (blue dashed and black dotted lines) plotted together with the solutions for skyrmion in the circular-cell approximation in the applied positive and negative magnetic field (red solid lines).

the homogeneous paramagnetic state. The typical contour plots of  $m_z$ -component of the magnetization and the modulus  $m$  in the hexagonal skyrmion lattice near the ordering temperature are depicted in Fig. 6.4 (b). It is seen that the central hexagon of the contour plot for  $m_z$ -component has been rotated in comparison with the hexagon with constant value of the magnetization length (Fig. 4.6 (a)). Moreover, this hexagon is enclosed by six triangular regions with the magnetization opposite to that in the center of the "main" hexagon. Such a redistribution of the magnetization at the outskirts of the lattice cell might be explained by the fact that the total energy density along the apothem of the hexagon (dotted black line in Fig. 4.7) is larger than the energy along the diagonal (dashed line in Fig. 4.7). Therefore, the system tries to suppress energetically unfavourable regions by squeezing the value of the modulus [XII,XIV,XV].

The solutions for skyrmion lattices in this chapter are obtained by using finite differences for gradient terms and adjustable grids to accommodate modulated states with periodic boundary conditions (see description of the numerical recipes in Sect. 4.5.1). In addition to the angular degree of freedom, high-temperature solutions were minimized also with respect to the length of the magnetization vector in each point of the numerical grid.

As a cross-check of obtained results, I have used the circular-cell approximation as described in Sect. 4.5.1. According to the method, the hexagonal cell is replaced by a circle, and one has to solve the system of differential equations (6.7) with the boundary conditions:

$$\theta(0) = \pi, \theta(R) = 0, m(R) = m_2, m(0) = m_1. \quad (6.18)$$

Solving these equations, where the order parameters depend only on one spatial coordinate, is essentially easier than rigorous solution for the 2D magnetization structures. In Fig. 6.4 (c), (d) I have plotted the angular and longitudinal profiles for the skyrmions in the circular-cell approximation (red lines) and from the numerical simulations on the two-dimensional grid along perpendicular directions in the hexagon (dotted black and dashed blue lines). The circular-cell approximation describes surprisingly well the skyrmion structures and their transformation with temperature and magnetic field inspite the triangular regions with opposite magnetization and slight difference for the longitudinal profiles in the applied magnetic field (Fig. 6.4 (d)). Moreover, such an approximation allows to analyse the processes with skyrmion lattices from another perspective and to plot dependences to be hardly achieved for rigorous 2D solutions. As an example I consider the process of condensation of isolated skyrmions into the lattice.

### 6.4.1. Condensation of isolated skyrmions into the lattice

In the region II of the phase diagram a transition of a hexagonal skyrmion lattice into the homogeneous state is of the first order on the contrary to the second-order phase transition in the "low-temperature" region I. Thus, the hysteretic magnetization process between homogeneous state and skyrmion lattice is expected. The

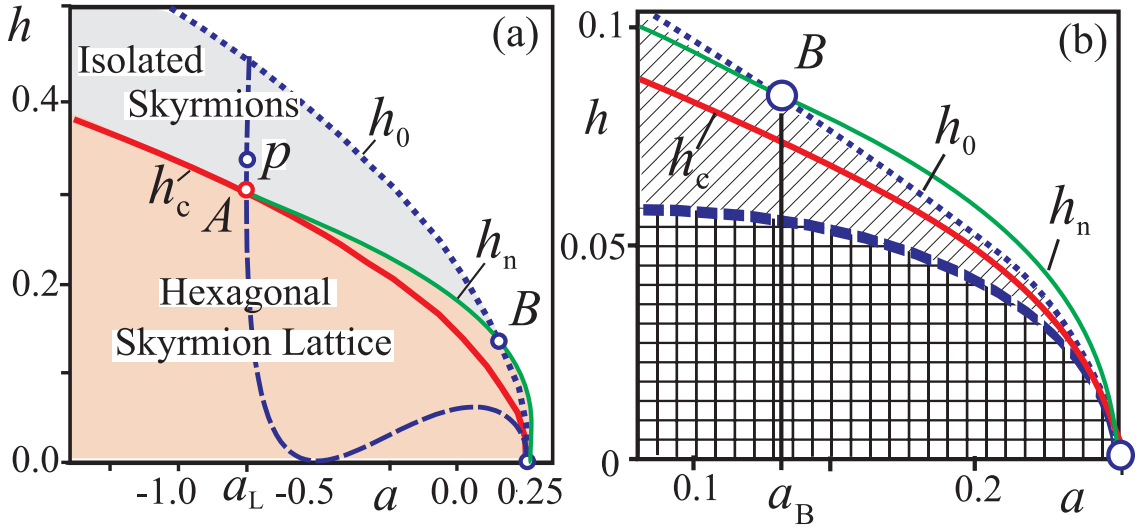


Figure 6.5.: (a) Phase diagram - magnetic field  $h$  vs. temperature  $a$ . Below the line  $h_c$  skyrmions condense into a hexagonal lattice. For  $a < a_L$  the transition is second-order phase transition of nucleation type. For  $a > a_L$  the transition becomes first-order phase transition. The hexagonal skyrmion lattice exists as metastable state up to the nucleation field  $h_n$ . For temperatures between points A and B,  $h_n < h_0$ , for larger temperatures  $a_B < a < a_N = 0.25$  the isolated skyrmions disappear at lower fields than the dense skyrmion lattice,  $h_0 < h_n$ . For clarity, line  $h_n$  is only schematically given in panel (a), numerically exact data are shown in panel (b).

hysteretic character of the transition can be illustrated by plotting the energy density of skyrmion bound states (Fig. 6.6 (a)) depending on the modulus  $m_2$  at the outskirts of the lattice cell (see boundary conditions of Eq. (6.18)). In the interval of magnetic fields  $h_h < h < h_n$  the energy density has two minima corresponding to homogeneous state and hexagonal skyrmion lattice, respectively. The fields  $h_h$  (not shown in Fig. 6.5) and  $h_n$  mark the boundaries where homogeneous state and skyrmion lattice lose their stability, respectively. On the line  $h_c$  (Fig. 6.5) the energy of the hexagonal lattice equals that of the homogeneous state. In the interval  $h_c < h < h_n$  the hexagonal skyrmion lattice exists as a metastable state.

Solutions for  $\theta(\rho)$  and  $m(\rho)$  in some points of the curve of energy density are plotted in Fig. 6.6 (b), (c). I start from the usual skyrmion bound state (point 1) and gradually decrease the modulus on the boundary of the lattice cell. Angular profile becomes more localized (point 2) and for some value of  $m_2$  there is no skyrmion lattice anymore. Instead of the hexagonal lattice the system of differential equations (6.7) has a solution for a modulated state with the modulus in the center and at the outskirts pointing in the same direction (point 3 with  $\theta(0) = \theta(R) = \pi$ ). During this process modulus in the center  $m_1$  goes through zero and the magnetization in the center is reversed to the other side. Decreasing  $m_2$  further, the homogeneous state is reached.

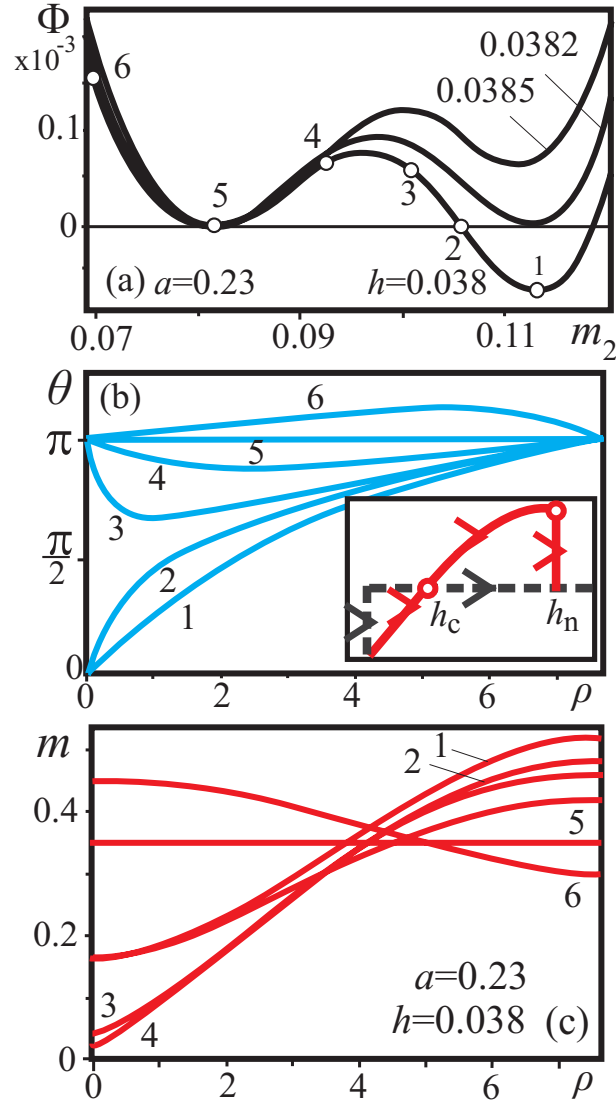


Figure 6.6.: Energy density  $\Phi$  (Eq. (6.6)) in dependence on the modulus  $m_2$  at the boundary of skyrmion lattice cell (a) (see boundary conditions of Eq. (6.18)) exhibits two pronounced minima corresponding to  $-\pi$ -skyrmion lattices (points 1) and homogeneous state (point 5). Changing the modulus  $m_2$  as a parameter one can smoothly turn the hexagonal skyrmion lattice into the homogeneously magnetized state. Profiles  $\theta = \theta(\rho)$  (b) and  $m = m(\rho)$  (c) make it possible to trace the process of the transformation: in the intermediate points 3 and 4 the system of differential equations (6.7) has as a solution modulated states with the magnetization in the center and at the periphery pointing in the same direction (in the present case, along the field); in the point 5 the homogeneous state with  $\theta = 0$ ,  $m = m_0$  shows up. Such a magnetization process bears pronounced hysteretic character and takes place in the field interval  $h_h < h < h_n$ .

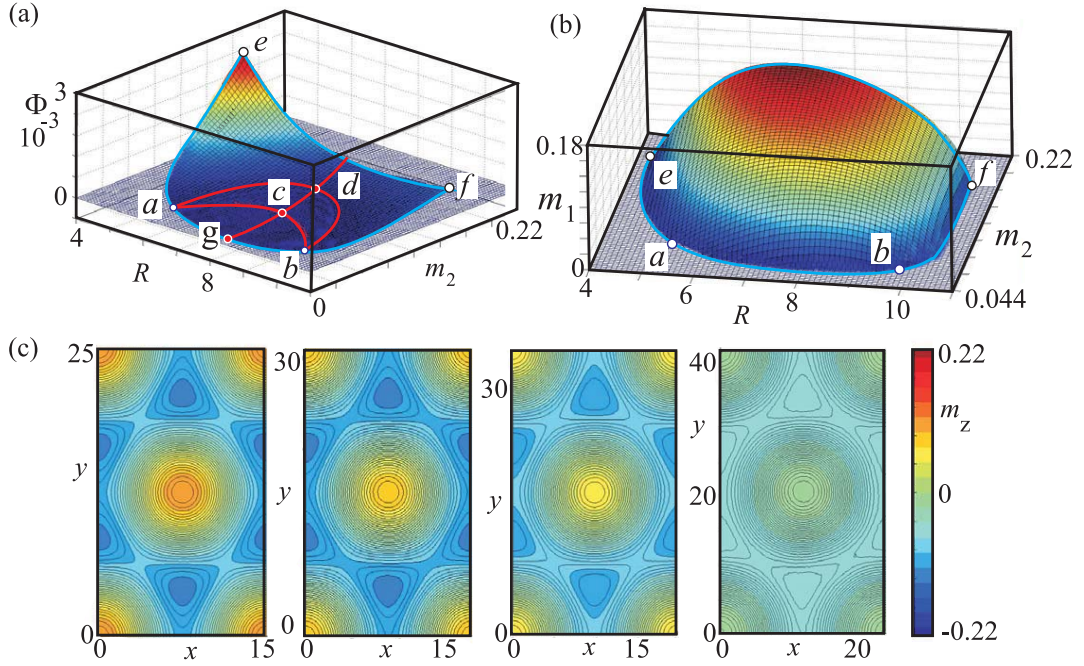


Figure 6.7.: (a) Difference of energy densities of hexagonal skyrmion lattice and homogeneously magnetized state plotted as a surface in dependence on the radius  $R$  of the lattice cell in circular-cell approximation and modulus at the boundary  $m_2$  in correspondence with Eq. (6.7) and boundary conditions (6.18). The minimum in the point  $c$  contains the equilibrium skyrmion lattice  $m_z$ -component of which is shown in the first snapshot of (c). (b) modulus in the center of the lattice cell plotted as a surface in dependence on the radius  $R$  and  $m_2$ . (c) the succession of snapshots of the skyrmion lattice along the line  $c - b$ . Deviation from the minimum of energy leads to the destruction of the lattice in the point  $b$  (see text for details).

### 6.4.2. Peculiar properties of bound skyrmions in the region of confinement

As it was already noted, strong interplay between longitudinal and angular variables is the main factor in the formation and peculiar behaviour of chiral modulations in the region of confinement. The confined skyrmions drastically differ from their "low-temperature" counterpart considered in chapter 4. Some properties of them can be described by the dependence of the radial structure on the moduli in the center  $m_1$  and at the boundary  $m_2$  in the circular-cell approximation as it was introduced in section 6.4.1. The skyrmions in the confinement region can exist only as bound states ideally as a condensed lattice. Trying to expand the skyrmion lattice, one immediately destroys it. In Fig. 6.7 (a) I have plotted the energy density of the hexagonal skyrmion lattice with respect to the homogeneous state in dependence on the radius  $R$  and the modulus  $m_2$  at the boundary of a lattice cell

( $a = 0.23$ ,  $h = 0.03$ ). In Fig. 6.7 (b) the modulus  $m_1$  in the center of skyrmion cell in dependence on the radius  $R$  and  $m_2$  is depicted.

The equilibrium state of the lattice corresponds to the minimum of the energy density (point c). For fixed modulus  $m_2$  and variable radii  $R$  the minimum of the energy density is located at the line  $g - c - d$ . In the point  $d$  (and at the line  $a - d - b$ ) the energy density becomes zero, and homogeneous state has lower energy than skyrmion lattice in the region  $a - e - f - b - d - a$ . In the point  $g$  the modulus  $m_1$  in the center of the lattice cell goes through zero, and the lattice disappears. Such a process of the lattice destruction by squeezing the modulus in the center takes place in whole at the line  $e - a - g - b - f$  (Fig. 6.7 (a), (b)).

With fixed radius  $R$  and variable modulus  $m_2$  the minimum of energy density is localized at the line  $a - c - b$ . The sequence of the snapshots of the lattice exhibits the states along the line  $c - b$  with the final homogeneous state reached in the point  $b$ .

By playing with the modulus  $m_2$  at the outskirts of the lattice cell I can demonstrate also the transformation of the skyrmion lattice from the state with magnetization in the center opposite to the applied magnetic field ( $-\pi$ -skyrmions) to the state with the magnetization along the field ( $+\pi$ -skyrmions). In Fig. 6.8 (a) I have plotted the energy density (Eq. (6.6)) in dependence on  $m_2$  which exhibits two pronounced minima with  $\pm\pi$ -skyrmion lattice in each of them. On the path from  $+\pi$ -skyrmions (point 5) to  $-\pi$ -skyrmions (point 1) transitional structures as homogeneous state (point 3) or different modulated states with the same direction of the magnetization in the center and at the boundary (point 4) are met.

### 6.4.3. The structure of staggered half-skyrmion lattices

The half-skyrmion lattice depicted in Fig. 6.14 (a) represents a special case of modulated state near the ordering temperature which does not have "low-temperature" counterpart with a fixed modulus. A lattice of half-skyrmions is a solution for 2-dimensional energy functional (6.3) and has been calculated by brute-force energy minimization (it is impossible to exploit the circular-cell approximation in this case). The condensed square structure has been described as a staggered and chiral lattice composed of half-skyrmions with four of them forming one unit conventional square lattice cell with lattice parameter  $L$  (Fig. 6.14). These four half-skyrmions are arranged in a staggered up/down pattern. One 4th plaquette cell with side lengths  $L/2$  of this structure is what I will call a square half-skyrmion cell. The field configuration of this half-skyrmion has the magnetization perpendicular  $m = (m_x; m_y; m_z) = (0; 0; \pm m_0)$  at the center,  $r = (L/4; L/4)$ . However,  $|\mathbf{m}|$  is a spatially varying function with  $m_0 > 0$  being the maximum value of this soft magnetization order parameter in the structure. Around this center, the magnetization vector circulates once through the full circle. At the edge  $C$  of this square cell,  $m$  is in the plane. Thus, the polar angle  $\theta = \arccos(\mathbf{m} \cdot \hat{\mathbf{z}})$  of the structure rotates from 0 to  $\pi/2$  from center to edge of the square cell. It is clear that this is not the full skyrmion, it is only a piece of a skyrmion solution and it cannot exist as an isolated



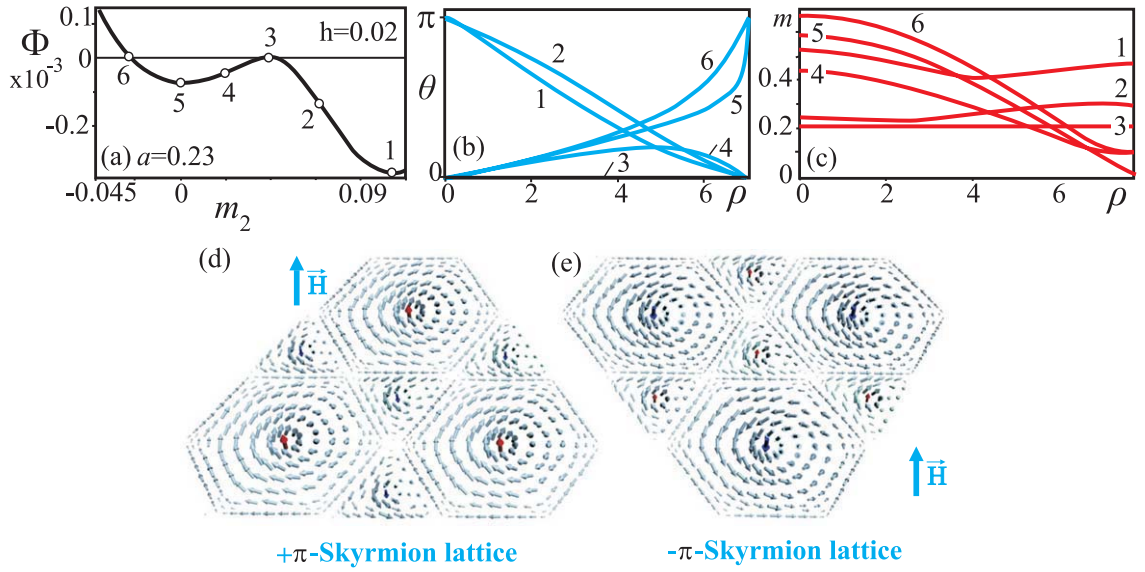


Figure 6.8.: Energy density (Eq. (6.6)) in dependence on the modulus  $m_2$  at the boundary of skyrmion lattice cell (a) exhibits two pronounced minima corresponding to  $+\pi$  and  $-\pi$ -skyrmion lattices (points 5 and 1, respectively). Changing the modulus  $m_2$  as a parameter one can smoothly turn one skyrmion lattice into the other. Profiles  $\theta = \theta(\rho)$  (b) and  $m = m(\rho)$  (c) make it possible to trace the process of the transformation: in the intermediate point 4 the system of differential equations has as a solution modulated states with the magnetization in the center and at the periphery pointing in the same direction (in the present case, along the field); in the point 3 the homogeneous state with  $\theta = 0$ ,  $m = m_0$  shows up.

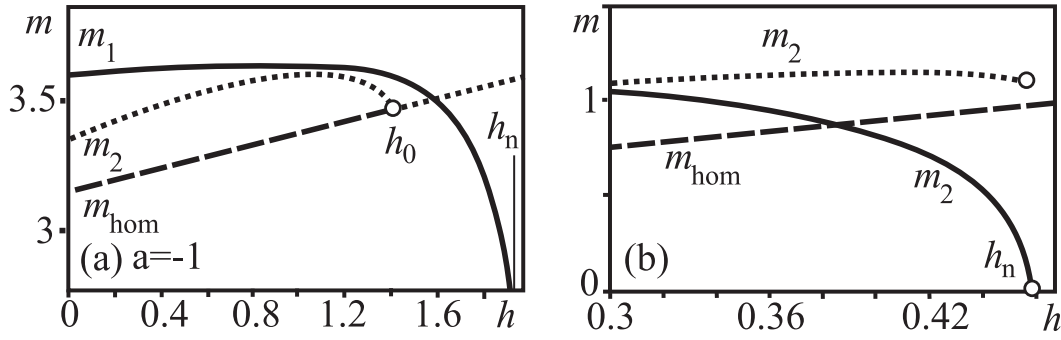


Figure 6.9.: Dependences of moduli in the center  $m_1$  and at the boundary  $m_2$  of the skyrmion cell on the applied magnetic field  $h$  for two values of reduced temperature  $a = -1$  (a) and  $a = 0.14$  (b). In the first case (a) modulus  $m_2$  at the outskirt "meets" the modulus of the homogeneous state  $m_{\text{hom}}$  for  $h = h_0$ . The period of the lattice in this point expands infinitely and only isolated skyrmions can exist. With  $h = h_n$  marking the transition into homogeneous state, the modulus  $m_1$  in the isolated skyrmion goes through zero. In the second case (b) the modulus  $m_1$  in the center of the skyrmion cell shrinks to zero faster than the lattice expands into the isolated skyrmions. The bound and isolated skyrmions are two distinct branches of solutions which cannot be turned each into other (the oscillations of order parameters are very pronounced for  $a > a_B$ ).

localized structure. The topological charge of such a cell

$$Q = \frac{1}{4\pi} \int_0^{L/2} \int_0^{L/2} dx dy \mathbf{m} \cdot [\partial_x \mathbf{m} \times \partial_y \mathbf{m}] \quad (6.19)$$

is  $Q = 1/2$ . Thus, from the topological point of view, the square (sub)-cells of the lattice structure could be identified with merons [287]. The value of  $Q$  depends on the integration region being only a finite part of the 2D plane. Only the definite choice of the square cell fixes this value of  $Q$  unambiguously. Following terminology proposed, e.g., by Rajaraman and co-workers [287] I call the textures in such square cells half-skyrmions. The arrangement of half-skyrmions necessitates that the magnetization  $m = 0$  at  $(L/2; L/2)$  passes through zero to match the half-skyrmion configurations in the interstitial regions between the radial and chiral skyrmionic cores. Here, the corresponding field configuration of the in-plane unit vector  $\mathbf{m} = (m_x; m_y; 0)$  is an anti-vortex.



## 6.5. The field-driven transformation of skyrmion lattices near the ordering temperature

### 6.5.1. Transformation of $-\pi$ -skyrmion lattice

In the applied magnetic field the hexagonal  $-\pi$ -skyrmion lattice disappears at the lability line  $h_n$ : to the left side of the point B (Fig. 6.5) the lattice releases the free isolated skyrmions (the oscillations of the order parameters are almost undetectable for  $a < a_B$ ); to the right side of the point B the skyrmion lattice transforms into homogeneous state with modulus in the center of the lattice cell going through zero. Therefore, the temperature  $a_B$  can serve as another characteristic landmark together with the confinement temperature  $a_L$ .

In Fig. 6.9 I have plotted dependences of moduli in the center  $m_1$  and at the boundary  $m_2$  of the lattice cell on the magnetic field for two different values of reduced temperature  $a = -1$  (Fig. 6.9 (a)) and  $a = 0.14$  (Fig. 6.9 (b)) which characterize the described behavior.

In the first case ( $a = -1$ ) the modulus at the outskirts of skyrmion lattice becomes equal to that of the homogeneous state, the lattice expands and only isolated skyrmions can exist. Then with increasing magnetic field, modulus  $m_1$  in the center of isolated skyrmion goes through zero and the skyrmion collapses. Such a case corresponds to the major part of the phase diagram for  $a < a_B$ . The evolution of skyrmion lattices under a magnetic field closely agrees with the behavior studied earlier for the low-temperature limit [21,69]: the transition mechanism at the high-field limit is of the nucleation type with isolated skyrmion excitations appearing below the instability line  $h_0$ .

In the second case ( $a = 0.14$ ), however, the modulus  $m_1$  in the center of the skyrmion goes through zero while the skyrmion lattice still is intact. Such a lattice does not set free isolated skyrmions. Isolated skyrmions exist as a different branch of solutions and cannot condense into the lattice. As an example of such an isolated skyrmion, I consider its structure for some parameters  $a$  and  $h$  where oscillations in the skyrmion asymptotics are pronounced (for instance, for  $a = 0.21$ ,  $h = -0.048$ ). The isolated skyrmion is embedded into the homogeneously magnetized state, and the size of the numerical grid is chosen to guarantee the full decay of oscillations in the skyrmion tail. In Fig. 6.10 (a) I have plotted the dependences of modulus and  $z$ -component of the magnetization through the cross section of isolated skyrmion. Contour plots of each component of the magnetization are depicted in 6.10 (b).

For the purpose of investigation of skyrmion-skyrmion interaction, I introduce two skyrmions into a square sample and define the interaction energy per skyrmion  $\varepsilon_{\text{int}}$  versus the inter-skyrmion distance  $L$  (Fig. 6.11). Due to the strongly oscillatory character of this dependence two isolated skyrmions will tend to locate at some discrete, equilibrium distances from each other and to be placed in minima of inter-skyrmion energy  $\varepsilon_{\text{int}}$ . On the other hand, single isolated skyrmion (minimum corresponding to  $L = 0$ ) cannot elongate into the pair of skyrmions because of the high potential barrier toward the minimum with finite  $L$  (the first deepest minimum

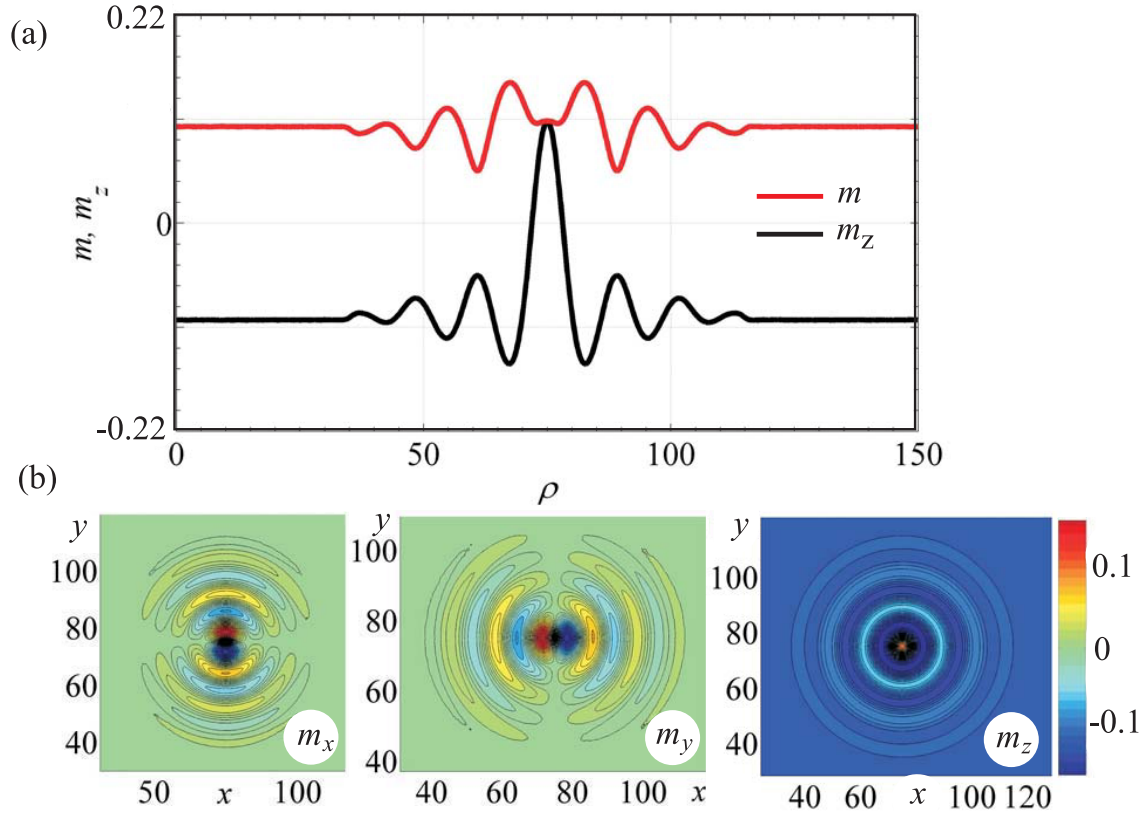


Figure 6.10.: (a) Structure of isolated skyrmion characterized by the dependencies of the modulus (red line) and  $m_z$ -component of the magnetization (black line) in the cross-section for  $a = 0.21$ ,  $h = -0.048$ ; (b) contour plots of the components of the magnetization.

of  $\varepsilon_{\text{int}}$ ). Adding skyrmions one by one an optimal number of skyrmions in the cluster is found - the isolated skyrmions tend to form the hexagonal lattice with the densest space filling. The deepest minimum of  $\varepsilon_{\text{int}}$  for two interacting isolated skyrmions is very close to the period of hexagonal skyrmion lattice existing for the same control parameters. Importantly, in the very narrow region between the lines  $h_0$  and  $h_n$  (Fig. 6.5 (b)) skyrmions can exist only as bound states in the form of perfect hexagonal lattice or different cluster formations [XII,XIV,XV].

In Fig. 6.12 I depict the process of transformation of the  $-\pi$ -skyrmion lattice into the homogeneous state for  $a = 0.23$  and some characteristic values of the applied magnetic field  $h$ . Due to the "softness" of the magnetization modulus the field-driven transformation of the skyrmion lattice evolves by distortions of the modulus profiles  $m(\rho)$  while the equilibrium period of the lattice does not change strongly with increasing applied field. Despite the strong transformation of the internal structures the skyrmion lattice preserves *axisymmetric* distribution of the magnetization near the center of the skyrmion lattice cell (Fig. 6.12). As for "low-temperature" skyrmions with constant modulus, the local energetic advantage of skyrmion lattices with soft modulus over helicoids is due to a larger energy reduction in the "double-

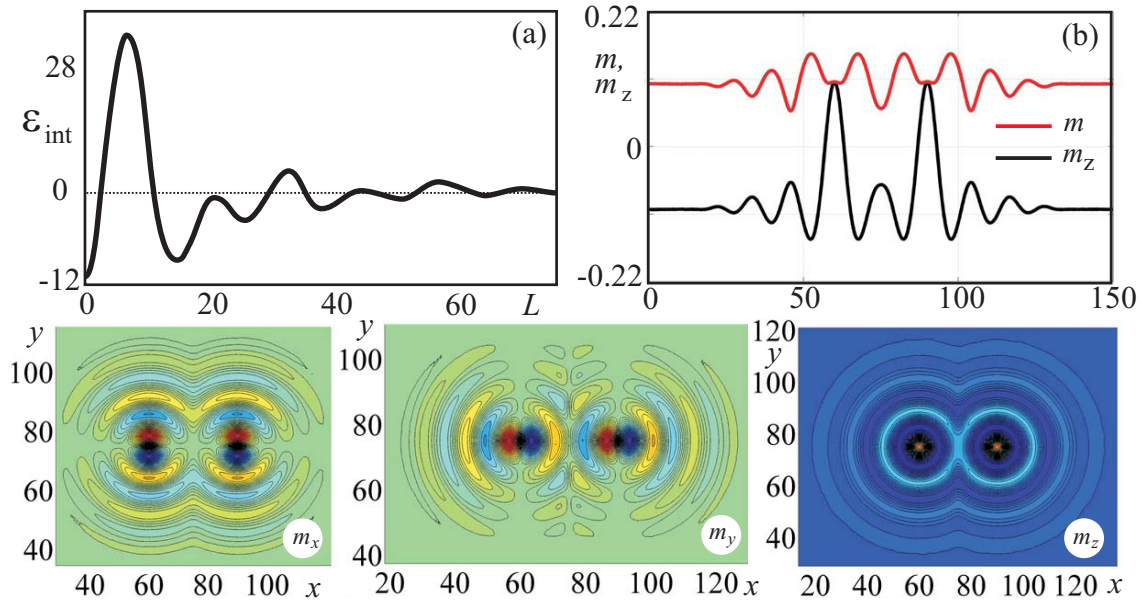


Figure 6.11.: (a) The skyrmion-skyrmion interaction energy  $\varepsilon_{\text{int}}$  plotted in dependence on the distance  $L$  between the centers of two isolated skyrmions. (b) Dependencies of the modulus (red line) and  $m_z$ -component of the magnetization (black line) in the cross-section of two interacting isolated skyrmions for  $a = 0.21$ ,  $h = -0.048$  corresponding to the first (deepest) minimum of the interaction energy  $\varepsilon_{\text{int}}$ ; (c) contour plots of the components of the magnetization.

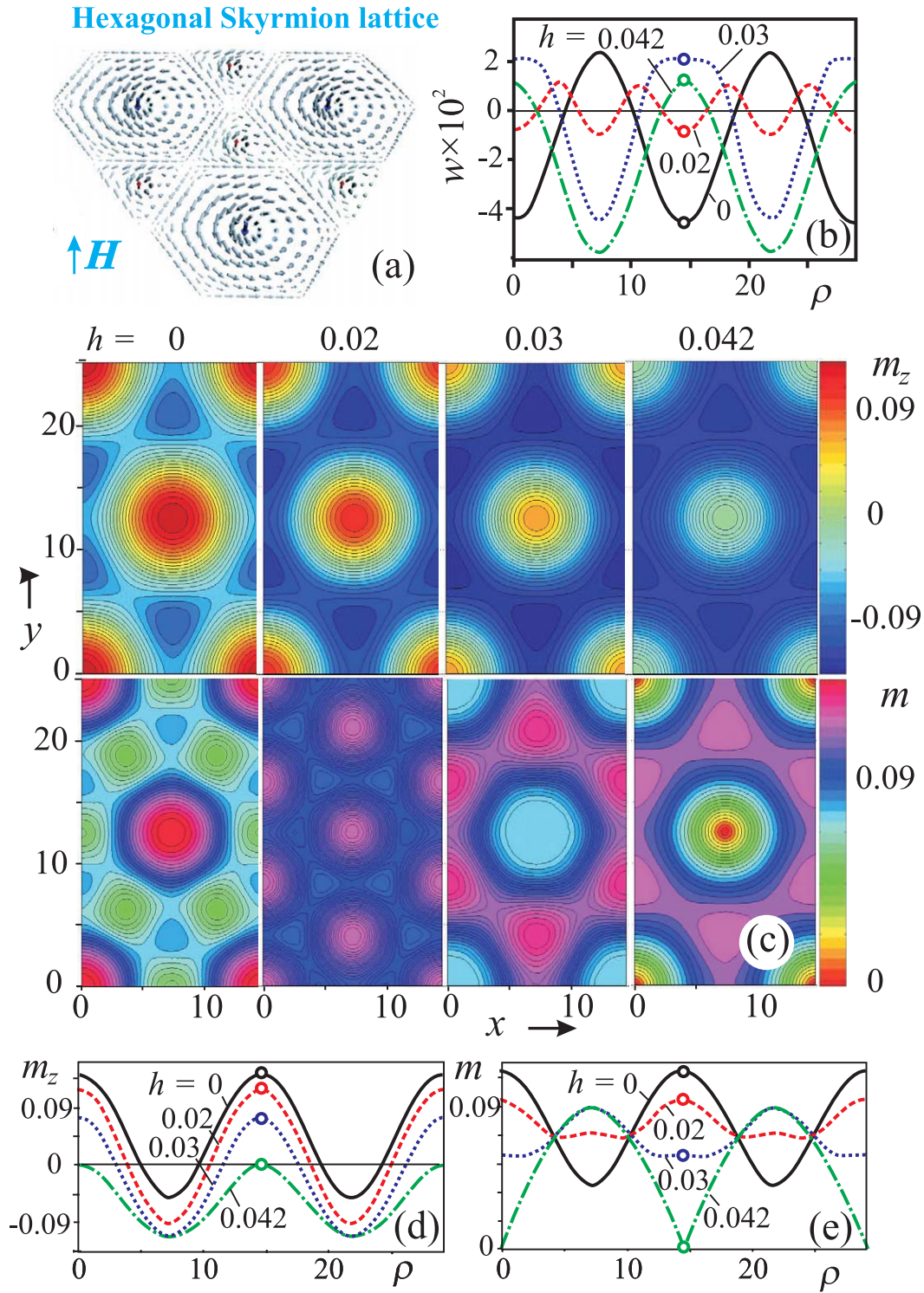


Figure 6.12.: Numerically exact solutions of hexagonal skyrmion lattice (a) for  $a = 0.23$  and different values of the applied magnetic field shown as contour plots of the modulus  $m$  and  $m_z$ -component of the magnetization (c) as well as their diagonal cross-sections (d), (e). The diagonal cross-section of the energy density is shown in (b).

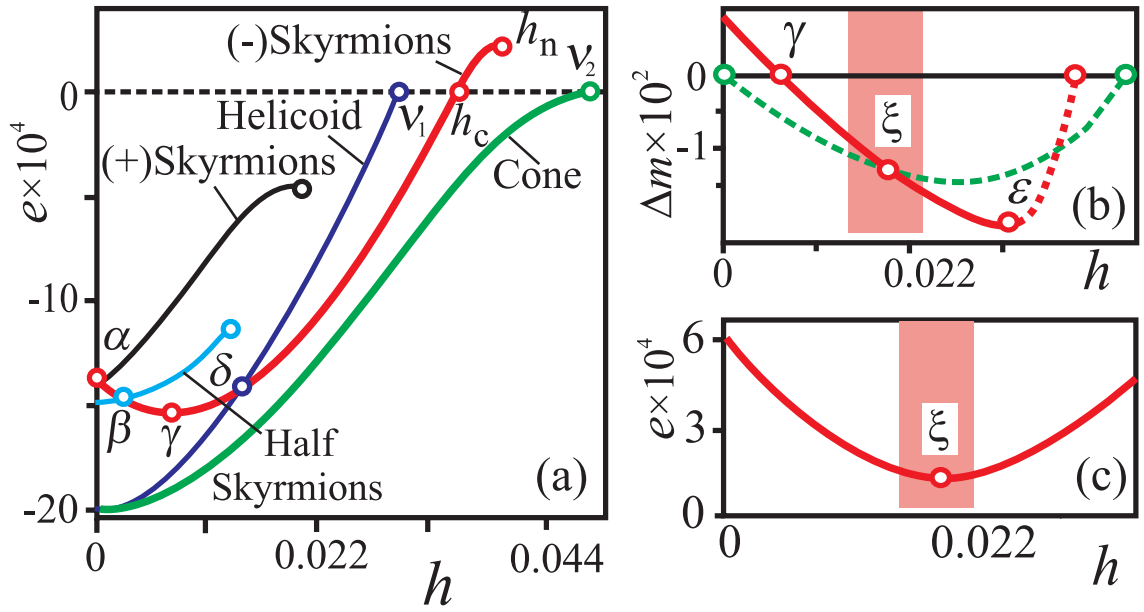


Figure 6.13.: (a) Dependences of energy densities in all considered modulated structures on the applied magnetic field  $h$  ( $a = 0.23$ ), the energy density is calculated with respect to the homogeneously magnetized state; (b) differences of the averaged magnetization along the applied magnetic field of  $-\pi$ -skyrmion lattice (red line) and conical phase (green dashed line) with the modulus  $m_0$  of the homogeneously magnetized ferromagnetic state; (c) energy density of the  $-\pi$ -skyrmion lattice with respect to the conical phase exhibits the minimum in the field (point  $\xi$ ), where average magnetizations along the field of cones and skyrmions are equivalent.

twisted" skyrmion cell core compared to "single-twisted" helical states [31, 38].

The energy density of the skyrmion lattice with respect to the homogeneous state for the considered magnetization process is plotted in Fig. 6.13 (a). With increasing magnetic field the energy density of skyrmion lattice decreases, and in the point  $\gamma$  reaches the minimum. In the minimum of the energy density the averaged value of  $m_z$ -components of the  $-\pi$ -skyrmion lattice (Fig. 6.13 (b)) equals the magnetization of the homogeneous state  $m_0$  (6.9).

In the point  $\xi = 0.02$  (Fig. 6.13 (b)) the average magnetization  $m_z$  along the field in the skyrmion lattice intersects the magnetization of the cone. This point corresponds to the minimum of the energy difference between skyrmion lattice and conical phase (Fig. 6.13 (c)). The structure of the  $-\pi$ -skyrmion lattice in this point has a peculiar nature. The modulus in the center of skyrmion acquires the same value as in the center of triangular regions (Fig. 6.12 (c)), and the distribution of the modulus in the skyrmion lattice becomes periodic with the doubled period as compared to initial skyrmion state in the point  $\alpha$ . The distribution of the energy density along  $y$ -direction (red dashed line in Fig. 6.12 (b)) also indicates the special structure of the lattice in the minimum  $\xi$ .



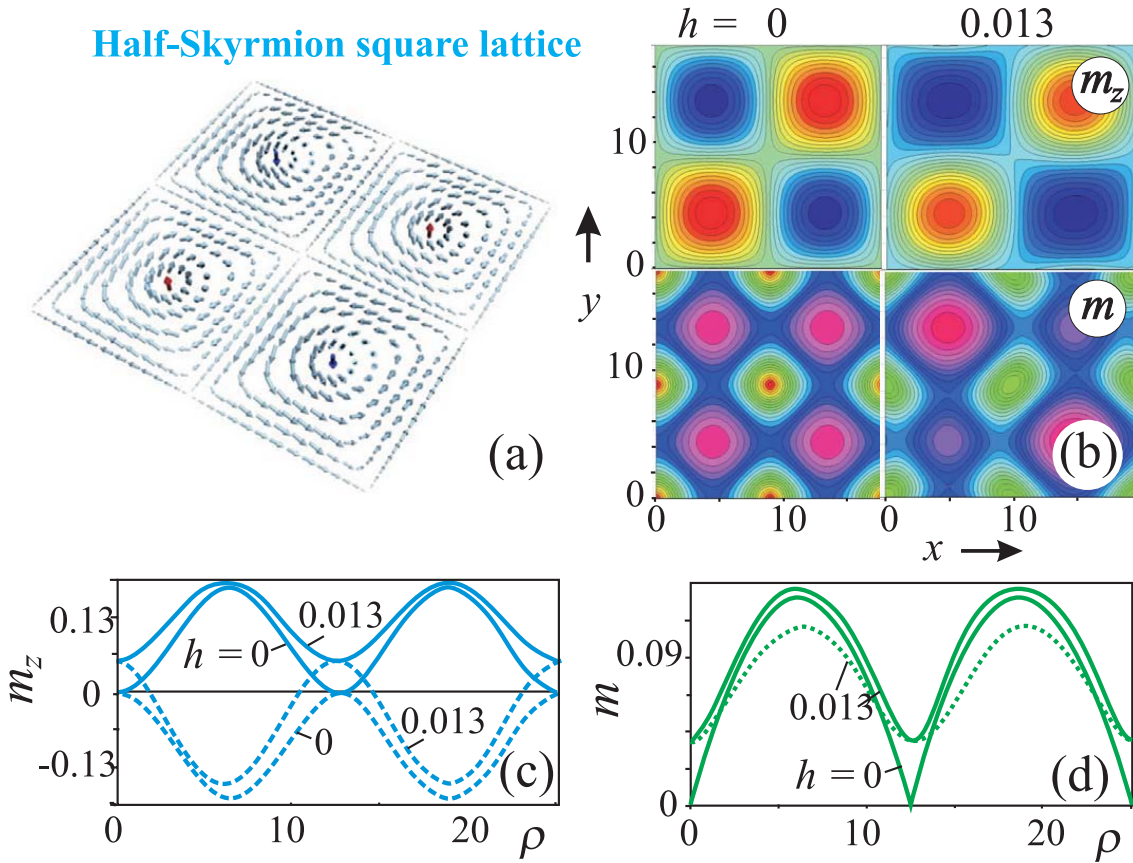


Figure 6.14.: Structure of the two-dimensional half-skyrmion lattice, derived as a minimum energy solution for the equation (6.3). (a) overview showing the distribution of the magnetization vectors in the base plane. (b) numerically exact solutions of square skyrmion lattice for  $a = 0.23$  and different values of the applied magnetic field shown as contour plots of the modulus  $m$  and  $m_z$ -component of the magnetization. (c),(d) the diagonal cross-sections of contour plots (b).

Since it is the point with the minimal energy difference with respect to conical phase, additional small energy contributions can stabilize skyrmion lattices for the field around the point  $\xi$  (shaded region in Fig. 6.13 (c)).

The increasing magnetic field leads also to the increase of skyrmion energy density, the field gradually suppresses the antiparallel magnetization in the cell core and reduces the energetic advantage of the "double-twist" (Fig. 6.12 (c)). At the line  $h_n$  the lability threshold of the lattice is achieved: the magnetization modulus in the cell center becomes zero (see magnetization profile for  $h = 0.042$  in Fig. 6.12 (d), (e)).

### 6.5.2. Field- and temperature-driven transformation of the staggered half-skyrmion lattice

The dependence of the energy density on the applied magnetic field for staggered half-skyrmion lattice is plotted in Fig. 6.13 (a) (blue line). The energy density has a minimum relative to the homogeneous state for  $h = 0$  and is symmetric with respect to the direction of the applied magnetic field.

The average  $m_z$ -component of the half-skyrmion lattice equals zero as it is in the homogeneous background. For  $h = 0$  the square half-skyrmion lattice is energetically more favourable than the densely packed hexagonal lattice, but any increase of the magnetic field leads only to the increase of its energy density.

In the magnetic field the relative area of half-skyrmion plaquettes magnetized along the field grows at the cost of the oppositely magnetized plaquettes. For some value of magnetic field (point  $\beta$ ) the energies of the square and  $-\pi$  hexagonal skyrmion lattices are equivalent. Zero magnetization along the defect lines between up and down pointing plaquettes increases in the field. These interstitial regions serve as nuclei of triangular regions, since for some limiting magnetic field the half-skyrmion lattice becomes unstable and transforms into the hexagonal  $-\pi$ -skyrmion lattice. Contour plots of the  $m_z$  and  $m$  for  $h = 0.013$  exhibit already the elongation of the half-skyrmion lattice toward hexagonal one (Fig. 6.14 (b)).

The defect lines are also the reason of the instability of half-skyrmion lattice with decreasing temperature. As it costs additional energy to make the magnetization zero along the particular line, the half-skyrmion lattice can exist only in vicinity of the ordering temperature  $a_N$ . For some critical temperature  $a$  the half-skyrmion plaquettes undergo elliptic instability and elongate to form a (defected) spiral state (Fig. 6.15). The properties of intermediate structures between the spiral and half-skyrmion lattice and the question of their stability have still to be resolved (Fig. 6.15). Apparently, such a structure is stabilized by the variation of the modulus which retains the square symmetry. As the difference of the moduli in "positive" and "negative" plaquettes becomes negligible, the spiral state with constant temperature-defined modulus arises.

### 6.5.3. Field-driven transformation of $+\pi$ -skyrmion lattice

The  $+\pi$ -skyrmion lattice undergoes also a transformation toward the more stable  $-\pi$ -skyrmion lattice as it was described for square half-skyrmion lattice (see sect. 6.5.2). Magnetic field applied along the magnetization in the skyrmion center stretches  $m_1$  and compresses  $m_2$  (see boundary conditions of Eq. (6.18)). Such a process leads only to the increase of the energy density (Fig. 6.13 (a)): the  $+\pi$ -skyrmion lattice is the state with the largest energy density of all modulated phases under consideration.

As soon as  $m_2 = 0$ , the  $+\pi$ -skyrmion lattice loses its stability. In this sense, the magnetization process is reminiscent of the  $-\pi$ -skyrmion lattice in which  $m_1 = 0$  in the point of the lattice instability (see sect. 6.5.1). In increased magnetic field the modulus at the boundary of the skyrmion  $m_2$  will be directed along the field. As it

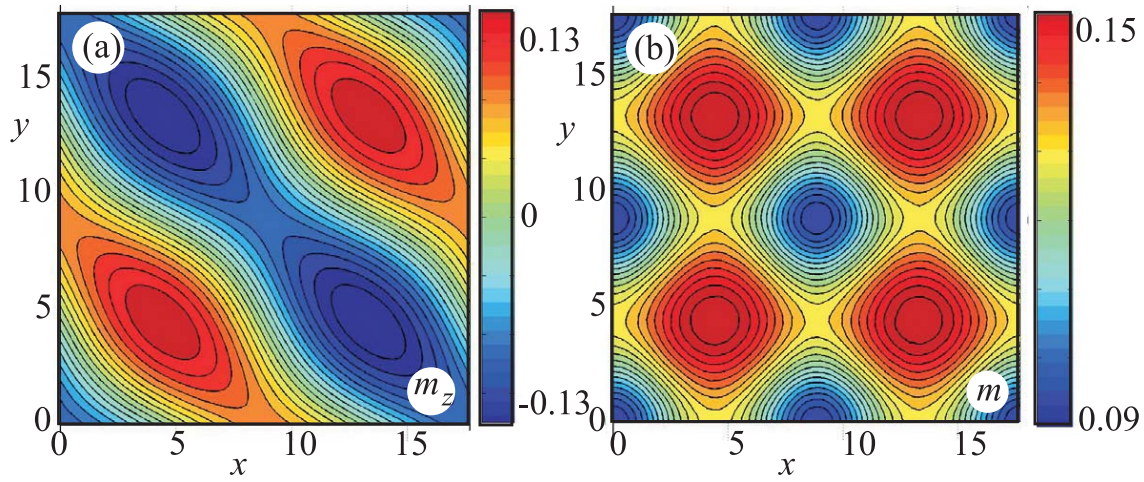


Figure 6.15.: Contour plots of the modulus  $m$  (b) and  $m_z$ -component of the magnetization (a) of a two-dimensional intermediate modulated structure between half-skyrmion lattice and spiral state with constant modulus. While the structure exhibits the difference of the moduli in oppositely magnetized plaquettes and maintains its square symmetry, it is apparently stable (this questions demands additional investigation).

was explained in sect. 6.4.2 (Fig. 6.8), such a state with the magnetization vectors pointing along the field direction in the center of skyrmion and at the outskirts represents only the intermediate state toward the energy minimum with  $-\pi$ -skyrmion lattice. In Fig. 6.16 I display the process of the transformation of  $+\pi$ -skyrmion lattice into  $-\pi$ -skyrmions with the help of contour plots (Fig. 6.16 (d)) exhibiting distribution of the modulus  $m$  and  $m_z$ -component of the magnetization in the elementary cell as well as their dependences on the spatial coordinate in the diagonal cross-section (Fig. 6.16 (b), (c)).

## 6.6. Phase diagram of solutions for cubic helimagnets

In cubic helimagnets the Dzyaloshinskii-Moriya energy includes contributions with gradients along all three spatial directions. This stabilizes chiral modulations with propagation along the direction of an applied field as *cone* phases [99]. For the isotropic model  $\Phi(\mathbf{m})$  (6.3) the cone phase solution with the fixed magnetization modulus and rotation of  $\mathbf{m}$  around the applied magnetic field:

$$\psi = z, \quad \cos(\theta) = \frac{h}{m}, \quad m = \frac{|a - 0.25|}{2}, \quad (6.20)$$

is the global energy minimum in the whole region where modulated states exist (green line in Fig. 6.13 (a)).

In Fig. 6.17 (a) I plotted the phase diagram of solutions for isotropic cubic he-



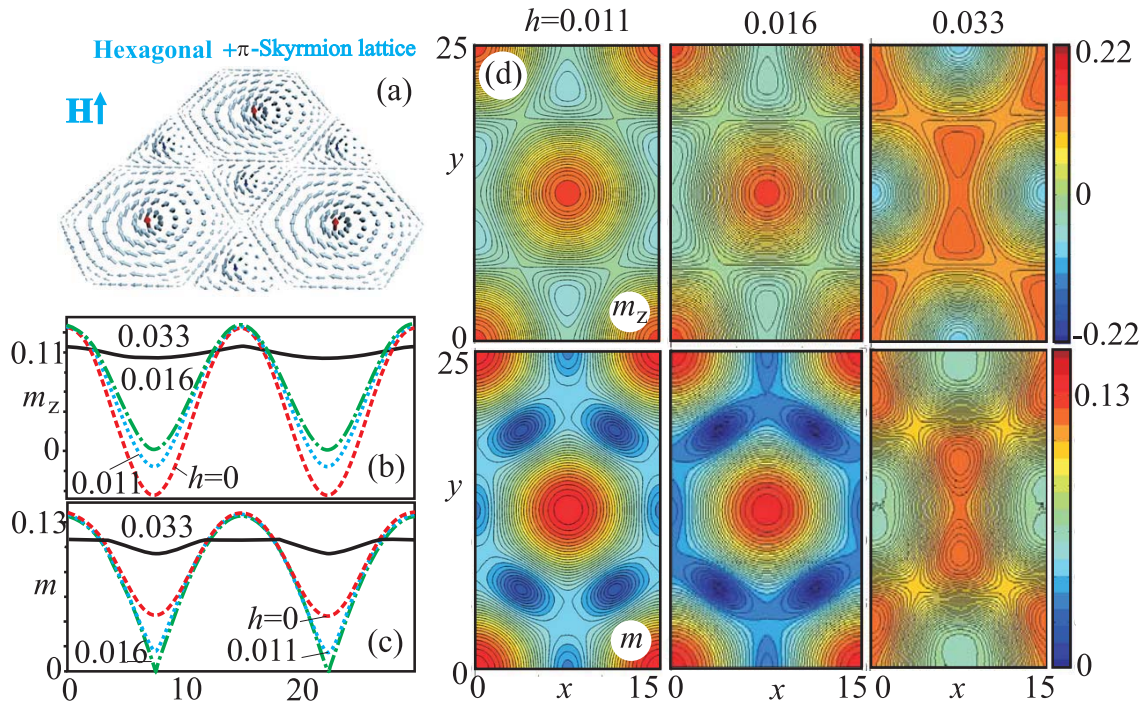


Figure 6.16.: Structure of a two-dimensional  $+\pi$ -skyrmion lattice, derived as a solution for the model's equation (6.3). (a) overview showing the distribution of the magnetization vectors in the base plane: magnetic field is applied along the magnetization in the center of the skyrmion. (b), (c) Distributions of the modulus and the  $m_z$ -component of the magnetization in the diagonal cross-sections of contour plots (d) for different values of the applied magnetic field. (d) Numerically exact solutions of  $+\pi$ -skyrmion lattice for  $a = 0.23$  and different values of the applied magnetic field shown as contour plots of the modulus  $m$  and  $m_z$ -component of the magnetization characterize the process of the transformation of  $+\pi$ -skyrmion lattice into the more stable  $-\pi$ -skyrmion lattice.

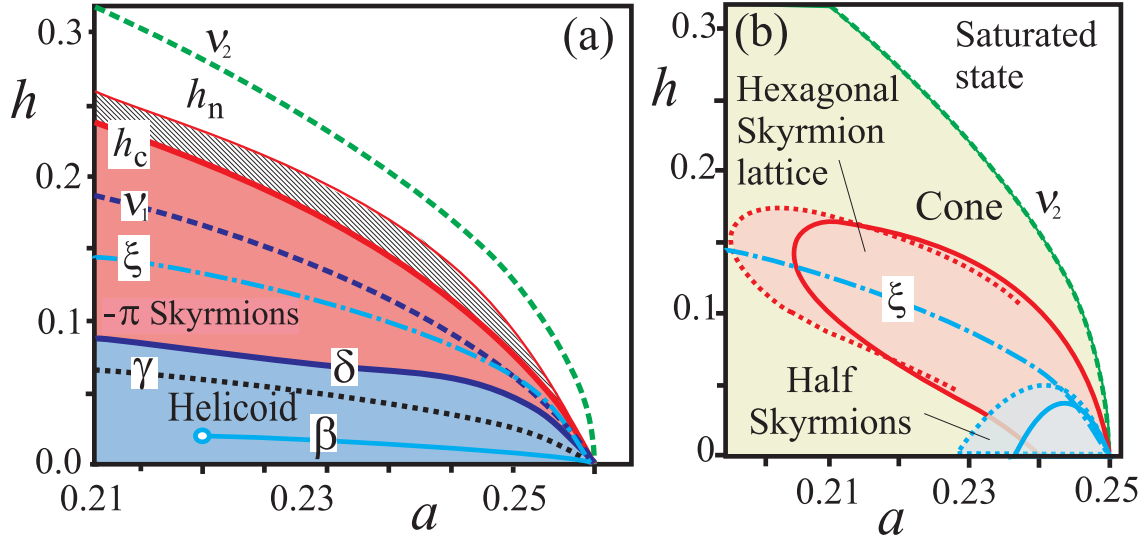


Figure 6.17.: (a) Details of the phase diagram near the ordering temperature show the existence regions for different modulated states according to the energy dependences of Fig. 6.13 (a). Lines for first order transitions:  $\beta$  square half-skyrmion lattice  $\leftrightarrow$  hexagonal skyrmion lattice,  $\delta$  helicoid  $\leftrightarrow$  hexagonal skyrmion lattice. Lines  $\nu_1$  and  $\nu_2$  mark the transition from the helical and conical equilibrium phases into the paramagnetic phase, respectively. In the interval of magnetic fields  $h_c < h < h_n$  (hatched region) the  $-\pi$ -skyrmion lattice exists as metastable state with respect to the homogeneous state. In the point  $\gamma$  the energy density of  $-\pi$ -skyrmion lattice achieves minimum. (b) Magnetic phase diagrams of cubic helimagnets with exchange anisotropy  $b = -0.05$  and the applied field along (111) (solid) and (001) (dashed) axes (a) contains regions with thermodynamically stable hexagonal and square half-skyrmion lattices.

limagnets according to the model functional (6.3). I showed lines for transitions between different metastable states in accordance with Fig. 6.13 (a).

For cubic helimagnets, the energy density (6.3) has to be supplemented by anisotropic contributions,

$$\Phi_a = b \sum_i (\partial m_i / \partial x_i)^2 + k_c \sum_i m_i^4, \quad (6.21)$$

where  $b$  and  $k_c$  are reduced values of exchange and cubic anisotropies [99]. In the section 4.9 on the example of modulated states with the fixed length of the longitudinal order parameter  $m$ , I showed already that these anisotropic interactions impair the ideal harmonic twisting of the cone phase (for details see sect. 4.7.4 and sect. 4.9) and lead to the thermodynamic stability of skyrmion states. The same is true also for the modulated states with soft length of the modulus  $m$  as shown in the equilibrium phase diagram (Fig. 6.17 (b)).

The difference between the energy of the hexagonal skyrmion lattice  $W_{sk}$  and of the cone phase  $W_{cone}$  calculated for the isotropic model,  $\Delta W_{min} = W_{sk} - W_{cone}$ , has minima along a curve  $\xi(a)$ . See Fig. 6.13 (c)) which reaches the critical point  $\xi(a_N) = 0$  as

$$\Delta W_{min} = 0.0784(0.25 - a). \quad (6.22)$$

Weak exchange anisotropy of a cubic helimagnet, therefore, creates a pocket around  $a_N$ , where the hexagonal skyrmion lattice becomes the global energy minimum in a field (Fig. 6.17 (b)). This case is realized in cubic helimagnets with negative exchange anisotropy ( $b < 0$ ) as in MnSi [99]. This anisotropy effect provides a basic mechanism, by which a skyrmionic texture is stabilized in applied fields. Thus, the basic Bak-Jensen model [99] (Eq. 4.1) possibly can explain the observation of a skyrmion phase at finite fields in MnSi - so-called "A-phase" [79, 273, 276]. The exchange anisotropy  $b < 0$  also leads to the thermodynamic stability of half-SLs (Fig. 6.17 (b)). The stabilization of these textures may be responsible for anomalous precursor effects in cubic helimagnets in zero field [31, 62, 81].

The thermodynamic signature of the transition from the paramagnetic state into the A-phase in experiment is very similar to that into the precursor state in zero magnetic field that has been put into evidence by the observations of Pappas et al. [81].

## 6.7. Chiral modulations in non-Heisenberg models

A generalization of isotropic chiral magnets proposed in Ref. [31] replaces the usual Heisenberg-like exchange model by a non-linear sigma-model coupled to a modulus field with different stiffnesses. This yields a generalized gradient energy for a chiral isotropic system with a vector order parameter, which is equivalent to the phenomenological theory in the director formalism [31, 38] of liquid crystals:

$$\sum_{i,j} (\partial_i m_j)^2 \rightarrow \sum_{i,j} (\partial_i m_j)^2 + (1-\eta) \sum_{i,j} (\partial_i m)^2 \rightarrow m^2 \sum_{i,j} (\partial_i n_j)^2 + \eta \sum_i (\partial_i m)^2. \quad (6.23)$$

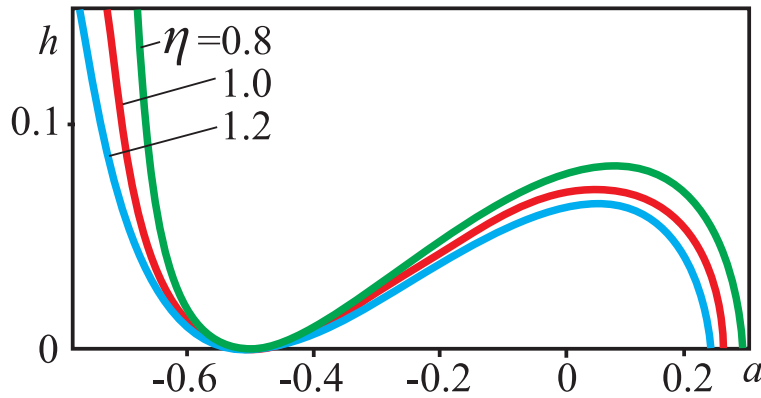


Figure 6.18.: Critical line (6.14) in the case of non-Heisenberg model for different values of parameter  $\eta$  in (6.23).

Parameter  $\eta$  equals unity for a "Heisenberg" model, in chiral nematics  $\eta = 1/3$  [38].

For  $\eta > 1$  the field- and temperature-driven evolutions of skyrmion and helical states is qualitatively the same as for  $\eta = 1$  (see Fig. 6.13 (a) for the energy dependencies of different modulated phases on the field). However for the thermodynamical stability of skyrmions, higher values of additional anisotropic contributions must be applied. The endpoints of the lines bounding the confinement region are shifted to the left (i.e. in the region of lower temperatures) with respect to  $a_N = 0.25$  (blue line in Fig. 6.18). Therefore, the conical phase can exist for higher temperatures in comparison with skyrmions.

For  $\eta < 1$  on the contrary, the additional "softness" of the longitudinal order parameter makes the confined chiral modulations extremely sensitive to the applied magnetic field, temperature, and anisotropic energy contributions: different chiral states undergo a very complex sequence of phase transitions (see section 6.7.1). In zero magnetic field the region of confinement extends to the temperatures higher than  $a_N$  (green line in Fig. 6.18). This means that skyrmions and helicoids can exist and compete for the thermodynamical stability for  $a > a_N$ . Cones appear only for  $a < a_N$  independent on the value of  $\eta$ .

The phase diagram of states plotted in Fig. 6.21 (a) for  $\eta = 0.8$  deserves a careful consideration.

### 6.7.1. Field- and temperature-driven transformation of modulated states for $\eta = 0.8$

In Fig. 6.21 (b) the energy densities of all considered modulated phases are plotted with respect to the energy of the conical phase. The snapshots of the contour plots for  $m_z$ -components of the magnetization in particular points of these curves are shown in panels (c) and (d). These contour plots provide basic insight into the transformation of different modulated phases in the applied magnetic field.

#### A. Transformation of the $-\pi$ -skyrmion lattice in applied magnetic field

For  $\eta = 0.8$ , the hexagonal lattice of  $-\pi$ -skyrmions represents the metastable state with the largest energy density from all skyrmion textures. In the applied magnetic field the energy density of  $-\pi$ -skyrmion lattice increases (red line in Fig. 6.18 (b), points  $m_1$  and  $m_2$ ), and eventually at some critical magnetic field  $h(m_3)$  the skyrmion lattice undergoes the transformation toward spiral state with the lower energy density. At the field  $h(n_3)$  the first-order phase transition occurs between metastable helical and  $-\pi$ -skyrmion states. To obtain numerical solution for  $-\pi$ -skyrmion lattice, the temperature  $T_k$  of the Monte-Carlo annealing must be relatively low (see section 4.5.1). Otherwise,  $-\pi$ -skyrmions transform into the state with the lowest energy for  $h < h(m_3)$  and even for  $h = 0$ . For  $h < h(n_3)$ ,  $-\pi$ -skyrmions turn into the half-skyrmion square lattice; for  $h(n_3) < h < h(m_3)$  - into the helicoid.

In Fig. 6.21 (d) the structure of skyrmion lattice is characterized by the contour plots for  $m_z$ -component of the magnetization. Magnetic field applied along the magnetization in the centers of triangular regions (blue triangles surrounding the main hexagon in Fig. 6.21 (d), points  $m_1$  and  $m_2$ ) increases significantly their fraction with respect to the parts of the lattice with opposite directions of the magnetization. In the point  $m_3$  the lattice loses its stability and elongates into the spiral. In Fig. 6.21 (d) (point  $m_3$ ) the initial moment of the transformation is shown.

#### *B. Transformation of the $+\pi$ -skyrmion lattice in applied magnetic field*

$+\pi$ -skyrmion lattice is the metastable state in the interval of magnetic fields  $0 < h < h(n_1)$ . In the point  $n_1$  the first-order phase transition occurs between half- and  $+\pi$ -skyrmion lattices. In the interval of fields  $h(n_1) < h < h(n_2)$ ,  $+\pi$ -skyrmions are the global minimum of the system. In the point  $n_2$  the helicoids (see paragraph *D* of the present section) replace the skyrmions by the first-order phase transition. In the phase diagram (Fig. 6.21 (a)) the region of thermodynamical stability of  $+\pi$ -skyrmions is displayed by the hatching. For  $h < h(n_1)$   $+\pi$ -skyrmions can be easily transformed into the square lattice of half-skyrmions as shown by the dotted line in Fig. 6.18 (b). Therefore, the temperature of the Monte-Carlo annealing must be sufficiently low.

In the applied magnetic field the fraction of the skyrmion lattice with the magnetization along the field grows rapidly at the expense of the triangular regions with the opposite magnetization (point  $p_1$  in Fig. 6.21 (d)). For the fields  $h > h(n_2)$ , there are two scenarios for the evolution of this skyrmion lattice: in the first variant, the  $+\pi$ -skyrmion lattice turns into the helicoid as it was described also for  $-\pi$ -skyrmions; alternatively,  $+\pi$ -skyrmions may transform into the homogeneous state.

#### *C. Transformations of the half-skyrmion lattice*

For  $\eta < 1$ , half-skyrmion lattice is the global minimum of the system in the interval of magnetic fields  $0 < h < h(n_1)$  (blue line in Fig. 6.21 (b)). Additional energy costs to make the magnetization zero along particular directions in the square lattice are lower than for  $\eta > 1$ . As a result, the region of square lattice stability broadens essentially. For  $\eta = 0.8$  half-skyrmion lattice is thermodynamically stable in the temperature interval  $0.152 < a < 0.265$ ,  $h = 0$  (see phase diagram in Fig. 6.21 (a)).

In the applied magnetic field, as it was also described in section 6.5.2, the relative area of plaquettes in the half-skyrmion lattice magnetized along the field grows at the cost of the oppositely magnetized plaquettes ( $h_2$  in Fig. 6.18 (c)). For  $h > h(n_1)$  the half-skyrmion lattice may either transform into the more stable  $+\pi$ -skyrmion lattice (point  $h_3$  in Fig. 6.21 (c)) with the subsequent transformation into the helicoid or elongate into the spiral state through intermediate structures shown in Fig. 6.21 (c),  $h_4$ . Energy density has a local minimum for such modulated states (see also Fig. 6.15).

The region of thermodynamical stability of half-skyrmion lattice is marked by blue color in Fig. 6.18 (a).

#### D. Transformation of helicoids in the applied magnetic field

For definiteness, one-dimensional helical states will be considered to propagate along  $y$ -coordinate axis; applied magnetic field is directed along  $z$  (Fig. 6.19 (a)). Rotating magnetization  $\mathbf{m}$  is written in spherical coordinates,

$$\mathbf{m} = m(y) (\sin \theta(y), \cos \theta(y), 0), \quad (6.24)$$

with  $\theta(y)$  being the angle of the magnetization with respect to  $z$  axis and  $m(y)$  - the longitudinal order parameter.

Energy density of such a helical state after substituting (6.24) into Eq. (6.3) can be written as

$$\Phi = m^2 \left( \frac{d\theta}{dy} \right)^2 - m^2 \frac{d\theta}{dy} + \eta \left( \frac{dm}{dy} \right)^2 + am^2 + m^4 - hm \cos \theta \quad (6.25)$$

The Euler equations

$$\begin{aligned} \frac{d^2\theta}{dy^2} + \frac{2}{m} \frac{dm}{dy} \frac{d\theta}{dy} - \frac{1}{m} \frac{dm}{dy} - \frac{h}{2m} \sin \theta &= 0, \\ \frac{d^2m}{dy^2} - \frac{m}{\eta} \left( \left( \frac{d\theta}{dy} \right)^2 - \frac{d\theta}{dy} + a + 2m^2 \right) + \frac{h}{2\eta} \cos \theta &= 0 \end{aligned} \quad (6.26)$$

with boundary conditions

$$\theta(0) = 0, \theta(p/2) = \pi, m(0) = m_1, m(p/2) = m_2 \quad (6.27)$$

describe the structure of the helicoid in dependence on the values of the applied magnetic field  $h$ .  $p$  is a period of the helicoid.

In Fig. 6.19 (b)-(e) I have plotted the dependences  $m = m(y)$  (c) and  $\theta = \theta(y)$  (b) as well as  $dm/dy(y)$  (e) and  $d\theta/dy(y)$  (d) in the helicoid for different values of the field. In zero magnetic field the magnetization with the constant modulus performs the single-mode rotation around the propagation direction. The longitudinal and

angular order parameters are analytically defined as

$$m = \sqrt{\frac{0.25 - a}{2}}, \theta = \frac{y}{2}. \quad (6.28)$$

Increasing magnetic field  $\mathbf{h}||z$  destroys the single-mode character of rotation in the helicoid: magnetic field stretches the value of the magnetization along the field ( $m_2$  in Fig. 6.19 (c)) and squeezes it for the opposite direction ( $m_1$  in Fig. 6.19 (c)). The angular profiles become strongly localized (blue lines in Fig. 6.19 (b)). Dependences of derivatives for corresponding order parameters are also highly non-linear (Fig. 6.19 (d), (e)): the magnetization vector tries to rotate faster in the parts of the helicoid opposite to the field.

For some critical value of the magnetic field (in Fig. 6.19 for  $a = 0.23$ , this critical field is 0.024) the value of  $m_1(0)$  decreases to zero. In the further increasing magnetic field as a possible solution of Eq. (6.26) and, therefore, a candidate of the helicoid evolution, I considered the one-dimensional spiral state with the following boundary conditions:

$$\theta(0) = 0, \theta(p/2) = \theta_0, m(0) = m_1, m(p/2) = 0. \quad (6.29)$$

In Fig. 6.20 the same characteristic features for this spiral state as in Fig. 6.19 are depicted. The length of the magnetization along the field continuously increases, whereas the angle  $\theta(p/2)$  decreases.

Considered helicoid is the global minimum of the system in the range of fields,  $h(n_2) < h < h(\nu_1)$  (Fig. 6.21 (b)). In the point  $n_2$  it replaces by the first-order phase transition the  $+\pi$ -skyrmion lattice. Point  $\nu_1$  marks the first-order phase transition with homogeneous state. For  $h > h(\nu_1)$  such a helicoid can still exist, but as a metastable solution with the positive energy density. In Fig. 6.21 (a) the region of the helicoid stability is shown by the light violet color.

### 6.7.2. Phase diagram of solutions for $\eta = 0.8$

The magnetic phase diagram (Fig. 6.21) calculated for  $\eta = 0.8$  includes pockets with square half-skyrmion lattice, hexagonal lattice with the magnetization in the center of the cells parallel to the applied magnetic field (i.e.  $+\pi$  according to terminology introduced in section 6.4.2), and helicoids with propagation transverse to the field. At low fields, a half-skyrmion staggered lattice is the global minimum of the system. At lines E-A and A-C this lattice undergoes a first-order phase transition into the conical phase and the  $+\pi$ -skyrmion lattice, correspondingly. At higher field,  $+\pi$ -skyrmion lattice competes with a helicoidal phase with the line B-C being the line of a first-order phase transition between them. In contrast, the  $-\pi$ -skyrmion lattice states expected to form a metastable low-temperature phase in chiral cubic helimagnets (see chapter 4), do not exist near magnetic ordering in this model. Critical points of this phase diagram have the following coordinates: A=(0.209,0.029), B=(0.204,0.036), D=(0.265,0), E=(0.152,0).

The phase diagram shows that both helicoidal kink-like and skyrmionic precursors may exist.

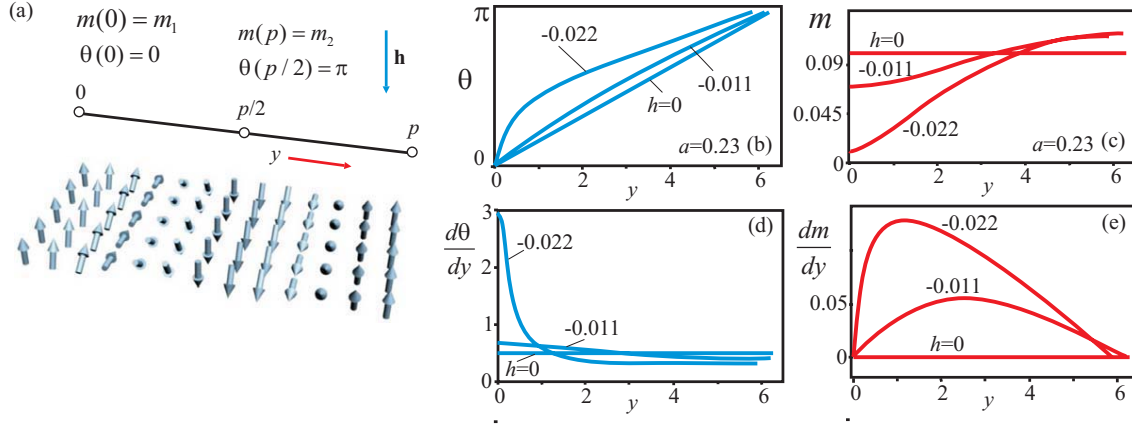


Figure 6.19.: Solutions for the helicoid presented as dependences  $\theta(y)$  (b),  $d\theta/dy(y)$  (d),  $m(y)$  (c),  $dm/dy(y)$  (e) demonstrate strong transformation of the helical structure in the applied magnetic field for  $a = 0.23$ . Longitudinal value of the magnetization along the field gradually increases, whereas opposite to the field - decreases (see sketch in (a) and longitudinal profiles in (c)). Angular profiles become more localized (see solutions in (b)). In a critical magnetic field  $h = -0.024$  the magnetization opposite to the field is equal to zero,  $m_1(0) = 0$ .

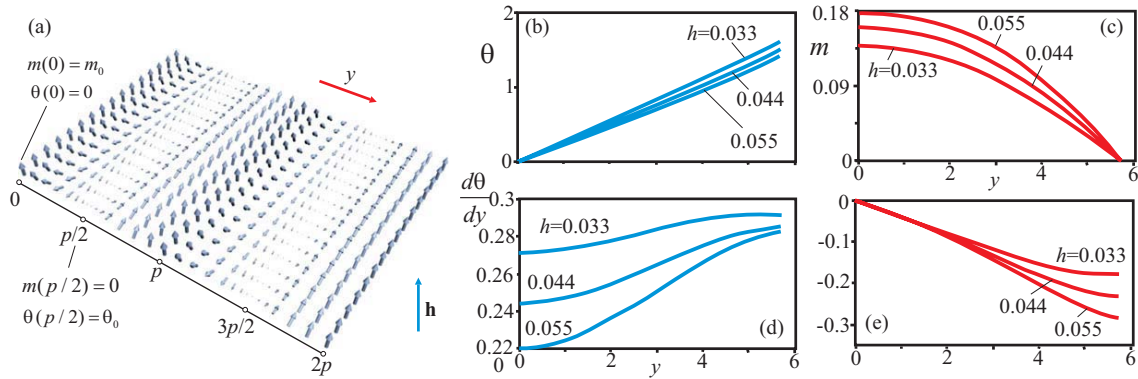


Figure 6.20.: Solutions for the one-dimensional modulated state with boundary conditions (6.29) presented as dependences  $\theta(y)$  (b),  $d\theta/dy(y)$  (d),  $m(y)$  (c),  $dm/dy(y)$  (e). Such a state is considered as a possible scenario for the evolution of a helicoid in a strong magnetic field. In (a) the structure of the helical state is presented schematically.



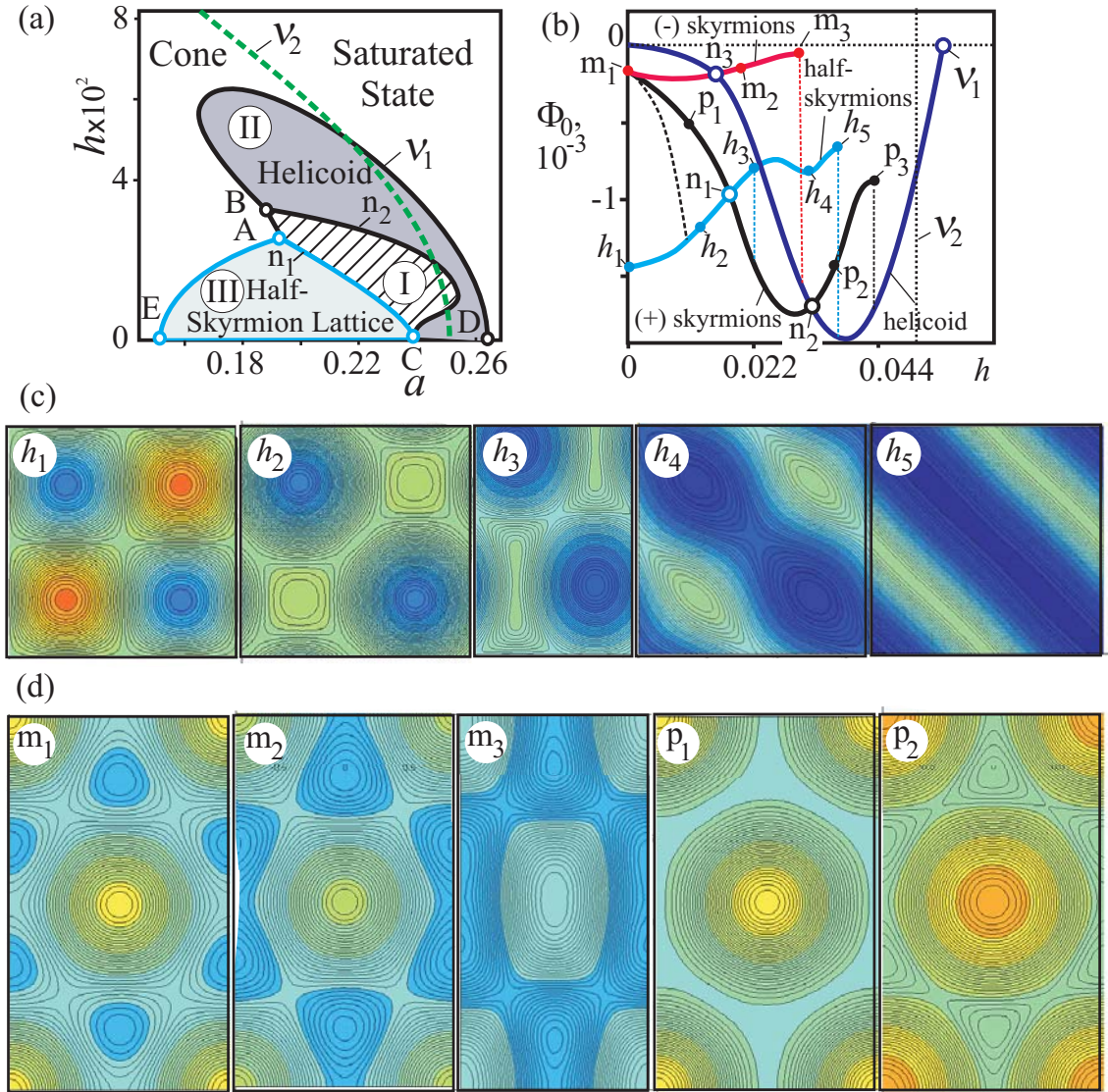


Figure 6.21.: (a) Theoretical phase diagram for chiral magnets near magnetic ordering according to the modified non-linear sigma-model [31]. In larger applied fields, i.e. in the A-region, a densely packed full skyrmion lattice is found in region (I). The helicoid transverse to an applied field is reentrant in region (II). Region (III) is a half-skyrmion lattice with defects. (b) Dependences of energy densities in all considered modulated phases on the applied magnetic field  $h$  ( $a = 0.23$ ) calculated with respect to the conical phase. The evolution of skyrmion states is shown in (c) and (d) with the help of contour plots for  $m_z$ -component of the magnetization.

## 6.8. Conclusions

In the present chapter, I have investigated the basic phenomenological model for chiral ferromagnets (Eq. (6.3)). I obtained rigorous solutions for skyrmions and analytical solutions for one-dimensional helical and conical states in the whole range of the control parameters - the reduced values of temperature,  $a$ , and magnitude of the applied magnetic field,  $h$  (see Eqs. (6.4), (6.1)). I have analysed the transformation of the modulated phases under the influence of the magnetic field and temperature and constructed the phase diagrams of states in Figs. 6.2, 6.17, 6.21. Here, I highlight the most important results of the present chapter:

(a) By analysing solutions for localized isolated skyrmions (section 6.3), it was found that inter-skyrmion coupling being repulsive in a broad temperature range becomes oscillatory near the ordering temperature. This may be explained by "softening" of the magnetization modulus at high-temperatures and strong interplay of angular and longitudinal order parameters. Isolated skyrmions attracting each other may form clusters and confined skyrmion lattices corresponding to minima of skyrmion-skyrmion interaction energy (see Fig. 6.11). Similar effects take place also for helical states [284, 285].

(b) Temperature interval in the phase diagram of Fig. 6.2 may be divided in low- and high-temperature parts: in the main part ( $a < a_L = -0.75$ , see section 6.3.3) skyrmions are regular chiral modulations with repulsive inter-skyrmion interaction (described in chapter 4). In the high-temperature region ( $a > a_L$ ) spatial variation of the modulus defines the magnetization processes. The confinement temperature  $a_L$  is a fundamental parameter of a chiral magnet delineating the border between two different regimes of chiral modulations. The width of high-temperature interval  $\Delta a_2$  is determined by the ratio of isotropic and anisotropic (DMI) exchange (see Eq. 6.15).

(c) Near the ordering temperature skyrmion and helical textures are confined: they can exist only as bound states in the form of clusters or lattices. Trying to push the skyrmions away from the equilibrium (i.e. trying to decrease or increase the period of the skyrmion lattice) leads to the their annihilation (Fig. 6.7): the farther (closer) the skyrmions from each other the smaller the modulus in the center, and for some critical distance between them, only the homogeneous state is present.

(d) Confined skyrmion and helical textures arise from the disordered state through a rare case of an instability-type nucleation transition. Decreasing the temperature from paramagnetic region leads to the appearance of skyrmion matter already in the form of lattice. And opposite, the magnetization modulus in skyrmionic lattice gradually decreases to zero with approaching the Curie temperature from the low-temperature part. However, the lattice retains its symmetry up to the critical point.

(e) The properties of confined chiral modulations investigated in this chapter reveal a noticeable similarity with characteristic peculiarities of cubic helimagnets near the ordering temperatures and known as "precursor states" and "A-phase anomalies". This allows to suggest that induced by the softening of the magnetization magnitude the crossover and confinement of chiral modulations is the basic physical mechanism underlying anomalous properties of "precursor states" in chiral magnets.

(f) As the energy differences between different modulated phases in the confinement region are very small, additional energy contributions result in changes of relative phase stabilities and may cause drastic modification of phase diagrams: cubic anisotropy stabilizes  $-\pi$ -skyrmions in the particular interval of the magnetic field and half-skyrmions in zero field, whereas in the non-Heisenberg model square half-skyrmions transform into the  $+\pi$ -skyrmions and eventually into the transversal spirals with increasing magnetic field.



## 7. Supercooled and glass-forming liquids as skyrmionic textures

In the present chapter, the concept of skyrmionic textures in chiral magnetic systems has been extended to continuum models for glass-forming liquids [288]. These models describe the frustrated tiling of space by incompatible locally preferred clusters of a molecular liquid within a generalized elastic theory. The field theory for the local order-parameter includes antisymmetric couplings derived from the decurving of ideal template units into flat space. As a qualitatively new feature, model with softened modulus of the local intensity of the order parameter was proposed in Ref. [92]. The corresponding classical field theory allows the stabilization of skyrmionic localized states and extended textures. The notion of a glassy structure as an entangled network of defect lines is replaced by the complex geometry of an elastic and frustrated continuum that can display both "rotation" or twisting and longitudinal suppression of the ideal local order. The skyrmions in the simplest version of the frustration models are close, but soft relatives of the hedgehog solutions in Skyrme's original  $SU(2)$  symmetric model for nucleons. It is argued that stable skyrmions are formed at elevated temperatures in molecular liquids and that their condensation into frustrated textures underlies the stability of supercooled and glassy states.

### 7.1. Introduction

In the present chapter I consider simplified field theoretical approaches which offer a general insight into the mechanism of supercooling and the glass-transition [288]. Such theoretical approaches may be treated as a counterpart to the atomistic models, such as molecular dynamics simulations, which commonly address the structure of metallic supercooled liquids and glasses or other simple glass-forming molecular liquids. Continuum theories become a starting point for a refined continuum mechanics that could address plastic behavior in glasses.

One approach for a statistical continuum theory has been based on the concept of locally preferred structural units and their geometrical incompatibility, which frustrates a regular tiling of the whole space. Thinking of the metallic glasses as a model objects consisting of identical spherically symmetric atoms with interaction via soft pair potentials, Frank [289] noted that the ground state of four such atoms is a perfect tetrahedron. Twenty such tetrahedra can be combined to form a regular icosahedron. This icosahedron is really the most stable cluster instead of densest crystalline fcc or hcp hard-sphere packings. However, in three dimensions this locally preferred structure (tetrahedral or icosahedral) cannot propagate freely to tile

the whole space. This underlies the notion of geometric frustration: the five-fold symmetry axes of the icosahedron prevents a space-filling crystalline arrangement of such units without defects.

An important step in deriving a continuum theory for such states of a condensed matter system was made on one hand by Sadoc, Kleman and Mosseri [290, 291], and on the other by Nelson and co-workers [292, 293]. This approach consists in using the ideal structure of polytope  $\{3, 3, 5\}$  [294] as a reference state in a curved three-dimensional space  $S^3$ . Then a regular and unfrustrated tiling by a dense icosahedral packing is possible. Going back from the reference state to the actual configuration in "flat" Euclidian space  $E^3$  necessarily forces in topological defects that perturb the ideal structure. The most relevant defects for the physics of atomic glasses are "disclinations". Disclinations are associated with the breaking of rotational symmetry, and they are line defects in three dimensions. The corresponding approaches of mapping from  $S^3$  to  $E^3$  were developed in Refs. [39, 291–293, 295–297]. The gradient energies in these approaches are expressed in terms of covariant derivatives, e.g. with respect to a constant curvature of the  $S^3$ , which encodes the uniform geometric frustration of the ideal template structure (for comprehensive reviews on these approaches, see Refs. [288, 298]). The frustration models share the geometrical construction with gauge-field theories. However, in the frustration models the constant-curvature covariant derivatives are fixed. Therefore, one can consider these models for glass-forming condensed matter as frozen gauge-field theories [299].

In section 7.2 I introduce the frustration models for dense glass-forming and supercooled liquids. I show that such models allow the formation of dense skyrmionic textures, i.e. topologically non-trivial continuum states with localized units [35, 300]. In section 7.3 I demonstrate the similarity of the continuum frustration models in the theory of supercooled liquids and glasses with Landau-Ginzburg theories containing Lifshitz invariants [31, 41, 233]. The solutions for skyrmion states in the frustration models for liquids and glasses are presented in section 7.4. In section 7.5 a few physical consequences of this skyrmion picture are discussed.

## 7.2. The frustration models for glasses

An elastic energy term which is obtained in the standard approach by decurving the template into flat space is linear in spatial derivatives of the local order parameter describing the intensity and orientation of the local structural features (averaged over a certain volume), i.e. a set of local "vector order-parameters"  $\mathbf{Q}_n(\mathbf{r})$  is obtained by projecting a local particle configuration onto the surface of a tangent 4D hypersphere with appropriate radius to accommodate polytope  $\{3, 3, 5\}$  and then much in the fashion of Landau-Ginzburg theory a free-energy functional of this local order parameter is derived [293, 297]. Frustration is introduced via the covariant derivative entering the gradient term:

$$(\partial_\mu - i\tilde{\kappa}\hat{L}_{0\mu}^{(n)})\mathbf{Q}_n \quad (7.1)$$

and the absolute values (modulus or intensities) of the vectors  $|\mathbf{Q}_n|$ . Here, the matrices  $\hat{L}_{0\mu}^{(n)}$  are generators of SO(4) rotations without slip in the  $(0, \mu)$  plane where 0 denotes the direction in the four-dimensional space which is perpendicular to the tangent Euclidian space described by the coordinates  $m = x, y, z$ .  $\tilde{\kappa}$  is the inverse radius of the hypersphere  $S^3$ .

Frustration arises from the fact, that the covariant derivative cannot be made zero everywhere. In the framework of the differential geometry making the covariant derivative vanish along a curve amounts to parallel transporting the local order parameter along the curve. In the approach of Nelson this is done by "rolling" the tangent 4D sphere  $S^3$  with the ideal icosahedral template along the chosen curve in Euclidian space. Frustration then means that one cannot extend such a parallel transport to the whole space. Rolling the sphere without slip along the closed circuit results in the fact that initial and final values of order parameter after such parallel transport will be different. The magnitude of this difference is proportional to the curvature  $\tilde{\kappa}$ . In turn, the presence of a non-zero curvature comes from the non-commutativity of generators  $\hat{L}_{0\mu}^{(n)}$  and non-abelian group SO(4).

An explicit construction, see Ref. [297], yields a free energy expression of the type

$$F_g = \frac{1}{2} \sum_n \left[ K_n |(\partial_\mu - i\tilde{\kappa}\hat{L}_{0\mu}^{(n)}) \mathbf{Q}_n|^2 + f_n(|\mathbf{Q}_n|) \right], \quad (7.2)$$

where

$$f_n(x) = r_n x^2 + O(x^2) \quad (7.3)$$

are homogeneous functions, the sum over  $n$  is restricted to representations of SO( $d+1$ ) that leave invariant the ideal template, and  $K_n$  are normalization constants.

### 7.3. SU(2) model of metallic supercooled liquids and glasses and the relation to the Skyrme model

Now I make some transformations of the free-energy functional. Sachdev and Nelson [297] noted that the Gaussian free energy Eq. (7.2) with a set of many-component order parameters  $\mathbf{Q}_n$  can be strongly simplified by using the homomorphism between the SO(4) group and  $SU(2) \otimes SU(2)$ , as two SU(2) groups decouple. So, instead of the group SO(4) I now have to deal with a single SU(2) group. Also I consider a simplified model for one particular vector  $\mathbf{Q}_{12}$  to represent the most important structural features of a template. Then one can write the local order parameter for this particular  $n$  in terms of rotation matrices  $D$  (Wigner matrices) representing the SO(4) group:

$$\mathbf{Q}(\mathbf{r}) = q D^\dagger(\mathbf{r}) \mathbf{Q}^0 D^\dagger(\mathbf{r}) \quad (7.4)$$

Here,  $q$  is a real number representing the magnitude of the order parameter. Then, employing the simplest representation of the SU(2) group by  $2 \times 2$  unitary matrices

$U$  the free energy of one  $SU(2)$  field can be written in the following form:

$$F_{su2} = \frac{1}{2} K \left\{ (\partial_\mu q)^2 - q^2 \text{Tr}[U^\dagger \partial_\mu U - \frac{i\bar{\kappa}}{2} U^\dagger \sigma_\mu U]^2 \right\} + f(q), \quad (7.5)$$

where  $\sigma_\mu$  are Pauli matrices:

$$\sigma_1 = \begin{pmatrix} 0 & 1 \\ 1 & 0 \end{pmatrix}, \quad \sigma_2 = \begin{pmatrix} 0 & -i \\ i & 0 \end{pmatrix}, \quad \sigma_3 = \begin{pmatrix} 1 & 0 \\ 0 & -1 \end{pmatrix}, \quad (7.6)$$

On this stage of our transformations one is able to compare this form of energy with that considered by Skyrme for his  $SU(2)$  model of nuclear matter [35]. First of all, a field with  $SU(2)$  group structure can support non-trivial topological textures. In fact, the form of Skyrme's radial hedgehog solution

$$U = \exp[iF(\rho) \mathbf{r} \cdot \vec{\sigma}] \quad (7.7)$$

is applicable to the free energy for metallic glasses. However, the principal difference is that the stabilization of these localized hedgehog solutions with a finite definite diameter in Skyrme's non-linear sigma model stems from a higher-order gradient term. On the contrary, in this type of free energy the solutions are stabilized by the terms linear in the gradients.

Making additional transformation of the free-energy functional one can reveal the similarity between the  $SU(2)$  model and the chiral magnets. I rewrite the  $SU(2)$  form of energy in terms of a 4-component unit vector  $\Phi$

$$\Phi = (\phi_0, \vec{\phi}) \equiv (\phi_0, \phi_1, \phi_2, \phi_3) \quad (7.8)$$

with the modulus of this vector being unity

$$|\Phi| = \phi_i \phi_i = 1 \quad (7.9)$$

by the parametrization of matrix  $U$ :

$$U = \phi_0 \hat{1} + \phi_\mu \sigma_\mu. \quad (7.10)$$

where  $\hat{1}$  is a unitary matrix. Then, the free energy can be written in the following form

$$F_{so4} = K q^2 (\partial_\alpha \phi_i)^2 + K \eta (\partial_\mu q)^2 + \kappa q^2 [\phi_\mu \partial_\mu \phi_0 - \phi_0 \partial_\mu \phi_\mu - \varepsilon_{\alpha\beta\gamma} \phi_\alpha \partial_\beta \phi_\gamma] + f(q) \quad (7.11)$$

where  $\kappa$  is the curvature,  $\varepsilon_{\alpha\beta\gamma}$  is the totally antisymmetric tensor, summation over greek indices is over the coordinates  $x, y, z$  in the physical space  $E^3$ , while summation over latin indices runs over the 4 vector components.

$$f(q) = a q^2 + b q^4 + O(q^5). \quad (7.12)$$



One can now compare the energy functionals (7.11) representing the frustration model for dense super-cooled liquids and glasses with the theory of chiral ferromagnets.

$$F_{so3} = A m^2 (\partial_\nu n_\mu)^2 + A \eta (\partial_\nu m)^2 + D \varepsilon_{\alpha\beta\gamma} m_\alpha \partial_\beta m_\gamma + f_m(m) \quad (7.13)$$

where

$$f_m(m^2) = a m^2 + b q^4 + O(m^5). \quad (7.14)$$

It is evident that the structure of both models is almost identical. For the case of a 3-component magnetization vector  $m$  it was shown that the energy terms linear in gradients stabilize nonhomogeneous distributions of the magnetization. Physically these energy contributions stem from Dzyaloshinskii-Moriya interactions. Also, as in the case of a chiral metallic ferromagnetic system, as discussed in Ref. [31], the authors have modified the elastic energy or longitudinal stiffness by a factor  $\eta$ . The physically sensible range of parameter  $\eta$ , namely, from zero to unity, allows large modulations of the order parameter magnitude. For metallic glasses the energy contributions are the same, and they are a consequence of the inherent frustration in the models. The softening of the modulus  $m$  or the intensity  $q$  is the crucial point of both models that allows to shrink the magnitude of the order-parameter vectors at the outskirts of the multiple twisted skyrmionic objects, e.g. near certain lines or points in extended textures which mark the defects in the fixed modulus fields like in liquid crystals with constant modulus of the director vector. Thus, with the softened version of the order parameter for 4D case, I replace the notion of localized defects as disclination lines by the picture of a smooth but more complex geometrical adaptation of the ordering. The necessary network of disclinations in the  $SO(4)$  picture of a dense hard-sphere packing with ideal icosahedral template is replaced by regions with suppressed order-parameter intensity.

## 7.4. Soft skyrmions in the $SU(2)$ model

Now I present in details the results of calculations for the model  $SU(2)$  for isolated and extended skyrmion textures. Skyrme ansatz in usual spherical coordinates  $(\rho; \theta, \varphi)$  reads as follows:

$$(\vec{\phi}, \phi_0) = \begin{pmatrix} \sin F(\rho) \sin \theta \cos \varphi \\ \sin F(\rho) \sin \theta \sin \varphi \\ \sin F(\rho) \cos \theta \\ \cos F(\rho) \end{pmatrix}. \quad (7.15)$$

Radial soft hedgehog skyrmions are described by the profile function  $F(\rho)$  and the radially varying modulus  $q(\rho)$ . The Euler-Lagrange equations from the variation of the free energy with this ansatz yield a boundary value problem for a system of

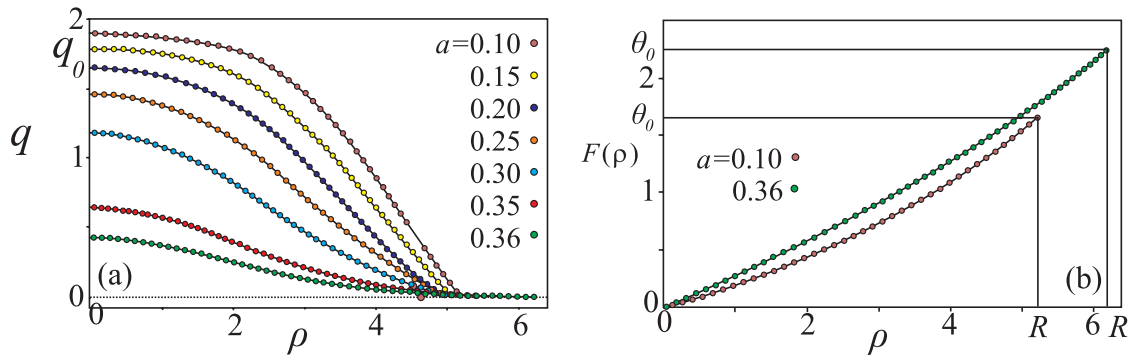


Figure 7.1.: Solutions for soft hedgehog skyrmions shown as dependences of  $q(\rho)$  (a) and  $F(\rho)$  (b). The intensity of the order parameter  $q$  disappears at the radius  $R$  whereas the angle  $F(R) = \theta_0$ .

ordinary differential equations:

$$\frac{d^2 F}{d\rho^2} + \frac{2}{\rho} \frac{dF}{d\rho} - \frac{\kappa}{q} \frac{dq}{d\rho} + \frac{2}{q} \frac{dq}{d\rho} \frac{dF}{d\rho} - \frac{2\kappa}{\rho} \sin^2 F - \frac{\sin 2F}{\rho^2} = 0 \quad (7.16)$$

$$\frac{d^2 q}{d\rho^2} + \frac{2}{\rho} \frac{dq}{d\rho} - \frac{q}{\eta} \left[ \left( \frac{dF}{d\rho} \right)^2 + \frac{2 \sin^2 F}{\rho^2} - \kappa \frac{dF}{d\rho} - \kappa \frac{\sin 2F}{\rho} + a + 2bq^2 \right] \quad (7.17)$$

with boundary conditions

$$q(0) = q_0 > 0, F(0) = 0; \pi, q(R) = 0, F(R) = \theta_0. \quad (7.18)$$

Modulus in the center has the maximum, and is zero on the outskirts. The angle  $F$  starts to rotate from initial value zero or  $\pi$ , and has some value  $\theta_0$  near the radius.

Typical examples of skyrmion cells obtained by numerically solving the Euler equations are shown in Fig. 7.1. The dependence of modulus  $q$  on the distance from skyrmion center  $\rho$  has the bell shape while the angle  $F$  changes almost linearly in the radial direction. Expansion into series near zero

$$F(\rho) = \pi + \tan(\alpha)\rho, \quad (7.19)$$

$$q(\rho) = q_0 \left( 1 + \frac{a + 3 \tan^2 \alpha + 2bq_0^2 - 3\kappa \tan \alpha}{6\eta} \rho^2 \right) \quad (7.20)$$

and radius  $R$

$$F(\rho) = \theta_0 - \frac{1}{2}(R - \rho), \quad (7.21)$$

$$q(\rho) = (R - \rho) \tan \beta + \frac{\tan \beta}{R} (R - \rho)^2 \quad (7.22)$$

reflects the characteristic features of calculated solutions. In the center of skyrmion core the angle  $\alpha$  (see Eq. (7.19)) defines both the slope of the straight line  $F(\rho)$  and the parabolic dependence of the modulus  $q$ . On the outskirts the modulus  $q$  linearly

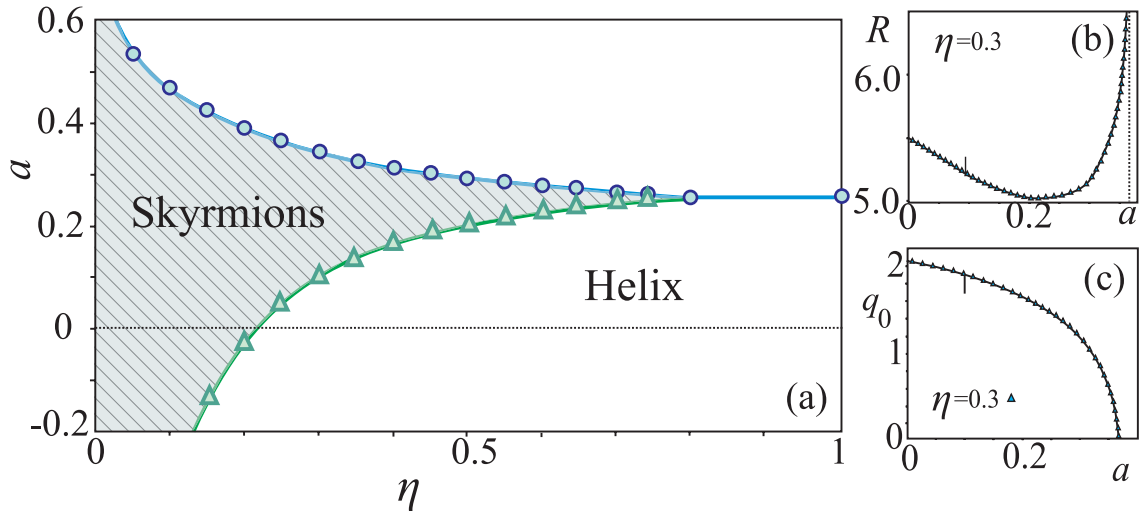


Figure 7.2.: (a) Phase diagram of solutions for the frustration model Eq. (7.11) of supercooled and glass states. The high-temperature (and low density) liquid state is separated from a uniform helical state or a crystalline state by the formation of localized skyrmionic states (dashed blue region) and condensed phases formed from such units. (b), (c) dependences of the radius  $R$  of the skyrmion cell and the modulus in the center  $q_0$  on the temperature  $a$  for the particular cut of the phase diagram with  $\eta = 0.3$ .

depends on  $\rho$  whereas the angle  $F$  is determined by the parameters of the geometry. In the calculations I have optimized the energy with respect to the modulus in the center  $q_0$ , to the radius  $R$ , and to the value of rotation angle  $\theta_0$ . It is clearly seen that the profiles strongly depend on the temperature. For high temperatures the amplitude  $q_0$  decreases and the systems transforms into disordered state.

As well, one is able to construct the phase diagram of solutions as shown in Fig.7.3. Here, the small values of  $\eta$  lead to the broadening of interval of skyrmionic states. The upper line marked by circles is the line of the second order phase transition into disordered state. By approaching this critical line the radius of the skyrmion cell (Fig. 7.3(b)) grows unlimitedly with zero modulus  $q_0$  (7.3(c)). The lower line marked with triangles indicates the transition into the helical state. This state is akin to the crystalline phase with constant modulus. But it is assumed that these two states below line  $a = 0$  are never reached. Instead, the system in the liquid nucleates first skyrmions, which then condense into mesophases. So, the skyrmions lock the system into a certain topologically disordered state. However, the dense packing of these molecular units is again frustrated. It is impossible to arrange these spherical objects without frustration as it was shown for the spheres in Frank's icosahedral packing.

In Fig. 7.3 I present schematically the solutions. In this figure I depicted only three-component vector with marking the fourth component by color. The length of these vectors changes according to the modulation with the function  $\sin F(\rho)$ . When the length becomes zero the fourth component is maximal, i.e. red or blue. One can

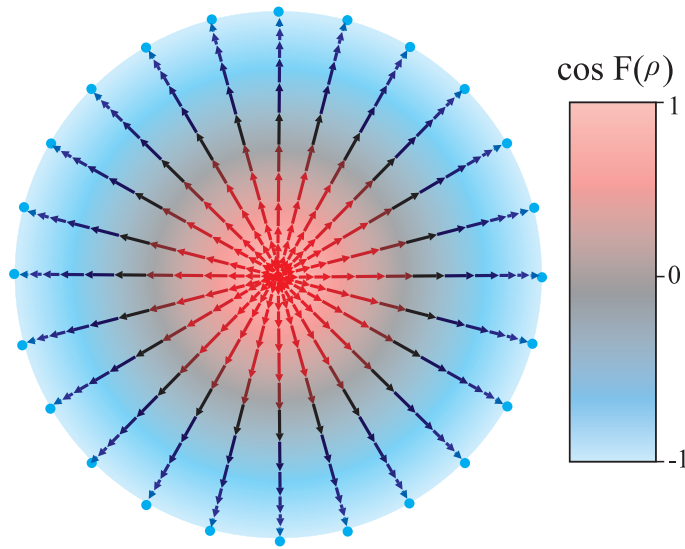


Figure 7.3.: Schematic representation of the skyrmion solution. The fourth component of the vector  $\Phi$  is marked by the color.

consider various projections of 4D space on 3D one. And some of them are presented here.

## 7.5. Discussion

The identification of skyrmionic textures in the frustration models has a number of attractive features. It explains a cross-over or precursor effects in liquids [301] by the formation of skyrmions, which have a definite size encompassing a larger group of molecules. In simple molecular liquids, the size of such skyrmions will possibly contain about 100 atoms, as the ideal  $\{3, 3, 5\}$ -polytope has 120 vertices. Such units will be long-term stable or metastable in the cooled and dense liquid state.

At lower temperatures a condensation of skyrmionic quasi-static units must take place. The problem to pack molecular units now re-appears at the larger length scale of skyrmion diameters. However, the dense packing of skyrmionic units is even more arduous than that of spherical molecules with central pair interactions, because the skyrmions carry a 4-component vector as an orientational degree of freedom. An ideal dense packing requires a structure with "antiferromagnetic" correlations between neighboring skyrmions. In fact, aggregates of few skyrmions as models for nuclear matter again show a preference for icosahedral organization [302], while extended skyrmion matter mostly form densely packed half-skyrmion crystals with antiparallel (iso)spin structure [303]. In both types of localized and extended textures, the skyrmions may lose their identity and form various other shapes. Similar ideas are currently debated with respect to favorable clusters in metallic multi-component alloys [304, 305]. In such atomistic models, a hierarchy of units forming larger units must be organized as aperiodic space-filling pattern. The uniform frustration models identify such patterns as condensed skyrmionic phases.

## 7.6. Conclusions

Application of the concept of frustration to liquids boils down to the following summary of propositions: a liquid is characterized by a locally preferred structure which is different than that of the crystalline phase. This local structure is an arrangement of molecules that minimizes some local free energy. But the local structure cannot tile the whole place. This is precisely the content of the concept of frustration. It is possible to construct an abstract reference system in which the effect of frustration is turned off and to develop a statistical mechanical approach. The free energy of the frustrated system is almost identical to the energy functional considered in micro-magnetics of non-centrosymmetric magnets. And this fact allows to obtain insights on the mechanism for glassiness from this frustration model. One can describe the defects in a continuous way as regions with suppressed order-parameter intensity instead of a complex network of disclinations. Then for the metallic glasses I show the possibility of formation of specific skyrmion states stabilized by linear gradient terms. According to the constructed phase diagram these skyrmions are stable in some interval of temperatures, and can even prevent the transition into helix state or crystalline phase, locking the system in this state. But packing these spherically symmetric objects also induces inherent frustration. The frustration which is related with the packing problem of skyrmionic balls is much more severe on longer length scales.



# Conclusions

In the present thesis, tools of the micromagnetism (the main principles of the micromagnetism have been described in **chapter 1**) have been used to address the wide spectrum of problems in magnets on nanoscale. In **the first part** of the thesis the interplay of magnetocrystalline and surface-induced anisotropies have been considered as applied to magnetic nanolayers, nanoparticles, and nanowires/nanotubes. Within the phenomenological theories, homogeneous and inhomogeneous distributions of the magnetization vector have been derived in dependence on material parameters of nanosystems and applied magnetic field. Corresponding phase diagrams of states have been constructed. In **the second part** of the thesis the specific inhomogeneous distributions of the magnetization (skyrmions) have been comprehensively investigated in magnets with chiral Dzyaloshinskii-Moriya interactions. Present understanding of the skyrmionic magnetic states has been described with a view on recent experimental observations in chiral cubic helimagnets. The question of thermodynamical skyrmion stability has been theoretically addressed. Surface-anisotropy as a probable additional energy contribution stabilizing skyrmions with respect to one-dimensional helical modulations has been considered.

The major part of calculations in the present thesis has been done by using the self-elaborated numerical code, validity of which has been additionally tested on classical micromagnetic problems. Further, the main results of the thesis are summarized following the sequence of the chapters:

## Part I.

**Chapter 2.** In this chapter I have considered the interplay between intrinsic and surface/interface-induced magnetic anisotropies in the influence on the magnetization processes in nanomagnetic systems, namely, in magnetic nanolayers and nanoparticles. Micromagnetic theory to describe a magnetic-field-driven reorientation in nanomagnets with cubic and uniaxial anisotropies has been developed. Within the phenomenological model, I have obtained solutions for the magnetization orientations in competing phases and plotted the phase diagrams in internal field components. Taking into account demagnetizing effect of the layer (particle) surfaces, the phase diagrams in external field components with the regions of multidomain (multiple) states have been constructed. The main peculiarities of existence regions of multidomain states with different number of phases have been analysed. Calculated phase diagrams provide the theoretical basis to classify different types of the magnetization reversal and to analyse the switching processes in magnetic nanostructures. In particular, the results of chapter 2 have been applied for the the-

---

oretical analysis of the magnetization processes as observed experimentally in a novel class of condensed-matter systems – thin films of diluted magnetic semiconductors (Ga,Mn)As. For nanolayers magnetized perpendicularly to the surface, the geometrical parameters of stripe domains as functions of a bias field have been calculated. On the basis of the known solutions for the magnetization in homogeneous phases, different types of isolated domain walls have been modelled and their magnetization profiles have been obtained. It has been shown that the applied magnetic field and values of the competing anisotropies essentially modify the equilibrium parameters of such walls. In the second part of chapter 2 the values of surface-induced uniaxial anisotropy for ellipsoidal magnetic nanoparticles have been derived as functions of aspect ratios and particle sizes. It has been shown that induced uniaxial anisotropy stabilizes multiple magnetic states in the system with the possibility to switch between them. The phase diagrams with the stability regions for different phases and the transition fields between them have been plotted.

**Chapter 3.** In this chapter the phenomenological model of surface-induced anisotropy developed in Ref. [11] for magnetic nanolayers has been extended and generalized with respect to magnetic nanowires and nanotubes. With such a phenomenology a gradual penetration of surface-induced interactions into the volume of magnetic nanostructures have been modelled in nanoobjects with cylindrical symmetry. Possible inhomogeneous distributions of the magnetization in these nanosystems have been derived. It has been shown that large induced magnetic anisotropy from lateral surfaces of magnetic nanowires/nanotubes stabilizes non-collinear Bloch and Néel vortex-like states with the magnetization rotating either along or perpendicular to radial directions. Magnetization profiles and simplified analytical solutions for these vortex states have been comprehensively analysed by solving corresponding micromagnetic equations. The results of numerical simulations have been gathered in phase diagrams showing the occurrence regions for different vortex phases in dependence on the surface anisotropy constants, the radius, and the saturation magnetization of the underlying material. It has been also found that the transitions between topologically different vortices are first-order phase transitions, whereas vortices transform continuously into homogeneously magnetized state.

## **Part II.**

**Chapter 4.** In this chapter two - dimensional skyrmion states with constant value of the magnetization modulus considered within the circular - cell approximation in early papers of A. N. Bogdanov [21,69,70] have been derived as numerical solutions of two- dimensional lattice models. By implementing direct quantitative comparison, it has been found that skyrmion properties of rigorous and approximate "round" solutions are within the relative error value of about 2%. Within the standard Dzyaloshinskii model including only primary energy contributions (direct exchange, Dzyaloshinskii-Moriya coupling, and Zeeman energy) solutions for one-dimensional cones, helicoids, and for two-dimensional skyrmion states have been thoroughly analysed and their evolution in the applied magnetic field investigated. It has been shown that within the isotropic phenomenological model skyrmions are only metastable



---

solutions with respect to helices. Therefore, the quest for the means leading to skyrmion thermodynamical stability has been undertaken. It has been comprehensively demonstrated that small anisotropic forces like cubic, uniaxial, and exchange anisotropies not only determine the propagation directions of spirals and axes of skyrmions with respect to certain crystal directions, but also stabilize skyrmion textures in a broad range of magnetic fields. The equilibrium parameters of skyrmions, helices, and cycloids have been determined as functions of a bias magnetic field and the values of competing anisotropic interactions. The corresponding phase diagrams of states have been constructed. Finally some candidate materials for experimental observation of skyrmion textures have been described.

**Chapter 5.** In this chapter the interplay of volume and surface-induced energy contributions has been considered in the influence on the skyrmion states in confined mesoscopic systems - thin layers of liquid crystals and magnets. Numerical solutions of the micromagnetic equations with the surface anisotropy defining the boundary conditions have been determined. The solutions have clearly revealed complex evolution of the tubular skyrmions into specific double-twisted spherulites with effect from surface anisotropy. The process of condensation of such peculiar spherulitic states into the lattices (spherulitic matter) is different from condensation of skyrmions in bulk materials and is strongly defined by the surface anchoring and the force moving localized isolated units together. It has been found that thermodynamic stability of spherulitic extended matter can be assured in the vast part of the constructed phase diagram for the appropriately chosen ratios between internal and induced interactions. The question of dipole-dipole interactions with their effect on the skyrmion states in thin magnetic layers has been also addressed. Finally, theoretical findings of this chapter have been applied for explanation of modulated states experimentally observed in nanolayers of cubic helimagnets and liquid crystals.

**Chapter 6.** In this chapter the structures of skyrmion and helical states with soft modulus have been comprehensively analysed from a phenomenological perspective using the basic Dzyaloshinskii theory for isotropic chiral magnets. It has been shown that the magnetization in modulated phases near the ordering temperature becomes essentially inhomogeneous because longitudinal and orientational degrees of freedom couple. As a result, the solitonic chiral modulations, being repulsive in the vast temperature range far below the ordering temperature, develop attractive soliton-soliton interactions in the direct vicinity of Curie temperature. It has been found that near the ordering temperature skyrmions can exist only as bound states, and skyrmion lattices are formed by an unusual instability-type nucleation transition from the paramagnetic state. These attributes belong to a remarkable *confinement* effect of skyrmions and helicoids. A confinement temperature  $T_L$ , has been introduced to divide the temperature interval into a part with regular skyrmions modulations and a part with confined skyrmions. Numerical investigations on two-dimensional models have revealed the confinement effect on different skyrmion lattices, namely, on  $\pm\pi$ -hexagonal and  $\pi/2$ -square skyrmion lattices. Particularly, to a square half-skyrmion lattice much attention has been devoted as it has no analogue to textures

---

with smooth constant modulus. Thermodynamical stability of skyrmion states has been considered with the influence of small anisotropic contributions and within the non-Heisenberg model. Theoretical results on such modulated states, belonging to the main achievement of the present thesis, allow to address the problem of unconventional magnetic ordering transitions and precursor phases known from experiments on the cubic helimagnets with chiral Dzyaloshinskii-Moriya couplings near the ordering temperatures. They also allow to establish the link between the "low-temperature" skyrmions with constant modulus theoretically investigated by A. N. Bogdanov et. al. [21, 69, 70] (also in chapter 4) and experimentally observed by Yu et al. [28, 29] with "high-temperature" skyrmions responsible for a number of precursor effects in the vicinity of the ordering temperature [80, 81]. The theory and results from numerical simulations demonstrate why a multitude of different small pockets of different phases is generically expected in a distinct temperature interval, interleaved between paramagnetic and helix magnetic state in non-centrosymmetric helimagnets MnSi and/or FeGe.

**Chapter 7.** In this chapter the concept of skyrmionic textures in condensed matter systems has been extended to continuum models of glass-forming liquids. Initially, the idea was published in Ref. [92]. In the present chapter numerical solutions confirming this idea have been obtained. It has been shown that the skyrmions appear as solutions for the field theory with a frozen gauge background describing the frustrated tiling of the space by incompatible locally preferred clusters. It has been also argued that stable skyrmions are formed at elevated temperatures in molecular liquids and that their condensation into frustrated textures underlies the stability of supercooled and glassy states, which may resemble the states in extended dense nuclear matter.

# List of original papers

This thesis is based on the following articles, which are referred to in the text by Roman numerals:

I. A. V. Bezus, A. A. Leonov, Yu. A. Mamalui, Yu. A. Siryuk, *Phase transitions in bubble-domain structures upon spin reorientation in garnet ferrite films*, Fiz. Tverd. Tela **46**, 277 (2004) [Phys. Solid State **46**, 283 (2004)]

II. A. A. Leonov, Yu. A. Mamalui, Yu. A. Siryuk, *Studies of the structure of a domain wall in magnetic films with competing anisotropies in the region of a spin-reorientation phase transition*, Izv. Ros. Acad. Nauk. Seriya Phys. (Proceedings of the Russian Academy of Sciences. The physical series), **69**, 1011 (2005).

III. Ya. I. Granovskii, A. A. Leonov, Yu. A. Mamalui, Yu. A. Siryuk, *Domain walls in magnetic films with angular domain structure*, Izv. Ros. Acad. Nauk. Seriya Phys (Proceedings of the Russian Academy of Sciences. The physical series), **70**, 956 (2006).

IV. Ya. I. Granovskii, A. A. Leonov, Yu. A. Mamalui, Yu. A. Siryuk, *Energy and orientation of Bloch type domain walls in magnets with competing anisotropies*, Functional materials, **13**, 526 (2006).

V. A. A. Leonov, I. G. Dragunov, A. N. Bogdanov, *Surface-induced anisotropy and multiple states in elongated magnetic nanoparticles*, Applied Physics Letters, **90**, 193112 (2007).

VI. A. A. Leonov, I. G. Dragunov, U. K. Rößler, A. N. Bogdanov, *Phenomenological model of surface-induced anisotropy in magnetic nanostructures*, Functional materials **15**, 109 (2008).

VII. A. A. Leonov, U. K. Rößler, A. N. Bogdanov, *Phenomenological theory of magnetization reversal in nanosystems with competing anisotropies*, J. Appl. Phys. **104**, 084304 (2008).

VIII. A. B. Butenko, A. A. Leonov, A. N. Bogdanov, U. K. Roessler, *Theory of vortex states in magnetic nanodisks with induced Dzyaloshinskii-Moriya interactions*, Phys. Rev. B **80**, 134410 (2009).

IX. A. B. Butenko, A. A. Leonov, A. N. Bogdanov, U. K. Roessler, *Influence of the Dzyaloshinskii- Moriya interaction on vortex states in magnetic nanodisks*, J. of Phys.: Conf. Ser. **200**, 042012 (2010).

X. U. K. Rößler, A. A. Leonov, A. N. Bogdanov, *Skyrmionic textures in chiral*

---

*magnets*, J. of Phys.: Conf. Ser. **200**, 022029 (2010).

XI. A. B. Butenko, A. A. Leonov, U. K. Röbner, A. N. Bogdanov, *Stabilization of skyrmion textures by uniaxial distortions in noncentrosymmetric cubic helimagnets*, Phys. Rev. B **82**, 052403 (2010).

XII. U. K. Röbner, A. A. Leonov, A. N. Bogdanov, *Chiral Skyrmionic matter in non-centrosymmetric magnets*, J. of Phys.: Conf. Ser. **303**, 012105 (2011).

### Materials

XIII. H. Wilhelm, M. Baenitz, M. Schmidt, U. K. Röbner, A. A. Leonov, A. N. Bogdanov, *Precursor phenomena at the magnetic ordering of the cubic helimagnet FeGe*, arxiv: 1101.0674v1, accepted to Phys. Rev. Lett.

XIV. A. A. Leonov, A. N. Bogdanov, U. K. Röbner, *Confinement of Skyrmion states in noncentrosymmetric magnets*, arxiv: 1001.1292v3, submitted to New J. of Phys.

XV. U. K. Röbner, A. A. Leonov, A. N. Bogdanov, *Crossover of inter-skyrmion coupling and precursor effects in noncentrosymmetric ferromagnets*, submitted to Phys. Rev. B.

# Conferences

Results of investigations included in the thesis have been presented at the following scientific conferences:

1. International Symposium ODPO-2003 , Sochi, Russia, 8-11 September, 2003  
(poster): A. V. Bezus, A. A. Leonov, Yu. A. Mamalui, Yu. A. Siryuk, *Calculation of the phase diagram of the magnetization spin reorientation in ferrite-garnet magnetic films.*
2. International Conference of Functional Materials ICFM-2003, Crimea, Ukraine, Partenit, October 6-11, 2003  
(talk): A. A. Leonov, Yu. A. Mamalui, *Phase diagram of reorientation phase transition in uniaxial ferrite-garnet magnetic films in external magnetic field.*
3. XIX International School-Seminar "New magnetic materials for microelectronics", Moscow, Russia, June 28- July 2, 2004  
(poster): A. V. Bezus, A. A. Leonov, Yu. A. Mamalui, Yu. A. Siryuk, *Influence of the domain structure on the spontaneous spin-orientation transitions in magnets with competing anisotropies.*
4. Young scientist day YSD-2005, Kiev, Ukraine, June 1-3, 2005  
(talk): A. A. Leonov, Yu. A. Mamalui, Yu. A. Siryuk, *Influence of the domain structure on the spontaneous spin-orientation transitions in magnets with competing anisotropies.*
5. International Conference of Functional Materials ICFM-2005, Crimea, Ukraine, Partenit, October 3-8, 2005  
(poster): Ya. I. Granovskii, A. A. Leonov, Yu. A. Mamalui, Yu. A. Siryuk, *Rosette of the domain walls in thin films.*
6. International Conference of Functional Materials ICFM-2007, Crimea, Ukraine, Partenit October 1-6, 2007  
(poster): A. A. Leonov, I. E. Dragunov, U. K. Rößler, A. N. Bogdanov, *Phenomenological model of surface-induced anisotropy in magnetic nanoparticles.*
7. Humboldt-Kolleg "Current Science in Ukraine: Humboldt-Club Ukraine General Assembly", Kiev, Ukraine, January 11-12, 2008

---

(talk): A. A. Leonov, I. E. Dragunov, U. K. Röbber, A. N. Bogdanov, *Influence of surface-induced anisotropy on magnetization processes in magnetic nanostructures.*

**8.** The Annual Meeting of the Deutsche Physikalische Gesellschaft and DPG - Spring meeting of the Division Condensed Matter, Berlin, Germany, February 25 - 29, 2008

(talk): A. A. Leonov, I. E. Dragunov, C. Pfeiderer, U. K. Röbber, A. N. Bogdanov, *Skyrmion states in confined condensed matter systems with intrinsic or surface-induced chirality.*

(poster): A. A. Leonov, U. K. Röbber, A. N. Bogdanov, *Surface anisotropy and vortex states in ferromagnetic nanowires and nanotubes.*

**9.** Conference of young scientists "Physics on Low Temperatures", Kharkov, Ukraine, May 20-25, 2008

(talk): A. A. Leonov, I. E. Dragunov, C. Pfeiderer, U. K. Röbber, A. N. Bogdanov, *Skyrmion states in confined condensed matter systems with intrinsic or induced chirality.*

(poster): A. A. Leonov, U. K. Röbber, A. N. Bogdanov, *Surface anisotropy and inhomogeneous distributions of the magnetization in ferromagnetic nanowires and nanotubes.*

**10.** 424. WE-Heraeus-Seminar "Magnetism meets Semiconductors. Spin phenomena in heterostructures and novel materials", Bad Honnef, Germany, 05-07 January, 2009

(poster): A. A. Leonov, U. K. Röbber, A. N. Bogdanov, *Micromagnetic analysis of magnetization reversal in nanolayers of diluted magnetic semiconductors.*

**11.** IFW Winterschool, Oberwiesenthal, Germany, January 19-22, 2009

(talk): A. A. Leonov, U. K. Röbber, A. N. Bogdanov, *Localized and modulated states in confined geometries: chiral nematics and non-centrosymmetric magnetic nanostructures.*

**12.** The Annual Meeting of the Deutsche Physikalische Gesellschaft and DPG - Spring meeting of the Division Condensed Matter, Dresden, Germany, March 22 - 27, 2009

(poster): A. A. Leonov, U. K. Röbber, A. N. Bogdanov, *Micromagnetic analysis of magnetic nanosystems with competing anisotropies.*

(talk): A. A. Leonov, U. K. Röbber, A. N. Bogdanov, *Supercooled and glass-forming liquids as skyrmionic textures.*

**13.** Topological Order: From Quantum Hall Systems to Magnetic Materials. APCTP-MPIPES Seminar and Workshop, Dresden, Germany, June 29 - July 24, 2009

(poster): A. A. Leonov, U. K. Röbber, A. N. Bogdanov, *Skyrmionic textures in chiral magnets.*

---

**14.** The International Conference on Magnetism - ICM 2009, Karlsruhe, Germany, July 26-31, 2009

(poster): A. B. Butenko, A. A. Leonov, A. N. Bogdanov, U. K. Röbler, *Influence of the Dzyaloshinskii-Moriya interactions on vortex states in magnetic nanodisks.*

**15.** 449. WE-Heraeus-Seminar "Rashba and related spin-orbit effects in metals", Bad Honnef, Germany, 06-08 January, 2010

(talk): A. A. Leonov, U. K. Röbler, A. N. Bogdanov, *Skyrmion textures in chiral magnets.*

**16.** The Annual Meeting of the Deutsche Physikalische Gesellschaft and DPG - Spring meeting of the Division Condensed Matter, Regensburg, Germany, March 21 - 26, 2010

(talk): A. A. Leonov, U. K. Röbler, A. N. Bogdanov, *Skyrmion textures in non-centrosymmetric cubic helimagnets.*

**17.** UPV-EHU "Spintronics Days", Bilbao, Spain, 27-28 July, 2010

(talk): A. A. Leonov, U. K. Roessler, A. B. Butenko, A. N. Bogdanov, *Phenomenological theory of skyrmion states in magnets with intrinsic and induced chirality.*

**18.** Joint European Magnetic Symposia, Krakow, Poland, 23-28 August, 2010

(talk): A. A. Leonov, A. N. Bogdanov, U. K. Röbler, *Chiral skyrmions in magnetic layers with surface-induced Dzyaloshinskii-Moriya interactions.*

**19.** The Annual Meeting of the Deutsche Physikalische Gesellschaft and DPG - Spring meeting of the Division Condensed Matter, Dresden, Germany, March 12 - 16, 2011

(talk): A. A. Leonov, A. B. Butenko, A. N. Bogdanov, U. K. Röbler, *Precursor states and skyrmion confinement in cubic helimagnets.*

(poster): F. N. Rybakov, A. A. Leonov, A. B. Butenko, A. N. Bogdanov, U. K. Röbler, *Skyrmion textures in cubic helimagnets with competing cubic and exchange anisotropies.*

(poster): A. A. Leonov, M. Baenitz, W. Schnelle, M. Schmidt, U. K. Roessler, and H. Wilhelm, *Scaling study on magnetic ordering transition and specific heat in the cubic helimagnet FeGe.*

**20.** International Workshop "Spin chirality and Dzyaloshinskii-Moriya interaction", St.-Petersburg, Russia, 25-27 May, 2011

(talk): A. A. Leonov, A. N. Bogdanov, U. K. Röbler, *Theoretical studies on phase diagrams of chiral magnets.*

---



# List of Abbreviations

1D.....	One-dimensional
2D.....	Two-dimensional
3D.....	Three-dimensional
AE.....	Anisotropic exchange
AFM.....	Antiferromagnetic or antiferromagnet
CA.....	Cubic anisotropy
CCA.....	Circular-cell approximation
DDI.....	Dipole-dipole interaction
DM.....	Dzyaloshinskii-Moriya
DMI.....	Dzyaloshinskii-Moriya interaction
FM.....	Ferromagnetic or ferromagnet
IS.....	Isolated skyrmion
LC.....	Liquid crystals
ME.....	Magneto-electric
SA.....	Surface anisotropy
UA.....	Uniaxial anisotropy

---

# Bibliography

- [1] J.I. Martin, J. Nogues, K. Liu, J. L. Vicente, I. K. Schuller, J. Magn. Magn. Mater. **256**, 449 (2003).
- [2] S. D. Bader, Surface Science **500**, 172 (2002).
- [3] R. Skomski, J. Phys.: Condens. Matter **15**, R841 (2003).
- [4] H. Zabel, J. Phys.: Condens. Matter **11**, 9303 (1999).
- [5] M. T. Johnson, P. J. H. Bloemen, F. J. A. den Broeder, J. J. de Vries, Rep. Prog. Phys. **59**, 1409 (1996).
- [6] F. Wilhelm *et al.*, Phys. Rev. Lett. **85**, 413 (1999).
- [7] B. Stahl *et al.*, Phys. Rev. Lett. **84**, 5632 (2000).
- [8] M. Takahashi, M. Tsunoda, and H. Shoji, Vacuum **59**, 814 (2000).
- [9] J. Gui, H. Tang, Li-P. Wang *et al.*, J. Appl. Phys. **87**, 5383 (2000).
- [10] K. E. Johnson, J. Appl. Phys. **87**, 5365 (2000).
- [11] A. N. Bogdanov, U. K. Rößler, K.-H. Müller, J. Magn. Magn. Mater. **238**, 155 (2002).
- [12] P. Pouloupoulos, and K. Baberschke, J. Phys.: Cond. Matter **11**, 9495 (1999).
- [13] T. Ando, E. Ohta, and T. Sato, J. Magn. Magn. Mat. **163**, 277 (1996).
- [14] W. J. M. de Jonge, P. G. H. Bloemen, and F. J. A. den Broeder, *Ultrathin Magnetic Structures* (Springer-Verlag, Berlin, 1994), Vol. 1.
- [15] P. Blomqvist, K. M. Krishnana, and Er. Girt, J. Appl. Phys. **95**, 8487 (2004).
- [16] T. Mewesa, H. Nembach, M. Rickart, and B. Hillebrands, J. Appl. Phys. **95**, 5324 (2004).
- [17] G. Y. Guo, J. Magn. Magn. Mat. **176**, 97 (1997).
- [18] P. Weinberger, L. Szunyogh, Comp. Mat. Sc. **17**, 414 (2000).
- [19] S. K. Kim, J. B. Kortright, Phys. Rev. Lett. **86**, 1347 (2001).

- [20] A. N. Bogdanov, U. K. Röbller, Phys. Rev. Lett. **87**, 037203 (2001).
- [21] A. Bogdanov, A. Hubert, J. Magn. Mater. **138**, 255 (1994).
- [22] A. Bogdanov, A. Hubert, phys. stat. sol. (b) **186**, 527 (1994).
- [23] N. S. Kiselev, A. N. Bogdanov, R. Schäfer, and U. K. Röbller, arXiv: 1102.2726v1 (2011).
- [24] A. Hubert, R. Schäfer, *Magnetic Domains* (Springer, Berlin 1998).
- [25] S. Heinze *et al.*, accepted to Nature Physics (2011) (see also APS March Meeting 2010, March 15-19,2010, abstract L34.014).
- [26] J. M. Higgins *et al.*, Nano Letters **10**, 1605 (2010).
- [27] M. Bode, M. Heide, K. von Bergmann, P. Ferriani *et al.*, Nature **447**, 190 (2007).
- [28] X. Z. Yu, Y. Onose, N. Kanazawa *et al.*, Nature, **465**, 901 (2010).
- [29] X. Z. Yu, N. Kanazawa, Y. Onose *et al.*, Nature Mater. **10**, 106 (2011).
- [30] A. Schmeller, J. P. Eisenstein, L. N. Pfeiffer, and K. W. West, Phys. Rev. Lett. **75**, 4290 (1995); C. Bäuerle, Yu. M. Bunkov, S. N. Fisher, H. Godfrin, and G. R. Pickett, Nature **382**, 332 (1996).
- [31] U. K. Röbller, A. N. Bogdanov, C. Pfeleiderer, Nature **442**, 797 (2006).
- [32] C. Rebbi, G. Soliani, *Solitons and Particles* (World Scientific Pub. Co., Singapore, 1984).
- [33] R. H. Hobart, Proc. Phys. Soc. Lond. **82**, 201 (1963).
- [34] G. H. Derrick, J. Math. Phys. **5**, 1252 (1964).
- [35] T. H. R. Skyrme, Proc. Roy. Soc. Lon. **260**, 127 (1961).
- [36] I. E. Dzyaloshinskii, J. Phys. Chem. Sol. **4**, 241 (1958).
- [37] T. Moriya, Phys. Rev. **120**, 91 (1960).
- [38] D. C Wright, N. D. Mermin, Rev. Mod. Phys. **61**, 385 (1989).
- [39] J. P. Sethna, Phys. Rev. Lett. **51**, 2198 (1983).
- [40] J. P. Sethna, Phys. Rev. B **31**, 6278 (1985).
- [41] I. E. Dzyaloshinskii, J. Sov. Phys. JETP-USSR **19**, 960 (1964).
- [42] I. E. Dzyaloshinskii, J. Sov. Phys. JETP-USSR **20**, 223 (1965).

- 
- [43] I. E. Dzyaloshinskii, J. Sov. Phys. JETP-USSR **20**, 665 (1965).
- [44] Yu. A. Izyumov, Sov. Phys. Usp. **27**, 845 (1984).
- [45] A. N. Bogdanov, U. K. Rößler, M. Wolf, and K. -H. Müller, Phys. Rev. B **66**, 214410 (2002).
- [46] A. P. Levanyuk, D. G. Sannikov, Fiz. Tverd. Tela **18**, 1927 (1976); **18**, 423 (1976) [Sov. Phys. Solid State **18**, 1122 (1976); **18**, 245 (1976)].
- [47] H. Z. Cummins, Phys. Rep. **185**, 211 (1990).
- [48] P. G. De Gennes and J. Prost, *The Physics of Liquid Crystals* (Oxford University Press, Oxford, 1993), 2nd ed.
- [49] E. H. Brandt, Rep. Prog. Phys. **58**, 1465 (1995).
- [50] E. H. Brandt, Phys. Rev. B **68**, 054506 (2003).
- [51] B. Lebech, J. Bernhard, and T. Freltoft, J. Phys.: Condens. Matter **1**, 6105 (1989).
- [52] T. Sato, T. Ando, T. Oku *et al.*, J. Magn. Magn. Matt. **140**, 1785 (1995).
- [53] K. Adachi, N. Achiwa, and M. Mekata, J. Phys. Soc. Japan **49**, 545 (1980).
- [54] S. Maruyama, H. Tanaka, Y. Narumi *et al.*, J. Phys. Soc. Jap. **70**, 859 (2001).
- [55] R. Bügel, A. Faißt, H. V. Löhneysen *et al.*, Phys. Rev. B **65**, 052402 (2002).
- [56] A. Zheludev, S. Maslov, G. Shirane *et al.*, Phys. Rev. Lett. **78**, 4857 (1997).
- [57] M. D. Lumsden, B. C. Sales, D. Mandrus *et al.*, Phys. Rev. Lett. **86**, 159 (2001).
- [58] B. Roessli, J. Schefer, G. Petrakovskii *et al.*, Phys. Rev. Lett. **86**, 1885 (2001).
- [59] N. Hur, S. Park, P. A. Sharma *et al.*, Nature **429**, 392 (2004).
- [60] M. Mostovoy, Phys. Rev. Lett. **96**, 067601 (2006).
- [61] T. Kimura, T. Goto, H. Shintani, K. Ishizaka, T. Arima, and Y. Tokura, Nature, **426**, 55 (2003).
- [62] C. Pfleiderer, D. Reznik, L. Pintschovius *et al.*, Nature **427**, 227 (2004).
- [63] Y. Yanase, M. Sigrist, J. Phys. Soc. Jap. **76**, 124709 (2007).
- [64] J. Beille, J. Voiron, M. Roth, Sol. State Comm. **47**, 399 (1983).
- [65] S. V. Grigoriev, Y. O. Chetverikov, D. Lott, *et al.*, Phys. Rev. Lett. **100**, 197203 (2008).

- [66] P. Ferriani, K. von Bergmann, E. Y. Vedmedenko *et al.*, Phys. Rev. Lett. **101**, 027201 (2008).
- [67] M. Curcic, B. van Waeyenberge, A. Vansteenkiste *et al.*, Phys. Rev. Lett. **101**, 197204 (2008).
- [68] J. Honolka, T. Y. Lee, K. Kuhnke *et al.*, Phys. Rev. Lett. **102**, 067207 (2008).
- [69] A. N. Bogdanov and D. A. Yablonsky, Zh. Eksp. Teor. Fiz. **95**, 178 (1989) [Sov. Phys. JETP **68**, 101 (1989)].
- [70] A. Bogdanov, A. Hubert, J. Magn. Magn. Mater. **195**, 182 (1999).
- [71] A. N. Bogdanov, U. K. Rößler, C. Pfleiderer, Physica B **359**, 1162 (2005).
- [72] G. Blatter, M. V. Feigelman, V. B. Geshkenbein *et al.*, Rev. Mod. Phys. **66**, 1125 (1994).
- [73] A. B. Butenko, A. A. Leonov, U. K. Rößler, A. N. Bogdanov, Phys. Rev. B **82**, 052403 (2010).
- [74] A. N. Bogdanov, M. V. Kudinov, D. A. Yablonskii, Sov. Phys. Solid State **31**, 1707 (1989).
- [75] A. E. Filippov, Zh. Eks. Teor. Fiz. **84**, 971 (1997).
- [76] A. N. Bogdanov, A. A. Shestakov, Phys. Solid State **40**, 1350 (1998).
- [77] A. N. Bogdanov, U. K. Rößler, M. Wolf *et al.*, J. Magn. Magn. Mater. **272-276**, 332 (2004).
- [78] D. Lamago, R. Georgii, C. Pfleiderer *et al.*, Physica B **385-386**, 385 (2006).
- [79] S. Mühlbauer, B. Binz, F. Jonietz *et al.*, Science, **323**, 915 (2009).
- [80] K. Kadowaki, K. Okuda, and M. Date, J. Phys. Soc. Jpn, **51**, 2433 (1982).
- [81] C. Pappas, E. Lelievre-Berna, P. Falus *et al.*, Phys. Rev. Lett., **102**, 197202 (2009).
- [82] C. Pappas, E. Lelievre-Berna, P. Bentley *et al.*, Phys. Rev. B, **83**, 224405 (2011).
- [83] H. Wilhelm, M. Baenitz, M. Schmidt *et al.*, arXiv:1101.0674v1 (2011).
- [84] *Annual Progress Report of the Department of Solid State Physics* (Risoe National Laboratory, Roskilde, Denmark, 1992) ed. by J. Als-Nielsen, J. Skov Pedersen, and B. Lebech.
- [85] S. M. Stishov, A. E. Petrova, S. Khasanov *et al.*, J. Phys.: Condens. Matter. **20**, 235222 (2008).

- 
- [86] S. M. Stishov, A. E. Petrova, A. A. Shikov *et al.*, Phys. Rev. Lett. **105**, 236403 (2010).
- [87] Y. Ishikawa, K. Tajima, D. Bloch, and M. Roth, Solid State Comm. **19**, 525 (1976).
- [88] W. Münzer, A. Neubauer, T. Adams, S. Mühlbauer, C. Franz, F. Jonietz, R. Georgii, P. Böni, B. Pederson, M. Schmidt, et al., Phys. Rev. B (R) **81**, 041203 (2010).
- [89] S. V. Maleyev, in Proceedings of the 8th International workshop on Polarized Neutrons in Condensed Matter Investigations, 2011, edited by W. Bouwman, N. van Dijk, and A. van Well (unpublished).
- [90] B. Binz, A. Vishwanath, V. Aji, Phys. Rev. Lett. **96**, 207202 (2006).
- [91] P. G. de Gennes, in *Fluctuations, Instabilities, and Phase transitions*, ed. T. Riste, NATO ASI Ser. B, vol. 2 (Plenum, New York, 1975).
- [92] U. K. Rößler, A. N. Bogdanov, J. of Non-Crys. Sol. **354**, 4198 (2008).
- [93] S. Chikazumi, *Physics of Ferromagnetism* (Oxford University Press, Oxford, 1997), 2nd ed.
- [94] A. I. Akhiezer, V. G. Bar'yakhtar, and S. V. Peletminskii, *Spin Waves* (North-Holland, Amsterdam; Interscience (Wiley), New York, 1968).
- [95] W. Döring, Mikromagnetismus, in: *Handbuch der Physik*, Vol. 18/2, ed. by S. Flügge (Springer, Berlin, Heidelberg, New York, 1966).
- [96] S. Blundell, *Magnetism in Condensed Matter* (Oxford University Press, Oxford, 2001).
- [97] L. D. Landau and E. M. Lifshitz, *Statistical Physics. Course of Theoretical Physics* (Pergamon, Oxford, 1997), Vol. V.
- [98] I. E. Dzyaloshinskii, Sov. Phys. JETP **5**, 1259 (1957).
- [99] P. Bak and M. H. Jensen, J. Phys. C: Solid State Phys. **13**, L881 (1980).
- [100] O. Nakanishi, A. Yanase, A. Hasegawa, and M. Kataoka, Solid State Comm. **35**, 995 (1980).
- [101] H. Kronmüller, M. Fähnle, *Micromagnetism and the Microstructure of Ferromagnetic Solids* (Cambridge University Press, Cambridge, 2003).
- [102] L. Néel, J. Phys. Rad. **15**, 225 (1954).
- [103] G. Bochi, C. A. Ballentine, H. E. Inglefield *et al.*, Phys. Rev. B **53**, 1729 (1996).

- [104] L. D. Landau, E. Lifshitz, Phys. Z. Sovjetunion **8**, 153 (1935).
- [105] F. Bloch, Zs. Phys. **74**, 295 (1932).
- [106] A. Hubert, *Theorie der Domänen Wände in geordneten Medien* (Springer-Verlag, Berlin, 1974).
- [107] H. Murakawa *et al.*, Phys. Rev. Lett. **103**, 14701 (2009).
- [108] A. B. Butenko et al. Phys. Rev. B **80**, 134410 (2009).
- [109] G. E. Brown and M. Rho, *The multifaceted skyrmion* (New Jersey: World Scientific, 2010).
- [110] F. J. A. den Broeder, W. Hoving, and P. J. H. Bloemen, J. Magn. Magn. Mater. **93**, 562 (1991).
- [111] R. Chang, J. S. Yang, J. C. A. Huang, C. H. Lai, J. Phys. Chem. Sol. **62**, 1737 (2001).
- [112] Y. J. Tang, X. Zhou, X. Chen, B. Q. Liang, W. S. Zhan, J. Appl. Phys **88**, 2054 (2000).
- [113] Z. H. Wang, G. Cristiani, H. U. Habermeier, A. C. Bland, Phys. Rev. B **72**, 054407 (2005).
- [114] C. H. Lai, Y. H. Wang, C. R. Chang, J. S. Yang, Y. D. Yao, Phys. Rev. B **64**, 094420 (2001).
- [115] A. H. Macdonald, P. Schiffer, N. Samarth, Nature Materials **4**, 195 (2005).
- [116] M. Sawicki, Acta Physica Polonica A, **106**,119 (2004).
- [117] T. Dietl, J. König, A. H. MacDonald, Phys. Rev. B **64**, 241201 (2001).
- [118] M. Sawicki, Matsukura, A. Idziaszek, T. Dietl, G. M. Schot, C. Reuster, C. Gould, G. Karczewski, G. Schmidt, W. Molenkamp, Phys. Rev. B **70**, 245325 (2004).
- [119] M. Sawicki, K.-Y. Wang, K. W. Edmonds, R. P. Campion, C. R. Staddon, N. R. S. Farley, C. T. Foxon, E. Papis, E. Kamińska, A. Piotrowska, T. Dietl, B. L. Gallagher, Phys. Rev. B **71**, 121302(R) (2005).
- [120] M. Sawicki, J. Magn. Magn. Mater **300**, 1 (2006).
- [121] A. A. Leonov, I. G. Dragunov, A. N. Bogdanov, Appl. Phys. Lett. **90**, 193112 (2007).
- [122] N. Duxin, M. P. Pileni, W. Wernsdorfer, B. Barbara, A. Benoit, D. Mailly, Langmuir **16**, 11 (2000).



- 
- [123] M. Jamet, W. Wernsdorfer, C. Thirion, V. Dupuis, P. Melinon, A. Perez, and D. Mailly, *Phys. Rev. B* **69**, 024401 (2004).
- [124] W. Wernsdorfer, C. Thirion, N. Demoncy, H. Pascard, and D. Mailly, *J. Magn. Magn. Mater.* **242-245**, 132 (2002).
- [125] W. Wernsdorfer, E. Bonet Orozco, K. Hasselbach, A. Benoit, D. Mailly, O. Kubo, H. Nakano, and B. Barbara, *Phys. Rev. Lett.* **79**, 4014 (1997).
- [126] G. P. Moore, J. Ferre, A. Mougin, M. Moreno, L. Däweritz, *J. Appl. Phys.* **94**, 4530 (2003).
- [127] X. Liu, Y. Sasaki, J. K. Furdyna, *Phys. Rev. B.* **67**, 205204 (2003).
- [128] U. Welp, V. K. Vlasko-Vlasov, A. Menzel, H. D. You, X. Liu, J. K. Furdyna, T. Wojtowicz, *Appl. Phys. Lett.* **85**, 260 (2004).
- [129] K. Y. Wang, M. Sawicki, K. W. Edmonds, R. P. Campion, S. Maat, C. T. Foxon, B. L. Gallagher, T. Dietl, *Phys. Rev. Lett.* **95**, 217204 (2005).
- [130] L. V. Titova, M. Kutrowski, X. Liu, R. Chakarvorty, W. L. Lim, T. Wojtowicz, J. K. Furdyna, M. Dobrowolska, *Phys. Rev. B* **72**, 165205 (2005).
- [131] X. Liu, W. L. Lim, L. V. Titova, M. Dobrowolska, J. K. Furdyna, M. Kutrowski, T. Wojtowicz, *J. Appl. Phys.* **98**, 063904 (2005).
- [132] A. Pross, S. J. Bending, K. Y. Wang, K. W. Edmonds, R. P. Campion, C. T. Foxon, B. L. Gallagher, M. Sawicki, *J. Appl. Phys.* **99**, 093908 (2006).
- [133] K. Y. Wang, K. W. Edmonds, L. X. Zhao, M. Sawicki, R. P. Campion, B. L. Gallagher, C. T. Foxon, *Phys. Rev. B* **72**, 115207 (2005).
- [134] M. Albrecht, G. Hu, I. L. Guhr, T. C. Ulbrich, J. Boneberg, P. Leiderer, G. Schatz, *Nature Materials* **4**, 203 (2005).
- [135] T. Shono, T. Hasegawa, T. Fukumura, F. Matsukura, H. Ohno, *Appl. Phys. Lett.* **77**, 1363 (2000).
- [136] U. Welp, V. K. Vlasko-Vlasov, X. Liu, J. K. Furdyna, T. Wojtowicz, *Phys. Rev. Lett.* **90**, 167206 (2003).
- [137] T. Fukumura, T. Shono, K. Inaba, H. Koinuma, F. Matsukura, T. Hasegawa, H. Ohno, *Physica E* **10**, 135 (2001).
- [138] A. Pross, S. Bending, K. Edmonds, R. P. Campion, C. T. Foxon, B. Gallagher, *J. Appl. Phys.* **95**, 7399 (2004).
- [139] L. Thevenard, L. Largeau, O. Mauguin, G. Patriarche, A. Lemaitre, N. Vernier, J. Ferré, *Phys. Rev. B.* **73**, 195331 (2006).

- [140] E. C. Stoner, E. P. Wohlfarth, *Phylos. Trans. R. Soc. London* **A420**, 559 (1948).
- [141] E. J. Torok, H. N. Oredson, A. L. Olson, *J. Appl. Phys.* **35**, 3469 (1964).
- [142] A. I. Mitsek, *Phys. Status Solidi B* **59**, 309 (1973).
- [143] A. I. Mitsek, N. P. Kolmakova, and D. I. Sirota, *Fiz. Met. Metalloved.* **38** (1), 35 (1974).
- [144] G. Asti, F. Bolzoni, *J. Magn. Magn. Mater.* **20**, 29 (1980).
- [145] Y. T. Millev, J. R. Cullen, H. P. Oepen, *J. App. Phys.* **83**, 6500 (1998).
- [146] H. P. Oepen, Y. T. Millev, H. F. Ding, S. Putter, J. Kirschner, *Phys. Rev. B* **61**, 9506 (2000).
- [147] A. Thiaville, *J. Magn. Magn. Mater.* **182**, 5 (1998).
- [148] V. G. Baryakhtar, A. N. Bogdanov, D. A. Yablonskii, *Usp. Fiz. Nauk* **156** (1), 47 (1988) [*Sov. Phys.Usp.* **31**, 810 (1988)].
- [149] I. E. Dragunov, S. V. Bukhtiyarova, I. V. Zhikharev, A. N. Bogdanov, U. K. Röbller, *Fiz. Tverd. Tela* **48**, 1504 (2006) [*Phys. Solid State* **48**, 1591 (2006)].
- [150] U. K. Röbller, S. V. Bukhtiyarova, I. V. Zhikharev, A. N. Bogdanov, *J. Magn. Magn. Mater.* **290-291**, 772 (2005).
- [151] A. N. Bogdanov, I. E. Dragunov, U. K. Röbller, *J. Magn. Magn. Mater.* **316**, 225 (2007).
- [152] K. I. Belov, A. K. Zvezdin, A. M. Kadomtseva, R. Z. Levitin, *Usp. Fiz. Nauk* **119**, 447 (1976) [*Sov. Phys.Usp.* **19**, 574 (1976)].
- [153] D. Melville, W. Khan, and S. Rinaldi, *IEEE Trans. Magn.* **12**, 1012 (1976).
- [154] T. Poston and I. Stewart, *Catastrophe Theory and Its Applications* (Pitman, London, 1978).
- [155] A. Yelon, O. Voegeli, E. W. Pugh, *J. Appl. Phys.* **36**, 101 (1965).
- [156] E. J. Torok, *J. Appl. Phys.* **36**, 952 (1965).
- [157] C. R. Chang, D. R. Fredkin, *J. Appl. Phys.* **63**, 3435 (1988).
- [158] C. R. Chang, D. R. Fredkin, *J. Appl. Phys.* **69**, 2431 (1991).
- [159] M. I. Kaganov, A. A. Yagubov, *Fiz. Met. Metalloved.* **36** (6), 1127 (1973).
- [160] A. N. Bogdanov, I. Ya. Granovskii, *Fiz. Tverd. Tela (Leningrad)* **29** (10), 2913 (1987) [*Sov. Phys. Solid State* **29** (10), 1674 (1987)].

- 
- [161] V. G. Baryakhtar, A. N. Bogdanov, D. A. Yablonskii, *Fiz. Tverd. Tela* (Leningrad) **29** (10), 116 (1987) [*Sov. Phys. Solid State* **29** (10), 65 (1987)].
- [162] A. N. Bogdanov, I. E. Dragunov, *Fiz. Nizk. Temp.* **24**, 1136 (1998) [*Low. Temp. Phys.* **24**, 852 (1998)].
- [163] A. N. Bogdanov, A. V. Zhuravlev, U. K. Rößler, *Phys. Rev. B* **75**, 094425 (2007).
- [164] F. Y. Yang, C. H. Chang, C. L. Chien, T. Ambrose, J. J. Krebs, G. A. Prinz, V. I. Nikitenko, V. S. Gornakov, A. J. Shapiro, R. D. Shull, *Phys. Rev. B* **65**, 174410 (2002).
- [165] K. Pappert, C. Gould, M. Sawicki, J. Wenish, K. Brunner, G. Schmidt, L. W. Molenkamp, *New J. of Phys.* **9**, 354 (2007).
- [166] D. Y. Shin, S. J. Chung, S. Lee, X. Liu, J. K. Furdyna, *Phys. Rev. Lett.* **98**, 047201 (2007).
- [167] L. Thevenard, L. Largeau, O. Mauguin, A. Lemaître, K. Khazen, H. J. von Bardeleben, *Phys. Rev. B* **75**, 195218 (2007).
- [168] A. Dourlat, V. Jeudy, C. Testelin, F. Bernardot, K. Khazen, C. Gourdon, L. Thevenard, L. Largeau, O. Mauguin, A. Lemaître, *J. Appl. Phys.* **102**, 023913 (2007).
- [169] C. Gourdon, A. Dourlat, V. Jeudy, K. Khazen, L. Thevenard, A. Lemaître, *Phys. Rev. B* **76**, 241301 (2007).
- [170] J. J. Versluijs, M. A. Bari, J. M. D. Coey, *Phys. Rev. Lett* **87**, 026601 (2001).
- [171] M. Yamanouchi, D. Chiba, F. Matxukura, H. Ohno, *Nature (London)* **428**, 539 (2004).
- [172] J. Honolka, S. Masmanidis, H. X. Tang, M. L. Roukes, D. D. Awschalom, *J. Appl. Phys.* **97**, 063903 (2005).
- [173] A. W. Holleitner, H. Knotz, R. C. Myers, A. C. Gossard, D. D. Awschalom, *J. Appl. Phys.* **97**, 10D314 (2005).
- [174] A. Sugawara, T. Akashi, P. D. Brown, R. P. Campion, T. Yoshida, B. L. Gallagher, A. Tonomura, *Phys. Rev. B* **75**, 241306(R) (2007).
- [175] A. Sugawara, H. Kasai, A. Tonomura, P.D. Brown, R. P. Campion, K. W. Edmonds, B. L. Gallagher, J. Zemen, T. Jungwirth, *Phys. Rev. Lett.* **100**, 047202 (2008).
- [176] A. N. Bogdanov, D. A. Yablonskii, *Fiz. Tverd. Tela* **22**, 680 (1980), [*Sov. Phys. Solid State* **22**, 399 (1980)].

- [177] C. Kooy, U. Enz, Philips Res. Repts. **15**, 7 (1960).
- [178] A. H. Bobeck, E. Della Torre, *Magnetic Bubbles*, (North-Holland Publishing Company, Amsterdam 1975).
- [179] V. Gehanno, Y. Samson, A. Marty, B. Gilles, A. Chamberod, J. Magn. Magn. Mater. **172**, 26 (1997).
- [180] O. Hellwig, A. Berger, J. B. Kortright, E. E. Fullerton, J. Magn. Magn. Mater. **319**, 13 (2007).
- [181] B. Barbara, Solid State Sciences **7**, 668 (2005).
- [182] Q. A. Pankhurst, J. Connolly, S. K. Jones, J. Dobson, J. Phys. D, **36**, R167 (2003).
- [183] F. J. Lazano, A. Larrea, A. R. Abadia, J. Magn. Magn. Mat. **257**, 346 (2003).
- [184] S. I. Cha, C. B. Mo, K. T. Kim, S. H. Hong, J. Mater. Res. **20**, 2148 (2005).
- [185] W. Wernsdorfer, E. Bonet Orozco, K. Hasselbach, A. Benoit, D. Mailly, O. Kubo, H. Nakano, B. Barbara, Phys. Rev. Lett. **79**, 4014 (1997).
- [186] A. Fert, L. Piraux, J. Magn. Magn. Mater. **200**, 338 (1999).
- [187] D. J. Sellmyer, M. Zheng, R. Skomski, J. Phys.: Condens. Matter **13**, R433 (2001).
- [188] A. Maurer, F. Ott, G. Chaboussant, Y. Soumare, J.-Y. Piquemal, G. Viau, Appl. Phys. Lett. **91**, 17250 (2007).
- [189] D. A. Allwood, G. Xiong, C. C. Faulkner, D. Atkinson, D. Petit, R. P. Cowburn, Science **9**, 1688 (2005).
- [190] D. H. Reich, M. Tanase, A. Hultgren, L. A. Bauer, C. S. Chen, G. J. Meyer, J. Appl. Phys. **93**, 7275 (2003).
- [191] A. Leonhardt, M. Ritschel, R. Kozhuharova, A. Graff, T. Mühl, R. Huhle, I. Mönch, D. Elefant, and C.M. Schneider, Diamond Rel. Mater. **12**, 790 (2003).
- [192] H. J. Elmers, J. Hauschild, H. Höche, U. Gradmann, H. Bethge, D. Heuer, U. Köhler, Phys. Rev. Lett. **73**, 898 (1994).
- [193] B. Leven, G. Dumpich, Phys. Rev. B **71**, 064411 (2005).
- [194] L. Belliard, J. Miltat, A. Thiaville, S. Dubois, J. L. Duvail, L. Piraux, J. Magn. Magn. Mater. **190**, 1 (1998).
- [195] K. Nielsch, R. B. Wehrspohn, J. Barthel, J. Kirschner, U. Gösele, S. F. Fischer, H. Kronmüller, Appl. Phys. Lett. **79**, 1360 (2001).

- 
- [196] Y. Henry, H. Ounadjela, L. Piraux, S. Dubois, J.-M. George, J.-L. Duvail, *Eur. Phys. J. B* **20**, 35 (2001).
- [197] Y. C. Sui, R. Skomski, K. D. Sorge, D. J. Sellmyer, *Appl. Phys. Lett.* **84**, 1525 (2004).
- [198] M. Mertig, R. Kirsch, W. Pompe, *Appl. Phys. A* **66**, 8723 (1998).
- [199] G. Tourillon, L. Pontonnier, J. P. Levy, V. Langlais, *Electrochem. Solid-State Lett.* **3**, 20 (2000).
- [200] F. Tao, M. Guan, Y. Jian, J. Zhu, Z. Xu, Z. Xue, *Adv. Mater.* **18**, 2161 (2006).
- [201] S. Hampel, A. Leonhardt, D. Selbmann, K. Biedermann, D. Elefant, Ch. Müller, T. Gemming, B. Büchner, *Carbon* **44**, 2316 (2006); C. Müller, S. Hampel, D. Elefant, K. Biedermann, A. Leonhardt, M. Ritschel, B. Büchner, *Carbon* **44**, 1746 (2006).
- [202] H. Terrones, F. López-Urías, E. Muñoz-Sandoval, J. A. Rotdríguez-Manzo, A. Zamudio, A. L. Elías, M. Terrones, *Solid State Sciences* **8**, 303 (2006).
- [203] X. Ma, H. Zhang, J. Xu, J. Niu, Q. Yang, J. Sha, D. Yang, *Chem. Phys. Lett.* **363**, 579 (2002).
- [204] T. Zhang, C. G. Jin, T. Qian, X. L. Lu, J. M. Bai, X. G. Li, *J. Mater. Chem.* **14**, 2787 (2004).
- [205] K. Shantha Shankar, A. K. Raychaudhuri, *Mater. Sci. Eng. C* **25**, 738 (2005).
- [206] J. Curiale, R. D. Sánchez, H. E. Troiani, A. G. Leyva, P. Levy, *Appl. Phys. Lett.* **87**, 043113 (2005).
- [207] M.-T. Chang, L.-J. Chou, C.-H. Hsieh, Y.-L. Chueh, Z. L. Wang, Y. Murakami, D. Shindo, *Adv. Mater.* **19**, 2290 (2007).
- [208] J. Bachmann, J. Jing, M. Knez, S. Barth, H. Shen, Sanjay Mathur, U. Gösele, K. Nielsch, *J. Am. Chem. Soc.* **129**, 9554 (2007).
- [209] F. Tian, J. Zhu, D. Wei, *J. Phys. Chem. C* **111**, 12669 (2007).
- [210] B. Das, K. Mandal, Pintu Sen, S. K. Bandopadhyay, *J. Appl. Phys.* **103**, 013908 (2008).
- [211] X. Y. Zhang, G. H. Wen, Y. F. Chan, R. K. Zheng, X. X. Zhang, N. Wang, *Appl. Phys. Lett.* **83**, 3341 (2003).
- [212] Y. Rheem, B.-Y. Yoo, W. P. Beyermann, N. W. Myung, *Nanotechnology* **18**, 015202 (2007).
- [213] R. Ferré, K. Ounadjela, J. M. George, L. Piraux, S. Dubois, *Phys. Rev. B* **56**, 14066 (1997).

- [214] U. Ebels, J.-L. Duvail, P. E. Wigen, L. Piraux, L. D. Buda, K. Ounadjela, Phys. Rev. B **64**, 144421 (2001).
- [215] R. Arias, D. L. Mills, Phys. Rev. B **63**, 134439 (2001)
- [216] T.-M. Nguyen, M. G. Cottam, H. Y. Liu, Z. K. Wang, S. C. Ng, M. H. Kuok, D. J. Lockwood, K. Nielsch, U. Gösele, Phys. Rev. B **73**, 140402(R) (2006).
- [217] P. Bruno, Phys. Rev. B **39**, 865 (1989).
- [218] V. V. Ivanovskaya, C. Köhler, G. Seifert, Phys. Rev. B **75**, 075410 (2007).
- [219] S. Dubois, J. Colin, J. L. Duvail, L. Piraux, Phys. Rev. B **61**, 14315 (2000).
- [220] A. Kumar, S. Fähler, H. Schlörb, K. Leistner, L. Schultz, Phys. Rev. B **73**, 064421 (2006).
- [221] J. De La Torre Medina, M. Darques, L. Piraux, J. Phys. D: **41**, 032008 (2008).
- [222] C. Antoniak *et al.*, Phys. Rev. Lett. **97**, 117201 (2006).
- [223] A. Thiaville, A. Fert, J. Magn. Magn. Mater. **113**, 161 (1992).
- [224] T. Shinjo, T. Okuno, R. Hassdorf, K. Shigeto, T. Ono, Science **289**, 930 (2000).
- [225] U. K. Rößler, A. N. Bogdanov, K.-H. Müller, IEEE Trans. Magn. **38**, 2586 (2002).
- [226] A. N. Bogdanov, U. K. Rößler, K.-H. Müller, J. Magn. Magn. Mater. **242-245**, 594 (2002).
- [227] A. N. Bogdanov, U. K. Rößler, K.-H. Müller, J. Magn. Magn. Mater. **238**, 155 (2002).
- [228] A. N. Bogdanov, U. K. Rößler, arxiv: 0101262 (2001).
- [229] T. Nagai, H. Yamada, M. Konoto, T. Arima, M. Kawasaki, K. Kimoto, Y. Matsui, Y. Tokura, Phys. Rev. B **78**, 180414(R) (2008).
- [230] A. Crépieux, C. Lacroix, J. Magn. Magn. Mater. **182**, 341 (1998).
- [231] U. K. Rößler, *et al.*, arXiv: 1009.4849 (2010).
- [232] A. A. Leonov, A. N. Bogdanov, U. K. Rößler, arXiv:1001.1992v3 (2010).
- [233] A. Bogdanov, JETP Lett. **62**, 247 (1995).
- [234] A. A. Belavin, and A. M. Polyakov, Pis'ma Zh. Eksp. Teor. Fiz. **22**, 503 (1975) [JETP Lett. **22**, 245 (1975)].
- [235] N. Metropolis, A. W. Rosenbluth, M. N. Rosenbluth, A. H. Teller, and E. Teller, J. of Chem. Phys. **21**, 1087 (1953).

- 
- [236] K. Binder, D. W. Heerman, *Monte Carlo Simulation in Statistical Physics* (Springer, Berlin 1992), 2nd ed.
- [237] A. K. Rastogi, E. P. Wohlfarth, *phys. stat. sol. (b)* **142**, 569 (1987).
- [238] C. P. Sebastian *et al.*, arXiv: 0612225 (2006).
- [239] B. Barbara, C. Bécle, J.-L. Feron, R. Lemaire, and R. Pauthenet, *C.R. Acad. Sci. Paris* **267B**, 244 (1968).
- [240] B. Barbara, C. Bécle, R. Lemaire, and D. Paccard, *J. Physique* **32**, C1-299 (1971).
- [241] C. Wilkinson, F. Sinclair, and J. B. Forsyth, 5th Conf. on Solid Compounds of Transition Elements. Extended Abstracts, Uppsala 1976, p. 158.
- [242] E. Franus-Muir, M. L. Plumer, and E. Fawcett, *J. Phys. C* **17**, 1107 (1984).
- [243] M. L. Plumer and M. B. Walker, *J. Phys. C* **15**, 7181 (1982).
- [244] D. Bloch, J. Voiron, V. Jaccarino, and J. H. Wernick, *Phys. Lett. A* **51**, 259 (1975).
- [245] S. V. Grigoriev, S. V. Maleyev, A. I. Okorokov, Y. O. Chetverikov, R. Georgii, P. Böni, D. Lamago, H. Eckerlebe, and K. Pranzas, *Phys. Rev. B* **72**, 134420 (2005).
- [246] Yu. M. Koroteev, G. Bihlmayer, J. E. Gayone, E. V. Chulkov, S. Blügel, P. M. Echenique, Ph. Hofmann, *Phys. Rev. Lett.* **93**, 046403 (2004).
- [247] T. Hirahara, T. Nagao, I. Matsuda, G. Bihlmayer, E. V. Chulkov, Yu. M. Koroteev, P. M. Echenique, M. Saito, S. Hasegawa, *Phys. Rev. Lett.* **97**, 146803 (2006).
- [248] P. Oswald, J. Baudry, and S. Parkl, *Phys. Rep.* **337**, 67 (2000).
- [249] A. N. Bogdanov, *JETP Lett.*, **71**, 85 (2000).
- [250] W. H. Press, S. A. Teukolsky, W. T. Vetterling, B. P. Flannery, *Numerical Recipes - The Art of Scientific Computing* (Cambridge University Press, Cambridge, 2007), 3d ed.
- [251] N. S. Kiselev, I. E. Dragunov, U. K. Rößler, A.N. Bogdanov, *Appl. Phys. Lett.* **91**, 132507 (2007).
- [252] N. S. Kiselev, U. K. Rößler, A.N. Bogdanov, O. Hellwig, *Appl. Phys. Lett.* **93**, 162502 (2008).
- [253] O. Hellwig, A. Berger, J. B. Kortright, E. E. Fullerton, *J. Magn. Magn. Matter.* **319**, 13 (2007).

- [254] C. Bran, A. B. Butenko, N. S. Kiselev, U. Wolff, L. Schultz, O. Hellwig, U. K. Rößler, A.N. Bogdanov, V. Neu, Phys. Rev. B **79**, 024430 (2009).
- [255] N. S. Kiselev, I. E. Dragunov, V. Neu, U. K. Rößler, A. N. Bogdanov J. Appl. Phys. **103**, 043907 (2008).
- [256] Y. S. Lin, Y. O. Tu, Appl. Phys. Lett. **18**, 247 (1971).
- [257] Y. O. Tu, J. of Appl. Phys. **42**, 5704 (1971).
- [258] R. M. Hornreich, M. Kugler, S. Shtrikman, Phys. Rev. Lett. **48**, 1404 (1982).
- [259] A. N. Bogdanov, U. K. Rößler, A. A. Shestakov, Phys. Rev. E, **87**, 016602 (2003).
- [260] A. N. Bogdanov, A. A. Shestakov, J. of Exp. and Theor. Phys. **86**, 911 (1998).
- [261] I. I. Smalyukh *et al.*, Phys. Rev. E, **72**, 061707 (2005).
- [262] I. I. Smalyukh, Y. Lansac, N. A. Clark, and R. P. Trivedi, Nature Mater. **9**, 139 (2009).
- [263] M. Kawachi, O. Kogure, Y. Kato, Jap. J. Appl. Phys. **13**, 1457 (1974).
- [264] W. E. L. Haas, J. E. Adams, Appl. Phys. Lett. **25**, 263 (1974); Appl. Phys. Lett. **25**, 535 (1974).
- [265] V. G. Bhide, S. Chandra, S. C. Jain, R. K. Medhekar, J. of Appl. Phys. **47**, 120 (1976).
- [266] T. Akahane, T. Tako, Molec. Crystals liq. Crystals, **38**, 251 (1977).
- [267] S. Hirata, T. Akahane, and T. Tako, Molec. Crystals liq. Crystals, **75**, 47 (1981).
- [268] P. E. Cladis, M. Kleman, Molec. Crystals liq. Crystals, **16**, 1 (1972).
- [269] A. Stieb, J. Phys. France, **41**, 961 (1980).
- [270] S. Pirkel, P. Ribiere, P. Oswald, Liq. Cryst. **13**, 413 (1993).
- [271] M. Uchida *et al.*, Phys. Rev. B **77**, 184402 (2008).
- [272] J. W. Felix, D. Mukamel, R. M. Hornreich, Phys. Rev. Lett. **57**, 2180 (1986).
- [273] B. Lebech *et al.*, J. Magn. Magn. Mater. **140**, 119 (1995).
- [274] S. Kusaka *et al.*, Solid State Commun. **20**, 925 (1976).
- [275] T. Komatsubara, S. Kusaka, and Y. Ishikawa, in *Proceedings of the 6th International Conference on Internal Friction and Ultrasonic Attenuation in Solids* (University of Tokyo Press, 1977) p. 237.



- 
- [276] C. I. Gregory *et al.*, J. Magn. Magn. Mater. **104-107**, 689 (1992).
- [277] C. Thessieu *et al.*, J. Phys. Condens. Matter **9**, 6677 (1997).
- [278] A. Neubauer *et al.*, Phys. Rev. Lett. **102**, 186602 (2009).
- [279] Y. Ishikawa and M. Arai, J. Phys. Soc. Jpn. **53**, 2726 (1984).
- [280] Y. Ishikawa *et al.*, Phys. Rev. B **31**, 5884 (1985).
- [281] S. V. Grigoriev *et al.*, Phys. Rev. B **73**, 224440 (2006).
- [282] S. V. Grigoriev *et al.*, Phys. Rev. B **74**, 214414 (2006).
- [283] M. Date, K. Okuda, and K. Kadowaki, J. Phys. Soc. Jpn, **42**, 1555 (1977).
- [284] B. Schaub and D. Mukamel, Phys. Rev. B **35**, 6385 (1985).
- [285] M. Yamashita, J. Phys. Soc. Jap. **56**, 1414 (1987).
- [286] A. B. Borisov, and F. N. Rybakov, Low Temp. Phys. **36**, 766 (2010).
- [287] S. Ghosh, R. Rajaraman, Int. J. Mod. Phys. B **12**, 37 (1998).
- [288] G. Tarjus, S. A. Kivelson, Z. Nussinov, P. Viot, J. Phys.: Condens. Matter **17**, R1143 (2005).
- [289] F.C. Frank, Proc. Royal Soc. (London) Series A **215**, 43 (1952).
- [290] M. Kléman, J. F. Sadoc, J. Physique Lett. (Paris) **40**, L569 (1979).
- [291] J. F. Sadoc, R. Mosseri, J. Physique (France) **45**, 1025 (1984).
- [292] D. R. Nelson, Phys. Rev. B **28**, 5515 (1983).
- [293] D. R. Nelson, M. Widom, Nucl. Phys. B **240**, 113 (1984).
- [294] H. M. S. Coxeter, *Regular complex polytopes* (Cambridge University Press, 1991), 2nd edition.
- [295] N. Rivier, D. M. Duffy, J. Physique **43**, 43 (1982).
- [296] J. F. Sadoc, J. Physique Lett. **44**, 707 (1983).
- [297] S. Sachdev, D. R. Nelson, Phys. Rev. B **32**, 1480 (1985).
- [298] G. Venkataraman, D. Sahoo, Contemp. Phys. **26**, 579 (1985); *ibid.* **27**, 3 (1985).
- [299] Z. Nussinov, Phys. Rev. B **69**, 014208 (2004).
- [300] G. S. Adkins, C. R. Nappi, E. Witten, Nucl. Phys. B **228**, 552 (1983).

- [301] H. Shintani, H. Tanaka, *Nature Phys.* **2**, 200 (2006).
- [302] R. A. Battye, P. M. Sutcliffe, *Phys. Rev. Lett.* **86**, 3989 (2001).
- [303] M. Kugler, S. Shtrikman, *Phys. Rev. D* **40**, 3421 (1989).
- [304] D. B. Miracle, *Nature Mater.* **3**, 697 (2004).
- [305] H. W. Sheng, W. K. Luo, F. M. Alamgir, J. M. Bai, E. Ma, *Nature* **439**, 419 (2006).

# Acknowledgments

This thesis is a result of research carried out at Donetsk National University (Department of General Physics and Didactics of Physics), at Donetsk Institute for Physics and Technology (Department of Theory of Magnetism and Phase Transitions), and at Dresden Institute for Theoretical Solid State Physics. Many people have contributed to this project. I would like herein to thank all of them.

I would like to start with my first scientific supervisor, Prof. Dr. Vitalii A. Zablotskiy, and to thank him for his guidance during my immersion into amazing world of micromagnetic calculations. I want to thank him for learning me so much about micromagnetics and his constant advices on my diploma thesis at the Donetsk National University (Department of Radiophysics). I'd like to thank him for many of good opportunities he gave me, but none of them I made use of.

I would like also to express many thanks to my promoters Prof. Dr. Yu. A. Mamalui and Dr. Yu. A. Siryuk at Donetsk National University (Department of General Physics and Didactics of Physics) during my work on the post-graduate project "Spin-reorientation phase transitions in ferrite-garnet films with competing anisotropies (experiment and theory)". Discussions with Prof. Siryuk on the experimental magneto-optical methods of observations of domain structures in magnets have been always very useful and nice. I am indebted to Prof. Mamalui for her introductory remarks into solid state physics and magnetism. I have been always fascinated by her great physical intuition. My first pedagogical experience is also closely related to her name.

I am very grateful to Prof. Dr. Ya. I. Granovski for fruitful discussions and for giving me some knowledge on the elliptical functions as applied to micromagnetic simulations. He always gave me a confidence in the correctness of my results.

I want to thank Dr. A. V. Bezus for sharing with me not so particularly easy three years of post-graduate study at Donetsk National University. His talent to give the second life to old experimental setups by his head and hands is really incredible.

I am also very happy to express many thanks to Prof. Dr. S. V. Tarasenko who accepted me for scientific work at Donetsk Institute for Physics and Technology. I was not only advised by him on many subjects of the mathematical physics, but also enjoyed his subtle and sparkling sense of humor. The atmosphere he created in his department is hardly to forget. I am also pleased to thank all my colleagues from Department of Theory of Magnetism and Phase Transitions (Donetsk). Especially, the discussions and collaboration with Dr. I. E. Dragunov and Dr. A. V. Zhuravlev are appreciated. I also remember hard scientific war of words with Prof. Dr. V. N. Krivoruchko during the seminars which are ultimately very important to harden the

---

character of young physicist.

But the real work on the present thesis has been done at Dresden Institute for Theoretical Solid State Physics. I did not even think before that the physics can be so intensive, but at the same time very delightful! Here I met two my mentors, Prof. Dr. A. N. Bogdanov and Dr. U. K. Rößler, ready to teach me the best of their own knowledge and to help me with my problems and troubles. Ulrich Rößler has a paramount contribution to this work. He has not only read different draft versions of the thesis and given me very valuable comments, but also guided me into the world of numerical algorithms of micromagnetic calculations. His constant concern on the results and progress of skyrmionic physics prompted to achieve the main results of the present thesis. His passion in doing physics is "infectious". And his ability to read the scientific papers in all places on earth except dark ones needs a long time of hard training. I would like also to thank Prof. Dr. Alexei N. Bogdanov for the chance to do research in his group and to defend the present thesis. I am very thankful for numerous discussions with him and the knowledge he shared with me. The spectrum of the resolved micromagnetic problems in the present thesis has its source from his rich experience and distinctive understanding of physics.

I also would like to express special thanks to Prof. Dr. H. Eschrig for his guidance and continuous support. I am also obliged to Prof. Dr. J. van den Brink for the help with the defence of the thesis and for that particular spirit to score a success he introduced into the work of the department. I would like to thank all my colleagues for the admirable working hours: M. Richter, U. Nitzsche, A. Möbius, G. Rötzer, K. Koepernik, S. Schönecker, C. Neise and many others.

The discussions with many people at the conferences are of the special gratitude. Particularly, I am thankful to Prof. Dr. S. Blügel, Dr. H. Wilhelm, Dr. S. Heinze, Dr. S. V. Grigoriev, Dr. G. Bihlmayer, Dr. J.-H. Han, Dr. M. Zhitomirsky, Dr. R. Schäfer, Dr. V. Neu, Prof. Dr. E. Sherman, and Dr. V. Heera.

And finally, this work has been for sure impossible to finish without support and understanding giving to me by my parents, Leonov Alexandr and Galina and my brother Denys. Many deep thanks to all of you.

## Versicherung

Hiermit versichere ich, dass ich die vorliegende Arbeit ohne unzulässige Hilfe Dritter und ohne Benutzung anderer als der angegebenen Hilfsmittel angefertigt habe, die aus fremden Quellen direkt oder indirekt übernommenen Gedanken sind als solche kenntlich gemacht. Die Arbeit wurde bisher weder im Inland noch im Ausland in gleicher oder ähnlicher Form einer anderen Prüfungsbehörde vorgelegt. Die Arbeit entstand mit wissenschaftlicher Betreuung durch Prof. Helmut Eschrig am Leibniz-Institut für Festkörper- und Werkstoffforschung Dresden. Ich habe vorher kein anderes Promotionsverfahren eröffnet. Ich erkenne die Promotionsordnung der Fakultät Mathematik und Naturwissenschaften der Technischen Universität Dresden in der aktuell gültigen Fassung an.

---

Ort, Datum

---

Andriy Leonov